One and Two Photon Absorption of Atoms and Ions

A thesis submitted for the degree of

Doctor of Philosophy

Presented to:

The School of Physical Sciences, Faculty of Science and Health, Dublin City University

Author

Caroline Banahan

B. Sc.

Research Supervisor

Dr. Paul van Kampen

Declaration

I hereby certify that this material, which I now submit for assessment on the programme of study leading to the award of Doctor of Philosophy, Ph.D. is entirely my own work and has not been taken from the work of others save and to the extent that such work has been cited and acknowledged within the text of my work.

Signed: _____ **ID No.:** 50304476

Date: _____

To Mike and to my parents

Acknowledgements

First and foremost, I would like to thank my supervisor, Dr. Paul van Kampen. Over the past four and a half years he has encouraged, advised and guided me through my PhD. Despite all the difficulties I encountered his patience and support never failed to get me through them. I also extend this gratitude and thanks to Prof. John Costello for the insightful discussions and helpful suggestions he has made, all of which ensured a steady progression in this work. Sincere thanks to Deirdre Kilbane, who worked as a postdoc with me for nearly two years. Her commitment and hard work set a high standard that I tried to maintain.

I wish to thank the other members of the physics department, both past and present, who have made the day to day experiences so much more enjoyable. Past members: Eoin, Kevin, Jean-René, Deirdre, James, Brendan, Lynn; present folk: John, Ricky, Padraig, Vincent, Jiang-Xi, Mossy, Eanna, Conor McL, Conor C, Mairead, Pat Y, Colm, Paddy H., Paddy K., Alan, Stephen, Jack, David. Thanks for all those fruitful discussions over coffee and readiness to let me 'borrow' things from your labs. Thanks to David for spending a summer working with me...we were close to having that perfect beam profiler! A special thanks to John and Phil, my office and hiking buddies, who managed to keep a subtle balance between trick-acting and work, my experience here would never be the same without you guys. I wish everyone the best in their future endeavours.

I would also like to acknowledge Des Lavelle in the workshop and Pat Wogan who have the extraordinary ability of understanding the strange requests and ideas that I have thrown their way. Thanks also to Alan Hughes for his readiness to help with any query I sent his way. I wish to thank everybody in the physics department, in particular Lisa Peyton and Sheila Boughton, the school secretaries.

A special mention for my collaborators at Århus, in particular, John West, Finn Folkmann, Jean-Marc Bizau, Henrik Kjeldsen, Deirdre Kilbane and Shane Scully. I learned a lot of physics and improved (thankfully) with each trip I made. I admire the dedication and drive needed to work during one's 'slot' at the beamline and extend my thanks to each one.

Finally, thanks to my friends and parents for all your support, it was and is appreciated. Special thanks to Mike, who has kept me sane and happy through all the ups and downs.

Abstract

One and two-photon photoabsorption of atoms and ions is the primary focus of this study, with special emphasis on photoabsorption in a laser-produced strontium plasma. The dual laser plasma (DLP) technique has been employed to carry out these studies and adapted to include an optical parametric oscillator (OPO), tuneable in the visible wavelength range (410-700 nm), to permit two-photon and two-colour photoabsorption investigations. The OPO was tuned to one and two-photon resonances in Sr^{0} and Sr^{+} and the XUV photoabsorption spectrum was studied for various laser intensities and detunings from resonance. Fluorescence measurements were also made to elucidate the underlying excitation dynamics in the atom / ion after laser irradiation.

Absolute photoionization cross-section measurements of the Kr-isoelectronic sequence (Rb^{+}, Sr^{2+}) were made at the ASTRID storage ring at the University of Aarhus, Denmark. These results were complemented by measurements made with the DLP technique. Inner-shell excitation studies in Pb^{2+}, Bi^{3+} and Sr^{+} were also undertaken with the DLP technique. Detailed atomic structure calculations using the Cowan suite of codes, based on Hartree-Fock configuration interaction methods, were performed to generate synthetic spectra for comparison with experimental results.

Contents

Chapter 1

Atomic Spectroscopy and Structure

1.1 Introduction

Photoabsorption and photoionization measurements from the inner shells of atoms and ions have a distinguished history and have played an important role in developing our basic understanding of atomic structure. Using an extreme ultraviolet (XUV) photon to excite an inner shell electron above threshold permits the study of highly excited Rydberg states, of the ionization continuum, and of further excitations or structures which may lie embedded within the continuum. For N-electron atoms, such excitations demonstrate the many-body nature of the photon-atom interaction. Complexities arise between the various excitation channels available to the excited electron and how the other (N-1) electrons rearrange or relax after the interaction. The range of interesting phenomena observed has had a significant impact on theoretical models. The simple independent particle model (Hartree-Fock) [1] has had to be adapted to account for these electron-electron correlations, and other sophisticated models have been developed, e.g. many-body perturbation theory (MBPT) [2], the random-phase approximation (RPA [3] or RPAE [4] including exchange) and the R-matrix theory [5].

The symbiotic relationship between experiment and theory has fueled the constant advancement of experimental techniques and theoretical calculations. At the early stages of development, the availability of an XUV source with an appropriate spectral distribution was paramount to developing inner shell spectroscopy. The first investigations by Beutler [6] and co-workers in the 1930s used discharge lamps filled with inert gases (the use of this type of source was confined to photoexcitation in the 600 - 1200 Å VUV spectral range). They were limited to study easily vaporis-

able elements. In the 1960s synchrotron radiation was pioneered as a suitable photon source [7] for inner shell studies. Although initially limited to measuring photoionization cross sections of noble gases (where one could accurately determine the density in absorption cells) or ions with large photoionization cross sections to compensate for the low photon flux, this was improved considerably upon the introduction of insertion devices, (e.g., undulators that provided increased brightness) and with the development of more stable ion sources. Several experimental techniques developed alongside the use of synchrotron radiation to measure partial cross sections and examine the various decay products that resulted from the excitation or photoionization of atoms, e.g. angle- and spin-resolved electron spectroscopy, photoion spectroscopy and fluorescence spectroscopy. These techniques highlighted the many-electron nature of such processes and synchrotron radiation remains a powerful tool in atomic and molecular physics.

Photoexcitation and photoionization studies were not restricted to synchrotron radiation sources however, discharge type sources emerged in the 60s and 70s to cater for the demand of XUV sources. A BRV spark discharge [8] was developed in the early 60s. It worked by applying a discharge across an anode (typically made of uranium) to produce an ionized plasma that yields bright continuum emission in the XUV. A second similar discharge provided the species to be studied. By varying the timing between the two discharges different stages of ionization in the excited atomic discharge could be observed [9]. This method advanced through the use of high-power lasers [10] and led to the dual-laser plasma (DLP) technique [11], employed for the work presented in this thesis.

This technique developed with the discovery that when a laser pulse was tightly focused onto a high Z target, a continuum was produced extending into the XUV [12]. Employing a second laser to generate a plasma from an element one wished to study, one could perform photoabsorption measurements for neutral and many times ionized stages of the element. A simple and versatile technique, it provided both complementary and strong competition with synchrotrons for examining inner shell excitations. A wealth of photoabsorption measurements have been provided by the technique and several intriguing many-body processes were first observed using it. Chapter 2 introduces the DLP technique and outlines the experimental set-up used to perform inner-shell photoabsorption measurements in this work. The technique was used to study the 4p-subshell spectrum of Sr^+ (Chapter 5) and 5d excitation in the Hg I isoelectronic sequence of Pb^{2+} and Bi^{3+} (Chapter 6).

One of the most popular techniques used today to measure absolute photoionization cross sections at synchrotrons is the merged-beam technique [13]. Merging

a beam of atoms or ions over a known distance with a synchrotron radiation beam permits the determination of absolute photoionization cross sections. Such studies were driven not only from a fundamental atomic physics perspective but also by a strong astrophysical demand: absolute cross sections for ions abundant in space are necessary to generate accurate models for stellar atmospheres. The extensive theoretical projects established for these astrophysical requirements needed experimental validation, for example [14, 15], so a lot of effort has been made to bridge the gap between theory and measurements. During this work, a collaboration was formed with Århus University, Denmark to perform photoionization cross section measurements along the Kr I isoelectronic sequence, Rb^+ and Sr^{2+} with complementary photoabsorption measurements recorded using the DLP technique at DCU at higher resolution [16]. A brief overview of the experimental set-up at Århus is presented in Chapter 4 along with results from both techniques.

Selective excitation of atoms from the ground state to an excited state, and the subsequent probing of the atom to discern the dynamical processes that ensue, has flourished in recent years; see [17] for a comprehensive review. Single photoabsorption from the ground state limits the number of excited states accessed due to the dipole selection rules, but if one prepares the atom in an excited state (generally by promoting a valence electron into an excited state), and further probes the excited atom using a XUV photon, one can reach a manifold of excited states otherwise inaccessible from the ground state. Such pump-probe or two-colour experiments are performed using a cw-laser (pump) and a synchrotron source (probe) with the resulting ejected photoelectrons detected to determine partial photoionization cross sections into different channels. Incorporating polarisation into the experiment heightens selectivity of the initial states prepared and of the final states reached.

In this work, strontium atoms and singly charged ions are resonantly pumped in a laser-produced strontium plasma via an optical parametric oscillator (OPO) and a XUV continuum source (laser generated tungsten plasma) is used as the probe. We measure the XUV photoabsorption spectrum from the plasma at various time delays after pumping with the OPO and also study the fluorescence from the plasma to provide additional information on the dynamics of the process. Within our high density plasma, collisions dominate and we observe rapid ionization similar to what was observed in resonant laser driven ionization (RLDI) experiments [18]. In Chapter 3, results are presented for different pump wavelengths in both Sr and Sr^+ and a comparative study is made for the various excitation schemes.

The remainder of this chapter provides a short introduction into the theory of

atomic structure, focusing on the Hartree-Fock approximation and highlights important many-body effects associated with inner shell photoabsorption and photoionization.

1.2 Theory of Atomic Structure

The primary goal in atomic theory is to solve the Schrödinger equation for an *N*-electron atom ($N > 1$), applying a suitable Hamiltonian operator, in order to acquire the corresponding energy eigenvalues, E_n, for the wavefunctions (eigenfunctions), Ψ_n, describing the atomic system.

$$\hat{H}\Psi_n = E_n\Psi_n \tag{1.1}$$

The non-relativistic Hamiltonian, in atomic units[1], consists of the total kinetic energy of the *N* electrons plus the total potential energy due to their interaction with the nucleus and with each other:

$$H = \sum_{i=1}^{N}\left(-\frac{1}{2}\nabla_i^2 - \frac{Z}{r_i} + \xi_i(\vec{r_i})(\vec{l_i}\cdot\vec{s_i})\right) + \sum_{i>j}\frac{1}{r_{ij}} \tag{1.2}$$

Here *Z* is the nuclear charge of the atom, $\vec{r_i} = |r_i|$ is the distance of the i^{th} electron from the nucleus, $r_{ij} = |\vec{r_i} - \vec{r_j}|$ is the distance between the i^{th} and j^{th} electrons, and the summation $i > j$ is over all pairs of electrons. This expression assumes that the nucleus can be treated as a point charge with infinite mass. The last term in the first summation represents the sum over all electrons of the magnetic interaction energy between the spin of an electron and its own orbital motion. The spin-orbit interaction involves the angular portion of the wavefunction through the operators *l* and *s*, and has a pronounced effect on energy-level structures; it is therefore necessary to retain it explicitly in the Hamiltonian. The proportionality factor ξ_i is given by:

$$\xi(r) = \frac{\alpha^2}{2}\frac{1}{r}\left(\frac{dV}{dr}\right) \tag{1.3}$$

where α is the fine structure constant (1/137) and *V(r)* is an appropriate potential energy function for an electron in a multi-electron atom, as will be discussed shortly.

The wavefunction Ψ_n is a function of 4*N* variables, three space and one spin coordinate for each electron, and the quantum mechanical problem is extremely

[1]In atomic units, Planck's constant ($\hbar$), the electronic charge (e) and the reduced mass (μ) are all set to 1. This is done to simplify the form of the Hamiltonian operator and the other quantum mechanical operators. The atomic unit of energy is the Hartree = 27.2113961 eV.

complex. Exact solutions to Schrödinger's equation are known only for N = 1, i.e. for hydrogen-like ions. In this case the differential equation can be solved using the separation of variables technique. For $N \geq 2$, exact formal solutions are not known so it is necessary to use some approximate form of the wavefunctions. Even as early as 1929, Hylleraas generated accurate results for the ground state of helium using elliptic coordinates [19]. More elaborate forms of wavefunctions have been developed since [20, 21]. These approximations generally assume that the wavefunction contains several adjustable parameters which are varied so as to obtain the best possible function, as judged by some appropriate criterion.

1.2.1 The Central Field Model and Product Wavefunctions

For many-electron systems Hartree [22] proposed that the appropriate wavefunction could be obtained from a linear expansion of many one-electron functions u_i so that ψ could be expressed as:

$$\psi(1, 2, ..., N) = u_1(1)u_2(2)...u_N(N) \tag{1.4}$$

where 1, 2,....,*N* represent the four coordinates used to describe each electron. This leads to the central field approximation where the *N* electrons are assumed to move independently of each other in a spherically symmetric background potential, *V(r)*. An electron can then be described by a one-electron wavefunction

$$\varphi_i(r_i) = \frac{1}{r} P_{n_i,l_i}(\vec{r_i}) Y_{l_i,m_{l_i}}(\theta_i, \phi_i) \tag{1.5}$$

where $\vec{r_i}$ denotes the position (*r*,θ,ϕ) with respect to the nucleus. This differs from a one electron wavefunction only in the radial term, $P_{n_i,l_i}(\vec{r_i})$, which results from the change in the potential *V(r)* as it is no longer a simple Coulomb function, -$2Z/r_i$. To ensure Pauli's exclusion principle is upheld the wavefunction needs to be totally antisymmetric with respect to the exchange of any two electron coordinates. Fock [23] incorporated spin into the new one-electron functions and replaced the simple product function above with an antisymmetrised product. These new one-electron functions are called spin-orbitals (and are constructed to be mutually orthonormal).

$$\varphi_i'(r_i) = \frac{1}{r} P_{n_i,l_i}(r_i) Y_{l_i,m_{l_i}}(\theta_i, \phi_i) \sigma_{m_{s_i}}(s_i) \tag{1.6}$$

where σ represents the spin state. Thus a wavefunction which represents a given electronic configuration may be constructed from a linear combination of products of spin-orbitals. The antisymmetrical function may be written in the form of a

determinant:

$$\psi = \frac{1}{\sqrt{N!}} \begin{vmatrix} \varphi_1(1) & \varphi_2(1) & \cdots & \varphi_N(1) \\ \varphi_1(2) & \varphi_2(2) & \cdots & \varphi_N(2) \\ \vdots & & \ddots & \vdots \\ \varphi_1(N) & \varphi_2(N) & \cdots & \varphi_N(N) \end{vmatrix} \tag{1.7}$$

and is referred to as a determinantal function or a Slater determinant [24].

1.2.2 The Matrix Method

For multi-electron systems, one can express the total wavefunction, Ψ^k, as a linear combination of a set of orthonormal basis functions that are usually the wavefunctions of separate electronic configurations Ψ_b.

$$\Psi^k = \sum_b y_b^k \Psi_b \tag{1.8}$$

Typically the Ψ_b are calculated using a HF procedure, as in Eqn. 1.7. In practise it is necessary to truncate this set to a manageable number *M*, so the basis functions should be carefully chosen to preserve the accuracy of the calculations. Substituting Eqn. 1.8 into the Schrödinger equation gives:

$$\sum_{b'=1}^{M} \hat{H} y_{b'}^k \Psi_{b'} = E^k \sum_{b'=1}^{M} y_{b'}^k \Psi_{b'} \tag{1.9}$$

Multiplying this from the left by any one of the basis functions Ψ_b and integrating over all coordinates and summing over both possible directions of each of the *N* spins, one obtains:

$$\sum_{b'=1}^{M} H_{bb'} y_{b'}^k = E^k \sum_{b'=1}^{M} y_{b'}^k \langle \Psi_b | \Psi_{b'} \rangle \tag{1.10}$$

$$= E^k y_b^k \qquad (1 \leq b \leq M) \tag{1.11}$$

where $H_{bb'} = \langle \Psi_b | \hat{H} | \Psi_{b'} \rangle$. The relations in Eqn. 1.11 comprise a set of *M* simultaneous linear equations in the *M* unknowns $y_{b'}^k$. This set of equations has a non-trivial solution only if the determinant of the matrix ($H_{bb'}$ - $E^k \delta_{bb'}$) is zero:

$$|H - E^k I| = 0 \tag{1.12}$$

where *I* is the identity matrix. Expanding this determinant into a polynomial of

degree M in E^k, zeroes represent M different possible energy levels of the atom. Each of these values of E^k, substituted back into Eqn. 1.9, yields M-1 independent equations for the M-1 ratios:

$$\frac{y_b^k}{y_i^b}, b \neq i \tag{1.13}$$

The value of y_i^b is chosen such that

$$\sum_{b=1}^{M} |y_b^k|^2 = 1 \tag{1.14}$$

so that Ψ^k is normalised. For M greater than two or three, the only practical procedure is to diagonalise the Hamiltonian matrix numerically. If the expansion coefficients are written as a column vector,

$$Y^k = \begin{pmatrix} y_1^k \\ y_2^k \\ y_3^k \\ \vdots \\ y_M^k \end{pmatrix} \tag{1.15}$$

then Equations 1.11 may be written as a single matrix equation:

$$HY^k = E^k Y^k \tag{1.16}$$

and the problem is to find the M eigenvalues of E^k of the matrix H, together with the corresponding eigenvectors Y^k. Using numerical methods a matrix T is found that diagonalises H. Then the k^{th} diagonal element of the diagonalised energy matrix is the eigenvalue E^k,

$$T^{-1}HT = E^k \delta_{kb} \tag{1.17}$$

and the k^{th} column of T is the corresponding eigenvector Y^k,

$$HT = TE^k \delta_{kb} \tag{1.18}$$

Once the Hamiltonian matrix elements $H_{bb'}$ have been computed, the energy levels of the atom can be calculated.

1.2.3 Coupling Schemes

It is desirable for accurate calculations that each wavefunction Ψ_b, from Eqn. 1.8, be close to one of the actual eigenfunctions of the atom. The atom will have a definite value of *J*, the total angular momentum, and each Ψ_b will not only be an eigenfunction of *H*, but also of *J*, J^2 and J_z. The method for coupling together the various Ψ_b to obtain Ψ^k for a particular atom is determined by the relative importance of the various residual interactions not accounted for in the central field model. These interactions are dealt with in order of importance to ensure accurate calculations and a concise labelling scheme. Some common coupling schemes are presented below.

***LS* coupling**

For atoms with small *Z*, the most important residual interaction is the electrostatic repulsion between electrons. In this case it is appropriate to couple the orbital angular momenta, l_i, first to form the total orbital angular momentum *L*. Then the spin angular momenta are summed to give the total spin angular momentum *S*. *L* and *S* and then coupled to give *J*.

$$L = \sum_i l_i \qquad S = \sum_i s_i \qquad J = L + S \tag{1.19}$$

A *LS* coupled basis function or term designation is denoted $^{2S+1}L_J$.

***jj* coupling**

With increasing *Z*, the spin-orbit interactions become increasingly more important. In this case, basis functions are formed by first coupling the spin of each electron to its own orbital angular momentum, and then coupling together the various resultants j_i to obtain the total angular momentum *J*:

$$j_i = l_i + s_i \qquad J = \sum_N j_i \tag{1.20}$$

A *jj* coupled basis function is denoted [(l_1, s_1)j$_1$...,(l_N, s_N)j_N]*J*. This type of coupling scheme was found to be most appropriate in Chapter 6 for studying the 5d inner-shell spectra of Pb^{2+} and Bi^{3+}, both high *Z* elements.

***jK* (intermediate) coupling**

Frequently, the pure coupling schemes described above are not appropriate, such a situation is referred to as *intermediate coupling*. *jK* coupling is an intermediate coupling scheme, where the strongest interaction is the spin-orbit interaction of the more tightly bound electron, and the next strongest interaction is the spin-independent (direct) portion of the Coulomb interaction between the other electrons outside the closed subshells. This type of coupling mainly occurs when the

excited electron has a large angular momentum because such an electron tends not to penetrate the core and thus experiences only a small spin-dependent (exchange) Coulomb interaction. In the *jK* coupling scheme, energy levels tend to appear in pairs; the level pairs correspond to the two possible values of *J* that are obtained when *s* is added to the resultant, *K*, of all other angular momenta:

$$\begin{aligned} l_1 + s_1 &= j_1 \\ j_1 + l_2 &= K \\ K + s_2 &= J \end{aligned} \tag{1.21}$$

and the standard energy-level notation is $j_1[K]_J$.

Other intermediate coupling schemes

In this case, few of the eigenfunctions will be close to any basis function so a more appropriate basis set may be constructed. A common approach is to choose either an *LS* or a *jj* coupled basis and specify the eigenfunctions by their principal components. This approach was adopted in Chapter 5, where the 4p subshell spectrum of Sr^+ was studied. Both *LS* and *jj* coupling calculations were performed for 4p excitations and the nomenclature used to describe the various excited levels was based on the highest purity obtained for a particular configuration (in one of the coupling schemes).

1.2.4 The Hartree-Fock Equations

In any determinantal basis function that corresponds to a configuration, there are *q* different radial functions $P_{n_i l_i}(r)$, one for each subshell of equivalent electrons $n_i l_i^{w_i}$ ($1 \leq i \leq q$), where *w* is the occupancy within the subshell. The matrix elements $H_{bb'}$, and therefore the eigenvalues E^k, will depend on the detailed shapes of these radial functions. Using the variation principle, $P_{n_i l_i}(r)$ are determined by the criterion that they should minimise the calculated energy of the atom, within the limitations set by the orthonormalization conditions: $\langle\Psi|\Psi\rangle = 1$, or, equivalently $\langle\phi_i|\phi_j\rangle = \delta_{ij}$. This minimisation of E_{av} (the average energy of the particular electron configuration of interest) with respect to variations in the form of $P_{n_i l_i}(r)$ leads to a set of coupled differential equations known as the spherically averaged Hartree-Fock (HF) equations:

$$\left(-\frac{1}{2}\nabla_i^2 - \frac{Z}{r_i}\right) u_i(r_i) +$$

$$\sum_{j\neq i}\left[u_i(r_i)\int \frac{|u_j(r_j)^2}{r_{ij}} d\tau_j - \delta(m_{s_i}\cdot m_{s_j}) u_j(r_i)\int \frac{u_j^*(r_j)u_i(r_j)}{r_{ij}} d\tau_j\right] = \epsilon_i u_i(r_i) \quad (1.22)$$

The first term in Eqn. 1.22 corresponds to the sum of the kinetic energy and the nucleus-electron potential energy. The remaining terms on the left hand side correspond to the electron-electron interaction. The first term in the summation is of the form $u_i(r_i)V(r_i)$ and is a local potential energy term. It is known as the direct term and physically stands for the potential associated with the charge density due to all other electrons. The second term in the summation is known as the exchange term. Physically it is related to the interchangeability of indistinguishable electrons and it is inherent to the antisymmetry of the determinantal wavefunction. The parameter, ϵ, is the binding energy of an electron in subshell $n_i l_i$ according to Koopman's theorem [25].

The Hartree-Fock equations, or their equivalents for $P_{n_i l_i}(r)$, must be solved iteratively. One such method is to use the self-consistent field (SCF) method. This involves making an initial guess for the set of orbitals u_i, constructing the integrals in Eqn. 1.22 and obtaining a value of ϵ_{ij}. Then the resulting differential equations are solved for a new set of orbitals u_i. The integrals are then recomputed and the equations are resolved until a satisfactory degree of convergence (self-consistency) is reached.

1.2.5 Energies

When the Hartree-Fock equations have been solved to obtain a self-consistent set of radial functions $P_{n_i l_i}(r)$, these orbitals may then be used to obtain the energy of any specified combination of orbitals. It is convenient to describe the energy of a configuration in terms of an average value, E_{av}. This corresponds to a statistically weighted sum of the energies of all the terms within a configuration:

$$E_{av} = \frac{\sum_{levels}(2J+1)E_J}{\sum_{levels}(2J+1)} \quad (1.23)$$

where J is the total angular momentum of a level in a configuration and E_J its energy. A theoretical expression for E_{av} may be obtained and is given by:

$$
\begin{aligned}
E_{av} &= \sum_i \frac{1}{2}\int_0^\infty P^*_{n_i l_i}(r)\left[-\frac{d^2}{dr^2} - \frac{2Z}{r} + \frac{l(l+1)}{r^2}\right] P_{n'l}(r)dr \\
&+ \sum_{i>j}\left[\sum_{k=0}^{2l_i} F^k(ij)c^k(l_i m_{l_i}, l_i m_{l_i})c^k(l_j m_{l_j}, l_j m_{l_j})\right. \\
&- \left.\delta_{m_{s_i}}\delta_{m_{s_j}} \sum_{|l_i - l_j|}^{l_i+l_j} G^k(ij)[c^k(l_i m_{l_i}, l_j m_{l_j}]^2\right] \qquad (1.24)
\end{aligned}
$$

The contribution to E_{av} due to the spin-orbit interaction cancels out when all the terms of the configuration are added together, having been weighted as in Eqn. 1.23. The F^k and G^k terms are special cases of the more general R^k radial integral defined as:

$$
R^k(ij:tu) = \int_0^\infty \int_0^\infty P^*_i(r)P^*_j(r')\frac{r^k_<}{r^{k+1}_>}P_t(r)P_u(r')drdr' \qquad (1.25)
$$

where $r_>$ and $r_<$ are the maximum and minimum of the radial distances r and r' respectively. The F^k and G^k integrals are defined as $F^k(ij) = R^k(ij:ij)$ and $G^k(ij) = R^k(ij:ji)$ respectively and are commonly referred to as Slater integrals [24]. The coefficients $c^k(lm_l,l'm_{l'})$ contain all the angular dependence of the Hamiltonian and are called angular coefficients. Their value for the majority of common electronic coefficients have been tabulated, see for example [26].

1.2.6 Configuration Interaction

So far this section has been concerned with basis functions from just one configuration. In general, each computed eigenfunction, Ψ^k, will be a mixture of basis functions from all configurations included in a calculation; this is known as *configuration mixing* and is necessary due to the possibility of several configurations with the same total angular momentum having energy levels in close proximity (although CI between configurations with quite widely separated energy levels is not unheard of). Correspondingly, the computed energies will be different from the values that would have been given by a set of single-configuration calculations and is known as *configuration interaction perturbation*. Collectively both features are known as *configuration interaction* (CI). The practical consequence is that the Hamiltonian matrix will no longer be purely diagonal and will contain off-diagonal elements representing this configuration interaction.

1.2.7 Radiative Transitions

Once one has obtained the wavefunctions to accurately describe atomic states in terms of a multiconfiguration basis state, it is then possible to calculate the dipole allowed electromagnetic transitions between pairs of atomic states subject to dipole selection rules. The cross section for photoabsorption leading to the transition $a \rightarrow b$ between two bound states with normalised wave functions Ψ_a and Ψ_b in the dipole approximation is given by:

$$\sigma_{ab} = \frac{4\pi}{3c}\omega_{ba}|D_{ba}|^2\delta(E_a - E_b - E) \tag{1.26}$$

for non-polarised isotropic radiation, where

$$D_{ba} = \langle\Psi_b|D|\Psi_a\rangle = \langle\Psi_b|e\sum r|\Psi_a\rangle \tag{1.27}$$

is the matrix element of the dipole operator and $E = \hbar\omega = E_b - E_a$ the energy difference between the two states. As the electric dipole operator has odd parity, it follows that electric dipole transitions can only occur between states that have opposite parity[2]. Further selection rules imposed by application of the Wigner-Eckart theorem to calculate the matrix elements are:

$$\Delta J = J_b - J_a = 0, \pm 1 \tag{1.28}$$

with the restriction that $J_a = J_b = 0$ is not allowed.

The (absorption) oscillator strength or *gf* value of these permitted electric dipole transitions (observed in the form of their spectrum lines), is given by the expression:

$$f_{ab} = \frac{gf}{(2J+1)} \tag{1.29}$$

$$gf = \frac{1}{3}(E_b - E_a)S \tag{1.30}$$

where S is called the line strength of the transition and its square root is defined as $S^{1/2} = \langle\Psi_a|D|\Psi_b\rangle$. The oscillator strength is dimensionless, and has the physical significance of the effective number of classical electron simple harmonic oscillators that would absorb radiation of energy $\hbar\omega$ as strongly as does the atom. That is, if an electron is in state a, the total oscillator strength available for transitions to all other levels must add up to the classical value for one oscillator, $\sum_k f_{ak} = 1$. This is called the Thomas-Reiche-Kuhn sum rule for a one-electron spectrum. If N electrons are

[2]This restriction is due to the symmetry properties of the wavefunctions and the operator acting on them.

involved, then the sum is simply *N*. For an unperturbed Rydberg series accessed from the ground state, the normal course of intensity is for the first member to be the strongest, with a drop in intensity as the excitation energy increases. In hydrogen, the oscillator strength for photoexcitation to the *n*th level falls off as n^{-3} at large *n*. Also, for high *n*, many systems become more hydrogen-like, so often n^{-3} holds too.

It is convenient to introduce the differential oscillator strength, *df/dE*, to incorporate a smooth transition from the discrete spectrum into the continuum, this continuity across threshold is a fundamental property derived from the continuity in wavefunctions across threshold. The total cross section σ, which represents the absorption per unit energy (or frequency or wavelength) interval is related to the *df/dE* curve by:

$$\frac{\mathrm{d}f}{\mathrm{d}E}|_{n\to\infty} = K\sigma(E)|_{E=IP} \tag{1.31}$$

where *IP* is the ionization threshold and the constant *K* is chosen to satisfy the Thomas-Reiche-Kuhn sum rule.

1.3 Calculation of atomic structure

The conventional Hartree [22] and Hartree-Fock methods [23] have been developed extensively since they were first proposed and the HF method serves as an extremely suitable starting point from which the calculation of atomic structure can be accessed. The self-consistent field method for solving many-particle problems is convenient for detailed numerical computations, but the SCF approach does not include effects due to the correlation of the electron motions. Such *electron correlations* result in many important effects that occur in inner-shell excitations, such as double excitations and autoionization. Therefore many extensions and refinements of SCF methods have been developed to incorporate these processes. For example, multiconfiguration mixing (MCHF) [27], the random-phase approximation (RPA) [3], and relativistic theories for high *Z* ions (MCDF) [28] have all been applied successfully to many ionic and molecular systems. Other approaches view the atomic calculation quite differently, e.g. *R*-matrix method [5], but still obtain accurate results for electron-correlation effects. It is beyond the scope of this thesis to give a detailed account of the various approximations; instead I will focus on the calculations performed in this work using a code based on the configuration interaction Hartree-Fock approximation.

In this approximation, one uses large basis sets of configurations to obtain more accurate results. The mixing coefficients and the corresponding energy shifts ΔE

are obtained by diagonalisation of the energy matrix. Such large basis sets were necessary to obtain accurate results for the 4p-subshell spectrum of strontium II (Chapter 5). The atomic structure code used in this work was developed by Cowan and co-workers [29, 30]. It is based on the HF equations and uses the SCF method described earlier. It can also employ several other approximations, e.g. Hartree-Fock-Slater (HFS) and Hartree-Fock with exchange (HX). These introduce different approximate functions for the effective potential of the atom to include self-interaction energy corrections and apply different methods to approximate the HF exchange terms. The HF approximation was applied to the atoms studied in this work as it was found to give satisfactory results.

The *Cowan code* [30] is a suite of four programs which calculate atomic structure and spectra. It has several built-in functions to permit calculations for important atomic-photon interactions and subsequent relaxation effects such as photoionization cross sections, autoionizing rates, branching ratios, and dielectronic recombination rates. Collisional excitation rates can also be determined using the incorporated plane-wave Born (PWB) approximation (these have been calculated in Chapter 3). Briefly, one-electron radial wavefunctions (bound or free) are calculated for each electron configuration specified in an input file using the HF method[3]. For each configuration, the angular coefficients of the radial Coulomb integrals, F^k and G^k, are computed, as are the spin-orbit ξ integrals (Eqn. 1.3). The configuration-interaction Coulomb integrals R^k (Eqn. 1.25) between each pair of interacting configurations and the electric-dipole and / or electric quadrupole radial integrals between each pair of configurations are determined. The program can then evaluate and diagonalise the energy matrices to obtain the eigenvalues and eigenstates. For dipole transitions, the radiation spectra with wavelengths, oscillator strengths, radiative transition probabilities and radiative lifetimes are also computed. Depending on the particular user-defined options, the extra built-in utilities can also be availed of to obtain the various cross sections and / or rates described above.

From a fundamental theoretical point of view, using the values of E_{av}, F^k, G^k, ζ, and R^k directly from the computed HF radial wavefunctions makes these true *ab initio* calculations. In general, the theoretical values of E_{av} agree well with experiment, especially when relativistic and correlation corrections are included; in many cases strong configuration-interactions have to be taken into account by performing multi-configuration rather than single-configuration calculations. However, computed energy-level splittings resulting from electron-electron Coulomb interactions tend to be larger than observed by ten to fifty percent [30].

The reason for such poor energy-level splitting predictions is a direct conse-

[3] Approximate relativistic corrections are made to the atomic radial wavefunctions at this point [31].

quence of the neglect of the *LS*-term dependence of electron correlation. For a given configuration, levels having a high computed energy correspond to situations where the electrons lie close together, the strong Coulomb repulsion 'pushes' levels towards higher energy. These states therefore have the greatest correlation; if correlation corrections were included one would expect the computed energy reduction to be greater for the high levels than the low ones. A potential consequence of any explicit inclusion of correlation could then be a smaller computed energy-spread among the levels of a configuration. It is customary therefore, in *ab initio* calculations, to make at least some allowance for the cumulative effect of the infinity of small perturbations caused by the chance proximity of levels of the same parity by using scaled-down theoretical values of the single-configuration Coulomb integrals F^k and G^k. This semi-empirical correction has been justified qualitatively by the theoretical investigations of Rajnak and Wybourne [32, 33].

1.4 Inner shell processes

The work presented in this thesis is dedicated to studying the fundamental inner-shell processes that occur upon the interaction of energetic (XUV) photons with atoms and ions. The promotion of such tightly-bound electrons above threshold and the subsequent relaxation effects leads to many interesting phenomena. The development of experimental techniques to measure such processes and the theoretical techniques to reveal the physical processes underlying them has highlighted the many-electron nature inherent to inner-shell dynamics and overturned the simple one-electron independent particle picture of the central field approximation. The succeeding chapters give introductions to two techniques (the dual-laser plasma technique in Chapter 2, and the merged-beam method in Chapter 4) that have been developed and implemented to study inner-shell excitations; this section will focus on the intrinsic physical phenomena observed in the study of inner shell electrons. A brief description of inner-shell photoabsorption and photoionization is also presented.

1.4.1 Centrifugal barrier effects

Centrifugal barrier effects originate due to the balance between the repulsive term in the radial Schrödinger equation, which varies as $1/r^2$, and the attractive electrostatic potential experienced by an electron in a many-electron atom, which varies from atom to atom due to screening effects. The potential is given by:

$$V(r) + \frac{l(l+1)\hbar^2}{2mr^2} \tag{1.32}$$

Particularly, for d and f electrons (l_i = 2 and 3 respectively), the centrifugal term $l_i(l_i + 1)/r^2$ in the effective potential, results in a double-well structure. The result is an exclusion from the core region of these electrons (in neutral atoms) and they experience mainly a hydrogenic potential. This was first pointed out by Göppert-Mayer [34] and first observed in xenon by Ederer [35] where the 4d electron must tunnel through the potential barrier, leading to a *delayed onset* of 4d $\rightarrow \epsilon$f transitions[4]. However, as one moves from Z=54 (Xe) to Z=57 (La), the 4f wavefunction has moved from residing in the outer well to occupying the inner well. This effect is called *wavefunction collapse.*

The periodic table can be attributed to wavefunction collapse; in Ca I, the ground state is $4s^2$, as the centrifugal barrier is high enough to keep the 3d electron relatively far out. In Sc I and Ti I (Z=21 and 22 respectively) the 4s electrons are the least tightly bound and the 3d wavefunction is collapsed sufficiently so that a 3d electron is, on average, closer to the nucleus than a 4s electron. As Z increases further, the inner-well region of the effective potential (V_{eff}) becomes deeper and wider, which eventually results in the collapse of the 4d, 5d,... functions, and the formation of the second, third,... transition series of elements. The inner well of V_{eff} does not become sufficiently wide and deep to hold the 4f wavefunction until La where the lanthanide series of rare-earth elements begins. The collapse of the 5f wavefunction initiates the actinide series of elements. This phenomenon is also responsible for the subsequent sudden increase in binding energies of the 3d, 4d, 5d, 4f and 5f electronic orbitals[5].

For ions, the net charge seen by an electron at a distance far from the nucleus is $Z_c = Z - N + 1$, so the hydrogenic potential is:

$$-\frac{2Z_c}{r} + \frac{l(l+1)}{r^2} \tag{1.33}$$

and the hydrogenic well thus begins at:

[4] A more detailed discussion on 4d excitation is presented in Chapter 4

[5] It is actually only at Z = 58 (Ce) that a 4f electron becomes sufficiently tightly bound to appear in the ground configuration.

$$r = \frac{l(l+1)}{2Z_c} \tag{1.34}$$

and extends well into the electron-core for d electrons in singly ionized atoms (Z_c = 2), and for f electrons in 2- or 3-fold ionized atoms. Therefore, for a given ionization stage, the radial wavefunctions contract gradually with increasing Z, rather than collapsing suddenly.

Another important point concerned with wavefunction contraction is the strong term dependence that occurs. This arises due to the difference between the radial potentials for singlet and triplet states. Depending on the extent of contraction, one often needs to perform separate minimization calculations for certain configurations, e.g. $4p^5 4d5s^2\ ^1P$ term in Sr [36] and the $5d^9 6f\ ^1P$ term in Bi^{3+} [37] (see Chapter 6). These terms need to be treated separately because their energies contain large contributions from the exchange integral, G^k and when this has a large value, the effective central field differs greatly from that determined for the average energy of the configuration [38]. For excitation from the 4d subshell, the difference between the effective potential for singlet and triplet states is large enough to produce different degrees of contraction of the f orbitals for different terms. In La for example [39], while a prominent resonance is observed in the continuum of the singlet channel, the 4f triplet states are already collapsed, appearing as bound states below the associated threshold.

Specifically in relation to this thesis, we have measured partial and total photoionization cross sections for the 3d excitations in Rb^+ and Sr^{2+} in Chapter 4. Using the merged beam method we wished to study centrifugal barrier effects along the Kr I isoelectronic sequence for the 3d $\rightarrow$ *n*p, *m*f transitions, i.e. to study the extent of wavefunction contraction.

1.4.2 Photoionization

An atom in a discrete state may absorb a photon of sufficient energy to excite it above the ionization threshold and into the continuum. The transition probability for this process is usually expressed in terms of a photoionization cross section σ. The relationship between σ and oscillator strength may be obtained in differential form by considering a beam of photons travelling through an absorbing medium. This yields the equation [30]:

$$\sigma(\omega) = 4\pi\alpha a_o^2 \frac{\mathrm{d}f}{\mathrm{d}E} = 8.067 \cdot 10^{-18} \frac{\mathrm{d}f}{\mathrm{d}E} \quad (cm^2) \tag{1.35}$$

where *df/dE* is the oscillator strength per unit energy interval for either bound-bound or bound-free (continuum) transitions. All other symbols have there usual

meaning. For a discrete transition this corresponds to the integration of the absorption cross section over the profile of the spectral line. Cross sections are frequently measured in megabarns (1 Mb = 10^{-18} cm^2).

For simple cases, where the single - configuration approximation is valid, the calculation of *df/dE* is essentially identical to the calculation of the bound-bound oscillator strengths, except that the radial dipole matrix element is replaced by the bound-continuum matrix element. Because the continuum radial wavefunction is a smooth function of *E*, a continuous absorption spectrum is a smooth and featureless function of wavelength in this approximation. For highly ionized atoms where configuration-interaction effects are particularly small, and for photoionization of a single valence electron *nl*, this is particularly true. However, as discussed earlier, for inner-shell excitations configuration-interaction effects between discrete states embedded in the continuum result in asymmetric profiles or localised distortions in the cross section. Also, due to centrifugal effects one can observe widespread redistributions of the oscillator strength from one spectral region to another and as the above simple one electron expressions are not applicable, more sophisticated approaches such as many body perturbation theory are needed.

1.4.3 Auger decay

The vacancy created in the inner shell may be filled by an electron from any of the outer subshells. In some cases, this can occur as a radiative transition, with a photon carrying away the difference in energy between the two subshells. The probability that an inner shell vacancy decays in this manner is called the fluorescence yield, and is normally of the order of $\sim 10^{-4}$. For the most part, the filling of the inner-hole occurs via a non-radiative transition. If the excess energy is transferred to an electron in one of the other outer subshells giving it enough energy to become unbound and enter into the continuum, this relaxation process is known as the *Auger effect* and the secondary electron emitted is called the Auger electron [40]. It can be reasonably well described as a two-step process, leading to double ionization, because the primary and Auger electron are usually separate.

However, in some cases, e.g. post collision interaction (PCI) (the interaction between charged particles in the continuum after their release) the two-step description is inaccurate as both the primary and Auger electron interact. In this case, when ionization takes place close to threshold, a slow photoelectron is ejected. This process is rapidly followed by the decay of the core-ionized state and the release of an Auger electron. If the energy of the Auger electron is sufficiently large, the Auger electron overtakes the photoelectron and energy as well as angular momenta are exchanged. For both Auger and photoelectron spectra, PCI results in

energy shifts, line-shape distortion, asymmetry, and line broadening. The manner in which the inner vacancy is filled is described by different terminologies:

- **Standard Auger decay:** The initial vacancy leads to vacancies in subshells different in *n* and *l*, e.g. $3s^{-1} \rightarrow 4s^{-2}$.
- **Coster-Kronig decay:** After the decay of the initial vacancy, one of the subsequent two vacancies is in a different subshell of the *n* shell of the original vacancy, i.e. same *n* but different *l*, e.g. $3s^{-1} \rightarrow 3p^{-1}4s^{-1}$.
- **Super Coster-Kronig decay:** This refers to a particular case where the initial vacancy in the *n*th shell leads to two vacancies in subshells from the same *n*, e.g. $3s^{-1} \rightarrow 3p^{-2}$.

The decay rate for inner shell excited states is extremely fast compared to valence excited states (10^9 s^{-1}) and can range from 10^{13} s^{-1} up to 10^{18} s^{-1}. It follows therefore, that autoionizing and Auger resonances are often observed as broad features in photoabsorption spectra. One can make a distinction between both however. In autoionization, as it is the valence electrons that are involved in the decay process into the continuum, the autoionization width scales with *n* as $1/n^{*3}$ (just like the exciting electron in a Rydberg series), whereas the Auger width remains constant as it depends on the core hole being filled. As one progresses along a Rydberg series towards higher and higher *n*, the spacing between successive members also decreases as $1/n^{*3}$. Therefore, the presence of autoionization broadening does not tend to occlude higher Rydberg series by significant blending at high *n* - the limits tend to be instrumental rather than intrinsic. However, in the case of Auger broadening, which does not decrease with increasing *n*, the Rydberg series is effectively truncated. Photoelectron spectroscopy is the most widely used technique to measure the Auger effect which is an important process in solid state spectroscopy. One can use it to study the nature of core excitation in ionic solids; by examining the Auger structure, the nature of the core holes can be determined. On measuring the partial and total photoionization cross sections for 3d excitation in Rb^+ and Sr^{2+}, double photoionization was shown to dominate, that is, upon excitation the atom relaxed via Auger decay. The complete set of experimental and theoretical results from these studies are also presented in Chapter 4.

1.4.4 Autoionization

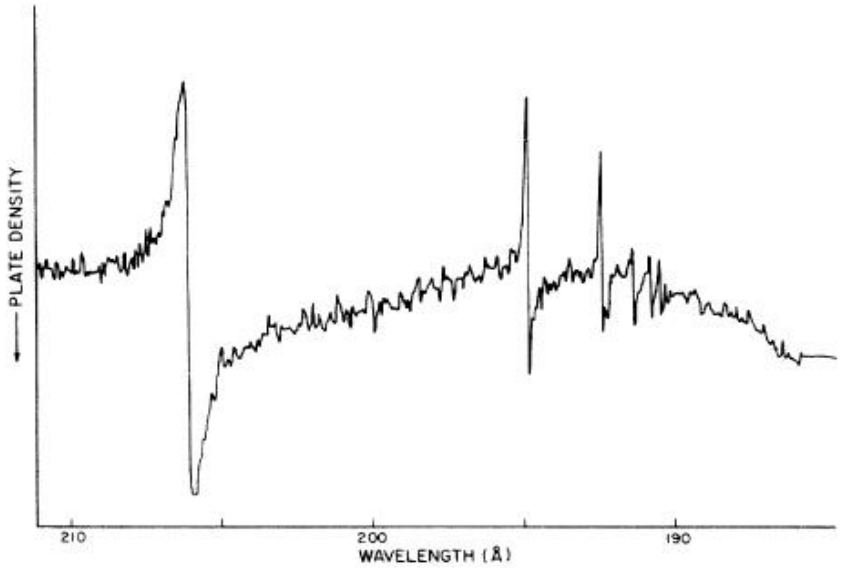

Figure 1.1: Beutler-Fano profiles of He $1s^2 \rightarrow 2sn$p and 2pns doubly excited autoionizing series [7].

As discussed in the preceeding section, many electron systems exhibit structure embedded in the continuum. Such features, that are neither discrete or continuous but a mixture of both, are referred to as autoionizing resonances. They were first discovered experimentally by Beutler [6] and the first theoretical approach to describe the asymmetric line shape was established by Fano [41]. For this reason they are often referred to as *Beutler-Fano resonances*, see Fig. 1.1. The photon energy required to excite an inner-shell electron is sufficient to promote the electron above threshold and into the continuum. Using perturbation theory Fano described what would happen if one considered turning on an interaction between a sharp state and the underlying continuum which were presumed initially to have no correlation. The unperturbed basis consists of a discrete bound state φ degenerate in energy with a band of continuum states ψ_E. In this simple case of one discrete state embedded in one continuum the two interfere to produce an asymmetrical resonance, in effect an interference fringe in the photoionization continuum. Using standard perturbation theory, a linear combination of degenerate states is formed, and then an appropriate initial combination of coefficients is selected. The wavefunction is then part discrete and part continuous

$$\Psi_E = a_\varphi \varphi + \int b_{E'} \psi_{E'} dE' \tag{1.36}$$

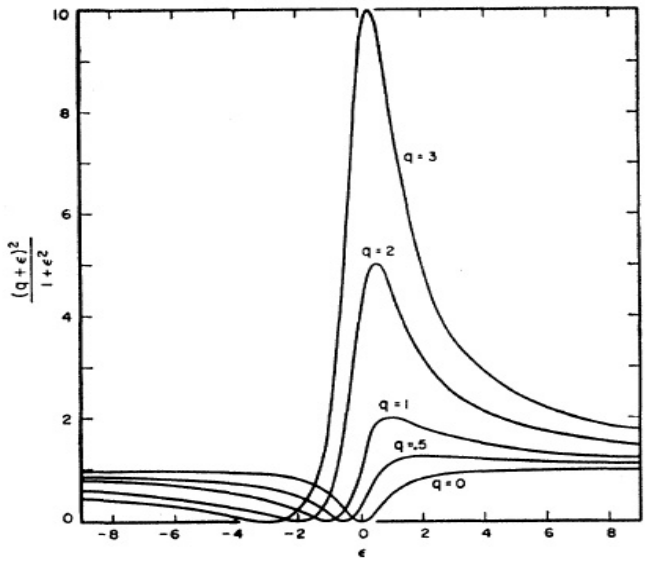

Figure 1.2: Natural line shapes for different values of *q* [41].

Fano used an off-diagonal perturbation *V* to describe this coupling, the Hamiltonian is then expressed as $\hat{H}$=$\hat{H}$+$\hat{V}$. The specific form of the operator which appears in *V* can be *any* interaction capable of coupling the discrete and continuum channels to each other, generally the electron-electron interaction is used e^2/r_{ij}. The interference between the two excitation paths can be expressed as a ratio between the transition probability for ending in the mixed state $|\langle\Psi_E|\hat{D}|i\rangle|^2$ to the transition probability ending in the featureless continuum $|\langle\psi_E|\hat{D}|i\rangle|^2$, $\hat{D}$ is the dipole operator and *i* is the initial state. Fano represented this interference with a single family of curves that are functions of a reduced energy variable ϵ, where ϵ is defined as:

$$\epsilon = \frac{E - E_r}{\frac{1}{2}\Gamma} \tag{1.37}$$

$\Gamma = \pi|V_E|^2$ and indicates the spectral width of the autoionized state φ. $|V_E|^2$ is a measure of strength of the configuration interaction and has dimensions of energy.

A parameter *q* is also defined and is a measure of the importance of the direct transition from *i* to the continuum compared to the transition via the autoionizing state. The characteristic asymmetric profiles of autoionizing resonances can thus be represented by a single family of curves:

$$\frac{|(\Psi_E|\hat{D}|i)|^2}{|(\psi_E|\hat{D}|i)|^2} = \frac{(q+\epsilon)^2}{1+\epsilon^2} = 1 + \frac{q^2 - 1 + 2q\epsilon}{1+\epsilon^2} \tag{1.38}$$

One can see in Fig. 1.2, that for $q \sim \geq 1$, the shape of the autoionizing resonance is asymmetric. For $q >> 1$ it becomes more symmetric and Lorentzian like, while

for $q \leq 1$, it is asymmetric, exhibiting a clear minimum at ϵ = -q. This reduces to a pure minimum in an otherwise smooth background for $q \ll 1$ and is referred to as a window resonance. There are some limitations to this formulism: the formula applies to a single, isolated resonance; the background continuum must be flat or vary only slightly over the width of the resonance; there must be no other channel contributing to resonance broadening. This last condition is the least likely to be satisfied. Generally, most autoionizing resonances are subject to several competing mechanisms for the ejection of an electron. Only if the excited state is built on a stable parent ion state, e.g. the ground state of the parent ion, and only if the resonance is coupled to one continuum does the Fano formula apply directly. These conditions are usually upheld in the energy range between the first and second ionization potentials where the smallest number of channels exist for the ejection of one electron. In the presence of several continua, the Fano formula still describes the general lineshape quite well but the cross section does not fall to zero near the resonance, i.e. the transmission window is 'filled in' by the presence of several continua. In Chapter 4, window resonances were observed for the 4s $\rightarrow$ np transitions in Rb^{+} and Sr^{2+} and their spectral profiles are fitted using Fano's parametrization.

1.4.5 Maxima and Minima in the continuum

As discussed earlier, one of the phenomena related to centrifugal barrier effects is *delayed onset*, this can result in maxima or *giant resonances* in the continuum spectrum. For Xe, it was found that the continuous absorption cross section rises to a peak 30 eV above the photoionization threshold and then falls off due to the delocalisation of the 4d wavefunction from the core. It has been found by studying isoelectronic and isonuclear sequences of Xe that the total oscillator strength for the 4d electrons obeys the Thomas-Reiche-Kuhn sum rule, that is, it equals ten. As the 4d wavefunction contracts into the inner well with increasing Z and ionization this total oscillator strength value is just redistributed among discrete 4d $\rightarrow$ nf transitions [42, 43]. From a theoretical point of view, many-body theory is required to properly reproduce these maxima and must include the role of collective and electron-electron correlation effects. To date, the RPAE (Random Phase Approximation with Exchange) has produced the most consistent results for the *ab initio* calculations of giant resonance cross sections. It involves taken into account both inter-electron interaction within the d or f subshells and statical rearrangement of outer electrons, due to the creation of a vacancy in the subshell [39, 44].

If one considers the differential oscillator strength $\mathrm{d}f/\mathrm{d}E$ introduced earlier, it normally decreases monotonically with increasing energy, roughly as $1/E$. This is only strictly correct for hydrogen but can apply to many other cases in photoab-

sorption from the ground state. It is possible however for excited state wavefunctions to possess a node. As a result the matrix element for photoionization, which involves an integration over the radius, splits into two contributions of opposite sign. Thus, there may exist an energy *E* at which there is a cancellation between the two contributions, and the matrix element vanishes. If more than one channel is available, the photoionization cross section will not go to zero but will exhibit a minimum, known as a 'Cooper minimum' [45].

When considering discrete transitions within a continuum, close to a Cooper minimum we see a very pronounced effect on the appearance of the discrete lines. Far from a Cooper minimum, the relative phase of the direct and indirect photoionization matrix elements changes little, and the discrete peaks appear as 'normal' resonances when the two matrix elements are in phase (or as window resonances described earlier when out of phase). When transversing a Cooper minimum, the relative phase changes, and the appearance of a peak may change from window to normal or vice versa. Such effects have been observed for example in the Ar-I isoelectronic sequence [46].

1.4.6 Plane-wave Born calculations

For the results presented in Chapter 3, where collisional processes play a dominant role, we availed of the plane-wave Born (PWB) approximation implemented in the Cowan suite of codes to calculate some collisional excitation rates in Sr I and Sr II. A brief description of the PWB approximation is thus presented here.

When the kinetic energy of a free electron is very large compared with *V(r)*, it is sufficient for some purposes to represent the continuum electron by a less accurate wavefunction. One can neglect *V(r)* and work in Cartesian co-ordinates to obtain the wavefunction *F* corresponding to a free electron, i.e. a plane wave:

$$-\left(\frac{\partial^2}{\partial x^2}+\frac{\partial^2}{\partial y^2}+\frac{\partial^2}{\partial z^2}\right)F=\epsilon F \tag{1.39}$$

A solution to this equation is:

$$F_k(r)=e^{i(k\cdot r)} \tag{1.40}$$

where $k^2 = \epsilon$ and is the kinetic energy of the free electron in Rydbergs. *k* represents a plane wave pointing in the direction **k** with de Broglie wavelength $\lambda = 2\pi/k$. If the free electron interacts with an *N*-electron atom (or ion) in a state *a* so as to excite the atom to a state *a'*, the free electron is inelastically scattered into a different plane-wave state $F_{k'}(r) = \exp(ik'\cdot r)$. By conservation of energy, $k'^2 = k^2 - \Delta E$ where ΔE is the excitation energy from *a* to *a'*. The states *a* and *a'* are represented by the usual

linear combination of antisymmetrized bound basis functions but the wavefunctions of the (N + 1)-electron system are described by non-antisymmetrized products of the target and free-electron functions, α[6]. This obviously will ignore the effects of exchange of the free electron with one of the bound electrons, but for high energies these effects are small enough to be neglected.

Applying the Hamiltonian operator[7], the reduced matrix element, $H_{aa'}$ is identical to the electric multipole matrix element, except the radial part of the operator, r_m, is replaced by $j_t(Kr_m)$, a spherical Bessel function [47], where $K = k' - k$, (the momentum transferred from the free electron to the atom). From this one can obtain a generalised oscillator strength:

$$gf_{JJ'}(K) = \frac{\Delta E}{K^2} \sum_{MM'} |\langle\alpha| \sum_m e^{iK\cdot r} |\alpha'\rangle|^2 \tag{1.41}$$

where $g = 2J + 1$ is the statistical weight of the level α and $e^{iK\cdot r}$ is expanded in terms of $j_t(Kr_m)$ [30]. In the limit where $K \rightarrow 0$, $f_{JJ'}$ is just the optical dipole oscillator strength. The quantity $f_{JJ'}$ is called the generalised oscillator strength because it satisfies for *any* K the same sum rules as the optical oscillator strength does:

$$\sum f_{JJ'}(K) = N \tag{1.42}$$

where N is the number of electrons in the atom. Applying the first Born approximation, the differential excitation cross section is given by:

$$I_{aa'}(\theta) = \frac{1}{16\pi^3} \frac{k'}{k} |H_{\alpha\alpha'}|^2 \tag{1.43}$$

$H_{\alpha\alpha'}$ is the matrix element obtained after applying the simplified Hamiltonian operator to the plane wave functions, $F_k(r)$.

The integrated cross section is evaluated in terms of the momentum transfer K to obtain:

$$Q_{aa'} = \frac{1}{8\pi^2} \int_{K_{min}}^{K_{max}} \frac{K}{k^2} |H_{\alpha\alpha'}|^2 dK \tag{1.44}$$

The total cross section $Q_{JJ'}$ (in units of πa_0^2), is obtained by summing $Q_{aa'}$ over M' (the magnetic quantum number, (as in section 1.2.3) and averaging over M. The

[6] $\alpha = |\gamma JM\rangle F_k$ where J is the total angular momentum of the system and M is the sum of the z-components of the spin-orbit and angular momentum quantum numbers. γ represents the other quantum numbers needed to describe the system.

[7] Due to the orthogonality of the functions F_k and the functions a and a', the one-electron terms of the Hamiltonian operator (kinetic-energy, electron-nuclear, and spin-orbit) contribute nothing to the matrix elements. The electron-electron terms only contribute if one coordinate is that of the free electron.

corresponding collision strength $\Omega_{JJ'}$ is:

$$\Omega_{JJ'} = \epsilon g Q_{JJ'}(\epsilon) = \frac{8}{\Delta E} \sum_{K_{min}}^{K_{max}} g f_{JJ'}(K) d(lnK) \tag{1.45}$$

All parameters have there usual meaning as described in this section. The results may be expected to be most accurate for neutral or weakly ionized atoms and for high energies (or for large values of the reduced energy $X = \epsilon/\Delta E$). Distorted-wave (DW) and close-coupling (CC) calculations employ a partial-wave expansion and include a large number of terms (l = 50-100) to achieve adequate convergence for this type of collision, whereas, in contrast, the PWB only needs to include 3 or 4 terms using the Bessel-function expansion. PWB values agree with DW and CC results to within 25 to 50% for X as small as 3 or 4. Although X is smaller for the collisional excitation rates we need to compute in Chapter 3, it is assumed they will give a reasonably accurate value.

1.5 Quantum Defect Theory

An extremely useful tool in spectroscopic analysis is multi-channel quantum defect theory (MQDT). For H and hydrogen-like ions, one can apply a basic Rydberg formula to accurately predict the position of energy levels along a Rydberg series, (a series where an electron in a configuration (nl) is excited to higher values of n away from the core):

$$E_n = I - \frac{R_m Z^2}{n^2} \tag{1.46}$$

I is the series limit, R_m is the Rydberg constant for an element of reduced mass m, n is the principal quantum number and Z is the nuclear charge.

For a N-electron atom, this formula has to be modified in two ways:

- Z is replaced by Z_c = Z - (N - 1), to account for screening of the nuclear charge by the N - 1 other electrons.
- When the outer electron penetrates into the charge distribution of the core electrons, the screening is not complete, and the outer electron interacts with a larger charge, Z_c + p, where p is called the penetration parameter. However, an alternative way of describing this is to make the denominator smaller rather than making the numerator larger. This requires a non-integer value for n, and is defined as the *quantum defect* δ and gives an effective principal quantum number, n^* = n - δ:

$$E_n = I - \frac{R_m Z_c^2}{(n-\delta)^2} \tag{1.47}$$

When first introduced, δ was derived empirically from studying spectral lines. It was found experimentally to be nearly constant for different series members, particularly for unperturbed series. The basic task of QDT was to construct a simple one-electron wavefunction for the Rydberg electron of a many-electron atom to account for it. This was achieved by dividing the space of the atom into two distinct regions: an inner region confined to a radius r_0 where all the electrons are present and interact strongly, and an outer region away from the core ($r > r_0$), where essentially only one electron is present. The purpose of the theory is to show that because of the presence of the core, the solution differs from the one-electron hydrogen wavefunction by an amount which depends entirely on δ. δ effectively embodies the many-body effects of the core and allows them to be included in an effective one-electron wavefunction. Seaton [48] showed that each discrete level E_n corresponds to a set of n^* values which simultaneously fulfil,

$$E = I_i - R_m/n_i^{*2} \tag{1.48}$$

and the determinantal equation that ensures compatible convergence of the radial wavefunction in all channels:

$$\det|\delta_{ij}\tan \pi n^* + R_{ij}| = 0 \tag{1.49}$$

In this case δ_{ij} is the delta function, and R is a reactance matrix that represents the effect of the short-range electron-core interactions. The long-range interactions are incorporated in the radial wavefunctions. Seaton also introduced a phase shift πn^* to ensure smooth extrapolation beyond the series limit into the continuum or open channel[8].

[8]Rydberg series as a whole, together with adjoining continuum, are regarded as a channel. The bound states are the *closed* part of the channel and the continuum states form the *open* part of the channel.

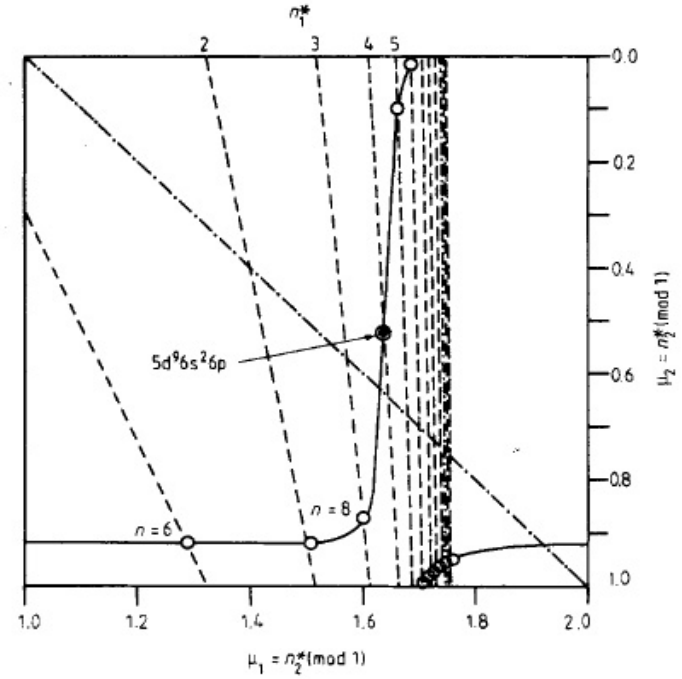

Figure 1.3: A two-dimensional Lu-Fano plot for the $6s^2 \rightarrow 6snp\ {}^1P_1$ and $5d^{10}6s^2 \rightarrow 5d^9 6s^2 6p\ {}^1P_1$ channels of mercury. The chain diagonal line is defined by $n_1^* = n_2^*$. The broken curves are the functions $n_1^*(n_2^*)$ and the full curves join all the points using Eqn. 1.49. There is an error in the labelling of the graph, the *x*-axis should read $\mu_2 = n_2^*(\text{mod } 1)$ and the *y*-axis label should read $\mu_1 = n_1^*(\text{mod } 1)$ [49].

In the case of two channels, Eqn. 1.49 can be written explicitly as:

$$\begin{vmatrix} \tan \pi n_1^* + R_{11} & R_{12} \\ R_{12} & \tan \pi n_2^* + R_{22} \end{vmatrix} = (\tan \pi n_1^* + R_{11})(\tan \pi n_2^* + R_{22}) - R_{12}^2 = 0 \tag{1.50}$$

The two effective quantum numbers belonging to each energy level are functionally related:

$$n_1^*(n_2^*) = \frac{n_2^*}{\sqrt{1 - (n_2^*)^2 \Delta}} \tag{1.51}$$

where n_1^* and n_2^* are the two effective quantum numbers of the level and Δ = (I_2 - I_1)/R. Because it is the nonintegral part of the effective quantum numbers which contains information about the mutual interactions between Rydberg series, it is customary in MQDT to consider them *modulo 1* i.e. taking account only of the fractional part, $\mu_1 = n_1^*(\text{mod } 1)$ and $\mu_2 = n_2^*(\text{mod } 1)$. It is conventional to plot $n_2^*(n_1^*)$ (mod 1) vs μ_1 for all known levels of the Rydberg series converging to the limits I_1

and I_2. Such graphs are called Lu-Fano graphs [50] and are often used to analyse interactions between series when only two distinct limits are involved.

The resulting curve will establish the empirical function $\mu_1(\mu_2)$ which describes the periodic nature of the series interaction. In the unit square, any horizontal line will intersect the $\mu_1(\mu_2)$ curve as many times as there are series converging to the I_2 limit. From the $\mu_1(\mu_2)$ curve, one can determine how many series converge to a given limit, what the character and degree of interaction of the series are. The crosses, as present in Fig. 1.3, represent levels usually assigned to 'perturbing' series, the perturbing levels normally lie on the sharply rising portions of the curves. If all interactions between series are weak, all unperturbed levels of the 'perturbed' series lie on the flat portions of the curves, i.e. with constant δ values. The magnitude of the gaps between successive curves provides a visual estimate of the strength of the interaction between different series. For this simple two channel case, one can use a least squares fit to fit the experimental points to Eqn. 1.49 in order to obtain values for δ_1, δ_2 (from the effective quantum numbers, $n^* = n - \delta$) and R. Once these parameter values have been determined, one can find the positions of missing energy levels or predict the positions of expected energy levels. One can of course extend this analysis to multiple channels too and include autoionization resonances in the continuum [51, 52, 53].

Lu-Fano graphs were constructed for the 4p-subshell spectrum of Sr^+ (Chapter 5) where no distinct coupling was evident for the innershell Rydberg series. In Bi^{3+} (Chapter 6) we observed strong perturbations among Rydberg series converging to $^2D_{3/2}$ and $^2D_{5/2}$ ionization limits. Although we did not carry out a full MQDT analysis, i.e. solve Eqn. 1.49 for Bi^{3+}, the Lu-Fano graph was a good visual aid for determining interlopers within the Rydberg series. Effective quantum numbers have been determined for individual Rydberg series in Sr^+ and Pb^{2+} and Bi^{3+}. Along with configuration interaction calculations this has provided useful insight into determining inter- and intra-series perturbations and provides an explanation for unexpected intensity distributions in some resonances.

The next chapter introduces the dual laser plasma technique that was employed during this work. A brief history of the technique is given and a description of the experimental set up follows. Details of the alterations made to study one- and two-photon resonant absorption in a laser produced strontium plasma are also provided.

Chapter 2

Laser produced plasmas and the dual laser plasma technique

2.1 The DLP Technique

The dual-laser plasma (DLP) technique [11] is now a well-established technique for the investigation of spectra of neutral to many-times ionized elements [54, 55]. One laser is used to generate an absorbing plasma from the element we wish to study, while after a given time delay another laser is focussed onto tungsten or a rare-earth target, to form the requisite extreme or vacuum ultra-violet backlighting continuum of about 10 ns duration. By varying the time delay between generation of both plasmas and probing the absorbing plasma at various spatial positions, one can build up a spatio-temporal profile of the plasma. This allows one to hone in on and select, to often a high degree of purity, a particular ion species of interest for further study.

The DLP technique was first used to study the extreme ultraviolet (XUV) photoabsorption of a laser produced aluminium plasma [10]. The laser pulse from a Nd:glass laser was split into two beams. One beam generated the absorbing aluminium plasma. The second beam was optically delayed and focussed onto the same target to generate a second plasma which was used as a probe. The radiation emitted from the probe plasma was predominantly line radiation and so the absorbance was measured at several discrete points only. The discovery of virtually line-free continuum emission from the spectra of laser produced tungsten, tantalum and uranium plasmas by Ehler and Weissler [56] provided the impetus to use high Z targets as continuum sources. Following on from this discovery, a group at University College Dublin (UCD) were the first to employ a rare earth continuum source (tungsten) to study photoabsorption from Li^+ using the DLP technique [57].

They successfully captured the doubly excited $1s^2\ ^1S_0 \rightarrow 2snp\ ^1P_1$ series in He-like lithium, the first such observation. Further investigations into the origin of this line-free emission by the same group determined that the complexity of the electronic structure in high Z elements, (samarium to ytterbium, Z = 62-70), leads to unresolved transition arrays (UTA) [58]. As an example, the $4d^{10}4f^6 \rightarrow 4d^9 4f^7$ transition array in the *LS* coupling framework, yields a massive 83,024 possible lines [12].

Nearly a decade after the first experiment, the UCD group introduced the use of two lasers to independently generate the continuum source and the absorbing plasma [59]. This brought the advantage of increased power density on target and a wide variable inter-plasma time delay range. Careful choice of target irradiance coupled with this wide time delay range established a new era of charge stage separation; low irradiance and long time delays ensured observation of neutral species, while the opposite yielded highly ionized ions. The basics of the technique having been developed at this stage, improvements were made alongside technological advancements. Three groups predominantly used this technique for extensive photoabsorption and photoionization measurements: University College Dublin, UCD, Dublin City University, DCU, and the University of Padua in Italy. A more detailed review of the vast number of experiments performed can be found in [11, 60, 61], while some breakthrough results are presented below.

A particular landmark experiment using this technique was performed by Kiernan *et al* in 1994 [62] . They recorded the first observation of a photo-induced triply excited state in neutral lithium, resulting in 'hollow' lithium. The $1s^2 2s\ ^2S \rightarrow 2s^2 2p\ ^2P$ transition was observed and the Fano profile of the autoionizing resonance was measured and parametrised. It was a severe test of the capabilities of the system due to the extremely small cross section for this transition (on the order of kilobarns) and the accumulation of several hundred scans was necessary. The results have since been refined at HASYLAB [63], Photon Factory [64] and Orsay [65] storage rings which have greater spectral resolution and sensitivity. As a result, many new hollow atom resonances were discovered at higher photon energies [66]. The DLP results also prompted many new advanced calculations [67, 68].

The study of isoelectronic sequences has provided insight into many fundamental aspects of the photoionization process such as relativistic effects, correlation effects, and orbital collapse. For example, a study of the Ar like ions K^+ and Ca^{2+} using the dual laser plasma technique [46] showed that the behaviour of the $3s \rightarrow np$ resonances changed radically along the sequence. On moving from Ar to K^+, a q-reversal is observed for the $3s \rightarrow np$ transitions, which have a distinct window-like appearance. In Ca^{2+} the main $3s \rightarrow 4p$ resonance is very weak and the higher np resonances have almost symmetric absorption profiles, indicating a much weaker

interaction with their associated ϵl continua. This was explained in terms of the positions of the 3s and 3p Cooper minima along the sequence. All 3s resonances lie below both Cooper minima in Ar, whereas in K^+, the 3s Cooper minimum lies in the discrete spectrum. This explains the weakness of the 3s $\rightarrow$ *n*p transitions. In Ca^{2+}, the 3s Cooper minimum lies below the discrete resonances while the 3p minimum lies just above the 3s $\rightarrow$ 4p resonance. This changes the imaginary part of the 3s $\rightarrow$ 4p amplitude and hence changes *q*. This work stimulated further theoretical interest [69] and exploited the capabilities of the DLP technique.

Another potential of the technique was displayed when Mosnier *et al* [70], studying the Mg I isoelectronic sequence: Mg, Al^+ and Si^{2+}, observed the 2p $\rightarrow$ 3s excitations from excited $2p^6 3s3p$ odd-parity levels. The recorded autoionizing states thus belonged to the $2p^5 3s^2 3p$ even-parity configuration. Previous studies of these ion stages were confined to ground state absorption [71] and this was the first DLP experiment to produce absorption spectra from an excited state. Through careful combination of space- and time-resolved photoabsorption scans Mosnier *et al* could optimise plasma conditions to perform these measurements, highlighting the versatility of the DLP technique. It should be noted however, that normally great efforts are made to ensure the contribution from excited states and metastable states is kept to a minimum. Metastable contributions are unwanted in DLP experiments and can swamp spectra making spectral assignments difficult and tentative [72].

Jannitti and co-workers at the University of Padua did substantial work using the DLP technique to record photoabsorption and photoionization spectra from which they extracted photoionization cross sections of light ions [73], in particular, of C, B and Be. They recorded the spectra of C^{2+}, C^{3+} and C^{4+} in the region of K-shell ionization and identified series of the type $1s^2 2s \rightarrow 1s2sn$p and $1s^2 2s \rightarrow 1s2pn$p converging to the 1s2s and 1s2p ionization limits [74, 75]. In 1995 they studied the L-shell photoabsorption spectra and K-shell photoionization spectra of C^{4+} where they calculated the inner-shell ionization cross section by a procedure which normalised their continuum measurements to the oscillator strength of a discrete transition in the valence spectrum. Using this procedure, they obtained a cross section of 0.6 ± 0.1 Mb at the K-shell threshold in C^{4+} which compared well with the theoretical value [76]. This was the first time an accurate photoionization cross section measurement was made in a greater than doubly ionized atom. This method was limited however to elements where accurate *gf* values existed, and the accuracy was reduced where contributions from other charge states were non-negligible.

The large number of photoabsorption and photoionization spectra measured in the past two decades employing this technique has challenged, developed and

vastly improved our knowledge of atomic physics. Of course the DLP experiments were not alone, with the advent of synchrotron radiation (SR), inner-shell measurements could also be performed at SR facilities. In the early years, reliable ion sources proved difficult and low photon flux coupled with low ion density limited photoionization cross section measurements to ions with large cross section values [77]. However, in the last few years, significant improvements in synchrotron light sources and the installation of ion sources on beamlines has led to a significant increase in absolute cross section measurements in ions. While in general the DLP systems have better spectral resolution and relative ease in generating single to highly ionized ions of almost any element, absolute cross section measurements can be performed much more readily at SR facilities. A more detailed overview is given in chapter 4 where complementary experiments were performed using both facilities. The DLP system was used to measure the photoabsorption spectra of the Kr I ions Rb^{+} and Sr^{2+} and employing the merged-beam technique at the ASTRID storage ring at Aarhus University, Denmark, absolute photoionization cross section measurements were made for the same ions.

Further inner-shell photoabsorption measurements are presented in this thesis employing the DLP technique. Chapter 5 presents the 4p-subshell spectra of Sr^{+} and Chapter 6 details the 5d excitation spectra of the Hg I isoelectronic sequence: Pb^{2+} and Bi^{3+}. The next section describes the DLP system installed at DCU and includes the alterations made during this work to study resonant laser driven ionization in a laser produced plasma (Chapter 3).

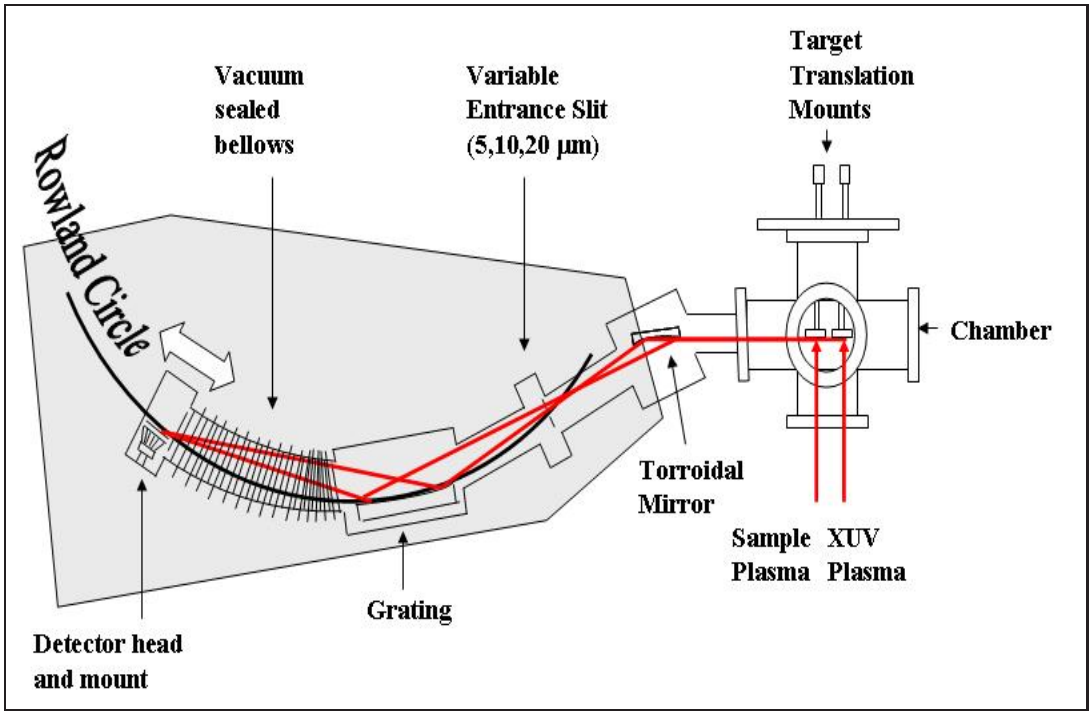

Figure 2.1: Schematic of the DCU DLP experimental system modeled from [78].

2.2 Experimental System

The XUV diagnostic system for the resonant pump-probe experiments described in Chapter 3 consists of an 8" six-way cross chamber coupled to a toroidal mirror chamber via a flexible coupling. Light incident on the mirror enters a 2.2 m grazing incidence spectrometer where it is diffracted onto a MCP (Micro-Channel Plate) unit with spectral image readout by a 1024 element photodiode array (PDA), as shown in Fig. 2.1. A Princeton EG&G controller (Model 1471A) collects, stores and processes spectral data under the control of a host computer. The interface, controller and detector collectively form an Optical Multichannel Analyser. The construction and operational set-up for the spectrometer are described by Kiernan [79] and Shaw [80]. The introduction of a Kentech fast gating unit for the MCP by Yeates [81] permits control over the gain of the system and enables time resolved measurements with resolution of a few nanoseconds. The dual laser plasma setup at DCU has been variously designed, and commissioned by past students [78, 79, 81, 82, 83] so only a brief description of the system is presented here. Emphasis is placed on the alterations made during my studies, in particular, the design of a new target chamber. The chamber was designed to incorporate flexible movement of both the sample targets and the numerous optics needed to carry out pump-probe type experiments (as detailed in Chapter 3). This addition to the

2.2 m grazing incidence spectrometer was paramount in performing these new experiments along with a new complex timing setup that needed to be implemented.

Briefly, we wanted to study the effects of resonantly coupling intense laser light to an atomic or ion resonance line in a laser produced plasma. The plasma is pumped via an OPO[1], tuneable in the visible (410-700 nm) range, and probed with a laser produced tungsten plasma which serves as a continuum source. Using the DLP technique we could monitor the change in the XUV photoabsorption signal of the plasma after laser-pumping. To further improve our knowledge of the energetic processes involved, we also monitored the fluorescence from the plasma after OPO irradiation. A new target chamber was designed to facilitate this experiment and the timing arrangement of the DLP was complicated with the addition of a third laser with different timing requirements. These changes are described in the succeeding sections.

2.2.1 Chamber

An 8" six-way cross (supplied by Kurt J. Lesker) was chosen as the target chamber for my experiments. We needed access to the targets in the chamber for three lasers and adequate space to include collecting optics for the optical fibre needed to perform fluorescence measurements. Fig. 2.2 presents the main attributes. The front port allows access to two lasers necessary to generate the absorbing and continuum plasmas for the DLP technique. The top port is used to focus the OPO 'pump' laser to intersect the optic axis of the XUV spectrometer at the point where the absorbing plasma lies. The side port provides a means to study the fluorescence from the excited plasma. The targets are mounted on micrometers for *z*-axis movement which permits spatial resolved probing of the laser-produced plasma. These micrometers, in turn, are mounted on a *x*, *y* moveable plate installed at the back of the chamber to give full 3D movement of the 'sample' targets in the chamber, see Fig. 2.3. Depending on the target used, a new position has to be found every $\sim$ 50 - 100 shots using the *x*, *y* movement as the target surface will have degraded considerably due to laser ablation.

A permanent optical holder is attached to the top port flange. A silver (100% reflecting) mirror mounted in a *x*, *y* holder guides the linearly-polarized OPO pulses through a Glan-Thompson prism. The light then passes through a convex (f=30 cm) lens used to focus the OPO into the absorbing plasma. The prism controls the OPO energy entering the chamber to study intensity effects in the experiments. The OPO is focussed down to a spot size $\sim$ 300 μm^2 in size.

As mentioned earlier, the fluorescence measurements are made using a optical

[1]Stands for Optical Parametric Oscillator and will be described presently.

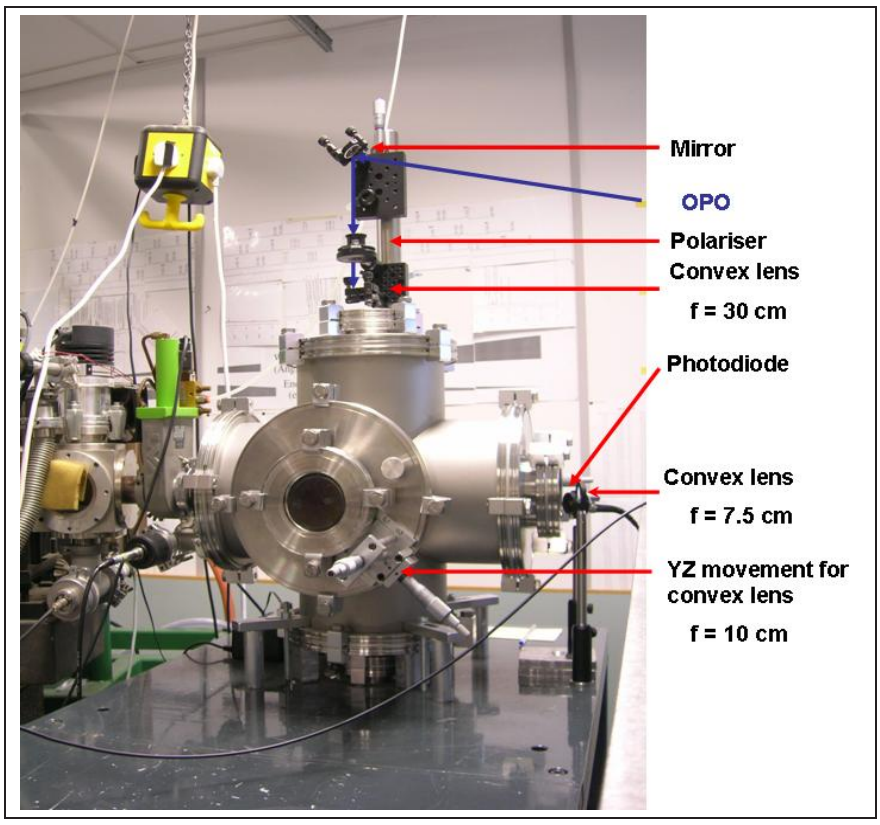

Figure 2.2: The six-way cross target chamber.

fibre which is coupled to an ICCD spectrometer. Initially we tried to place the fibre in the chamber via a Wilson seal on the front flange but it proved extremely difficult to align with the plasma. We had to avoid placing the fibre in line with the laser beam generating the absorbing plasma, so it had to be located at a significant distance from the plasma. Due to the weakness of the fluorescence and the remote distance of the fibre we could not obtain any signal above the noise floor of the ICCD. It was then decided to use a combination of optics inside and outside the chamber to focus the emitted light from the plasma onto the fibre. The fibre could then view the plasma along the direction of the optic axis through the side port window.

Fig. 2.4 is a schematic of the setup. The focusing lens inside the chamber (plano-convex, f = 10 cm) was mounted on a micrometer that passed through the front port to provide movement in the z direction. y movement was provided on the front flange using an additional adjustable plate designed and built in the DCU workshop. A convex f = 7.5 cm lens was placed outside the side port window to focus the light collected by the first lens onto the fibre. The fibre was pinned down to the optical bench holding the surelite / OPO system. All of these modifications

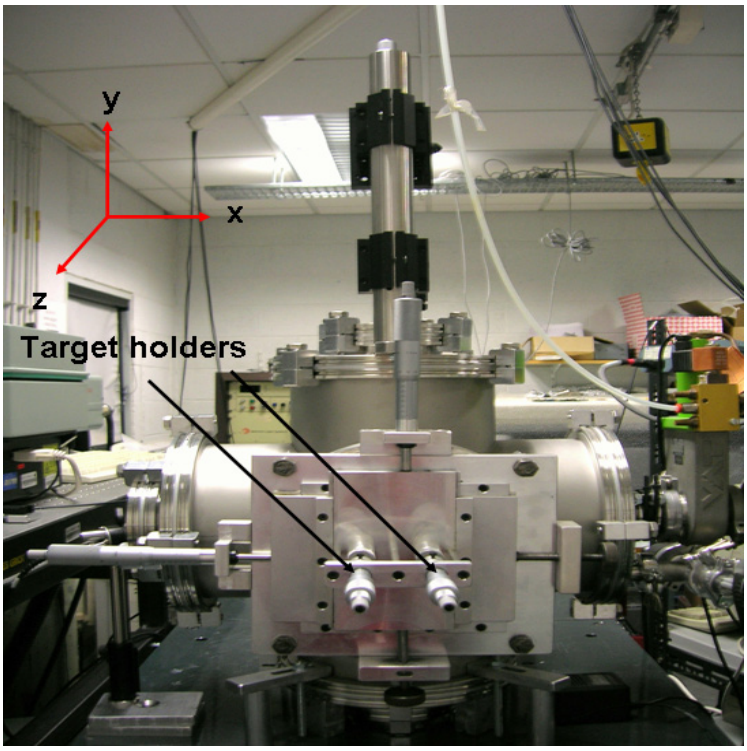

Figure 2.3: The XYZ movements for the targets in the chamber.

proved successful: sufficient movement of the targets and focussing elements allowed optimum conditions to be achieved for the pump-probe experiments. Once these variables were determined, they could remain fixed for a number of experiments until the targets needed replacement.

2.2.2 Toroidal Mirror

The toroidal mirror is housed in a separate vacuum between the entrance slit of the spectrometer and the DN40 gas-powered isolation valve. To prevent damage by plasma debris and to reduce the effects of pressure differentials after plasma generation, a glass capillary array (GCA) is placed between the chamber and mirror. The gold-plated mirror has two radii of curvature, R (major radius = 2100 mm) and r (minor radius = 111 mm), in the Y and X planes. The result is a longitudinal focus at the spectrometer's entrance slit to maximize light throughput and parallel light in the vertical to obtain uniform height along the different detector positions on the Rowland circle. Lines focused at the detector are 10 mm in height and 0.3 mm in width. The angle of incidence is set at 82° where the reflectivity of gold is high and aberrations are found to be negligible. The mirror is placed 400 mm from the chamber and 200 mm from the entrance slit to the spectrometer, which is the focus

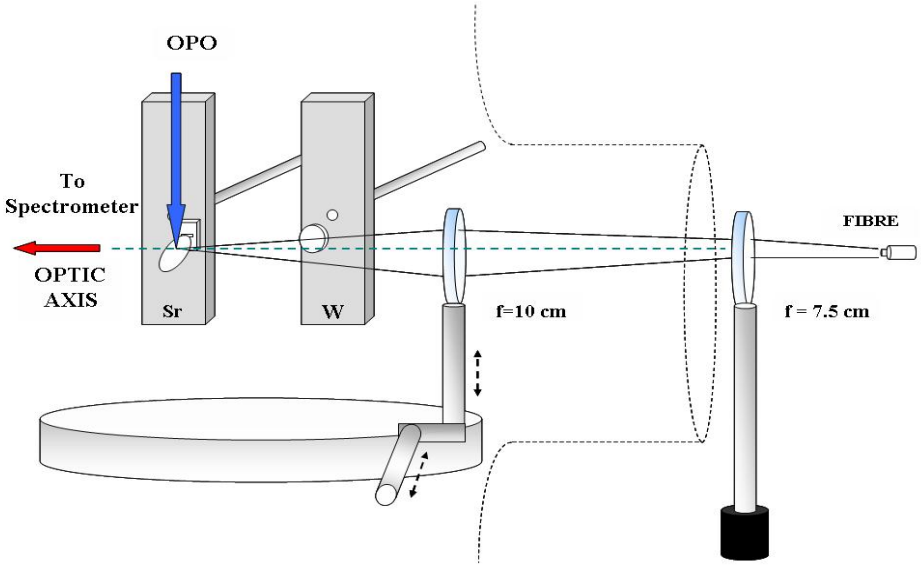

Figure 2.4: The optical layout for measuring fluorescence from the strontium plasma.

distance of the mirror.

2.2.3 2.2 m Grazing Incidence Spectrometer

The main components of the McPherson model 247M8, 2.217 m grazing incidence spectrometer are: a variable entrance slit, (set at 20 μm), a grating chamber housing the concave grating, (1200 lines / mm), a flexible bellows and guide rail system for moving the detector along the Rowland circle and a detector chamber. Light entering the spectrometer is incident on the grating at an angle of 16° with the blaze angle equal to 84.34°. After diffraction the light is dispersed and travels through a vacuum-sealed bellows to its final destination, the MCP / PDA detector. The detector moves along the Rowland circle, a mechanical counter indicates (in inches) the chordal distance from the centre of the grating to the approximate centre of the detector. According to our specifications, the accessible range of the instrument is $\sim$ 25-207 eV.

2.2.4 MCP/PDA

The MCP is a collection of parallel open channels each coated internally with a secondary emitting material to form a sort of continuous dynode like devices. The input face is coated with a photocathode material (Csl) and a large bias voltage (-1 kV) is placed across the device. The diffracted photons impinge on the MCP photocathode and are converted to electrons with a typical quantum efficiency of $\sim 20\%$. The

channels are 12 μm in diameter and separated by 15 μm at their centres. The active area of the matrix is 12.5 cm^2 and covers approximately a length of 40 mm along the focal plane of the spectrometer at the Rowland circle. The channel axes are biased at an angle of 80° to the incident photons to improve collection efficiency for the grazing incidence diffracted radiation. The primary photoelectrons are accelerated down the microchannel matrix resulting in secondary emission with a gain in excess of 10^4. The emerging output electron bunches are accelerated across a narrow vacuum gap ($<$ 1 mm) by a potential difference of up to +4 kV and impinge on a fibre optic bundle coated with visible photon-generating phosphor. The bundle reduces in diameter from 40 mm to 25 mm to match the length of the 1024 pixel PDA. Two parameters dictate the response of the detector: firstly, the MCP gain which is dependent on the negative voltage applied across the channels and secondly the resolution which depends on the positive potential difference applied across the 0.7 mm gap that separates the MCP from the phosphor coated fibre reducer.

The accumulated charge on the PDA is read out via a TTL pulse from the detector controller which is interfaced to a computer via a GPIB connection. Using software developed by Barry Doyle [82], the user can define a series of parameters such as number of shots accumulated, time delay between each shot, signal averaging etc. The detector controller can also be externally triggered allowing synchronization between lasers and the experiment. A Kentech fast-gating unit was commissioned by Yeates [84] to use the MCP in gating mode. It delivers a TTL pulse of variable bias and amplitude to the MCP head. It has three user adjustable outputs:

1. DC bias to bias the gap (0$>$4.5 kV).
2. DC bias of variable polarity to bias the MCP head (0$>$1 kV).
3. MCP transient pulse that can be superimposed on the MCP DC bias.

The MCP bias is fixed at -750 kV but by superimposing the transient pulse one can obtain a MCP DC bias of (-1.750 kV). As the gain of the system depends on the MCP bias, one can enhance the sensitivity of the detector to low flux considerably. This sensitivity was required for emission studies [84] and was not necessary for my photoabsorption experiments.

2.2.5 Resolving Power

A detailed study of the resolving power of the system was carried out by Kiernan [79] and Gray [78]. The performance of the system depends on both the reciprocal dispersion and resolving power. The separation of two wavelengths is defined by the dispersion while the resolving power is the ability to distinguish this separation. The resolving power is defined as

$$\frac{\lambda}{\Delta\lambda} = mN \tag{2.1}$$

where *m* is the order of the spectra, *N* is the number of ruled lines and $\Delta\lambda$ is the minimum wavelength separation that can be resolved. For a slit width *W*, an image width on the focal curve of the concave grating mounted on a Rowland circle corresponds to a wavelength separation of *Wd/R*, where *d* is the inter-groove spacings of the grating and *R* is the radius of curvature of the grating. Accordingly a theoretical linewidth of 0.008 Å is given within our specifications. This corresponds to approximately 4 pixels on the PDA.

Gray [78] measured the instrument broadening by recording the B^{2+} 2s-5p transition and found an instrument function of 4.2 meV per pixel. This translates to 4.5 meV when taking a Lorentzian fit and corresponds to a wavelength broadening of 0.01 Å (FWHM). The physical limitation imposed on the system by using a flat detector on the curved Rowland circle, results in a smearing of lines for pixel positions that are not tangent to the circle. Whitty [83] studied the variation in the FWHM of the Al $2s^2 2p^6 \rightarrow 2s^2 2p^5 3s$ transition at 160.074 Å as a function of detector setting. His findings showed that pixels 500-600 on the PDA satisfy the tangential condition, thus for accurate imaging of features of interest, one should image the photoabsorption spectrum within this pixel range. However in practise one uses the entire pixel range.

2.2.6 The ICCD camera and Shamrock Spectrometer

An ICCD camera attached to a Shamrock (SR-163i) spectrometer was used as the diagnostic tool to study fluorescence from the laser-excited plasma. The SR-163i is based on a Czerny-Turner spectrograph configuration as presented in Fig. 2.5. A manual micrometer drive on the spectrometer is calibrated to read 1 nm per 10 μm of travel for a 1200 g / mm grating. Manufacturer specifications give it a resolution of 0.17 nm for a 10 μm slit [2] with readout by a CCD camera with a spatial sampling period of 13 microns per pixel. A fibre adapter was mounted on the entrance slit port to couple light from the 200 μm optical fibre (SMA905 0.22 NA single mode)

[2] We operate with a 50 μm slit.

placed at the side window port of the chamber. The ICCD camera was an Andor DH5H7 model. The camera has 24 μm square pixels arranged in a 512$\times$512 2-D array. This array is coupled via a fibre optic coupler to a gated image intensifier. The intensifier enables amplification of incoming light and serves as an extremely fast shutter, $\sim$ 3.3 ns. The camera was operated in 'accumulate' mode, where the user can add together the data from a number of scans to create an accumulated scan. This improves the signal to noise ratio. Each measurement was made by accumulating over the same number of shots used during the XUV photoabsorption experiments. This ensured consistency between the XUV and optical measurements.

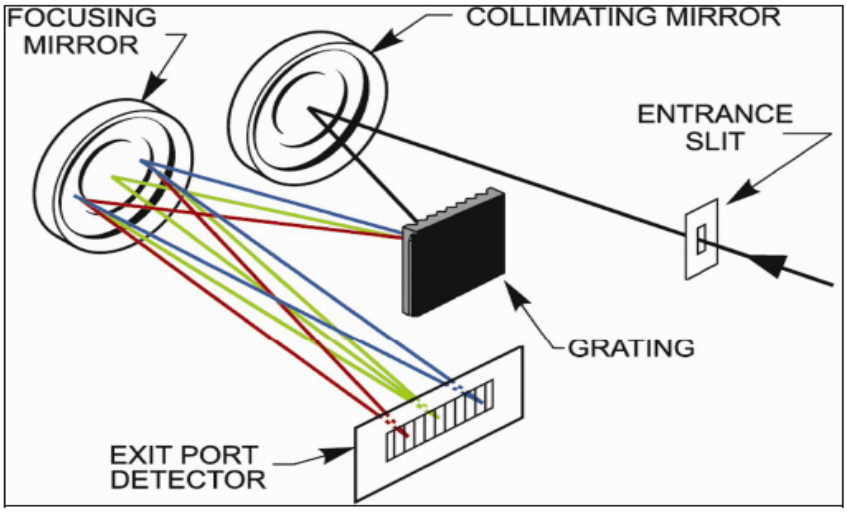

Figure 2.5: A typical layout of a Czerny-Turner spectrometer as used in our SR-163i model [85].

2.3 Data Acquisition and Laser Synchronisation

In our photoabsorption experiments, we need to ensure that the lasers generating the absorbing plasma and continuum source plasma are synchronised with our optical multichannel analyser. This can be easily achieved by using the internal timing of the detector controller to simultaneously provide a trigger to open the detector and fire both lasers. This set-up has been implemented and used successfully in all past Ph.D. studies at DCU. However, to perform the pump-probe experiments described in the next chapter, a more complicated timing scheme had to be developed. The following section details these adjustments.

2.3.1 Laser Details

Three lasers are used for the experiment. A Spectron SL803 Nd:YAG is focussed onto a tungsten target to generate the XUV source while a Spectron SL404 Nd:YAG is used to produce the absorbing plasma. The Surelite SL-II10 acts as the pump laser for the Panther OPO, see below for details. All three lasers were operated in Q-switched mode and externally triggered via Stanford delay generators with a shot to shot jitter of less than 1 ns.

Table 2.3.1. **Laser Specifications**

Parameter	Spectron SL803	Spectron SL404	Surelite SL II
Power Output	550 mJ	530 mJ	170 mJ
Pulse Duration	15 ns	15 ns	6 ns
Wavelength	1064 nm	1064 nm	355 nm
Q-switch delay	212 μs	173 μs	185 μs
Spot-size†	$\sim$ 200 μm^2 spot	$\sim$ 1 mm $\times$ 2 mm line plasma	$\sim$ 300 μm^2 spot
Intensity†	1*10^{11} W cm^{-2}	5*10^9 W cm^{-2}	2*10^8 W cm^{-2} ♭

† After focussing.

♭ This value is calculated assuming 20 mJ of energy enters the target chamber from the OPO after focussing.

An OPO is basically a resonator constructed with a non-linear gain medium. The Panther OPO is an optical parametric oscillator system generating mid-band radiation in the visible and near infrared spectral region. A generated wave (signal) is fed back by the resonator to the non-linear crystal causing further generation, or amplification, of the wave. It is analogous to a laser resonator except in this case the gain is a coherent process as opposed to a laser's population process.

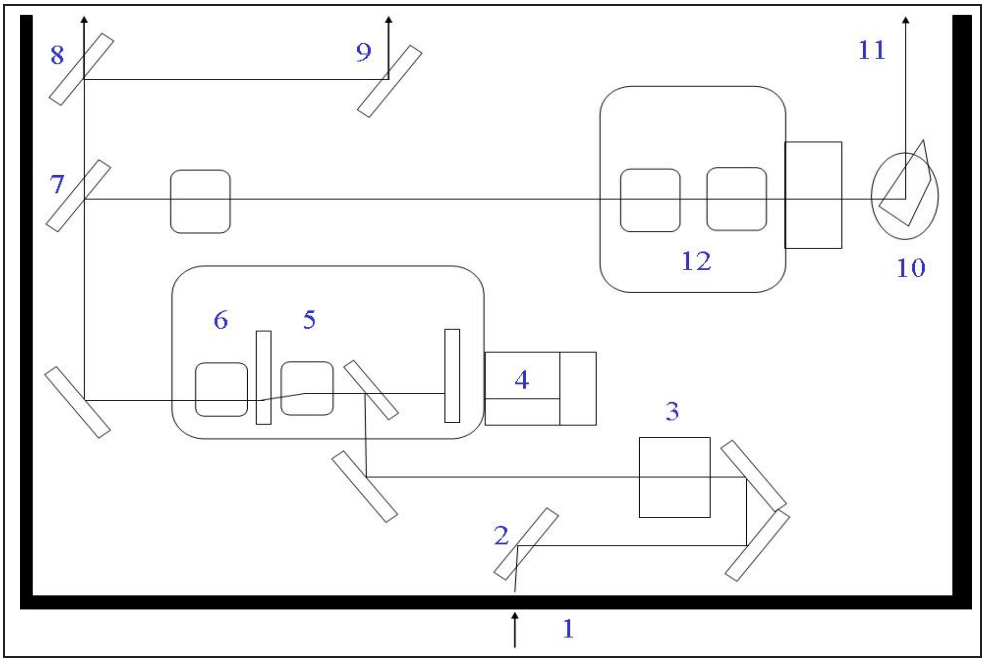

Figure 2.6: The optical layout of the Panther OPO [86]. (1) 355 nm pump beam, (2) 355 nm turning mirror, (3) pump attenuator, (4) beam dump, (5) oscillator crystal, (6) compensating crystal, (7) turning optic for doubling, (8) idler output, (9) signal output, (10) computer controlled prism stage, (11) doubled output and (12) frequency doubling crystals.

The Surelite laser provides the pump energy for the optical parametric conversion in the Panther OPO. An optical parametric process is a three photon interaction where the pump photon splits into a pair of less energetic ones, generally of different energy. The higher energy photon is referred to as the **signal**, while the lower energy photon is called the **idler**. Conservation of energy and momentum during the optical parametric process is achieved using a BBO (beta-barium borate) crystal, a birefringent material with different indices of refraction for different polarizations of light.

Energy conservation is satisfied when the sum of the signal and idler frequencies equal the pump frequency. However, as the resultant photons have different frequencies to the pump photon and therefore different velocities, linear momentum will not in general be conserved. If the idler and/or signal photons have polarizations orthogonal to each other, angles exist at which the crystal's frequency-dependent refractive index changes the idler and signal velocities so as to conserve linear momentum. The angle tuning of birefringent materials to produce a particular signal/idler pair (to conserve momentum) is called *phase matching*. Both the angular range over which it phase matches and its absorption characteristics determine a crystal's tuning range. The power output versus wavelength is shown in

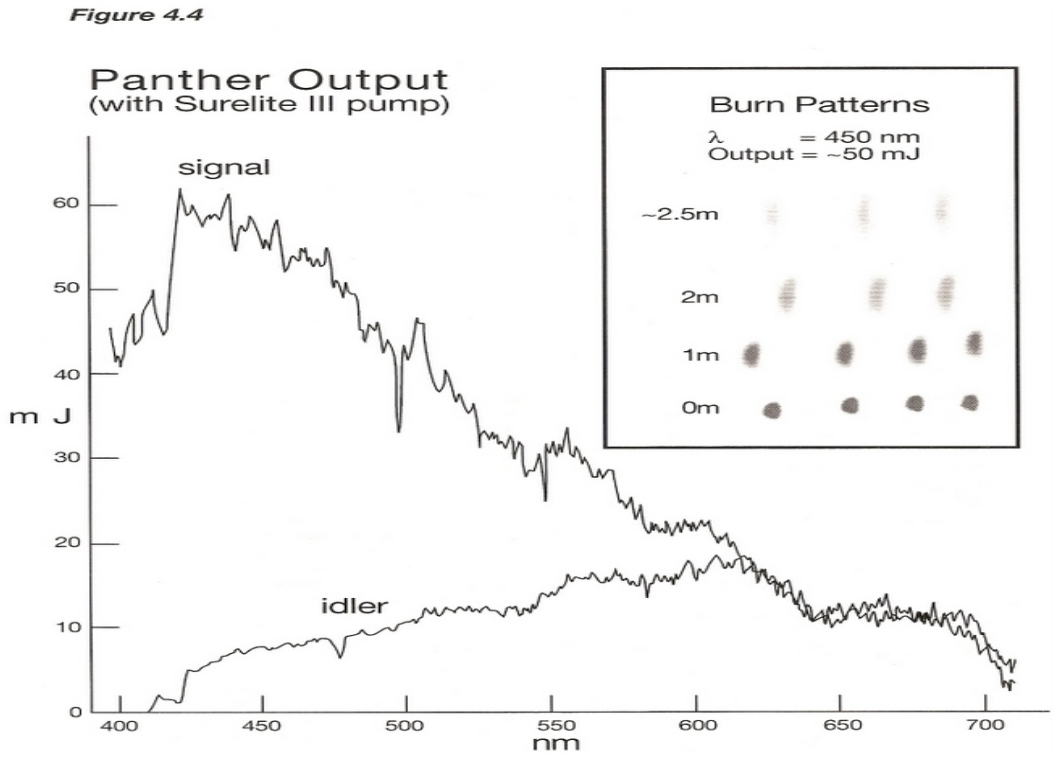

Figure 2.7: Panther Output (Surelite II pump).

Fig. 2.7. Only the signal output is used in this work. Currently for λ=430 nm, the maximum power output obtained from the OPO in the signal is 40 mJ.

2.3.2 Data Acquisition and Laser Synchronisation

Two EG&G controllers were used during this research, the 1460 and 1471a models. The 1460 controller was installed on the system before I started and was used initially to perform photoabsorption measurements in lead and bismuth. Data acquisition is initiated by applying a TTL positive going pulse to the Trigger Input connector of the detector controller. This pulse is user defined from the software and sent via the GPIB connection to the controller. Under the appropriate Data Acquisition (DA) modes, the system CPU will begin storing spectral data. One can avail of a TTL output pulse (TRIG OUT), from the controller via software, which can be used to externally trigger the experiment.

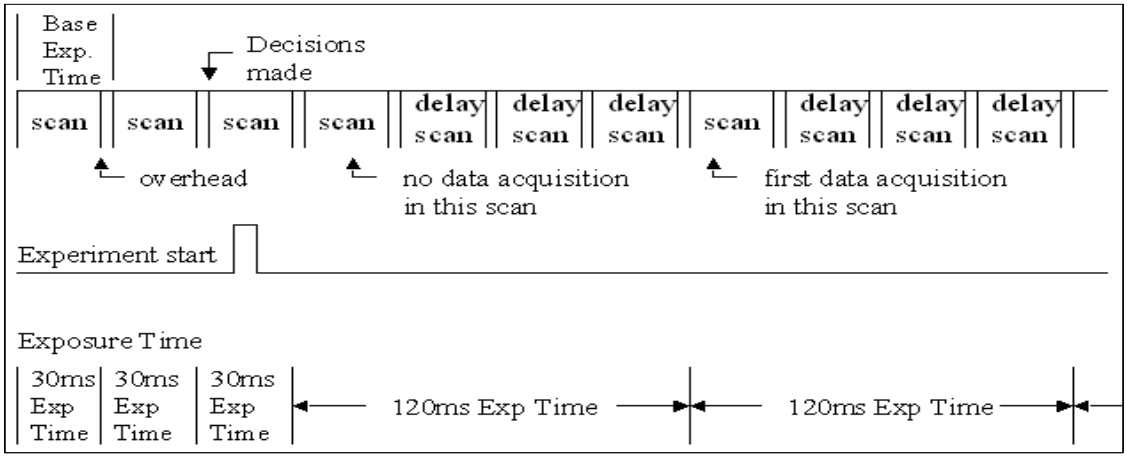

Figure 2.8: The exposure time of the PDA in normal synchronization mode.

- *Exposure time:* the total time between successive reads of a pixel. As pixels are scanned serially, the exposure time for any given pixel is skewed by one pixel time with respect to that of the preceding or following pixel.
- *Scan time:* The interval during which pixels are read / reset and data is transferred into the computer.
- *Overhead time:* Immediately follows each Scan Time and is provided to allow the host computer to make decisions regarding the next detector scan.
- *Delay scan:* Scan where the pixels are read and reset, but no data is taken. The photon flux is continuously integrated throughout each Delay Scan and many Delay Scans can be placed in series to achieve Exposure Times longer than the Base Exposure Time. These sets of ignored scans are interspersed with normal data acquisition scans to prevent detector saturation due to dark current buildup, thus one can achieve a better signal to noise ratio.

The 1024 element array on our system has a frame scan time of 30 ms, with a pixel readout of 28 μs. In normal synchronization mode (see Fig. 2.8), the Exposure Time must be set to an integer multiple of 30 ms. We operate in DA mode 4 which provides a Trig Out pulse after the experiment starts at the end of the first scan. It also takes into account any delay scans than may be incorporated into the experiment. This pulse was used to externally trigger the two Spectron lasers and synchronise them with the PDA / MCP detector. A typical photoabsorption experiment will have the following user-defined parameters:

Exposure Time	0.03
Scans	10
Ignore Scans	100
DA mode	4

Thus in normal sync mode, once the experiment begins, the first scan is read (30 ms duration) and then 100 scans are ignored to provide a delay of $\sim$ 3 second between successive laser shots as it takes 3 seconds (100 ignore scans * 30 ms) until the next scan is read again. Each experimental scan therefore takes 3.03 s which was deemed a suitable frequency to fire the Spectron lasers - the beam expanding telescopes in each Spectron system are optimised for pulse repetition rates of between 120 pulses per minute but a slower rate was used to improve laser flashlamp lifetimes. We repeated this procedure 10 times [Scan 10] to obtain signal averaging. This has been the general setup for the past few years. Unfortunately, the Surelite SL-II10 which pumps the OPO for my experiments has a 10 Hz rep rate so I needed to design a timing circuit that could effectively synchronise a 100 ms pulse with the pre-imposed 30 ms timing increment of the detector.

This was achieved using the external synchronization feature of another controller, the 1471A, which was installed on the system and used for the remaining experiments. In external sync mode, one can synchronise the scan readout of the PDA with a repetitive TTL signal from another source. The exposure time will then equal the period of this external sync pulse, see Fig. 2.9 for further details. Driving both the controller and Surelite with the same 10 Hz signal, the exposure time of the PDA could thus be set to 100 ms. As the Spectron lasers had been optimised to fire at 2 Hz by the manufacturer, we could now set up an experimental scan that would trigger the two Spectron lasers for this repetition rate by user-defining four delay scans instead of 10, (100 ms (start scan) + 4 ignore scans * 100 ms = 500 ms (2 Hz)).

One complication occurred however. The Trig Out pulse is always applied at the end of the first array scan which only takes 28.672 ms, (1024 array * 28 μs = 28.672 ms), once the experiment begins. As the intention was to use the Trig Out as a master pulse to fire all three lasers, they would be out of sync with the data acquisition by this amount. An appropriate solution was to add $\sim$ 72 ms to the Trig Out pulse thus creating a ”new 100 ms” pulse. This would ensure that the lasers fired at the start of a 100 ms scan exactly when the detector is read.

Using a DG353 Stanford delay/pulse generator, the ”new 100ms” pulse was generated. A TC4426 dual high-speed power mosfet chip was employed to AND gate the 10 Hz external synchronization signal with this ”100 ms” pulse to ensure accurate alignment between the data acquisition and lasers. We found that

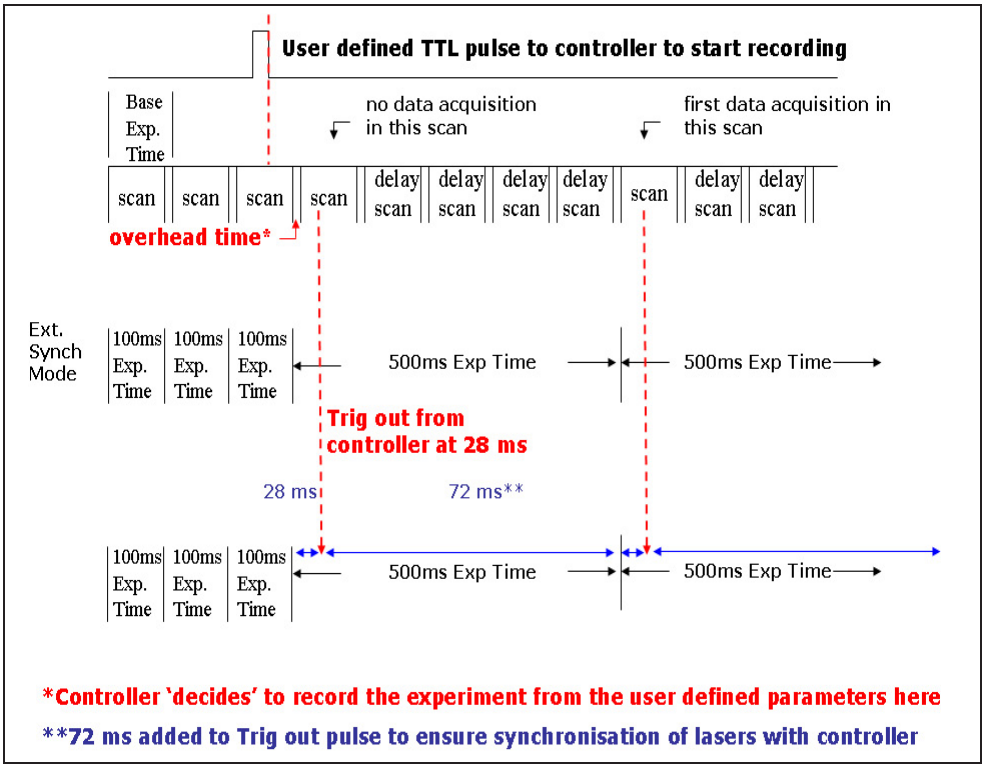

Figure 2.9: The exposure time of the PDA in external synchronization mode. Although the base exposure time has now been set to 100 ms, the Trig Out from the controller is still sent at $\sim$ 28 ms, the readout time from the PDA. If we used this pulse as the master trigger, the lasers would fire in between scans and be out of synch with the detector.

71.050 ms was the precise delay time needed to ensure the lasers fired in synch with the detector. The output of the AND gate was then used as the master trigger to fire the lasers, see Fig. 2.10. A DET210 high-speed silicon photodiode positioned at the side view port of the chamber was used to measure the overlap of the three laser pulses (to an accuracy of $\sim$ 1 ns). The MCP is used in gated mode and triggered to open when the lasers have fired for a duration of 4 ns. The OPO pulse duration at $\sim$ 6 ns is considerably less than that of the XUV source (15-25 ns) [87]. Hence the narrow gate is used to ensure that information recorded from the interaction region when the 6 ns OPO pulse is present. In this way one can significantly reduce background signal due to XUV absorption when the OPO signal is absent. The ICCD is externally triggered by this master pulse too so that all measurements are made simultaneously.

One final consideration is the spatial overlap of the OPO beam in the laser produced plasma. This was one of the most difficult tasks to perform for the pump-probe experiments presented in Chapter 3. No change in the XUV photoabsorption

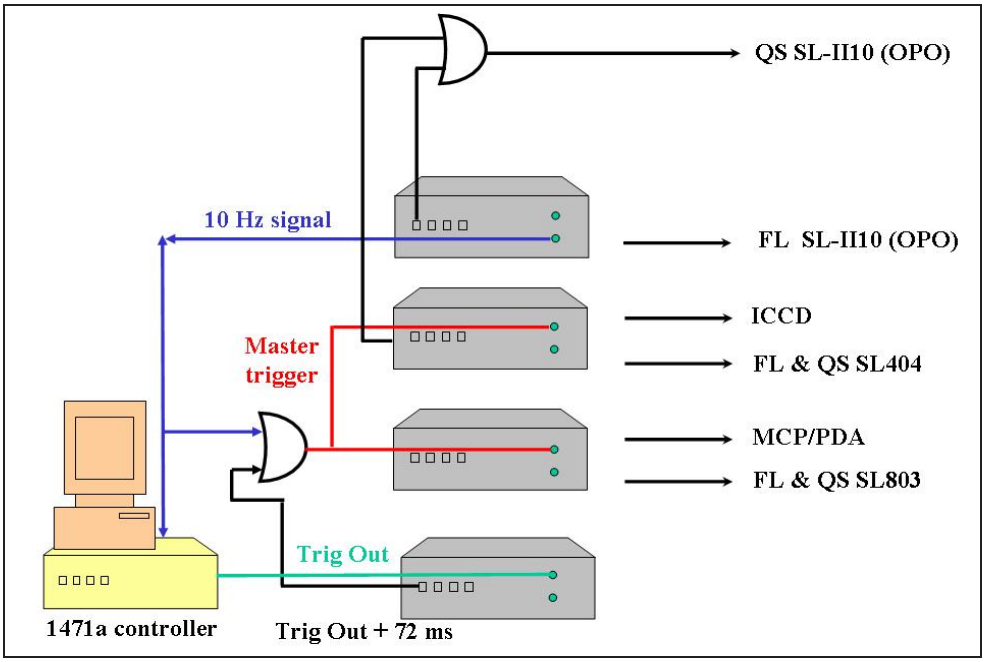

Figure 2.10: Laser Synchronization: A 10 Hz signal generated by a delay generator (DG - grey box) is used to rep both the surelite SL-II10 and the detector controller. Another DG is used to add 72 ms to the Trig Out pulse from the controller which is fed to an AND gate to generate the master trigger. This 'master' pulse is then used to trigger the other DGs. These in turn provide the relevant pulses to trigger the flashlamps (FL) and *Q*-switch (QS) the spectron lasers, and to gate both the MCP / PDA and ICCD detectors.

spectra[3] was observed unless the OPO beam overlapped the plasma exactly. Spatial overlap was achieved by setting the dual-laser plasma experiment to run in 'live' mode (continuous single-shot mode) and by adjusting the mirror in the *x*, *y* holder (fixed to the top port of the chamber), one could focus the OPO beam onto the plasma. One could view the neutral or singly-charged absorbance spectra from the strontium plasma on a monitor screen and ensure overlap of the OPO beam by observing a rise in the Sr^+ (for neutral strontium) and Sr^{2+} (for both Sr^0 and Sr^+) photoabsorption peaks after the end of the OPO pulse. Each pump-probe experiment was set up by tuning the OPO to the one-photon resonant wavelength, 460.7 nm in neutral strontium and 421.6 nm for Sr^+, and at the highest intensity, 3×10^8 W cm^{-2} until the same optimum ionization signal was observed.

[3]This change presents itself as a growth in photoabsorption resonances of single and / or doubly-charged ions.

Chapter 3

Resonant Laser Driven Ionization in Sr and Sr^+

3.1 Introduction

In the early 70s, Lucatorto and McIlrath [18] showed that tuning to a resonance line in a sodium vapour using a laser of moderate intensity (1 MW cm^{-2}) was a highly effective method of coupling energy into a dense atomic vapour. The observed ionization rate reached 95% of the initial excited-level population. This effect was named Resonant Laser Driven Ionization (RLDI). The same group performed RLDI experiments in a lithium vapour the following year and again reported a high ionization efficiency [88]. They proposed the following energy transfer mechanisms to explain the high degree of ionization:

1. Two-photon ionization out of the resonance level, for example:
   $Na(3p) + 2h\nu \rightarrow Na^+ + e^-(\epsilon)$

2. Laser-induced Penning ionization, for example:
   $Na(3p) + Na(3p) + h\nu \rightarrow Na^+ + Na + e^-(\epsilon)$

3. Superelastic collisional heating of excited state atoms by seed electrons generated during the first two processes, followed by electron impact ionization by these heated electrons:
   $Na(3p) + e^-(\epsilon) \rightarrow Na(3s) + e^-(\epsilon', \epsilon' > \epsilon)$
   $Na(nl) + e^-(\epsilon') \rightarrow Na^+ + 2\,e^-$

4. Direct collisional exchange of energy, followed by photoionization from a highly excited level:
   $Na(3p) + Na(3p) \rightarrow Na(5s) + Na(3s)$
   $Na(5s) + h\nu \rightarrow Na^+ + e^-(\epsilon)$

5. Promotion of atoms from the resonant level to higher lying levels by stimulated Raman scattering and subsequent single-photon ionization, e.g.
   Na(3p) + $h\nu$ $\rightarrow$ Na(4p) + $h\nu$' (hν' $<$ hν)
   Na(4p) + $h\nu$' $\rightarrow$ Na^+ + $e^-(\epsilon)$

6. Associative ionization to ionized dimers followed by photodissociation:
   Na(3p) + Na(3p) $\rightarrow$ Na_2^+ + $e^-(\epsilon < 0.1$ eV)
   Na_2^+ + $h\nu$ $\rightarrow$ Na + Na^+ + $e^-(\epsilon)$

Subsequent studies employing electron spectroscopy, ion detection and fluorescence measurements were made to disentangle the above processes. Skinner [89] investigated vapours of calcium, strontium and barium. He used a long pulse tunable laser, (300 ns, 1 MW cm^{-2}), tuned to resonance frequencies of the respective atoms and observed high ionization efficiencies. He reported a drop in fractional ionization at low densities (5×10^{14} cm^{-3}), which was a clear indication of the importance of the collisions in the ionization process. Studying the conversion of laser energy into potential energy of the ions (by monitoring the ion density as a function of laser intensity), strontium vapour was shown to reach a remarkable 42% efficiency. This work was continued in barium [90, 91], where the Hook method [92] was employed to monitor the population distribution of various excited atomic and ionic levels during and after laser-excitation. It was established that seed electrons were heated by superelastic collisions with laser-excited atoms and followed by electron-impact excitation and ionization. These processes as well as photoionization of high-lying levels, lead to the creation of more electrons. The electron density and concomitant ionization increased accordingly. Further explorations [93, 94, 95, 96, 97] confirmed the major role played by superelastic collisions with seed electrons.

A theoretical model was proposed by Measures [98, 99, 100] to explain laser ionization based on resonance saturation (LIBORS). The model assumes that the laser saturates the resonance level and initially provides seed electrons by various energetic processes. Superelastic collision quenching of the overpopulated resonance level, combined with the reduction of the ionization energy of the laser excited atoms is a main contributor to heating of the electrons within the medium. The super-elastically heated electrons proceed to collisionally excite electrons to high-lying states that can be further ionized in the laser field or by direct collisional ionization producing secondary electrons. Runaway collisional ionization of the upper levels occurs until superelastic heating can no longer balance collisional cooling and the electron temperature falls.

The full comprehensive LIBORS code treats the laser-excited atom as a 20-energy-level system and solves the subsequent set of energy and population rate equations

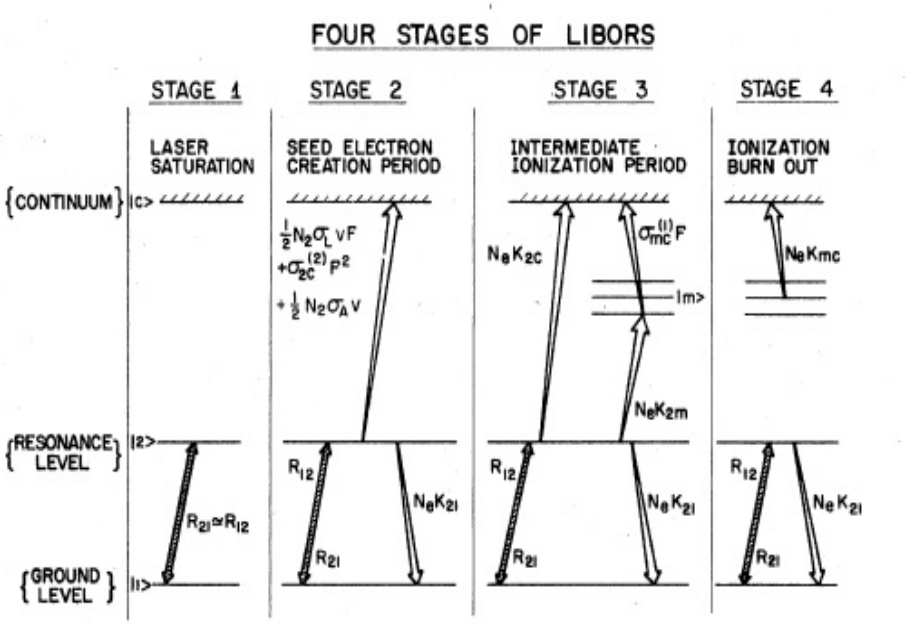

Figure 3.1: The four stages of LIBORS as described in the text [100].

by a fourth-order Runge-Kutta technique. It was successfully implemented to reproduce the observed ionization time in Na [101]. A more simple model was described in [100] where only the next (lowest lying) four optically connected (parity-allowed) levels from the resonance level were included. The model also assumes a steady-state temperature is reached after resonance saturation. The burnout time for ionization (peak) in the alkali metals was calculated using these simplifications for densities 10^{15}-10^{17} cm^{-3} and laser intensities 10^{5}-10^{8} W cm^{-2}. Good agreement (less than 5% variation) was found between these results and those obtained from the full LIBORS code in sodium.

More recently, Gamal *et al* [102] proposed a model that describes the transient kinetics of the ionization mechanisms, focusing on the time-dependent electron energy distribution function. In contrast to the LIBORS model, where Measures assumes that associative ionization and Penning ionization only occur at Stage 1 (see Fig. 3.1), Gamal *et al* [102] include these processes throughout. The computations were carried out under the experimental conditions of Hunnenkens *et al* [103] who tuned a cw dye laser (200 mW output) to resonantly excite a cesium vapour, 10^{16} cm^{-3}. From their model they concluded that electrons were mainly generated by associative and Penning ionization. Superelastic collisions heated these free electrons, which were then responsible for depopulating the highly excited states through electron impact collisions, resulting in the ionization signal observed.

As can be seen from this overview, most experimental and theoretical work has been confined to the alkali metals and alkaline earth metals as they possess optically accessible atomic resonance lines. The ionization process benefits from the low ionization potentials in these elements and the large number of intermediate levels that increase the energy of the atom in a stepwise manner to reach the ion. From the LIBORS model (Fig. 3.1) it can be seen that different stages dominate depending on which atom is excited. The differences are generally related to the initial seeding process: if a large number of seed electrons are generated, full ionization is generally achieved quickly, usually within nanoseconds. In some cases, intermediate levels play a more significant role, particularly where associative ionization is absent, as is the case for lithium [88]. At higher intensities, the time for complete ionization can decrease if the cross section for processes like two-photon resonant ionization and laser-induced Penning ionization is high.

This study is concerned with RLDI in Sr and Sr^+. Previous studies have been made of strontium vapours [89, 95, 96] and these results are presented in the results section through comparisons with our measurements. To our knowledge this is the first RLDI study that utilises a laser-produced plasma as the target sample. This atom / ion source complicates the experiment slightly as we have to contend with collective effects in the plasma but it allows the study of any element in different stages of ionization. At our densities, $\sim 10^{16}$ cm^{-3}, the collisional radiative (CR) model of equilibrium applies [104]. In this case, collisional effects dominate in the plasma. It includes electron collision processes causing transitions between excited state levels and three-body recombination. Therefore one can expect some initial population of excited state levels which is largely absent in atomic vapours. Bremsstrahlung is another important process in the plasma. It occurs when a free electron moving close to an ion is accelerated by the ion's Coulomb field, thereby emitting a photon. It is the main radiation process in low-Z plasmas and is also important in highly ionized high-Z ones. When a high-Z plasma is less ionized, as in our case, Bremsstrahlung provides a low background continuum on which line emission is superimposed. The inverse mechanism is known as inverse-Bremsstrahlung and is an effective method for coupling laser energy into the plasma [105]. Another difference in our study is the higher intensity of our laser, $\sim$ 100 MW cm^{-2} compared to the intensities used in previous studies, 1 - 10 MW cm^{-2}.

Using the DLP technique to isolate atomic strontium (Sr), and Sr^+ in the plasma, we tune to one-, two- and three-photon resonances in the atom or singly charged ion using an optical parametric oscillator, (OPO). We then compare the XUV photoabsorption and fluorescence measurements in the plasma with and without OPO

irradiation. By monitoring how the XUV absorption signal varies with time after laser-pumping, we can monitor the temporal evolution of ionization. Section 3.2 provides further details of the experiment. The fluorescence signal from the strontium plasma is recorded after irradiation with the OPO using a fibre coupled to a visible spectrometer with spectral readout via a gated ICCD camera. This allows us to observe the temporal profile of the excited strontium level distribution after the short resonant laser pulse excitation. This in turn permitted us to uncover the role played by highly excited states in the ionization process and illustrate the dominance of heating in the plasma by superelastic collisions with the laser-excited atoms/ions. Results show that resonant pumping is significant in ionizing the Sr^+ plasma but not as dominant when laser-exciting atomic strontium.

3.2 Experiment

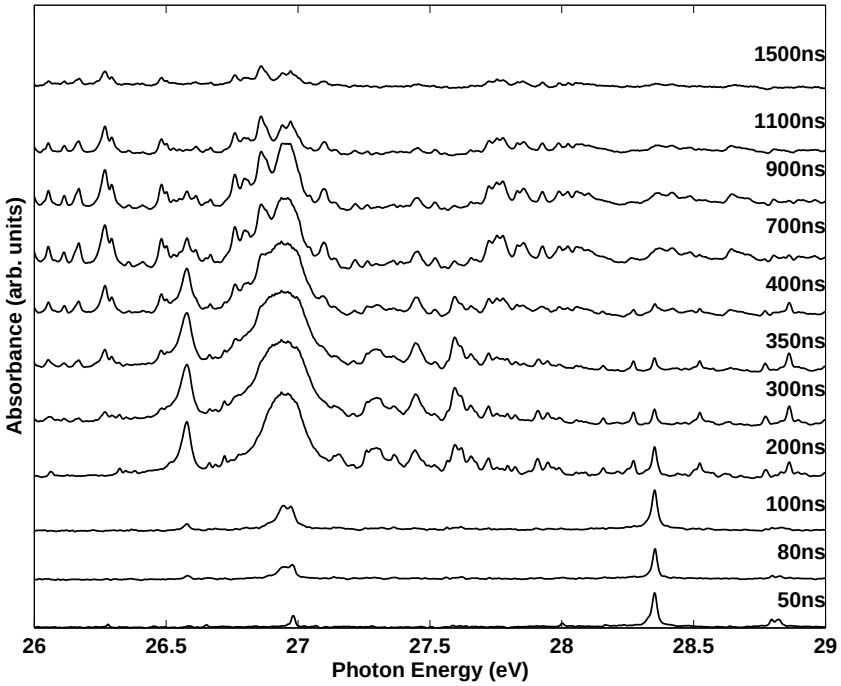

Figure 3.2: The temporal evolution of the photoabsorption spectrum of a strontium plasma 1.15 mm from the target surface. For the early time delays, 50-100 ns, Sr^{2+} dominates as characterised by the peak at 28.35 eV (see Chapter 4 for the Sr^{2+} photoabsorption spectrum). At 400 ns the photoabsorption spectrum of Sr^{+} is seen (Chapter 5 presents a detailed description of this spectrum) while for the later time delays, 1100-1500 ns, Sr^{0} is dominant.

Employing the DLP technique, a spatio-temporal profile of the strontium plasma was generated which permitted us to separate and isolate atomic Sr or singly charged Sr as required, see Fig. 3.2. A cylindrical lens (f = 30 cm) was used to focus the output of the Nd:YAG laser (15 ns, 410 mJ) to a line $\sim$ 4 mm in length and 1 mm in height for generation of Sr plasmas. Spectra were recorded at t_0 = 1200 - 1500 ns, after plasma generation and probed 0-0.2 mm from the target surface for optimum isolation of neutral Sr in the plasma. A knife-edge was used to decrease the plasma length (or line focus) to $\sim$ 2 mm for Sr^{+}. Displacement of the target from the optic axis of the spectrometer by Δx = 1 - 1.5 mm and t_0 = 450-500 ns provided the best isolation of Sr^{+}. The spectra were wavelength calibrated against known emission lines of aluminium, manganese and oxygen ions.

To study the effect of resonantly exciting strontium, the OPO (6 ns, $\sim 10^8$ W cm^{-2}) was focussed down to a spot size of $\sim$ 300 μm^2 in the strontium plasma, perpendicular to the XUV beam. The energy of the OPO beam was tuned by means of a polariser as described in Chapter 2. At the time t_0 where we had predominantly Sr

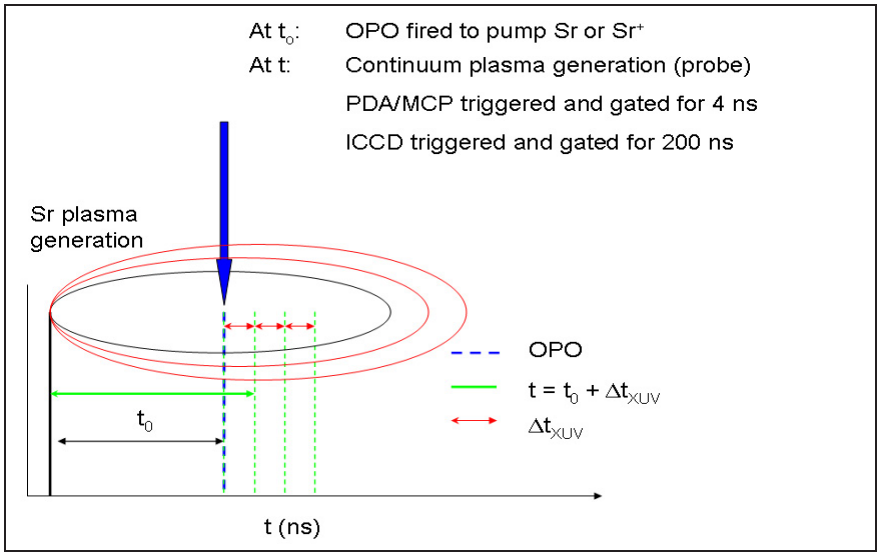

Figure 3.3: Basic timing diagram for our experiments.

or Sr^+ in the plasma, we irradiated the plasma with the OPO to excite the Sr atom or ion to a selected one- or multi-photon resonance. As described in Fig. 3.3, the XUV emitting plasma was used to probe the strontium plasma at various times Δt_{XUV} afterwards such that $t = t_0 + \Delta t_{XUV}$, and the MCP / PDA was triggered synchronously with the XUV probe (gatewidth = 4 ns). The ICCD was also incremented from this t_0 time, for the same time intervals, to study the temporal behaviour of the fluorescence lines so that one could simultaneously record the XUV / ionization signal and optical signal after OPO irradiation.

In our studies, we needed three different spectra for each value of Δt_{XUV}: I_0, the XUV beam in the absence of a strontium plasma; I_{DLP}, the transmitted XUV beam recorded a time Δt_{XUV} after the generation of the strontium plasma in the absence of the optical laser field, and I_{OPO}, the transmitted XUV beam recorded Δt_{XUV} after the generation of the strontium plasma *in the presence of the optical laser field.* In practice, we recorded spectra in the sequence I_0, I_{DLP}, I_0, I_{OPO}, I_0, I_{DLP}, ..., I_0 which allows interpolation of the I_0 values to find what the incident intensity would have been at the time the transmission spectra were recorded. In other words, each I_0 used to compute the photoabsorption spectra is an average of I_0 before $I_{DLP/OPO}$ and I_0 after.

The difference caused by irradiating with the optical laser field can then be displayed as follows. The absorbances $I_{DLP} \equiv \ln(\frac{I_0}{I_{DLP}})$ and $I_{OPO} \equiv \ln(\frac{I_0}{I_{OPO}})$ were calculated at the same time delay Δt_{XUV}, and difference spectra were obtained by $A \equiv I_{OPO} - I_{DLP}$. Thus a transition in the XUV region that was more pronounced after irradiation with the optical laser field showed up as a positive peak, and one

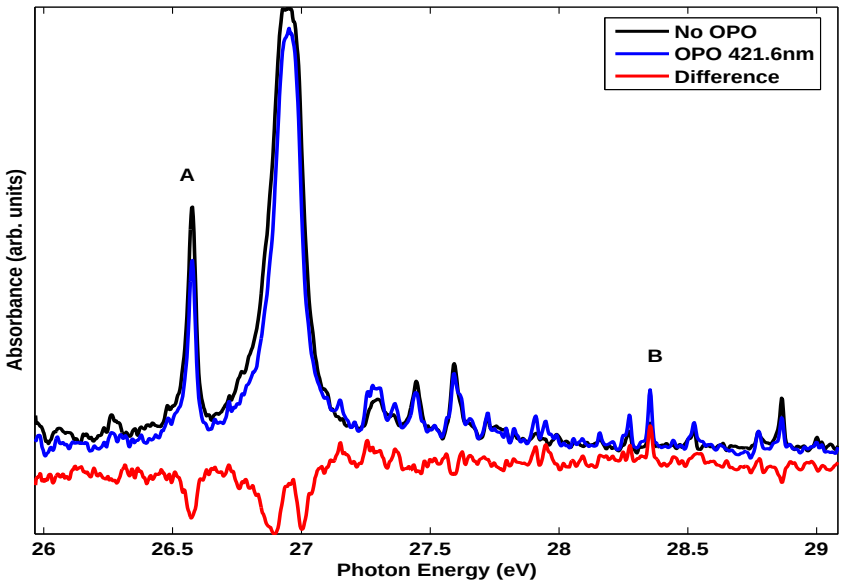

Figure 3.4: Difference spectrum after interrogating the strontium plasma 460 ns after generation where we have predominantly Sr^+. The OPO (0.7×10^8 W cm^{-2}) is tuned to the one photon resonance at 421.6 nm, and the irradiated plasma is probed by the backlighting continuum at the same time. The difference spectrum clearly shows an increase in the Sr^{2+} transition $4p^6 \rightarrow 4p^5 4d$ at 28.35 eV (B) [16] and a reduction in the ground state photoabsorption peaks of Sr^+ ((A) corresponds to the $4p^6 5s \rightarrow 4p^5 4d^2$ transition in Sr^+, see Chapter 5). Note also the improved resolution of the Sr^+ doublet ($4p^5 4d\ ^1P)5s\ ^2P_{3/2,1/2}$ (i.e. from the large resonance at 27 eV).

that was less pronounced showed up as a negative peak, as seen in Fig 3.4. This way of displaying the data also afforded us the advantage of increased resolution associated with differential absorption spectroscopy [106], as can be clearly see for the large resonance at 27 eV.

To perform the fluorescence studies, an optical fibre (SMA905 0.22 NA single mode) coupled to a SR163i-Andor visible spectrometer with a gated ICCD camera was utilized. A combination of a 50 μm entrance slit and 1200 lines/mm grating gives a resolution of 0.17 nm[1] and the ICCD has a 3.3 ns minimum gate width. A convex lens (f = 10 cm) was placed inside the chamber and a convex lens (f = 7.5 cm) outside the chamber to focus the emitting light from the plasma onto the fibre. The fibre viewed the plasma along the direction of the optic axis through the side port window, refer to Fig. 2.4 in Chapter 2. Emission from the plasma was then recorded for $t = t_0 + \Delta t_{XUV}$, as stated previously. We could thus monitor the temporal evolution of states enhanced by the presence of the OPO optical field (as can be seen in Fig. 3.5) and, in turn, interpret the role that metastable states play

[1] quoted for a 10 μm slit by the manufacturer

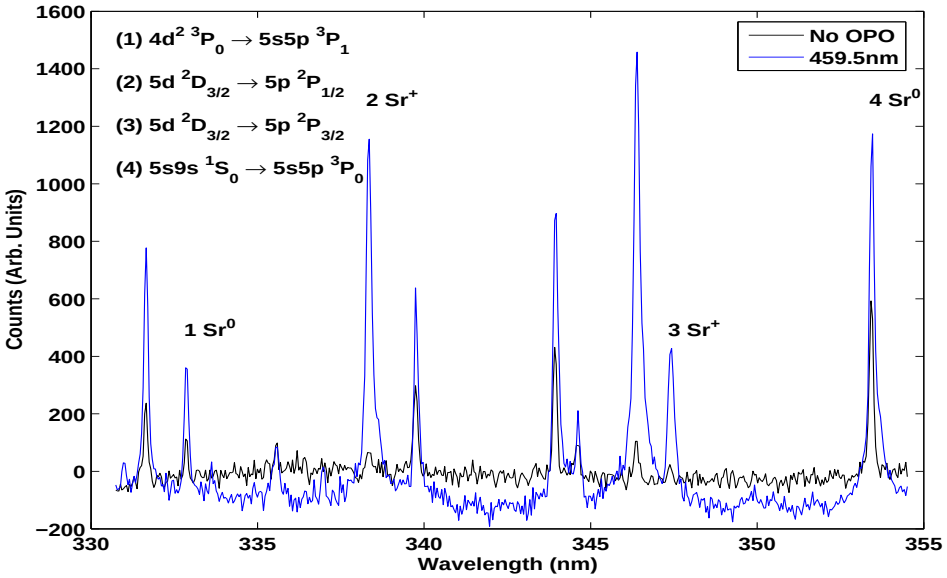

Figure 3.5: Fluorescence recorded on the spectrometer (331 - 355 nm, 200 ns gatewidth), 50 ns after OPO irradiation, λ=459.5 nm. The spectra are accumulated over 15 shots per data set and then averaged over 3 data sets. The black line is without the OPO and the blue line displays fluorescence after OPO irradiation. Note the presence of the ion lines (2, 3) after excitation. The other lines present are due to fluorescence from higher lying excited states to the 5s5p ^3P levels. The large peak at 346.4 nm is due to Sr^+, 5d $^2D_{5/2} \rightarrow$ 5p $^2P_{3/2}$.

in energy-pooling and the energetic mechanisms that lead to the ionization signal observed in the photoabsorption measurements. Further details are presented in the next section.

The spectrometer settings are displayed in Table 3.1 for the fluorescence measurements. These setting were chosen to ensure appropriate spectral coverage of fluorescence from excited state Sr and Sr^+ levels. Unfortunately due to the weakness of some signals, large gate widths of 200 ns were necessary for the neutral fluorescence. The gatewidth could be reduced (to 60 ns) for the 8.37 mm (404.84 - 427.64 nm) spectrometer setting due to a stronger signal. Although large gate widths are not ideal, the ICCD measurements made were sufficient to supply additional useful information on the energetic processes involved in the study. For resonant excitation in Sr^+, we could use gatewidths of 30 ns due to the strong emission signal from Sr^+ transitions. All signals were background corrected and fitted with a second order polynomial to ensure all peak bases were zeroed. This was necessary, as can be seen in Fig. 3.5, because the base level for the spectrum before and after OPO irradiation do not coincide, the blue line lies below 0 counts. After our second order polynomial fit, the base level for both spectra are the same. We measure the population difference by calculating the area under the fluorescence

peaks before and after the OPO and subtracting to obtain the difference.

Table 3.1: Spectrometer and ICCD settings for the fluorescence measurements for our resonant excitation studies in Sr^0

Spectrometer Position (mm)	λ_{range} (nm)	Ion Stage	Transition			λ (nm)	Gatewidth (ns)
6.88	330.90 - 354.60	Sr	$4d^2\ ^3P_0$	$\rightarrow$	$5s5p\ ^3P_1$	332.99	200
		Sr^+	$5d\ ^2D_{3/2}$	$\rightarrow$	$5p\ ^2P_{1/2}$	338.07	200
		Sr^+	$5d\ ^2D_{3/2}$	$\rightarrow$	$5p\ ^2P_{3/2}$	347.47	200
		Sr	$5s9s\ ^1S_0$	$\rightarrow$	$5s5p\ ^3P_0$	353.40	200
9.47	459.36 - 480.24	Sr	$5s5p\ ^1P_1$	$\rightarrow$	$5s^2\ ^1S_0$	460.70	200
		Sr	$5p^2\ ^3P_2$	$\rightarrow$	$5s5p\ ^3P_1$	472.23	200
9.85	478.19 - 498.40	Sr	$5s4f\ ^3F_4$	$\rightarrow$	$5s4d\ ^3D_3$	489.20	200
		Sr	$4d5p\ ^3D_3$	$\rightarrow$	$5s5p\ ^3P_2$	496.23	200
8.37	404.84 - 427.64	Sr^+	$6s\ ^2S_{1/2}$	$\rightarrow$	$5p\ ^2P_{1/2}$	416.18	60
		Sr^+	$5p\ ^2P_{1/2}$	$\rightarrow$	$5s\ ^2S_{1/2}$	421.60	60

3.3 Results

3.3.1 Sr

Firstly, we will give an overview of the most important results. For our Sr studies, we tuned the OPO to the one photon $5s^2\ ^1S_0 \rightarrow 5s5p\ ^1P_1$ line at 460.7 nm and to the two-photon $5s^2\ ^1S_0 \rightarrow 5s10s\ ^1S_0$ transition at 459.5 nm. A three-photon resonant wavelength, λ=435.0 nm, which tunes to the $5p_{3/2}12s_{1/2}$ level at 8.55 eV was also explored, as this level lies above the first ionization threshold at 5.695 eV. A non-resonant wavelength at 470.0 nm was also studied for comparison with the resonant excitation schemes. The ionization signal was measured in the form of the increase in Sr^+ transition at 26.57 eV ($4p^5 4d^2$) observed in the difference spectrum after laser excitation. With the OPO, even the strongest Sr absorption lines disappeared almost entirely, indicating nearly 100% ionization, at all OPO wavelengths, including the non-resonant wavelength of 470.0 nm. No laser-excited absorption was observed from the $5s5p\ ^1P_1$ level, its lifetime has been measured to be 4.8 ns [107], but collisions are expected to occur during this timescale thus preventing the observation of excited absorption.

Previous studies in strontium vapours have observed efficient but not complete ionization (for λ=460.7 nm and 459.5 nm) at lower intensities and densities [89, 95]. The difference spectra revealed a significant increase in both the Sr^+ and Sr^{2+} absorption resonances. The double ionization signal peaked at about $\sim$ 50 ns, and persisted up to 100 ns following the termination of the OPO pulse. This information could not be extracted from the previous studies and has provided a useful insight into our experiments. Combining these results with the fluorescence measurements permitted a detailed analysis of the various salient mechanisms needed to produce the high degree of ionization experimentally observed.

We now describe in more detail the experimental parameters used to perform this study. Once we had optimised atomic Sr in the plasma (almost 100%), we further probed it for various times $t = t_0 + \Delta t_{\mathrm{XUV}}$, as shown in Fig. 3.6, (t_0=1200-1500 ns depending on the optimum neutral Sr DLP signal). We looked at three intensities (0.7×10^8, 2×10^8, 3×10^8 W cm^{-2}) and 6 different time delays, Δt_{XUV} = 0, 50, 100, 150, 200 and 500 ns, for each of the three OPO wavelengths, λ = 460.7 nm, 459.5 nm and 435.0 nm. Due to time constraints, only measurements for the highest intensity were recorded for λ = 470.0 nm. A study was performed for more Δt_{XUV} values for the one-photon resonant case at high intensity. This was undertaken to ensure that the above 6 values adequately represented the temporal evolution of ionization and, having reviewed them, it was decided that they would give a satisfactory overview of the process. Over the recorded time intervals for the XUV signal,

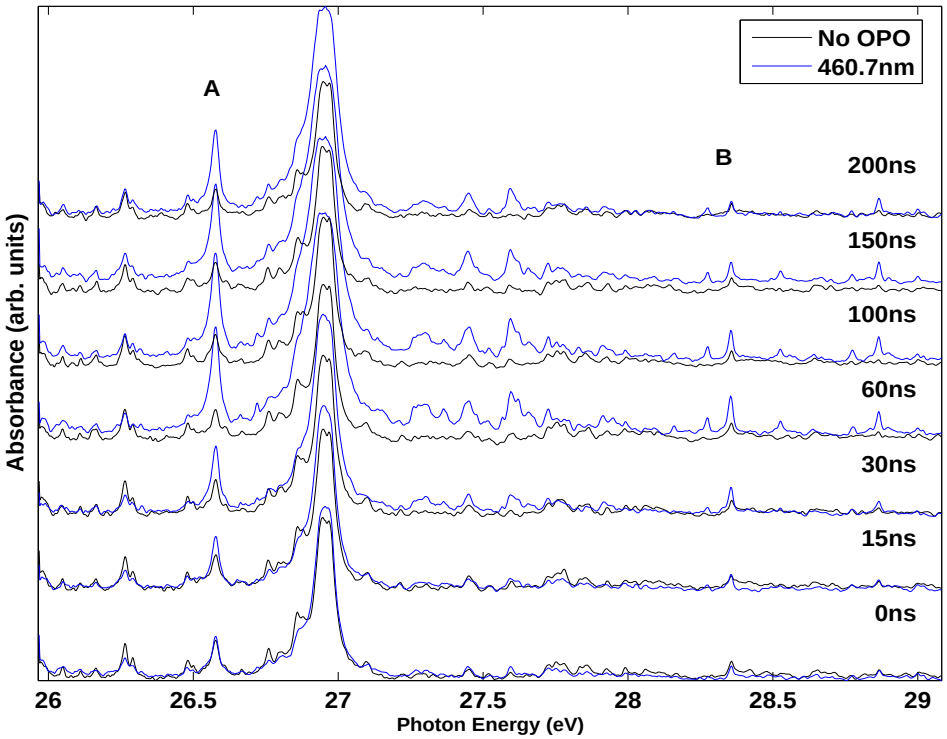

Figure 3.6: The XUV signal showing the temporal evolution of the strontium plasma after laser irradiation, λ = 460.7 nm, 3×10^{8} W cm^{-2}. Almost complete ionization is observed at 60 ns, the Sr^{2+} peak ($4p^{5}4d$) at 28.35 eV (B) appearing at 30 ns for the first time. Unfortunately there is overlapping of resonances in the 4p-subshell spectrum of Sr and Sr^{+}, the line at 26.57 eV is the $4p^{5}4d5s8d$ in Sr and the $4p^{5}4d^{2}$ resonance in Sr^{+} (A). Similarly the peak at 28.35 eV overlaps the $4p^{5}4d^{2}5d$ resonance in Sr.

the Sr^{+} signal reaches its maximum in each case at 100 ns, while the Sr^{2+} signal peaks somewhat earlier at 50 ns. The strongest Sr^{2+} signal occurs for λ=435 nm. The greatest reduction in Sr ground state absorbance at Δt_{XUV}=0 ns was seen for the one-photon resonant case, λ = 460.7 nm. From the difference spectrum (for λ=460.7 nm where more Δt_{XUV} values were used), almost complete ionization is achieved in the 30-50 ns delay range after the end of the OPO pump pulse. In fact the Sr vapour is heated significantly from 30 ns onwards with Sr^{2+} observed in the XUV signal.

Within the LIBORS model, the general consensus for the mechanism for rapid ionization is as follows (the non-resonant results suggest there's a little more going on and this will be discussed later): during the laser pulse a large number of seed electrons are generated in various energetic processes, the most important of which are:

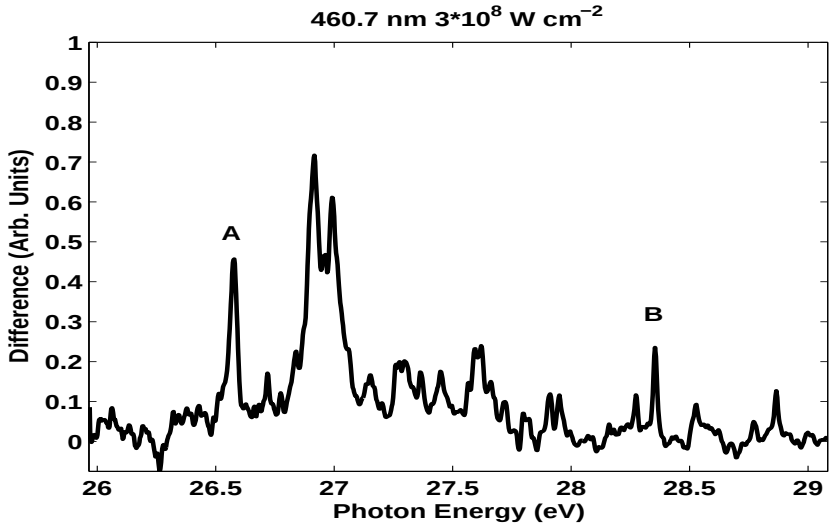

Figure 3.7: The difference spectrum for Δt_{XUV}=50 ns for one photon resonant excitation (λ=460.7 nm, 3×10^8 W cm^{-2}. The Sr^+ signal is measured by an increase in the $4p^5 4d^2$ peak at 26.57 eV (A) and the Sr^{2+} signal by an increase in the $4p^5 4d$ resonance at 28.35 eV (B).

(i) laser-induced Penning ionization:

$$Sr^* + Sr^* + h\nu \rightarrow Sr + Sr^+ + e^- + KE \tag{3.1}$$

(ii) associative ionization:

$$Sr^* + Sr^* \rightarrow Sr_2^+ + e^- + KE \tag{3.2}$$

(iii) and in some cases multi-photon ($n \geq 1$) ionization of the resonance level:

$$Sr^* + n\ h\nu \rightarrow Sr^+ + e^- + KE \tag{3.3}$$

Sr^* represents the laser-excited resonance state in the neutral atom, Sr^+ the strontium ion, Sr the ground state of the neutral atom and Sr_2^+ represents the dimer ion.

From the LIBORS model, one can estimate the seed-ionization rate, *S*, in strontium from:

$$S = N_2[\sigma_{2c}^{(2)} F^2 + \frac{1}{2} N_2 v(\sigma_A + \sigma_L F)] \tag{3.4}$$

where $\sigma_{2c}^{(2)}$ (cm^{4}s) is the two-photon photoionization cross section, *v* (cm s^{-1}) is the mean atom velocity, σ_A (cm^2) is the associative ionization cross section, σ_L (cm^{4}s) is the laser-induced Penning ionization-rate coefficient, N_2 is the population in the resonance level ($\sim GN_0$, where *G=g(1+g)*$^{-1}$ (*g* is the ratio of degeneracies of the

resonance level to ground state) and N_0 represents the initial atom density, F is the photon flux density (photons cm^{-2}s^{-1}).

As Eqn. 3.4 shows, only one value for the velocity, v, is used. It is assumed to be the most likely speed in a Maxwell-Boltzmann distribution. The model assumes laser saturation of the resonance level and from this a transcendental equation for the steady-state superelastic temperature, T_e^s, can be obtained:

$$T_e^s = \frac{E_{32}/k}{ln(1 + g\sum_{m\geq 3}\frac{f_{2m}}{f_{12}})} \tag{3.5}$$

E_{32} is the energy difference from the resonance level to the next highest optically connected level, k is the Stefan-Boltzmann constant, f_{2m} is the oscillator strength for a transition from the resonant level to higher lying m levels and f_{12} is the oscillator strength of the resonant transition. Oscillator strengths were obtained from the literature where available, otherwise, they were calculated using the Cowan code to give (from Eqn. 3.5) $T_e^s \sim 12600$K[2], $v \sim 7\times10^7$ cm s^{-1}. No specific cross sections were available for σ_A, σ_L or $\sigma_{2c}^{(2)}$ on Sr or its ions. However, for the alkalis $\sigma_{2c}^{(2)}$ is of the order of 10^{-48} cm^{4}s and $\sigma_L \sim 10^{-42}$ - 10^{-44} cm^{4}s, so we used these values in our calculation as a first approximation. Assuming an initial atomic density of $N_0 \sim 10^{16}$ cm^{-3}, at our highest intensity (F = 2×10^{26} photons cm^{-2}s^{-1}), S is approximately 6×10^{22} s^{-1}. This value is comparable to the rates for potassium (K) and sodium (Na) given in the Measures paper [100] as is to be expected since we use similar σ_A, σ_L and $\sigma_{2c}^{(2)}$ values. According to Eqn. 3.4, S will differ depending on these values.

Measures and Cardinal [100] noted that in the case of potassium, rubidium and cesium, the laser dependence of the ionization burnout time is weak for lower values of laser irradiance. This was understood in terms of the dominance of associative ionization. For higher intensities, laser-induced Penning ionization influences the initial seed processes more and results in a rapid fall in the peak ionization time. Thus, the values of σ_A, σ_L and σ_{2c}^2 can influence the ionization process and determine which stage dominates according to the LIBORS model. They did note however, that a strong intermediate ionization process (stage 3 in Fig. 3.1) can compensate for low seed electron generation, as in lithium and sodium, and still give relatively short burnout ionization times. The lack of cross section data in the literature for these processes in strontium, experimental or theoretical, prevented the full use of the the simple LIBORS model in this work, especially as just discussed, the computed ionization burn-out time is very sensitive to these values. There also

[2]This corresponds in electron volts to $\sim$ 1.6 eV. This temperature value is usually associated with neutral to singly-ionized plasmas using the collisional radiative model of Colombant and Tonon [104].

appears to be more to it than just LIBORS in our experiment, as suggested by our non-resonant results so we refrained from using the model.

In our experiments, we do not have any direct measurement of the electron energies in our plasma. It is therefore difficult to disentangle the individual processes giving rise to these seed electrons. Using mass spectrometry, Worden *et al* [108] confirmed that Sr_2^+ dimer ions are produced from laser-populated Rydberg states by the associative ionization process Sr(5s*nl*) + Sr($5s^2$) $\rightarrow$ Sr_2^+ + e^-. However, for their highest intensity (10 kW cm^{-2}, CW laser), the Rydberg states were destroyed by electron-impact ionization before an associative ionization collision could occur. At our intensities, 10^8 W cm^{-2}, it therefore seems unlikely that associative ionization would dominate; therefore two-photon ionization from the resonance level and laser-induced Penning ionization are more likely.

Following on from the initial processes, the seed electrons rapidly gain energy through superelastic collision quenching of the resonance-state population. These in turn can collisionally excite higher lying levels which will eventually reach the ground state of the ion. Ionizing collisions occuring between 5s5p atoms and atoms in higher excited states 5s*nl* also provide an increase in the ion ground state population. Shafranyosh and Snegurskaya [109] studied the formation of excited strontium ions after interaction of electrons with metastable strontium atoms. Measuring the ionization cross sections from ground state and metastable atoms (in the 5s5p ^3P levels), they observed that more than 35% of ions are formed in excited states after excitation from the metastable levels. Their calculated cross sections were computed using an electron energy of 15 eV. Although we expect our free electrons to have lower energy this process is nonetheless possible, particularly as our source is a plasma where metastable state formation occurs, see Fig. 5.3 in Chapter 5 for an example of metastable contribution in our plasma when studying 4p excitation in Sr^+.

Gedeon *et al* [110] calculated the electron-impact excitation from metastable states of Sr also. For small electron energies ($E < 5$ eV), the excitation cross section is larger, sometimes by an order of magnitude, for electron-impact excitations from the 5s5p ^3P to the following levels, 5s4f ^3F, 4d5p ^3F, and 5s6p ^3P, compared to the ground state. Thus it can be expected that the presence of metastable atoms in our plasma can only serve to enhance the ionization process. Transitions from both the 5s4f ^3F and 4d5p ^3F levels are recorded in our fluorescence studies. Although we cannot determine what processes generate seed electrons in our experiments, we can use our fluorescence measurements to study the resulting energetics which leads to the enhanced ionization observed. The following excitation schemes are expected to occur:

$$\text{Sr(5s5p)} + \text{Sr(5s}nl\text{)} \rightarrow \text{Sr}^+ + \text{Sr} + \text{e}^-(\text{E}_{5s5p} - \text{E}_{nl}) \quad (3.6)$$

$$\text{Sr(5s5p)} + \text{Sr(5s5p)} \rightarrow \text{Sr} + \text{Sr(5s}nl\text{)} + \Delta\text{E} \quad (3.7)$$

$$\text{Sr(5s}nl\text{)} + \text{e}^-(\epsilon') \rightarrow \text{Sr} + \text{e}^-(\epsilon'' > \epsilon') \quad (3.8)$$

$$\text{Sr(5s}nl\text{)} + \text{e}^-(\epsilon'') \rightarrow \text{Sr(5s}n'l\text{)} + \text{e}^-(\epsilon''' < \epsilon'') \quad (3.9)$$

where *n'* $<$ *n* and ΔE is the energy defect. All of the above heating mechanisms have been observed in previous experiments. Brechignac *et al* [95] observed an increase in stored atomic energy after laser pumping of the strontium vapour by monitoring the temporal evolution of populations in high lying strontium levels. They deemed collisional excitations with hot electrons as the dominant mechanism for heating the atom. Gouët *et al* [93] measured the "hot-electron" spectra from a laser-excited sodium vapour. The two main peaks observed originated from (a) very-low energy electrons produced by associative ionization which were then heated by two superelastic collisions and (b) electrons produced by ionization of 4d atoms through collisions with 3p atoms (in Na); these electrons, with energy ϵ = 2.11 eV - E_{4d}, are then heated by two superelastic collisions (Eqn. 3.6). Using a model that incorporated all of these processes, Gamal *et al* [102] successfully reproduced the experimental results of Hunnenkens *et al* [103] for laser-exciting a cesium vapour.

The cross section for superelastic collisions with the resonance state can be calculated by using the detailed balancing principle [98] which relates the collisional cross section for excitation of the same transition, σ_{12}:

$$\sigma_{21}(\epsilon_e) = [(\epsilon_e + E_{21})/E_{21}]\sigma_{12}(g_2/g_1) \quad (3.10)$$

Using the plane-wave Born approximation (Chapter 1, section 1.4.6) in the Cowan code [30], we calculated the excitation cross section for seed electrons of energies $\epsilon_e < 4$ eV, and obtained $\sigma_{12} \sim 6\times10^{-16}$ cm^2. This gives $\sigma_{21} \sim 5\times10^{-15}$ cm^2 for strontium. A similar value was calculated for Na [93] where superelastic collisions dominated the electron spectrum. Performing similar calculations we calculated the collisional excitation rates from the resonance level to the 5s6s, 5s5d and 5p^2 levels which are the next optically connected levels above the 5s5p resonance level. Table 3.2 displays the results, the energy values are presented with respect to the 5s5p $^1P_1$ level. All levels except the 5p^2 $^1S_0$ have accurately computed energy intervals. The calculated collisional rates are quite high and so we would expect enhanced population in these levels under our excitation conditions. To help confirm this our fluorescence studies provided the relevant insight. The excitation schemes used in our study are presented in Fig. 3.8.

Table 3.2: Calculated collisional excitation rates from the 5s5p $^1P_1$ to excited levels in Sr

Level	E_{calc} (eV)	E_{Moore} (eV)	gf_{calc}	K_{2m} (cm^3 sec^{-1})
5s6s $^1S_0$	1.10	1.10	0.50	2.66×10^{-7}
5s5d $^1D_2$	1.66	1.62	0.92	1.03×10^{-7}
5p^2 $^1D_2$	2.23	1.89	2.92	3.19×10^{-7}
5p^2 $^1S_0$	2.93	1.92	0.32	9.18×10^{-9}

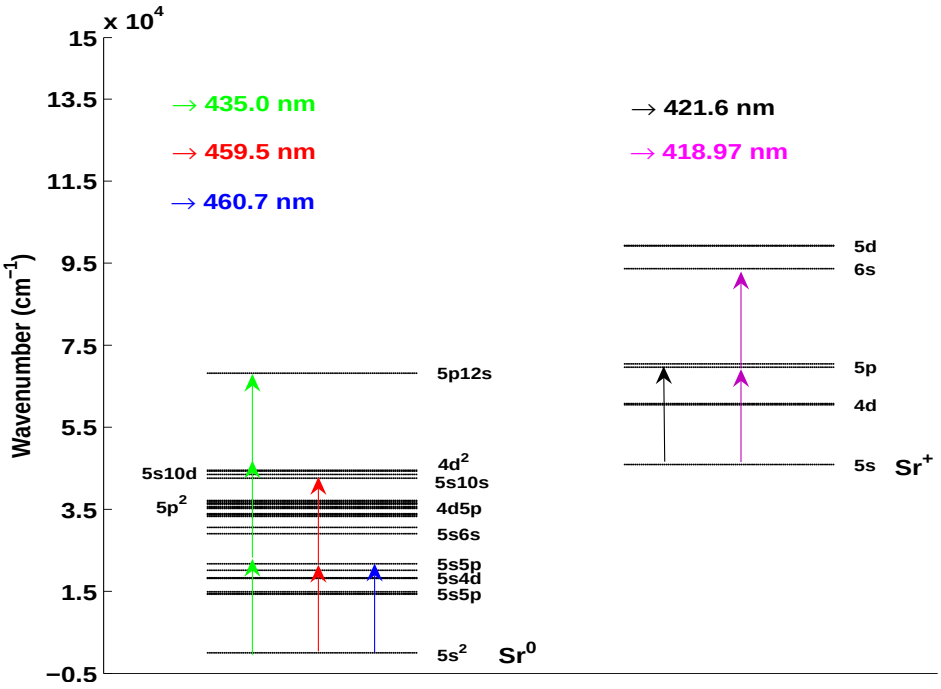

Figure 3.8: Energy diagram of the relevant levels in Sr and Sr^+ for the excitation schemes used in this study.

3.3.2 One-photon resonant absorption (λ = 460.7 nm)

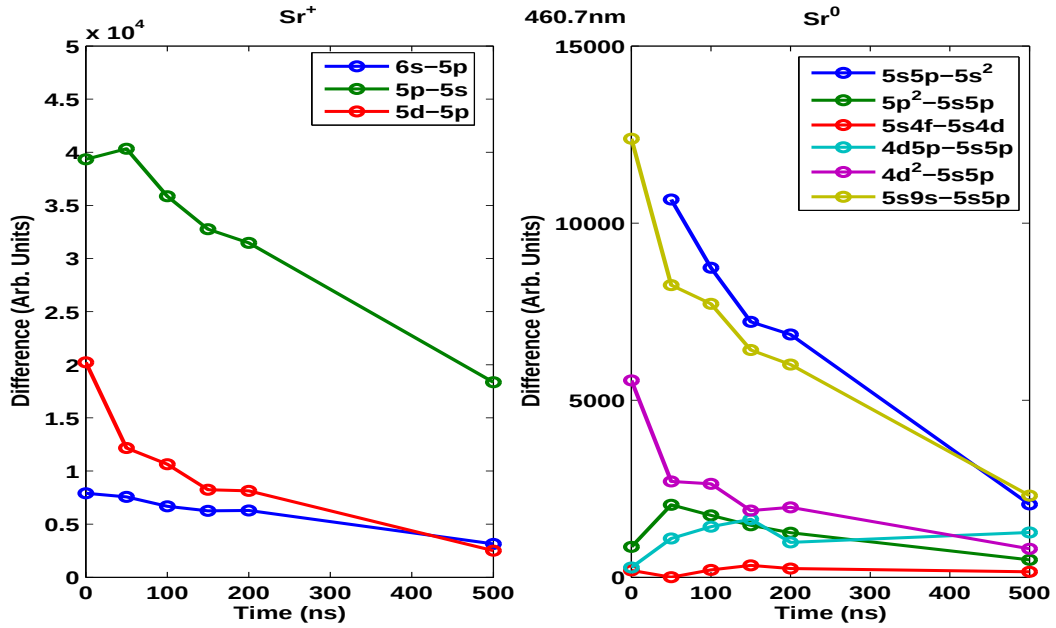

Figure 3.9: The difference fluorescence spectra from the laser irradiated strontium plasma (460.7 nm) for the highest intensity, 3×10^8 Wcm^{-2}. Each point corresponds to the area measured under the fluorescence line after OPO excitation minus the area of the natural fluorescence signal present in the plasma for the same time delay. For short time delays, there is a significant increase in the populations of the high lying Sr states and also the ion levels. Note all lines were recorded for a gatewidth of 200 ns, except the 6s (blue line) and 5p (green line) levels where a 60 ns gatewidth could be used. Therefore 0 ns on the graph corresponds to the population difference from 0-60 ns for those Sr^+ lines and 0-200 ns for the rest. The missing data point for the resonance transition is due to saturation of the ICCD at 0 ns; the laser is tuned to this transition and swamps the signal. While the magnitudes of the area under the peak may fluctuate, the shape of this graph is always reproducible.

Following the laser pulse, energy is transferred to the 5s5p ^3P metastable levels by radiative decay. From 0-200 ns, a large fraction of the initial population is stored in the manifold of metastable levels which slowly decreases in time. The loss of metastable population is due to superelastic collisions from the resonance state and excited neutral states, which in turn provide hot electrons that can excite the manifold of high-lying Sr(*5snl*) levels. This is validated by the large population difference observed in the 5s9s $^1S_0$ (5.29 eV) level and also in the doubly-excited 4d^2 $^3P_0$ (5.52 eV) level after laser excitation, as can be seen in Fig. 3.9. Similar population increases occurred in high lying levels in [95]. Collisional ionization from these highly excited levels gives rise to a growth in the free-electron density. From our XUV difference spectrum, the 4d^2 Sr^+ line at 26.57 eV appears $\sim$ 0-15 ns after

laser excitation (Fig. 3.6). In turn, these free electrons are heated by collisions within Sr^+ by the same processes (and more are generated) and so we observe eventually the $4p^6\ ^1S_0$ ground state of Sr^{2+}. This is confirmed by the appearance of the peak at 28.35 eV in the XUV difference spectrum in the delay range 30-100 ns.

Fluorescence from the 5p, 6s and 5d levels in the strontium ion display increased population in these levels 0-200 ns after OPO excitation as displayed in Fig. 3.9 (left hand panel). Furthermore, due to the smaller gatewidth employed at the 8.37 mm (405 - 428 nm) setting on the spectrometer, we can see a rise in the strength of the 5p $\rightarrow$ 5s 421.6 nm transition in the delay range 50-110 ns after termination of the OPO pulse. This may be due to the energy reservoir of highly populated Sr states, collisionally ionizing into the ground state or an excited state of Sr^+ and subsequently decaying. Superelastic collisions within Sr^+ will cause the electrons to gain energy; this will also result in population transfer to these levels during this time. It can be seen from Fig. 3.9 that the population of the high lying 5s9s and $4d^2$ strontium levels decreases with time, while the lower lying levels show a slight increase from 50-200 ns. From the XUV difference spectra, we know that the single ionization signal is strong during this time and peaks at 100 ns, i.e., cooling is not dominant during this period. The energetic processes driving this increase in population can be due to energy pooling from the highly populated resonance level or collisional excitation from this level promoting the atom to these excited states.

As the double ionization signal peaks and subsequently decreases after 50 ns, we have a cascading scenario where the excitation energy slowly moves down through the Sr^{2+} levels and further down through to the Sr^+ ion eventually reaching the Sr^+ 5s $^2S_{1/2}$ ground state, thus enhancing the single ionization XUV absorption signal. By 500 ns recombination results in the observed drop in both the XUV ionization signal and the Sr^+ ion fluorescence. Similar results are observed for the other exciting wavelengths (λ = 459.5 nm and 435.0 nm) at this intensity.

The ionization and fluorescence signals were also recorded for lower intensities as is shown in Fig. 3.10. Overall, all measurements displayed a reduced signal level as the OPO intensity decreased. The XUV ionization signal is still strong for one third of the highest intensity but decreases by nearly a factor of two for the lowest intensity. Clearly ionization does not vary linearly with intensity in our experiments. In the MW cm^{-2} regime total ionization was not observed by Skinner [89] or Brechignac *et al* [95] in a strontium vapour. As can be seen in Fig. 3.10, complete ionization does occur in our experiments from $\sim$ 70 MW cm^{-2} to 300 MW cm^{-2}, this is inferred by the lack of neutral Sr resonances in the difference spectra (i.e. only Sr^+ (and Sr^{2+}) resonances are observed at these intensities). It is clear from

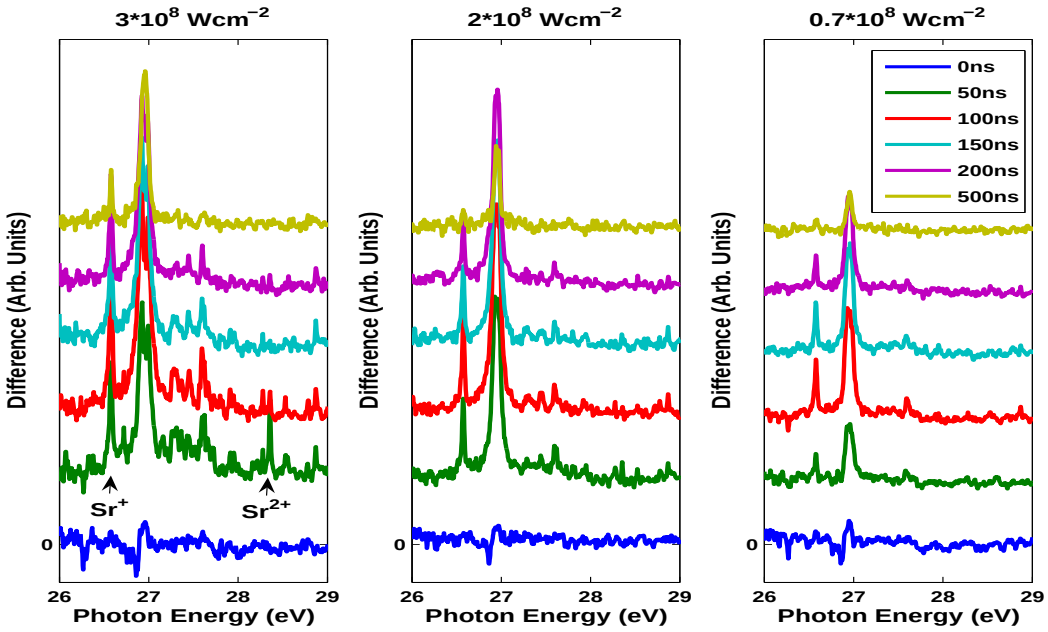

Figure 3.10: The difference spectra obtained after laser excitation to the Sr 5s5p $^1P_1$ resonance level, λ = 460.7 nm, for three different intensities. The ionization signal decreases with intensity but not linearly in this region, the double ionization signal is weak for the middle intensity value and non-existent for the lowest intensity.

Fig. 3.10 that the highest intensity, 300 MW cm^{-2}, results in superior heating of the plasma as a much larger Sr^{2+} peak is present.

The fluorescence measurements at low intensity, Fig. 3.11, attest to the reduced ionization efficiency. It proved difficult to extract some of the peaks from the background and all lines were considerably reduced. Nonetheless, some interesting features are apparent. There is only a slight enhancement in the high lying 5s9s and 4d^2 levels, yet the temporal profile of the single ionization signal is the same as for higher intensities. The fact that increased population in the highly excited levels does not affect the final (temporal) outcome of the ionization signal suggests that the initial energetic processes that generate the seed electrons dominate. Put differently, the intermediate ionization events such as collisional ionization / excitation appear to be less influential. At higher intensities, laser-induced Penning ionization and two-photon ionization of the resonance level would contribute more, resulting in greater seed electron generation and subsequent increased ionization rates. Overall, one-photon resonant coupling in strontium appears to be a very efficient means of coupling energy into the atom, particulary in the 10^8 W cm^{-2} regime. The next section presents the results for the other exciting wavelengths, λ=459.5 nm, 435.0 nm and 470.0 nm, corresponding to two-photon, three-photon and non resonant photon excitation respectively of neutral Sr.

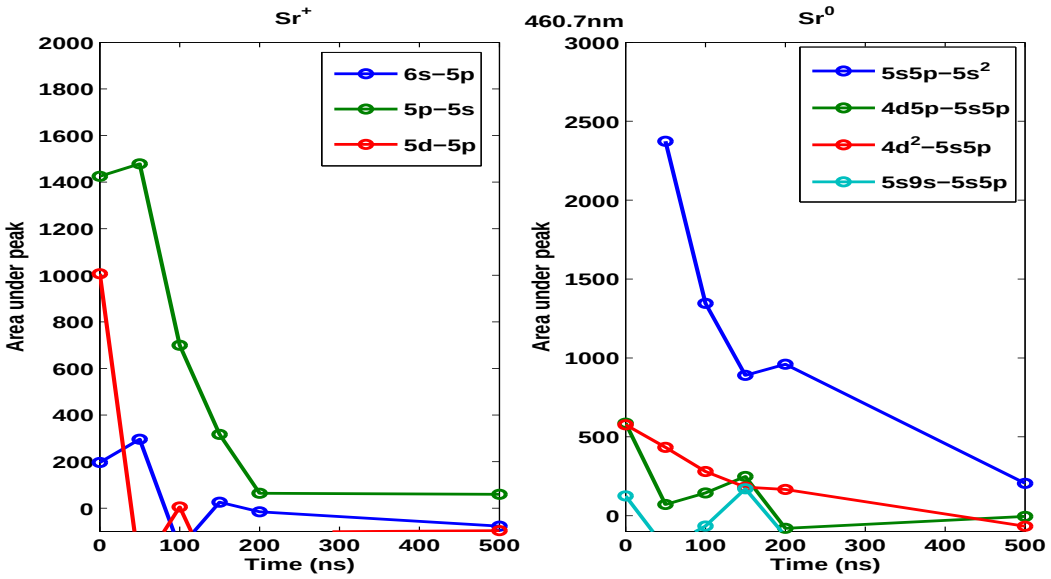

Figure 3.11: The difference fluorescence spectra for one-photon resonant absorption, λ=460.7 nm, 0.7×10^{8} Wcm^{-2}. The fluorescence signal was very weak for this intensity making it was difficult to extract the peaks from background noise. The points that fall below 0 reflect this fact.

3.3.3 Two-photon resonant absorption (λ = 459.5 nm)

In general, the experimental results for two-photon resonant absorption follow those for the one-photon case. However, a few differences appear. For the highest intensity the emission spectra show that the population densities of transitions to the 5s5p ^3P levels[3] are very weak and non-existent for early times, 0-200 ns. During the laser pulse, the atom is excited to the 5s10s ^1S level and since the resonance level (5s5p $^1P_1$) is not directly excited, the limited population of the 5s10s ^1S is distributed over a large number of higher lying states. Similar to λ=460.7 nm, the fluorescence and ionization signals grow rapidly following the termination of the OPO pulse and follow the same temporal profiles, see Fig. 3.12 for how the ionization signal varies in time with intensity. Brechignac *et al* [95] also noted a weaker fluorescence signal from the lower atomic levels when pumping to the 5s10s level too and although they also saw comparable ionization efficiencies for λ=460.7 nm and 459.5 nm, the latter reached peak ionization faster. Unfortunately, with the time-delays chosen in this work, we could not tell if this was also the case here (i.e. we would have had to use smaller time intervals than 50 ns to observe if the signal varied and this would have taken too much time). It would be expected to behave similarly as our results for λ=460.7 nm conform to their work.

[3]These levels are populated by radiative decay in the one-photon case.

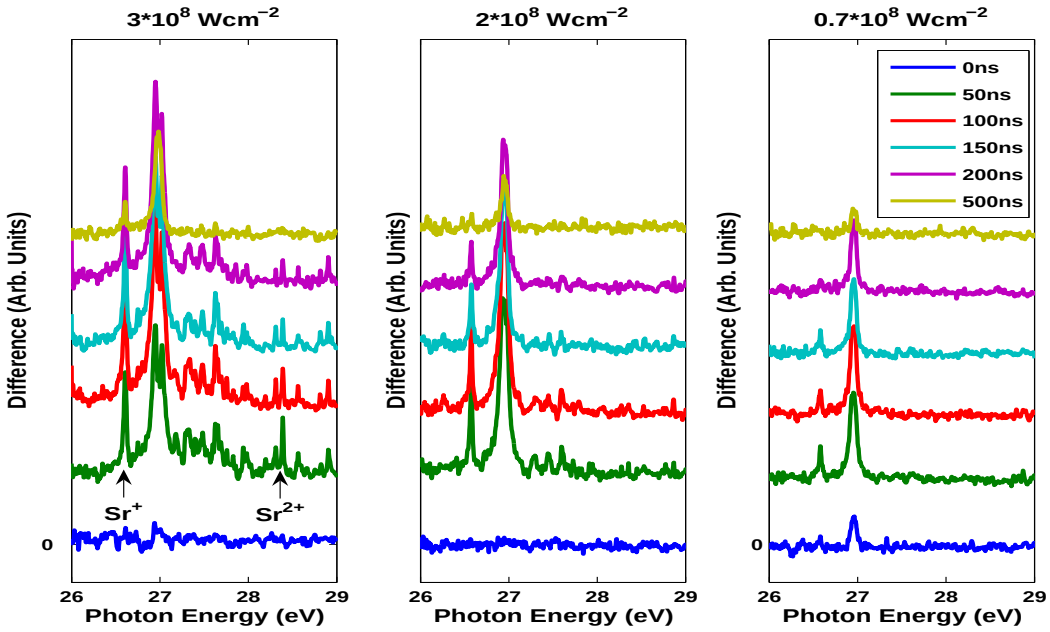

Figure 3.12: The difference spectra for two-photon resonant absorption, λ=459.5 nm, in Sr for three different intensities (a) 3×10^8 W cm^{-2} (b) 2×10^8 W cm^{-2} (c)0.7×10^8 W cm^{-2}. Similar to λ=460.7 nm, comparable single ionization signals are obtained for the highest two intensities (a and b) with a decrease for the lowest (c). Ionization is slightly reduced compared to one-photon pumping.

As mentioned previously, the greatest reduction in the $5s^2$ ground state population at early time delays occurs for one-photon resonant absorption case. Superelastic collisional quenching of the highly populated 5s5p $^1P_1$ level has been proposed as a strong contender for heating the seed electrons. One would not expect a similar population increase in the 5s10s level population after two-photon absorption, therefore other heating mechanisms must be invoked. Energy pooling of the 5s10s level is possible, as is collisional excitation. The atoms in this level need only $\sim$ 0.3 eV to be ionized, so less energetic processes can still provide the necessary energy for ionization. Multiphoton absorption could also explain the high ionization signal, particularly the presence of Sr^{2+}, but it is difficult to disentangle collisional processes from multiphoton absorption in our experiments. One possible way to determine this is by generating a log(N) vs log(I) plot, where N is the number density of ions and I is the laser intensity. If the slope of this plot has an integer value, n, where n is the number of photons absorbed, one could deem multiphoton absorption the major contributor to ionization. To do this, the area under the Sr^{2+} peak at 28.35 eV in the difference spectra and also the area under the large Sr^{+} resonance at 26.57 eV were calculated for the different intensities. The slope obtained was non-integer and so we can not differentiate between collisional

or photo-excitation / ionization in our experiments by claiming that one or other is dominant. Further progress would need detailed calculations including all processes so that the rates for the different photon and particle excitation processes could be computed and compared with the experiments.

3.3.4 Three-photon resonant absorption (λ = 435.0 nm)

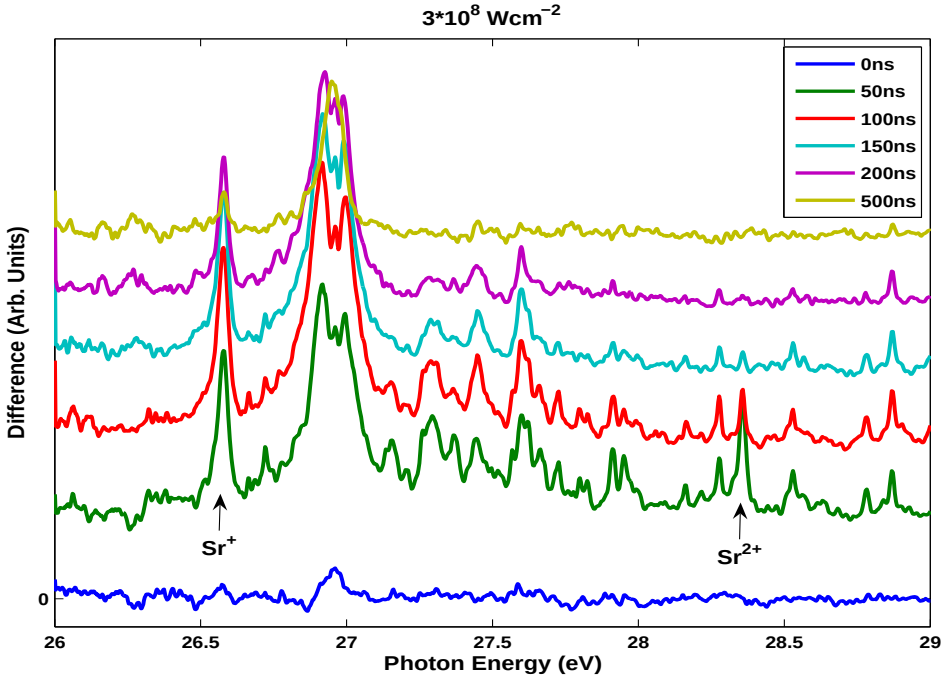

Figure 3.13: The difference spectra for λ=435.0 nm, 3×10^{8} Wcm^{-2}. The largest double ionization signal is obtained for three-photon pumping. The structure imposed on the large resonance at 27 eV is an artefact of subtraction due to Sr^0 peaks located at the same photon energy.

The wavelength λ=435.0 nm[4] is three-photon resonant with the $5p_{3/2}12s_{1/2}\ ^1P_1$ level, which lies $\sim$ 2.85 eV above the lowest ionization threshold, i.e. two-photon absorption from the $5s^2$ ground state can potentially promote the atom into the 5s ground state of the ion. The immediate promotion of atoms into states lying above threshold during the laser pulse results in a large number of ions in the $5p_{3/2,1/2}$ Sr^+ ion levels as can be seen from the fluorescence difference spectra, Fig. 3.14 (left hand panel). By 50 ns, a large double ionization signal is present and the single ionization signal is the highest recorded from the three resonant excitations. Fig. 3.15 provides

[4]Unfortunately, the XUV measurements recorded for 435.0 nm, 0.7×10^{8} Wcm^{-2}, are not available so we can only compare the fluorescence spectra in this case. The mid intensity values are unreliable, the OPO was striking the strontium target generating a plasma.

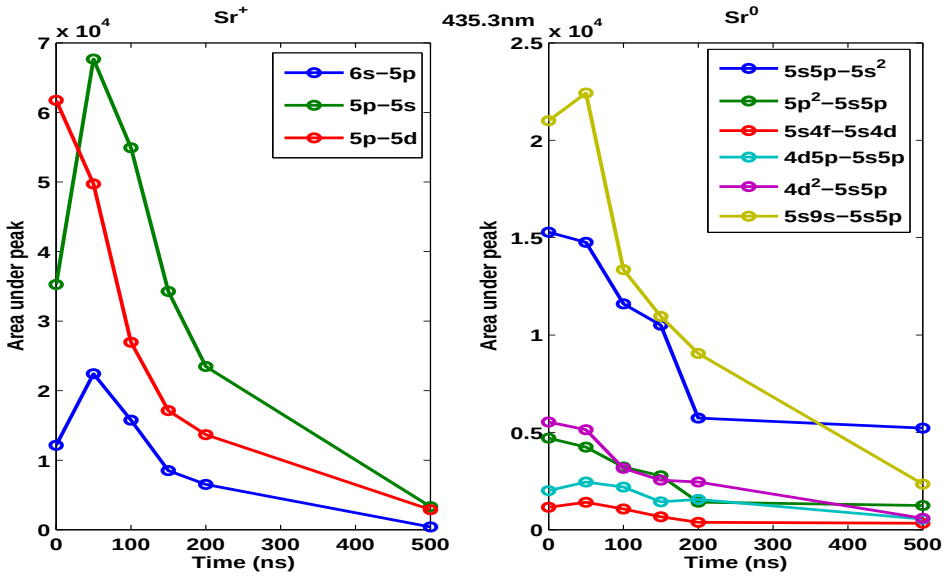

Figure 3.14: The fluorescence difference spectra for λ=435.0 nm, 3×10^{8} Wcm^{-2}.

a comparison for this time delay.

From the fluorescence spectra, even at the lowest OPO intensity (0.7×10^{8} Wcm^{-2}), the population of the 5p, 6s and 5d ion levels is double that for the one-photon resonant excitation (λ=460.7 nm). Fluorescence from the excited atomic levels is also greatly enhanced. One would expect more seed electrons to be generated during the laser pulse for λ=435.0 nm as it promotes the strontium atoms above threshold. This would explain the larger population distribution present in excited strontium levels. An increase is also observed in the 5p $\rightarrow$ 5s resonance line of Sr^{+} in the time delay range 50-110 ns, consistent with previous measurements for the other wavelengths.

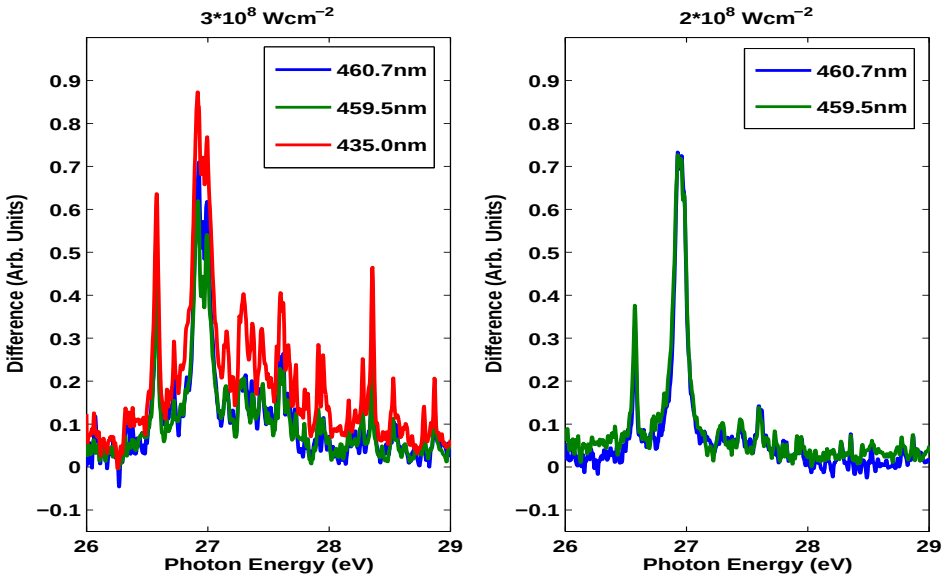

Figure 3.15: The difference XUV photoabsorption spectrum for Δt_{XUV}=50 ns at the highest OPO intensity for the three resonant excitations. Both the single and double ionization signals are highest for three-photon resonant excitation.

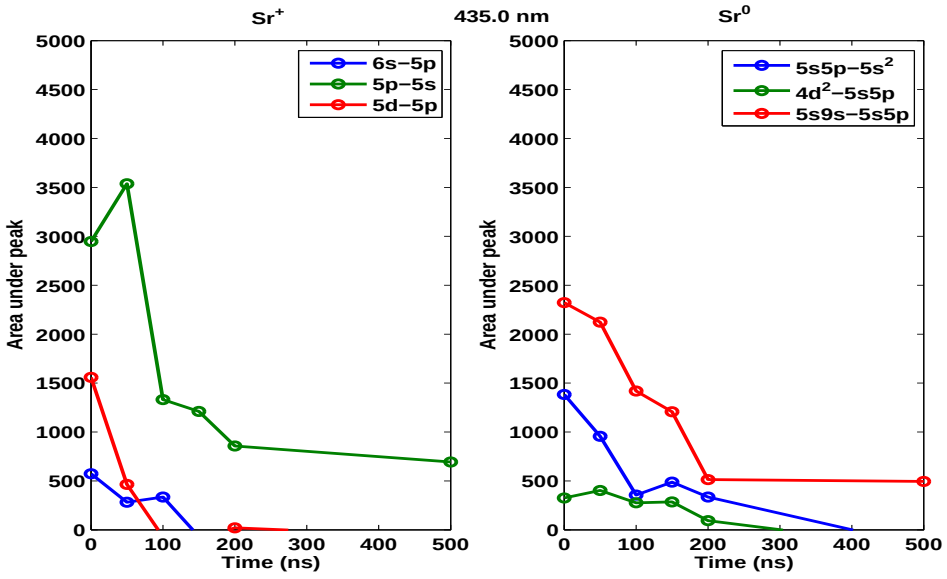

Figure 3.16: The fluorescence difference spectra for λ=435.0 nm, 0.7×10^8 Wcm^{-2}, where the greatest population increase for both excited Sr atoms and ions occurs.

3.3.5 Non-resonant absorption (λ = 470.0 nm)

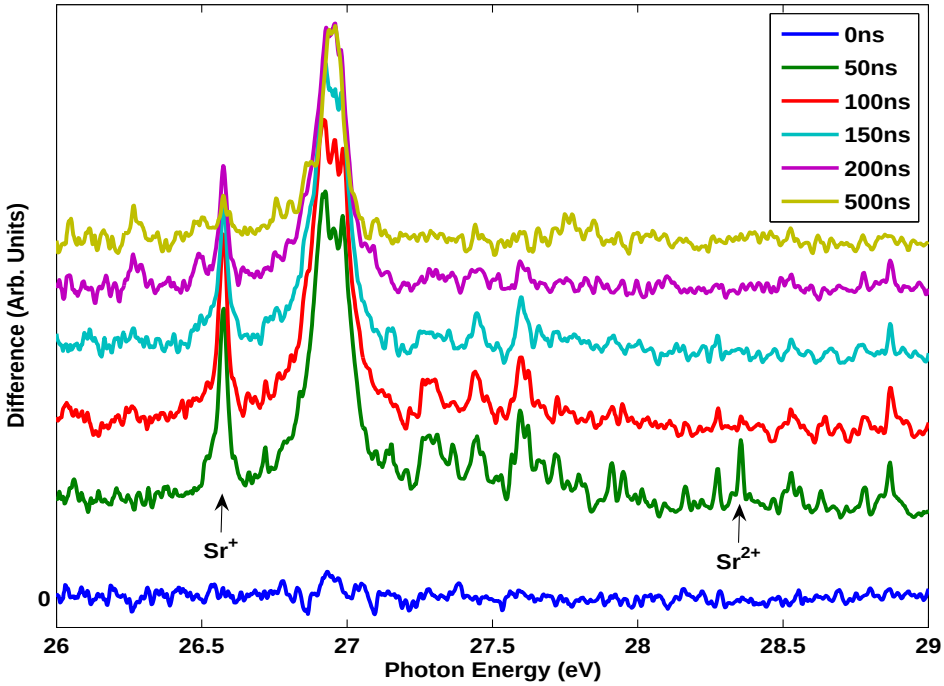

Figure 3.17: The difference spectra for λ=470.0 nm, 3×10^8 Wcm^{-2}. The ionization signal is slightly stronger compared to resonant excitation and the double ionization signal is somewhat weaker. This casts doubts on how dominant the resonant process is in the energetics of the system after laser irradiation.

To complicate matters further, when we irradiate the plasma with λ=470.0 nm (non-resonant), 3×10^8 Wcm^{-2}, we still see a strong ionization signal in the XUV photoabsorption spectra. The fluorescence is a lot weaker too which suggests a rapid increase in Sr^+ ground state ions. This implies that the resonant nature of the excitation process is not the only factor, which in turn suggests that the LIBORS model does not fully describe the processes going on in a laser produced plasma. From the $5s^2$ ground state, three photons need to be absorbed to overcome the threshold energy and this could be a possible explanation. Some other interesting results also appear. The photoabsorption spectra for Sr prior to laser irradiation is reduced compared to the previous experiments, the peak absorbance at 27 eV is $\sim$0.55 compared to $\sim$1.00,[5] yet surprisingly the ionization signal is the highest. We also see a Sr^{2+} signal in the difference spectrum but it is lower than for the resonant studies.

The fact that a similar ionization signal and temporal profile is observed for

[5]The lower absorbance can be attributed to a new target which proved difficult to obtain a similar signal and lack of time prevented improvement.

non-resonant pumping, suggests that the only real difference between the two cases of resonant vs non-resonant, might be the manner by which seed electrons are produced. In that case, clearly even the non-resonant case provides sufficient seed electrons to start / trigger the plethora of subsequent ionization processes efficiently.

3.3.6 Discussion

A noticeable difference in this study compared to previous ones, is that we have fluorescence from Sr levels prior to laser excitation. This pertains to the fact that our atom / ion source is a laser-produced plasma. From the collisional radiative (CR) model of Colombant and Tonon [104], one can deduce the electron temperature T_e in the plasma (prior to laser irradiation from the OPO) using the equation for irradiation at a laser wavelength λ (1.064 μm)

$$T_e = 5.2 \times 10^{-6} A^{1/5} (\lambda^2 \phi)^{3/5} \tag{3.11}$$

where A is the atomic number, ϕ is the mean laser power density, ($5{\times}10^8$ W cm^{-2}). In our case, $T_e \sim 1$ eV[6]. Using a simple Boltzmann distribution for the 5s9s $^1S_0$ level, we can expect a small population distribution in our strontium plasma prior to OPO excitation $\sim$ 1%. Similar distributions can be expected in other high lying Sr levels too. Of course, this value of T_e is the temperature after the laser pulse has ended and our plasma will have expanded and cooled down by 1200 ns. However, due to the intrinsic nature of plasmas and the high densities involved, we can still expect these levels to be populated by collisional excitations: this can only serve to enhance the ionization process. As soon as energetic electrons are available in the plasma, they can readily collisionally excite or ionize these populated levels.

As mentioned earlier, inverse bremsstrahlung is an important process in plasmas. From [99], one can make a direct comparison between the rate of laser energy deposited through LIBORS and inverse bremsstrahlung:

$$H = \frac{(GN_0^2 K_{21} E_{21}/4) 12 c^2 (kT_e)^{3/2}}{1.17 \times 10^{-7} N_0^2 \lambda^2 I} \tag{3.12}$$

where N_0 is the atomic density, c is the speed of light, λ(cm) is the laser wavelength, I is the laser irradiance, K_{21} is the rate of collisional excitation from the resonance level to the ground state. H represents the rate of laser energy deposition via LIBORS along the path of the laser beam compared with inverse bremsstrahlung. As the laser beam penetrates the plasma and is attenuated, the degree of coupling to the plasma is undiminished via LIBORS but inverse bremsstrahlung decreases with

[6]This differs from the steady-state temperature of Eqn. 3.5 from the LIBORS model, which is the temperature reached by the heated atomic vapour after laser saturation of the resonance level.

the laser irradiance, *I*. Thus *H* increases with penetration through the plasma. In strontium, for λ=460.7 nm, I=10^8 Wcm^{-2}, *H* equals 1.4$\times 10^{20}$, which is extremely high. This assumes saturation of the resonance level and would provide a nice explanation for the results presented in this work.

The unexpected results for non-resonant excitation (λ=470.0 nm) however, implies that some other processes not included in the LIBORS model are important in our plasma. Molecular dissociation may be such a process. The $X\ ^1\Sigma_g$ ground state of the strontium molecule arises from two ground state strontium atoms. This molecular state is only weakly bound with dissociation energy of about 1088 cm^{-1} [111]. The Sr_2 molecule can absorb a photon and be excited to the dissociation continuum of the $A\ ^1\Sigma_u$ state which leads to dissociation into two strontium atoms, one in the ground state 5s$^2\ ^1S_0$ and the other in the first excited state 5s5p $^1P_1$.

$$Sr_2\ X^1\Sigma_g \rightarrow (Sr_2)^* \rightarrow \text{Sr (5s5p } ^1P_1) + \text{Sr (5s}^2\ ^1S_0) \tag{3.13}$$

This was proposed by Baig *et al* [112] who studied the even parity 5s*n*d $^{3,1}D_2$ Rydberg series resulting from the 5s5p $^1P_1$ resonance level. They irradiated a strontium vapour using a dye laser covering the wavelength range 410-460 nm, which is just above the 5s5p $^1P_1$ level. As the laser was detuned by about 1200 cm^{-1} from the nearest real level for a two-photon transition, molecular dissociation of Sr_2 was deemed the dominant energetic process for population of the 5s5p level. The dissociation is very fast ($\approx 10^{-12}$s) and so it is possible for atoms in the 5s5p level to absorb a second photon from the same laser pulse ($\approx$ 5ns).

Irradiating the strontium atoms with the OPO tuned to λ = 470.0 nm, we are $\sim$ 422 cm^{-1} from the 5s5p $^1P_1$ level and so it is possible that a similar process occurs in our plasma. Subsequent superelastic heating of the free electrons could then take place and the LIBORS model may once again be appropriate. We do not observe strong fluorescence from the plasma however at this wavelength, which one would expect following on from the high ionization observed. Therefore, we can only tentatively propose molecular dissociation as a possible process for populating the 5s5p $^1P_1$ level followed by superelastic heating of electrons through collisions with this level.

3.3.7 One- and two-photon resonant laser pumping of Sr^+

It proved more difficult to isolate Sr^+ in the plasma, without some contribution from Sr^{2+} also being present. This can be explained by employing the CR model [104]. The ratio of number density of ion state *Z+1* to ion state *Z* is given by:

$$\frac{N_{Z+1}}{N_Z} = \frac{S(Z,T_e)}{\alpha_r(Z+1,T_e) + n_e\alpha_{3b}(Z+1,T_e)} \tag{3.14}$$

where *S(Z,T_e)*, α_r(*Z*,T_e), and α_{3b}(*Z*,T_e) are the collisional ionization, radiative recombination, and three-body recombination coefficients of an ion of charge *Z* at temperature T_e. From this equation one can compute the ratio $N_Z / \sum_{k=1}^{Z} N_k$, the fractional number density of charge *Z*, and plot its evolution as a function of T_e.

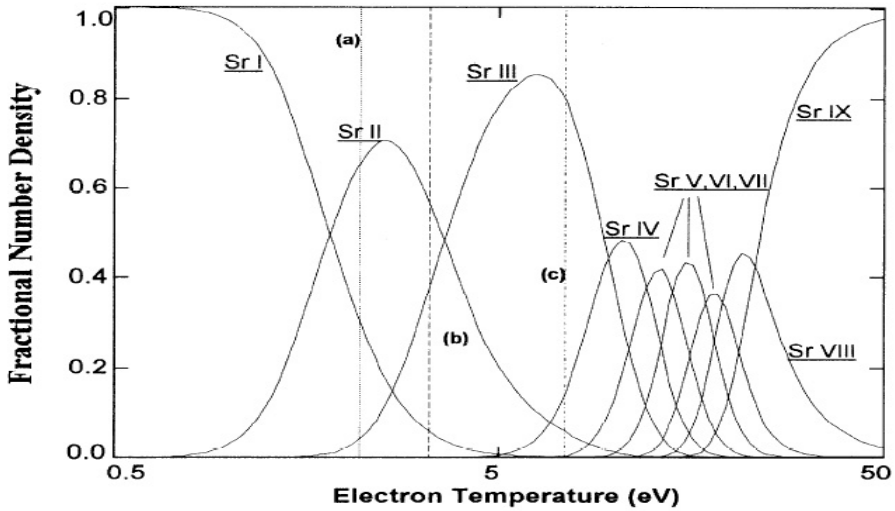

Figure 3.18: Fractional number densities according to the CR model of the charge states of strontium plotted with increasing electron temperature on a logarithmic scale, taken from [113].

For Sr^+, the estimated electron temperature, T_e, is $\sim$ 2 eV using Eqn. 5.1. Therefore we can expect some contribution from Sr^{2+} in our plasma. The strontium plasma was generally probed 1 mm from the target surface, t_0 = 450-500 ns after plasma generation. After interrogation with the OPO, the plasma was probed for times $t = t_0 + \Delta t_{XUV}$, Δt_{XUV} = 0, 15, 30, 60, 80, 100, 150, 200 ns. Probing the plasma for later time delays, 300-900 ns, showed both the ionization signal and the optical signal drop to zero in a steady manner, so that these later times were not deemed necessary to measure. We measured the XUV and fluorescence signals for four different OPO output energies: 20 mJ (3.0×10^8 W cm^{-2}), 15 mJ - (2.2×10^8 W cm^{-2}), 11 mJ - (1.7×10^8 W cm^{-2}) and 5 mJ - (7.5×10^8 W cm^{-2}).

3.3.8 One-photon resonant absorption of Sr^+ (λ = 421.6 nm)

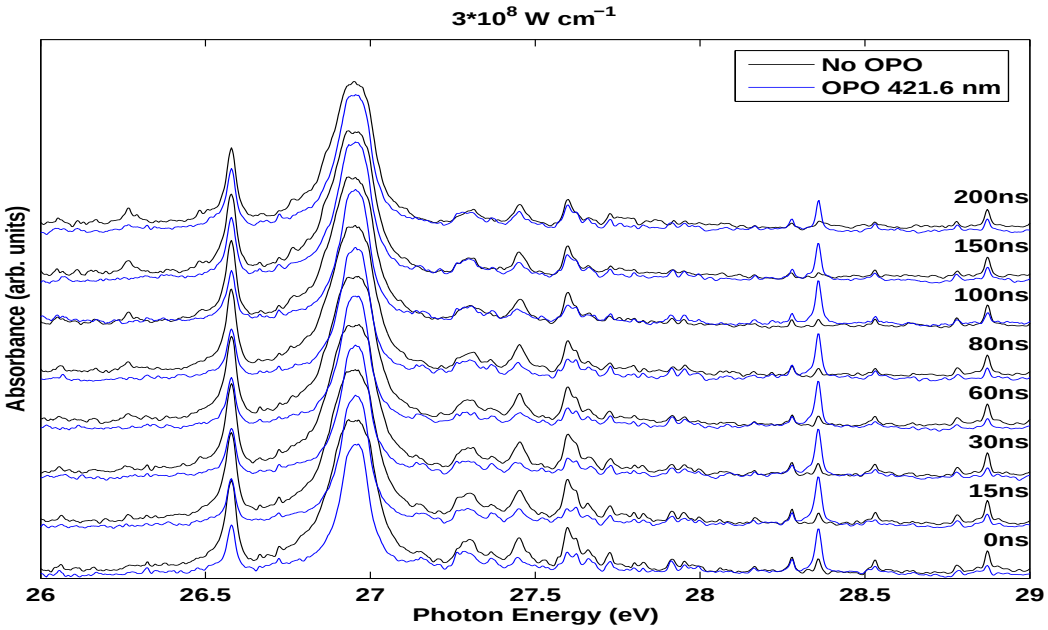

Figure 3.19: The temporal profile of the photoabsorption spectrum of Sr^+ with and without OPO irradiation, λ = 421.6 nm, 3×10^8 W cm^{-1}. One can see enhancement of the Sr^{2+} peak at 28.35 eV.

The Sr^+ results presented here are in stark contrast to the previous results for Sr. Tuning to the 5p $^2P_{1/2}$ resonance line at 421.6 nm or to the 6s $^2S_{1/2}$ line by two photon absorption, λ=418.97 nm, we never reach full ionization of Sr^+. This can be seen in Fig. 3.19 where the maximum absorbance reached by the Sr^{2+} peak at 28.35 eV is 0.57 compared to $\sim$ 0.9 in the 4p-photoabsorption spectrum of Sr^{2+} presented in chapter 4. When the plasma was irradiated with the OPO tuned to λ=425.0 nm, i.e., a non-resonant wavelength, we observed no ionization signal at all, see Fig. 3.20.

This conforms with the LIBORS model, where laser saturation of the resonance state acts as a source of energy for rapidly heating the medium. Measures *et al* [114] proposed a model to indicate the degree of plasma heating that can be achieved through superelastic laser energy conversion (SELEC). SELEC differs from LIBORS in that it refers to the rapid electron heating that occurs prior to an appreciable increase in the free-electron density; LIBORS models the entire interaction up to complete burn-out of the species been pumped. SELEC is based on a 3-level model: the ground state, a resonance state, and a higher lying excited state. The other intermediate states are ignored. A more complex model that includes these levels tended to overestimate the increase in T_e. The more comprehensive LIBORS code and the

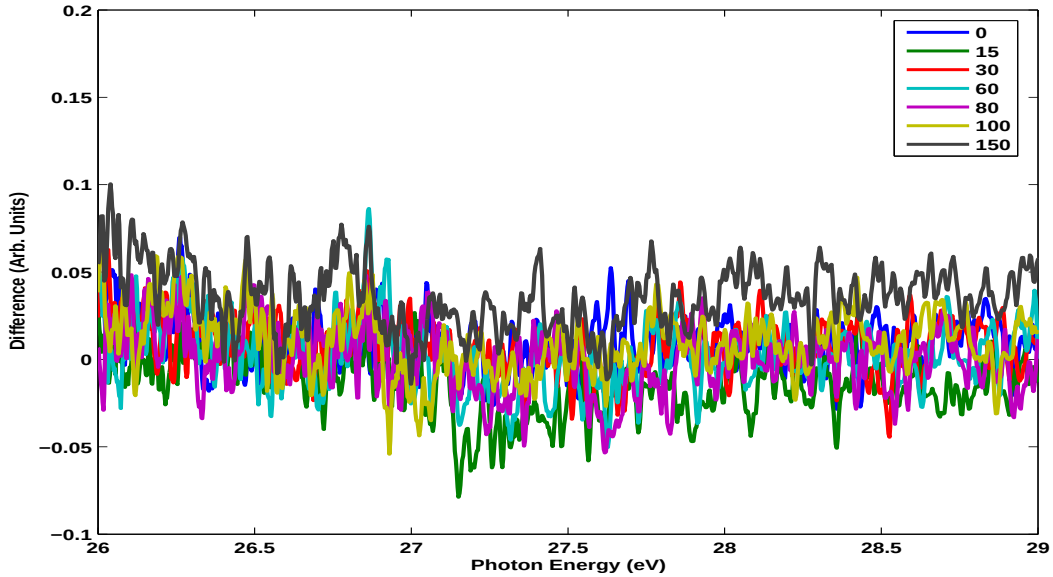

Figure 3.20: The difference spectrum of Sr^+ after laser irradiation, λ=425.0 nm, 15 mJ. No ionization was observed implying superelastic collision quenching of the resonance state is the primary source of heating in the plasma.

SELEC model produced comparable results. Assuming that the temperature is constant, and that the rate of change of the free-electron temperature is dominated by the resonance superelastic heating term, the SELEC heating time τ_H is given by:

$$\tau_H \simeq \frac{\theta_s^{3/2} - \theta_0^{3/2}}{GN_0K_{21}} \tag{3.15}$$

$$\theta_0 = kT_e/E_{21} \tag{3.16}$$

$$\theta_s \simeq -\frac{a}{ln(b[1 - exp(ln(b/a))])} \tag{3.17}$$

$$K_{21} = \frac{A\overline{f}_{12}}{gE3/2_{21}} \tag{3.18}$$

$$\frac{\mathrm{d}T_e}{\mathrm{d}t} = \frac{2}{3k}GN_0K_{21}E_{21} \tag{3.19}$$

$a = E_{32}/E_{21}$, $b = \overline{f}_{12}/g\overline{f}_{32}$, $A = 1.6\times10^{-5}$ and $\overline{f}_{mn} = f_{mn}\langle g\rangle$, f_{mn} being the oscillator strength and $\langle g\rangle$ the effective Gaunt factor for the $m \rightarrow n$ transition[7]. For Sr^+, level 3 was taken to be the 5d $^2D_{5/2}$ as it had the highest oscillator strength. Using this model, $dT_e/dt > 10^{13}$Ksec^{-1} was predicted for an initial Sr^+ ion density of 10^{16} cm^{-3} and a superelastic heating time (τ_H) of $\sim$ 0.5 ns was computed.

Once again, a non-linear dependence with OPO intensity is observed with the

[7]The Gaunt factor was set to the semi-empirical threshold value of 0.2 [115].

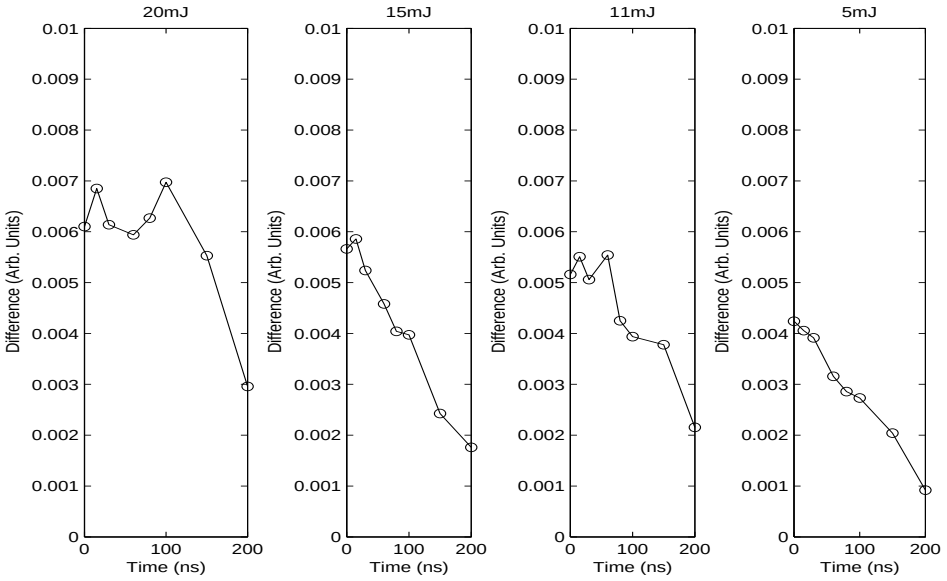

Figure 3.21: Temporal evolution of the ionization signal with intensity for λ=421.6 nm. Each point represents the area under the Sr^{2+} peak at 28.35 eV from the difference spectra. The largest reduction in the ground state peaks occurs at 15 ns coinciding with the peak in ionization.

highest gain in Sr^{2+} comparable for 11-20 mJ with a noticeable drop for the lower OPO energy, 5 mJ. This is displayed in Fig. 3.21, where one can see that the ionization signal peaks early at $\sim$15 ns. At the highest intensity there is a second peak in the ionization signal. The first peak in ionization coincides with the largest reduction of the Sr^{+} ground state resonances in the XUV spectra. This suggests that collisional ionization from the 5p resonance level occurs, i.e., superelastic collision quenching dominates just after termination of the OPO. The second peak or regrowth in ionization may be explained by our fluorescence results. We can see the 5d ^2D emission lines decrease in the range 60-100 ns. Collisional excitation from these 5d states can promote the system to higher intermediate levels. These in turn will act as an energy reservoir that will promote the ion in a stepwise manner to the Sr^{2+} ground state with time. This suggests stage 3 of the Libors model (as in Fig. 3.1), the intermediate ionization period, plays a leading role in the ionization process. This second peak observed is always reproducible for 20 mJ OPO output (but not so at 11 mJ, we suspect this is just an outlier).

From 200 ns onwards the fluorescence signal from the 5d, 6s and 5p levels are enhanced as the system cools. The energy reservoir is not infinite and heating processes are eventually balanced by cooling ones (Fig. 3.22). By $\sim$ 900 ns, fluorescence from these levels is close to zero.

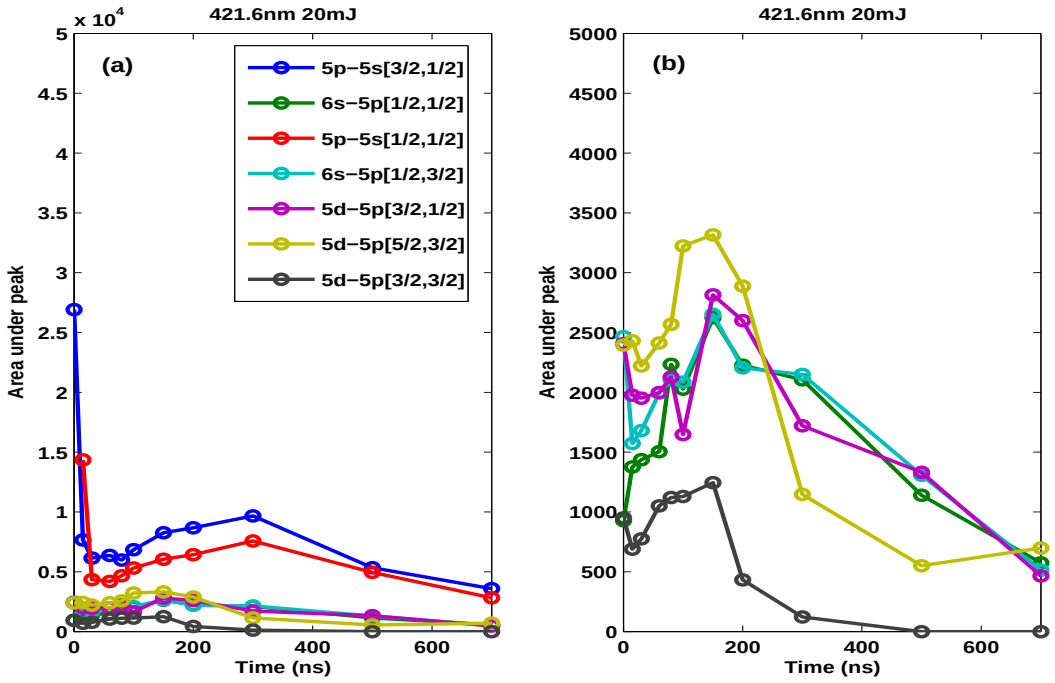

Figure 3.22: Plot of the temporal evolution of the fluorescence from the 5p, 6s and 5d levels in Sr^+ after OPO irradiation, λ=421.6 nm, 3×10^8 W cm^{-2} (20 mJ). One can see the onset of cooling at 200 ns. (b) A close up of fluorescence from the 5d and 6s levels. From 0-200 ns, for the lower intensities, there is only a slight drop in fluorescence, the initial gain in these levels from resonant pumping to the 5p $^2P_{1/2}$ level seems to be sustained by collisional excitations. A larger drop is observed for 3×10^8 W cm^{-2} which indicates more heated electrons are present to collisionally excite or ionize from these levels.

3.3.9 Two-photon resonant absorption in Sr^+ (λ = 418.97 nm)

In contrast to two-photon pumping in Sr ($5s^2 \rightarrow 5s10s$), the ionization signal is much weaker in Sr^+ (5s $\rightarrow$ 6s) for two-photon absorption as can be seen in Fig. 3.23. Comparing the ionization signals at high intensity, one-photon pumping to the resonant 5p level with the OPO tuned to 421.6 nm is twice as efficient as for the two photon case with the OPO tuned to 418.97 nm. Tuning the OPO to λ=418.97 nm, with a pulse energy of 5 mJ we barely see the Sr^{2+} $4p^54d$ peak at 28.35 eV. For the highest intensity, the temporal evolution of the ionization signal still shows a peak in the time delay range ~15-30 ns but no regrowth in the signal is observed, i.e. we do not observe a two-peaked ionization signal as was the case for λ = 421.6 nm. The initial energy coupled into the plasma via laser irradiation is not sufficient to generate / maintain a population in the intermediate levels. This in turn reduces the energy reservoir that may re-populate the Sr^{2+} ground state.

These results conform with those of Menard and Measures [96] who used the

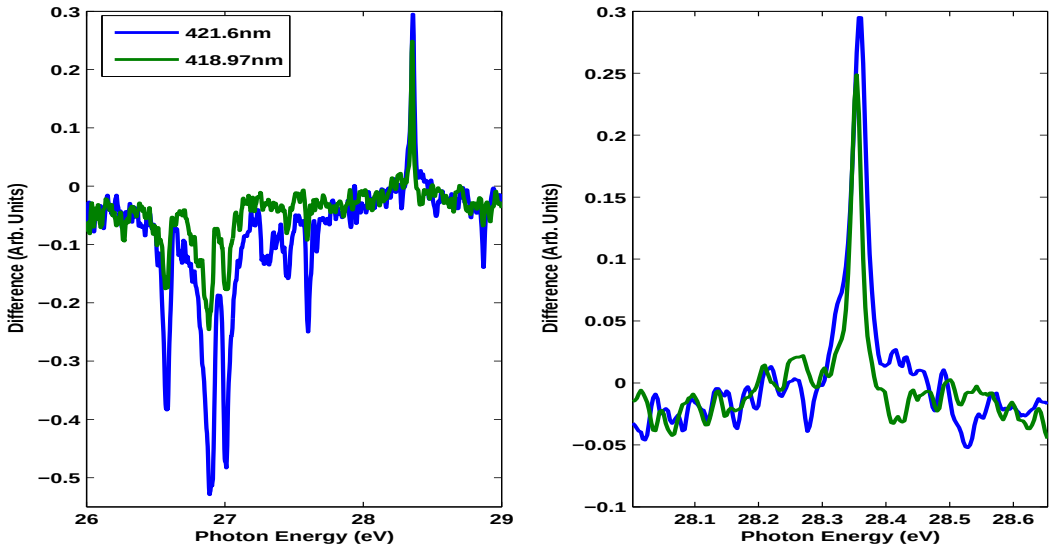

Figure 3.23: The difference spectrum for two OPO wavelengths, (421.6 nm, 418.97 nm) for a delay time of 15 ns after OPO irradiation. λ=421.6 nm results in better ionization and computing the area under the curve gives approximately double the efficiency at this wavelength compared to the 418.97 nm case.

same wavelengths to excite Sr^+ in a strontium vapour. They assumed two-photon ionization generated the Sr^+ ions in the vapour after laser irradiation. They observed that two-photon pumping to the 6s level was 50% as effective as pumping to the resonance level. Their results were based on fluorescence measurements from the 5f $^2F_{5/2,7/2} \rightarrow$ 5d $^2D_{5/2}$ level at 565.20 nm. They concluded that one and two-photon resonance pumping of low-lying levels in the ion is suitable to rapidly excite high-lying levels of the ion through superelastic laser energy conversion. These transitions were not observed in this work due to their intrinsic weakness.

One other noteworthy result is the enhanced resolution achieved from the difference spectrum. Lyon *et al* [116] measured the absolute photoionization cross section of Sr^+ and could resolve the large peak at 27 eV to a doublet, 4p^{5}4d ^{1}P 5s $^2P_{3/2,1/2}$, positioned at 26.95 eV and 26.97 eV respectively. However, from the difference spectra our 'doublet' is positioned at 26.88 eV and 26.99 eV. Unfortunately, this large resonance was saturated in our experiments which would result is severe broadening of the individual doublet components. After OPO excitation and subtraction to generate our difference spectra, this broadening would be imposed on the difference spectra.

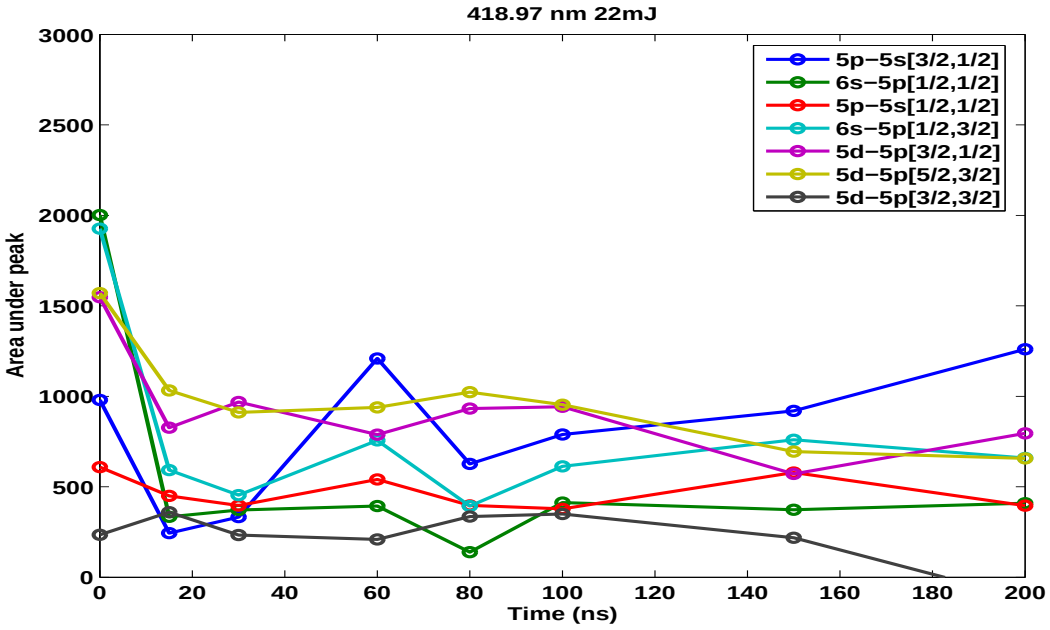

Figure 3.24: The temporal evolution of fluorescence from the 5d, 6s and 5p levels for λ=418.97 nm, 22 mJ. The signal is reduced compared to pumping to the 5p $^2P_{1/2}$ level and again this is no significant increase / reduction over the time period 0-200 ns.

3.4 Conclusion

We have presented results for one-, two- and three-photon resonant pumping in Sr and for one- and two-photon resonant pumping in Sr^+ for species densities on the order of 10^{16} cm^{-3}. In Sr, comparable ionization was observed for all wavelengths when irradiating the plasma with intensities $\sim 10^8$ W cm^{-2}. A non-linear drop in ionization was noted for lower intensities, going down to $\sim 10^7$ W cm^{-2} range. From 30 ns after laser excitation, almost complete ionization was achieved demonstrating the efficient coupling of laser energy into strontium. Fluorescence measurements enabled the study of the temporal evolution of atomic and ionic populations in higher lying levels after pumping and confirmed the rapid excitation to these levels. Irradiating the strontium plasma with λ=470.0 nm, a non-resonant wavelength, we also saw efficient ionization.

Complete ionization does not occur in Sr^+ for $\sim 10^8$ W cm^{-2} and pumping to the resonance level was twice as efficient as two-photon pumping to the 6s level. Furthermore, no ionization signal was observed for λ=425.0 nm, a non-resonant wavelength. This confirms the resonant nature of the excitation process and rules out multi-photon absorption in Sr^+ at these intensities. Superelastic laser energy conversion is the most probable process, we calculated a growth in $\mathrm{d}T_e/\mathrm{d}t$

$> 10^{13}\text{Ksec}^{-1}$ using the SELEC model.

While resonant pumping is necessary to generate the initial seed electrons in Sr^+ to start the ionizing processes (as in LIBORS), it appears that the energetic processes generating seed electrons in neutral Sr do not depend on resonantly populating levels within the atom. It is unclear with our experimental measurements what energetic processes cause ionization in this case, molecular dissociation is a possibility. However, what is clear is that whatever process generate these seed electrons initially in Sr, superelastic collisions is the most likely mechanism for heating the electrons subsequently (as in Sr^+), resulting in ionization of the atom. Further experimental work, for example, measuring the electron spectra from the laser-excited plasma may help uncover what other mechanisms play a role in the ionization observed.

Chapter 4

Absolute photoionization cross-sections of atomic ions

4.1 Overview of photoionization measurements

The work presented in this chapter was performed at the ASTRID storage ring at Århus University in Denmark and at the dual laser plasma experiment at DCU. The project was a joint collaboration between DCU (Caroline Banahan, Deirdre Kilbane, John Costello, Paul van Kampen), Queens University, Belfast (Shane Scully), Daresbury Laboratory, UK (John B. West), LIXAM, Orsay (Jean-Marc Bizau) and Århus University (Henrik Kjeldsen and Finn Folkmann). Absolute photoionization cross section measurements for various ions were performed using the merged-beam technique at ASTRID and complementary photoabsorption measurements were made using the DLP technique at DCU. All collaborators contributed to the work presented in this chapter and focus is placed on the experimental phase of the work where I made the most significant contributions.

Over the past few decades there has been a strong drive to measure the photoionization cross sections of neutral atoms and ions. The complex dynamics inherent to photoionization give it a prominent role in atomic physics research, providing insight into electron-electron correlation effects and unfolding the intrinsic nature of photon-matter interactions. From an applied perspective, emphasis has been placed on gathering measurements for elements abundant in stellar atmospheres where absolute cross section measurements assist in their modeling, and also in atmospheric physics / chemistry and fusion reactors. The astrophysical requirements resulted in a major theoretical collaboration to calculate the photoionization cross sections of nearly every element ranging from hydrogen to iron, in all ionization stages. The main contributors include: The OPAL Project [14], The

Opacity Project [15] and more recently The Iron Project [117, 118] and the Rmax project [119]. As always, these sophisticated theoretical models need experimental measurements to test their validity and stimulate further development.

Until the advent of synchrotron radiation (SR), the observation of the vacuum ultraviolet (VUV) to extreme vacuum ultraviolet (XUV) photon matter interactions, where photoionization is the dominant process, was limited to gases and to easily evaporable materials. Following the development of SR, the number of studies in this wavelength region increased. An important experiment entailed the observation of two-electron transitions (followed by autoionization) in the noble gases by Madden and Codling [7], which was followed by the theoretical studies of Fano and Cooper [41, 120, 121]. The development of windowless furnaces had a profound effect on this research area as they could be used to generate metal vapours for photoabsorption studies with synchrotron storage rings . A wealth of publications ensued for neutral absorption spectra in the XUV region, with pioneering work performed by Connerade and co-workers at the Bonn sychrotron facility, see [122] and references therein. The discovery of continuum emission from laser produced plasmas of high Z elements [58] initiated the evolution of the dual-laser plasma technique and it became a very important tool in the exploration of inner-shell studies in ions in the XUV and VUV regions.

Despite all of these developments, up until recently, obtaining absolute cross section measurements proved difficult. The main challenges arose from determining accurately the number density of the absorbing species in the case of neutral atoms, and having bright enough radiation sources to compensate for the low density in the case of ions. The first absolute photoionization measurements for ions were made on the Daresbury synchrotron radiation source (SRS) by Lyon *et al* [13, 123, 124] using a merged-beam layout where the ions and photons were merged collinearly over a distance of a few tens of cm. Although they were limited by the SR intensity to measuring cross sections $\geq\ 5\times\ 10^{-18}$ cm^2, they were able to measure the cross sections for certain elements, for example, the p $\rightarrow$ d resonances of the singly ionized alkaline earth metals (Ca^+, Sr^+ and Ba^+). With the advent of more intense SR sources, measurements for ions with lower cross sections became possible, hence, the past decade has seen a substantial increase of these measurements for a variety of ions, see [43] for a review and references therein.

The merged beam technique is the most widely used method of making atomic ion measurements using synchrotron radiation; synchrotron radiation facilities in Denmark (ASTRID), France (SuperACO), Japan (Photon Factory, SPring-8) and the USA (ALS) all employ this method. Its main advantages are: it provides high-resolution data, absolute cross sections can be measured directly, since the density

of the target ions can be determined; one has general freedom in selecting the ion source, e.g., Nielsen sources [125] and thermionic emitters [126] have been used in the past for singly-charged ions and electron cyclotron radiation (ECR) sources have successfully generated multiply charged ions [127]. The main disadvantage stems from the formation of ions in metastable states which in some cases can be a substantial fraction of the absorbing species thereby reducing the accuracy of the measurements. The accuracy of the absolute measurements is of the order of $\sim 10 - 20\%$. Apart from the presence of metastable species, uncertainties in the integrated form factor (a measure of photon-ion beam overlap) and uncertainties in the efficiency of the detectors contribute also.

As previously described in Chapter 2, the dual laser plasma technique can be used to make measurements on almost any element in any ion stage and has been an important source of experimental data on photoabsorption and photoionization of ions. It can provide complementary data to the absolute cross section measurements due to its capacity to provide better spectral resolution. The merged-beam technique provides absolute data directly comparable with theoretical calculations mentioned earlier, and is more selective in determining the charge of the parent species. For these reasons, collaborations were formed between groups who utilised these two techniques [128]. A brief description of the merged-beam set-up at ASTRID is given next followed by an introduction into the study performed by DCU and the collaborators listed at the beginning of this chapter. Results are presented in the final section.

4.1.1 Merged-Beam Layout

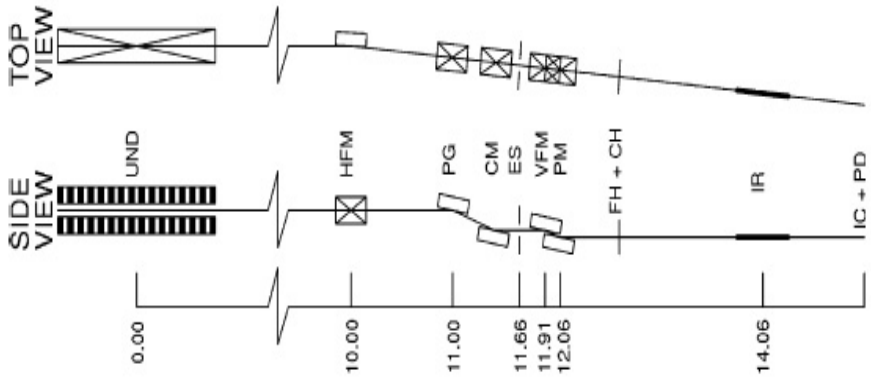

Figure 4.1: A schematic drawing of the undulator / Miyake-monochromator beam line at ASTRID, scale is in metres. UND: undulator; HFM: horizontal-focusing mirror (spherical, R = 150 m, θ = 87.5°); PG: plane grating (1200 lines / mm); CM: cylindrical mirror (R = 2.40 m); ES: exit slit; VFM: vertical-focusing mirror (spherical, R = 5.73 m, θ = 85.0-85.4°); PM: plane mirror; FH + CH: foil holder (for second-order absorbers) + chopper; IR: photon-ion interaction region; IC + PD: gas ionization chamber + Al_2O_3 photodiode. Diagram taken from [129].

A brief description of the undulator beamline at ASTRID is given in this section and an overview of the experimental procedure as the majority of my effort in this collaboration was spent in this area. A schematic layout of the photon beamline is given in Fig. 4.1. The undulator in the photon beam line contains 30 magnetic periods of 55 mm length and the gap can be varied to tune the first harmonic from 15 to 50 eV; for energies larger than this the higher harmonics are used. A spherical pre-mirror with an acceptance angle of 1 mR $\times$ 1 mR collects light from the undulator and focuses the light horizontally in the interaction region. A grazing incidence monochromator is used for fine wavelength tuning. Its design is based on the principle first described by Miyake *et al* [130] and further developed by West *et al* [131] for higher-order rejection. It comprises a vertically dispersing plane diffraction grating, (1200 lines / mm), focusing mirror and exit slit. Two vertically deflecting post-mirrors are positioned after the exit slit at grazing angles of 5°, one plane, one spherical, which provide a horizontal and parallel beam through the interaction region. The interaction region is $\sim$50 cm in length, and the ion beam is merged with the photon beam over this distance.

With regard to the Miyake monochromator, there is no entrance slit; the electron beam in the storage ring defines the magnitude of the source point. It was designed for a source point at infinity, whereas the source-point distance is $\sim$11 m at Århus.

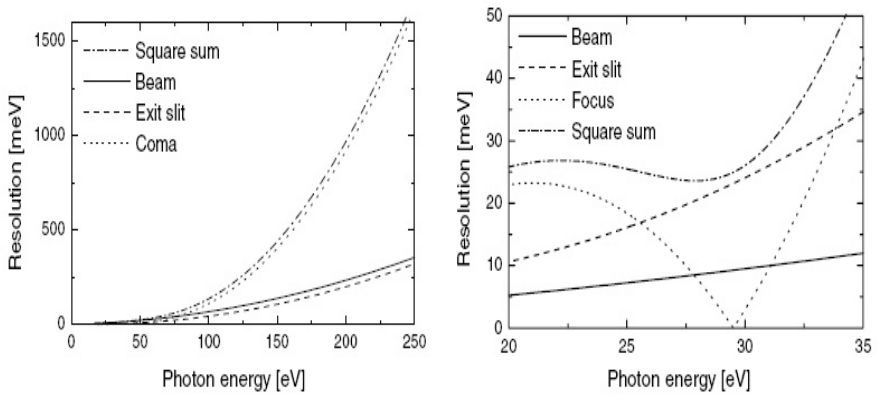

Figure 4.2: The calculated photon-energy resolution using optical path function theory (OPFT). Left: the cylindrical mirror is moved according to the photon energy; right: the cylindrical mirror is kept fixed in the position required for focusing the beam at the exit slit at 29.5 eV. Diagram taken from [129].

To ensure that light remains focused at the exit slit, it is therefore necessary to rotate and translate the mirror slightly. Unfortunately, the mechanism for moving the mirror was not designed for continuous movement during a scan and is only moved between scans. This impacts on the photon energy resolution, especially for the lower end of the photon energy range, where significant defocusing occurs, see Fig 4.2. The other main contributors to the photon energy resolution are the height of the electron beam in the ASTRID storage ring ($\sim$0.23 mm), the size of the exit slit and aberrations. The most significant aberration is coma, especially for photon energies greater than 75 eV. The resolving power ranges from 4000 at 17 eV to $\sim$ 1000 at 100 eV[1], and decreases rapidly at even higher energies. The photon beam line is optimised for high throughput and provides 3 - 5$\times 10^{12}$ photons/s from 15 eV to about 150 eV. To combat higher order radiation, the beam line is equipped with filters in the form of thin foils of Mg (25-50 eV), Al (35-70 eV) and Si (50-100 eV).

A noble-gas ionisation chamber is used to measure the current of the photoionised ions in order to deduce the photoabsorption cross section. It is also used to calibrate the photon-energy scale and the Al_2O_3 photodiode. The ionization chamber is a double-collector type originally developed by Samson [133], as in Fig. 4.3. Applying the Beer-Lambert's law, after traversing a distance *x* in a gas with density *n* and absorption cross section σ, the photon flux is reduced from I_0 to *I* according to

$$\frac{I}{I_0} = e^{(-n\sigma\ x)} \tag{4.1}$$

[1]For a slit width of 100 μm

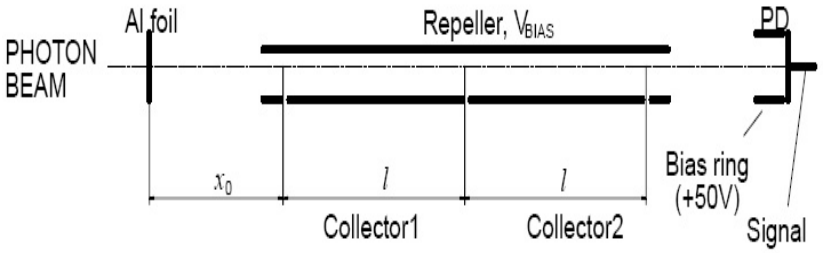

Figure 4.3: The noble-gas double ionisation chamber used on the merged-beam experiment. The gas is contained by a 1500Å Al foil, x_0 = 188 mm, l = 200 mm and the vertical distances from the centre line to the repeller and the collectors are 5 and 10 mm respectively. The small electrodes at each end of the collectors are grounded and installed to avoid fringing-field effects. PD = photodiode. Figure taken from Henrik Kjeldsen's thesis [132].

The recorded currents from the two collectors, J_1 and J_2 respectively, can be obtained from Eqn. 4.1:

$$J_1 = I_0 e e^{(-n\sigma\ x_0)}[1 - e^{(-n\sigma\ l)}] \tag{4.2}$$

$$J_2 = I_0 e e^{(-n\sigma(x_0+l))}[1 - e^{(-n\sigma\ l)}] \tag{4.3}$$

where e is the electron charge. From the above,

$$I_0 = \left(\frac{J_1}{J_2}\right)^{x_0/l} \frac{J_1^2/e}{J_1 - J_2} \tag{4.4}$$

$$I = \frac{J_1^2/e}{J_1 - J_2} \tag{4.5}$$

where J_1 and J_2 are the photo-ion currents as before. This is only true if one detected ion corresponds to one photoionization event. For high energies double photoionization is possible. It can be avoided for photon energies up to 78 eV if He gas is used. Also, as the ratio between single- and double-photoionization cross sections is known for He, corrections can be made.

The repeller electrode is kept at V_{bias} to force ions toward the collector and to prevent the electrons from hitting the collector. For high photon energies, the emitted electrons can have large kinetic energy and a large V_{bias} is necessary in order to retard the electrons. Secondary ionization can be problematic and must also be accounted for. The number of secondary-ionization events is proportional to the number of photoionization events, the target gas density and depends on the

photon energy. A correction factor of the form $(1 + c \cdot n)$ is applied to the photoionization current, where c is the mean value of the product of the cross section for ionization by electron impact and the interaction length. It can be minimised by appropriate selection of V_{bias}, target gas and ensuring the photon beam travels as close as possible to the repeller electrode.

Measurements of the photo-ion currents are always performed at three pressures, (0.01, 0.03 and 0.1 mbar), these values ensure the pressure is sufficiently high to be measured precisely and low enough to reduce secondary ionization. At high photon energies, secondary ionization cannot be avoided due to the photoelectrons' large kinetic energy and the use of very low pressure becomes necessary. In this case, the two collectors are coupled together, and the device is used as a single ionization chamber. Then J_1 and J_2 are measured at a low pressure (< 0.05 torr). The magnitude of the photon flux is obtained by:

$$I_0 = \frac{J_1 + J_2}{e\ exp(-n\sigma\ x_0)[1 - exp(-n\sigma(2l))]} \tag{4.6}$$

when n is determined from the pressure,

$$n = 3.218 \cdot 10^{16} P \tag{4.7}$$

Eqn. 4.7 is used to determine the number density and is valid at 298 K (ideal-gas law), n is measured in cm^{-3} and P is the pressure in torr, $2l$ is the total length of the two collectors (40 cm) and the photoionization cross section σ is taken from literature [134]. The calibration of the photodiode is performed by comparing the photodiode current with the magnitude of the photon flux determined with the ionization chamber.

The ion beam line is displayed in Fig. 4.4. The target ions are extracted from an ion source, mass separated, collimated and merged electrostatically with the photon beam. The interaction region consists of a biased cylinder, (600 V), in order to obtain a well defined interaction length by energy marking the photoionized ions[2]. It also discriminates against any charge-stripped background signal generated outside the interaction region. The cylinder is equipped with five *xy* scanners to measure the beam profiles and mutual overlap. The photoionized ion signal, the primary ion beam and the photon beam are separated by a deflection magnet. The primary ion beam is detected in a Faraday cup and the photoionized ions are further separated by an electrostatic analyser before the ions are detected by particle detectors - Johnston multipliers. More recently, a channeltron multi-

[2]Ions produced by photoionization in the interaction region will end up with 600 V extra energy ensuring one can distinguish between the target ions (A^q = 2 keV) and the photoionized ions (A^{q+1} = 2.6 keV), where q is the charge of the ion A.

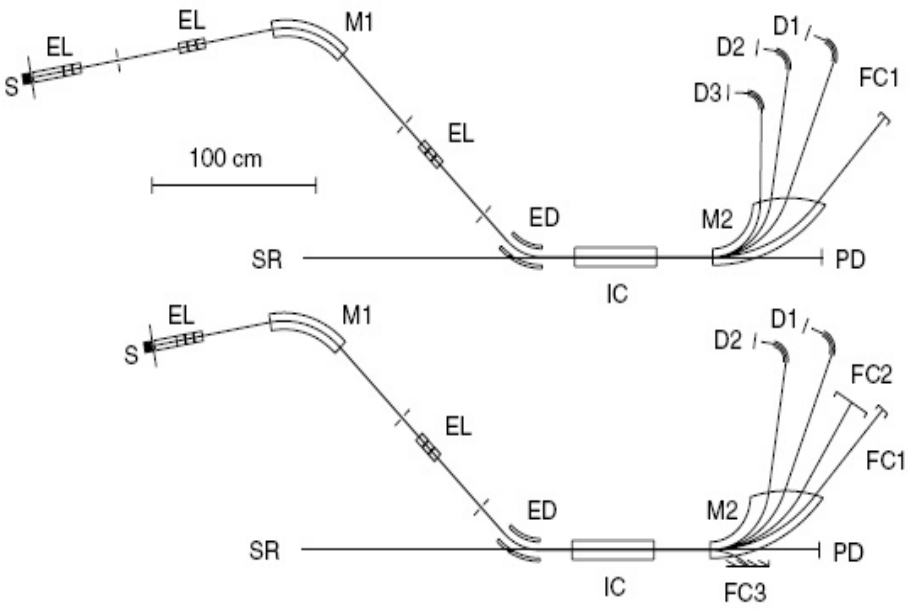

Figure 4.4: Ion beam layout of the merged-beam set-up at ASTRID showing the original set-up (top) and after the modification in 2002 (bottom). SR: Synchrotron radiation from the ASTRID undulator / Miyake-monochromator beam line; S: ion source; EL: Einzel lens; M1 and M2: deflection magnets; ED: electrostatic deflector; IC: interaction region; FC1-FC3: Faraday cups; PD: photodiode; D1-D3: particle detectors. Diagram taken from [129]

plier (CEM) [135] has been fitted in place of the Johnston multipliers. Here, the description of the system prior to this will be given to reflect the layout used for the measurements presented in the results section.

As one can see from the schematic, three Faraday cups are available at different positions as well as two detectors, this is a more recent setup to facilitate the study of negative and multiply charged ions [136, 137]. Using this setup, one can study a variety of different ionization channels simultaneously by applying the appropriate bias to the interaction region. To date, the following has been used: (1+ $\rightarrow$ 2+, 3+, 4+), (2+ $\rightarrow$ 3+, 4+), (3+ $\rightarrow$ 4+, 5+), (4+ $\rightarrow$ 5+, 6+), (1- $\rightarrow$ 1+) and (1- $\rightarrow$ 2+, 3+). For our experiment, ions were produced in a 10 GHz all permanent magnet electron cyclotron resonance (ECR) ion source [127] developed by CEA in Grenoble and used previously at the storage ring SuperACO [127, 138, 139, 140].

The absolute single- and double-photoionization cross sections are determined from the photoionization yield of the multiply charged ions using the following measured parameters:

$$\sigma = S \times \frac{e^2 \eta \upsilon F(\Delta x)(\Delta y)}{IJ\Omega l} \tag{4.8}$$

S is the charged ion rate, *e* the electronic charge, υ the velocity of the ions in the ion beam, *F* the form factor or overlap integral, Δx and Δy are the sampling intervals in the measurements of the beam profiles. *I* is the current of the source ions, measured by a Faraday cup while the photon beam intensity ($J/e\eta$) is measured by the photodiode. η is the photodiode efficiency, Ω the efficiency of the Johnston multiplier used to detect the multiply charged ions and *L* is the interaction path length.

The two-dimensional form factor $F_{xy}(z)$ at the point *z* along the beam axis is given by:

$$F_{xy}(z) = \frac{\int\int i(x,y)dxdy \int\int j(x,y)dxdy}{\int\int i(x,y)j(x,y)dxdy} = \frac{\sum\sum i(x,y) \sum\sum j(x,y)}{\sum\sum i(x,y)j(x,y)} \cdot \Delta x \Delta y \tag{4.9}$$

The parameters in this equation, *i(x,y)* and *j(x,y)*, are the ion current and the photon flux density, respectively, at the point *(x,y)*, whereas *i* and *j* are the corresponding current elements measured through the slits of the beam scanners contained in the interaction region. Δx and Δy are the horizontal and vertical step lengths in the beam profile scans. Generally it is sufficient to approximate the two-dimensional form factors $F_{xy}(z)$ by the product of two one-dimensional form factors $F_x(z)$ and $F_y(z)$. The variation of the form factors along the *z*-axis is approximated by a second order polynomial.

The efficiency of the detectors is obtained by deflecting a beam of relevant ion species with reduced counts into the Faraday cup and using a Keithley electrometer to measure the current *I*, this is then compared with the count rate *S* for the same ions deflected into the multiplier and the computed efficiency Ω is given by:

$$\Omega = \frac{Sqe}{I} \tag{4.10}$$

q is the charge of the ions, *e* is the electronic charge. A typical value obtained is 70%.

4.1.2 Experimental Procedure

In our experiment, we wished to study lowly charged members of the Kr I isoelectronic sequence, namely Rb^{+} and Sr^{2+}. We generated Rb^{+} and Sr^{2+} ions using an ECR source. The undulator gap was altered to select the appropriate harmonic necessary to give photons in the energy range needed, e.g, the first harmonic is ideal for a photon energy range of 15-45 eV while the third harmonic is used in the 45-120 eV photon energy range. The cylindrical mirror was then fixed to focus a particular photon energy on the exit slit. Usually a number of small energy ranges were chosen that centered on resonances of interest for each monochromator scan. As discussed earlier, the mirror operating in fixed-focus mode affects the resolution, so we generally focus at the photon energy of the resonance we wish to study. The exit slit size is chosen to give the best compromise between spectral resolution and photon flux. Beam profiles are recorded to ensure maximum overlap between the photons and the ion beam; generally one needs to translate or steer the ion beam to achieve this using electrostatic deflectors. The photoionised signal is subsequently deflected into a detector by appropriate magnetic (M2 and BEH (just before the detectors)) and electric fields (DEH / DEV, located after M2), while the primary ion beam is deflected into a Faraday cup.

During each photon-energy scan, the photoionisation signal from the detector, the background signal (photons are chopped), the photodiode and ion currents as well as the form factors are recorded as a function of photon energy. The background signal was recorded once for every 4 data points and the form factors were measured four times during a typical 2-hour scan. This was deemed satisfactory to give their accurate photon-energy and time dependence (or drift) whilst permitting the setup of several scans over the duration of the ion beam life time. A photodiode calibration was carried out each time the setting of the photon beam was changed, (shift of undulator harmonic, change of exit slit, translation of the cylindrical mirror in the monochromator). Using all of these measurements, the absolute photoionisation cross section of Rb^{+} and Sr^{2+} were obtained. The calculations were performed using programs written by Henrik Kjeldsen for his thesis [132] in MathCad 2000 Professional.

The DLP technique was used to record the vacuum ultraviolet (VUV) spectra of rubidium II and strontium III. In this case, the rubidium target was made from compressed rubidium chloride crystal pellets. This type of target is successful as long as transitions from the constituents do not overlap in the energy range of interest. Sr^{2+} was isolated in the plasma 1.5 mm from the target surface and 150 ns after plasma generation, while 1 mm and 400 ns provided the purest Rb^{+} ion spectra. Known aluminium emission lines were used to wavelength calibrate the spectra.

For the merged beam experiments, the Rb^+ and Sr^{2+} ions produced in the ECR source were accelerated through 2 keV potential difference and merged with the photons over an interaction length of 50 cm. The photon flux was typically $\sim 10^{12}$ photons s^{-1} / 0.1% bandwidth. The energy resolution was measured to be ~40 meV in the 4s-*n*p and *4*p region, and ~730 meV and ~1100 meV in the *3*d region for Rb^+ and Sr^{2+} respectively. The photon energy scale was calibrated using autoionization resonances in He (~60 eV), Ne (~47 eV) and Kr (~90 eV) with references obtained from [141, 142, 143]. The photodiode efficiency was obtained using the noble gas ionization chamber [133] containing 10-100 mTorr of Ne and measurements compared with the data from literature [134].

The measured absolute cross section data are expected to have an uncertainty of ~15%. This error comes mainly from the photodiode calibration, where the uncertainty in the higher-order content of the incident radiation is a component part. To suppress this Al (45-70 eV) and Si (70-85 eV) foils were inserted into the beamline.

4.1.3 Photoionization of Rb^+ and Sr^{2+} - Results

The aim of this work is to measure the 4s, 4p and 3d photoabsorption spectra of the Kr-isoelectronic sequence members, Rb^+ and Sr^{2+}, using the DLP technique and complement the results with absolute cross section measurements using the merged-beam technique. The study of isoelectronic sequences has provided useful insights into the changing nature of physical (Coulombic, exchange, spin orbit, etc.) interactions as the core charge changes. In the Kr I isoelectronic sequence, a decreasing centrifugal barrier causes dramatic changes in the photoionization spectra, as detailed below. This study builds on earlier work carried out jointly at DCU and UCD where the Ar-isoelectronic sequence [46, 69, 144] was studied using the DLP technique. This study of the 3s-subshell showed that due to configuration interaction between single and double electron excited states along the sequence, dramatic changes in the 3s-*n*p resonance profiles were observed. The profiles ranged from window resonances in Ar to almost symmetric absorption lines in Ca^{2+} due to a shift in the 3p Cooper minimun.

A similar study at DCU for the 4s-*n*p resonances in the Kr-isoelectronic sequence [145] again saw a drastic change in these resonance profiles from Kr to Rb^+ to Sr^{2+}. Interference between the direct and correlational amplitudes results in a minimum in the $\sigma_{4s}(\omega)$ cross section above the *4*s threshold at ~0.4 a.u. in Kr, which shifts towards the *4*s threshold in Rb^+ and lies below the threshold in Sr^{2+}. Consequently, the complex doubly excited resonances straddling the first 4s-5p resonance in Kr move to higher photon energy, blending with 4s-*n*p resonances, ($n \geq 6$), thus isolating the 4s-5p resonances in Rb^+ and Sr^{2+}. Yeates *et al* [81] continued

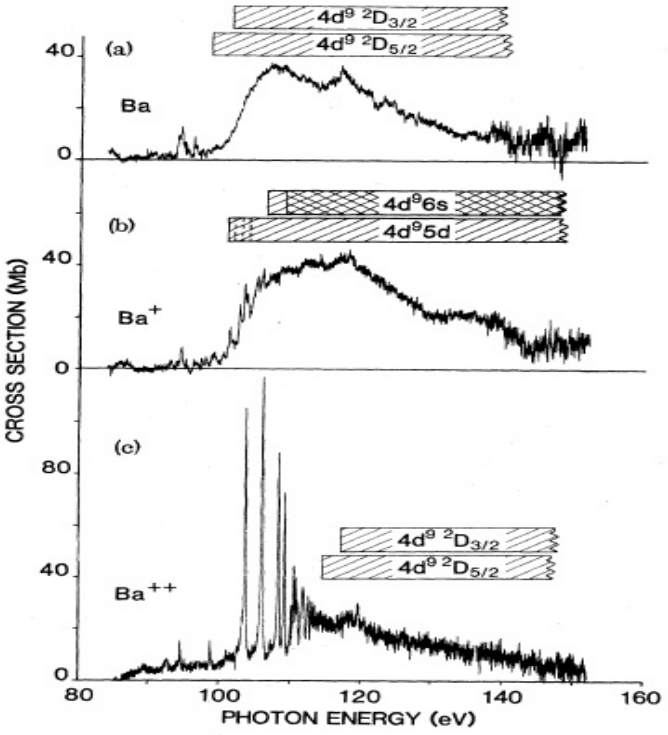

Figure 4.5: The experimental results of Lucatorto and McIlrath on Ba, Ba^{+} and Ba^{2+} [146] in the 4d excitation region.

this work in DCU by studying the next member of the Kr I isoelectronic sequence, Y^{3+}. They observed that the 4s-5p resonance drops below the 4p ionization threshold, so that the first autionizing member becomes the 4s-6p resonance. In contrast to the window resonances observed for the lower isoelectronic members, the 4s-6p resonance profile had a normal, slightly asymmetric shape. In this work, comparisons are made between the absolute photoionization cross section measurements for the 4s-*n*p resonances of Rb^{+} and Sr^{2+} and the previous results obtained with the DLP technique [145].

Previous studies on the *4*p-subshell spectra of the Kr I isoelectronic sequence [147, 148] provided values for the ionization potentials of Rb^{+} and Sr^{2+}, 27.2898 and 42.87 eV, respectively and the classification of some transitions from the ground state to $4p^5nd, ms$ levels. This work extends this study and further, identifies higher lying $4p^5nd, ms$ levels. Measurements are also performed for 3d subshell excitation in Rb^{+} and Sr^{2+}, motivated by the interesting and unexpected features observed in 4d-subshell excitation in the lanthanides. With reference to the latter, the lack of discrete $4d \rightarrow nf$ resonances and the $4d \rightarrow \epsilon f$ 'giant' resonances observed have stimulated numerous experimental and theoretical investigations, see for example [146, 149, 150, 151, 152, 153]. The lack of strength in the $4d \rightarrow nf$ transitions

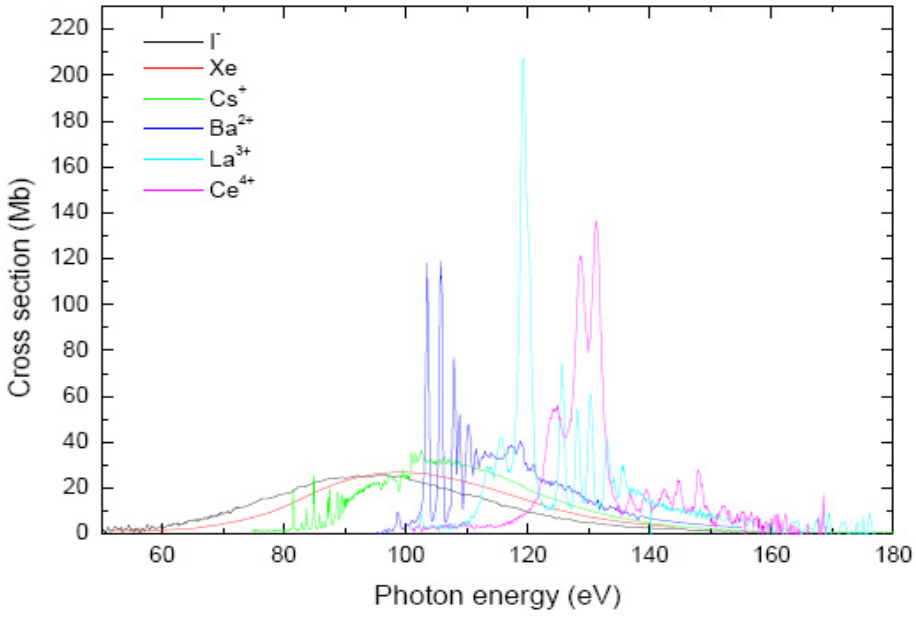

Figure 4.6: Comparison between the absolute photoionization cross sections for the isoelectronic xenon-like ions, I^-, Xe, Cs^+, Ba^{2+}, La^{3+} and Ce^{4+} [154] and references therein.

and in the near-threshold region for the ϵf continuum is referred to as *delayed onset*. Strong competition between the Coulombic attraction and the centrifugal repulsion results in a double-valley potential for the $l = 3$ channel, which in turn is responsible for exclusion of the *n*f wavefunctions from the core region. Above this delayed onset region, the *n*f wavefunctions can penetrate the core, resulting in the strong 'shape' resonances observed. For neutral atoms, the double-well barrier persists; the 4f wavefunction collapses into the inner well while the higher *n*f members are delocalised out of the core. Thus, a single strong 4d $\rightarrow$ 4f resonance is observed. In the case of ions, the double-well structure disappears with increasing atomic number Z or degree of ionization ζ, so that all of the *n*f orbitals are contracted. Therefore the 4d $\rightarrow$ *n*f transitions will be strong. This is clearly illustrated in Fig. 4.5 where Lucatorto and McIlrath [146] studied the Ba isonuclear sequence up to Ba^{2+} in the 4d resonance region.

The numerous experimental and theoretical investigations that ensued, [122, 138, 155, 156, 157, 158], were superseded by the absolute partial and total photoionization data that followed on Xe [159, 160, 161] and Ba ions [139]. Andersen *et al* [162] using the merged-beam set up at ASTRID, made absolute measurements on Xe^+ and Xe^{2+}. They discovered that the dominant partial cross section is due to double-photoionization. More than 90% of the total cross section in the 4d region could be attributed to $Xe^+ \rightarrow Xe^{3+}$. Similarly for Xe^{2+}, double photoionization was

dominant. In order to gain a better understanding of how the 4d $\rightarrow$ f spectra progresses as a function of nuclear change and ionization stage, Kjeldsen *et al* utilized the set up at Århus [129, 152, 154, 163] to measure the absolute photoionization cross sections for I^-, I^+, I^{2+}, Cs^+, Ba^+ - Ba^{3+}, La^+, La^{3+} and Ce^{4+}, see Fig. 4.6. They observed that in the isonuclear studies of I and Ba, the overall shape of the 4d $\rightarrow$ f oscillator-strength distribution remains static with increasing ionization. As the charge state increases strong resonance lines due to 4d $\rightarrow$ *n*f transitions appear which take up more of the total oscillator strength. Including measurements made from the Xe isoelectronic series, the general conclusion was that the total oscillator strength over the 4d region is close to ten for all atoms and ions. The experimental confirmation of this assertion from the systematic studies performed at ASTRID suggests that the 4d shell is fairly unperturbed by other shells (as only a small amount of oscillator strength is transferred to or from valence electrons in the energy region). The contraction of the 4f-wavefunction progresses from Xe via Cs^+ to Ba^{2+} and in contrast to the results for these lighter Xe-like ions, the *n*f wavefunctions are strongly contracted for La^{3+} and Ce^{4+}, as evidenced by the fact that the 4d $\rightarrow$ *n*f and *n*p resonances almost dominate the spectra as can be seen in Fig. 4.6.

Employing the DLP technique, McGuinness *et al* measured the 3d photoabsorption spectra of Sr I through to Sr IV and saw an increase in intensity of the 3d-*n*f transitions along the isonuclear sequence [113]. Using the HXR code, they calculated the 3d $\rightarrow \epsilon$p, ϵf cross sections. The 3d $\rightarrow \epsilon$p progresses hydrogenically while the 3d $\rightarrow \epsilon$f exhibits a Cooper minimum at threshold. The energy of this minimum does not change between Sr and Sr^{2+} and although the 3d $\rightarrow \epsilon$f cross section peaks closer to threshold with increasing ionization, the 3d ionization energy is also increasing so the total cross section as a function of energy is effectively unaltered. Similar photoabsorption measurements have been made for Rb^+ and Rb^{2+} [164, 165]. In contrast to Sr^{2+}, only 3d $\rightarrow$ 5p, 6p transitions are observed in the Rb^+ spectrum, the centrifugal repulsion experienced by the *n*f wavefunctions excludes them from the core region, giving 3d $\rightarrow$ *n*f transitions negligible oscillator strength. The purpose of this experiment is to measure the partial and total photoionization cross section measurements for Rb^+ and Sr^{2+} to further insight into 3d excitation.

4.2 Results

4.2.1 4s - *n*p resonances

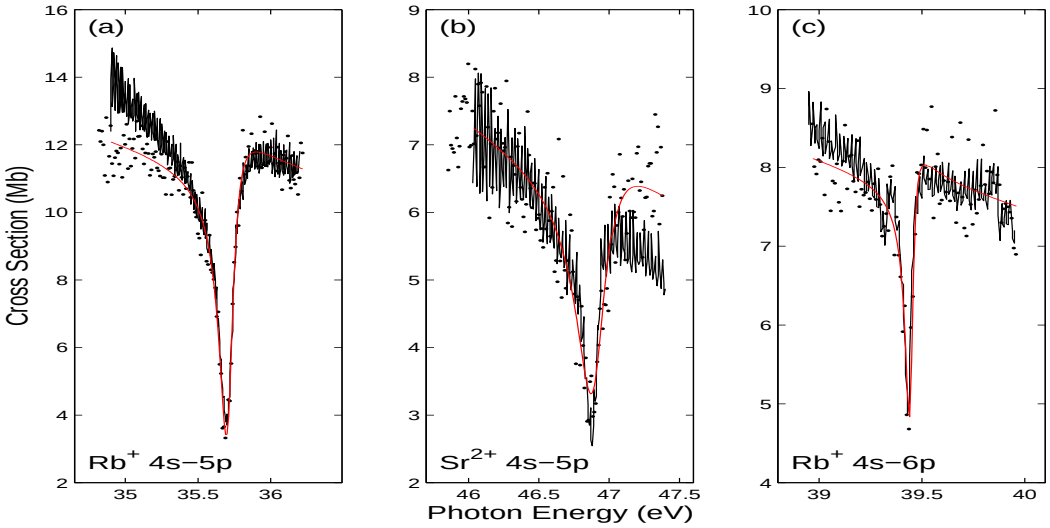

Figure 4.7: The experimental absolute single-photoionization cross sections for (a) the 4s→5p Rydberg resonance of Rb^+, (b) the 4s→5p Rydberg resonance of Sr^{2+}, and (c) the 4s→6p Rydberg resonance of Rb^+. Data from the dual laser produced plasma (black), absolute single photoionization (black dot), and Fano fit (red) are presented.

The absolute photoionization cross sections for the 4s→5p (Rb^+ and Sr^{2+}) and 4s→6p (Rb^+ only) Rydberg resonances measured at ASTRID are presented in Fig 4.7 along with the corresponding dual laser plasma photoabsorption spectra. Using the spectral profile function σ for an isolated resonance in photoionization [41, 120], we could compare both results and determine these window resonance profile parameters:

$$\sigma = \sigma_0 \left[1 - \rho^2 + \rho^2 \frac{(q+\epsilon)^2}{1+\epsilon^2} \right] \tag{4.11}$$

where ϵ=(E-E_r)/(Γ/2) is the reduced photon energy, E is the incident photon energy, Γ is the resonance width, and E_r is the resonance energy position. The Fano parameters ρ and q describe the strength and shape of the resonance, respectively. The 4p continuum was assumed to decrease linearly with photon energy in the region around the resonances. Table 4.1 contains the measured profile parameters of the 4s-*n*p resonances of Rb^+ and Sr^{2+} from this work[a] and compares them to previous work by Neogi *et al*[b] [145]. The discrepancy observed can be accounted for by opacity effects in the dual laser plasma experiments. It has been shown [78],

Table 4.1: Measured profile parameters of 4s $\rightarrow$ *n*p resonances of Rb^+ and Sr^{2+}.

profile parameter	Rb^+ $4s \rightarrow 5p$		
E_r (eV)	35.708 [a]	35.71 ± 0.02 [b]	35.714 [c]
Γ (eV)	0.117 [a]	0.09 ± 0.03 [b]	0.143 [c]
q	0.255 [a]	0.24 ± 0.06 [b]	0.267 [c]
ρ^2	0.40 [a]	0.40 ± 0.10 [b]	0.277 [c]
profile parameter	Sr^{2+} $4s \rightarrow 5p$		
E_r (eV)	46.91 [a]	46.89 ± 0.03 [b]	46.889 [c]
Γ (eV)	0.247 [a]	0.08 ± 0.03 [b]	0.116 [c]
q	0.268 [a]	0.28 ± 0.07 [b]	0.266 [c]
ρ^2	0.22 [a]	0.22 ± 0.05 [b]	0.22 [c]
profile parameter	Rb^+ $4s \rightarrow 6p$		
E_r (eV)	39.442 [a]		39.436 [c]
Γ (eV)	0.045 [a]		0.044 [c]
q	0.291 [a]		0.1955 [c]
ρ^2	0.28 [a]		0.28 [c]

[a] denotes values obtained from fitting the absolute cross section data.
[b] denotes values quoted in [145] for photoabsorption data.
[c] denotes values obtained from fitting the photoabsorption data [145] using the corrections to Γ and q described in the text.

that for optically thick plasmas [166], resonances are saturated resulting in broader profiles and reduced intensities, which in turn affects the profile width and *q* values of Fano-Beutler resonances. Optically thin spectra are taken to provide the best values. By reducing the widths in [145] by 30% and increasing the *q* values by $\sim$10%, good agreement is obtained with the absolute cross section data, see Table 4.1[c]. The larger width obtained in our experiments for the 4s $\rightarrow$ 5p resonance in Sr^{2+} compared to Neogi *et al* we suspect is due to a typo error in the published work, particularly as all other parameters match up very well.

4.2.2 4p $\rightarrow$ *n*s, *m*d region

Fig. 4.8 displays the absolute photoionization cross section for Sr^{2+} in the region of 4p $\rightarrow$ *n*s, *m*d excitations along with the DLP results and calculated spectrum. The discrete features observed were assigned with the aid of Hartree plus exchange plus relativistic corrections (HXR) of the Cowan code [30] and are dispayed in Table 4.2[3]. Further details on the calculations can be read in the published work [16]. Contributions from metastable states were observed in the photoabsorption spectrum. The closest lying metastable level ($4s^2 4p^5 5p$) has a calculated average energy of 28.388 eV and a separate calculation was made for potential metastable contributions from this level (green line in Fig. 4.8). The calculated metastable absorption

[3] All assignments were made by Deirdre Kilbane and are included here for completeness.

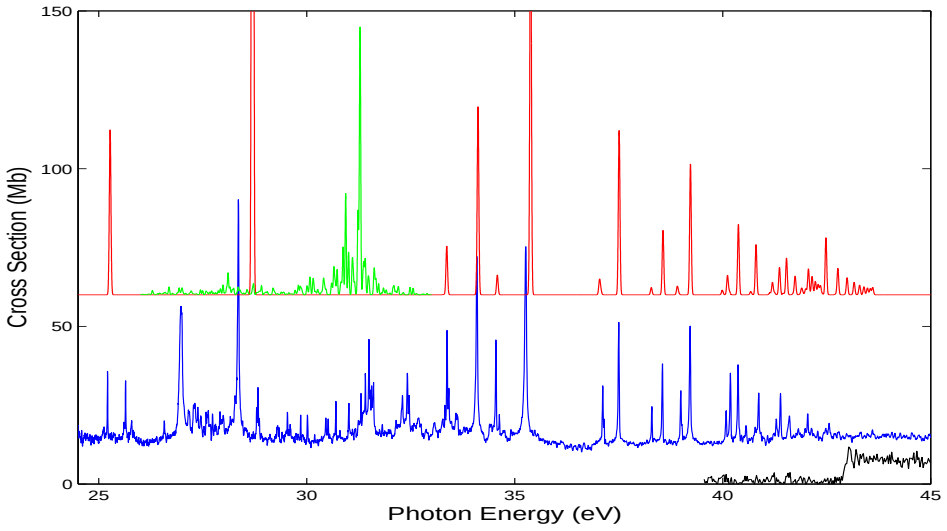

Figure 4.8: The experimental absolute photoionization cross section for Sr^{2+} in the region of 4p $\rightarrow$ *n*s, *m*d excitations. (blue) DLP, (black) absolute single- photoionization spectrum, (red) synthetic spectrum and (green) synthetic metastable spectrum ($\div 100$). See Table 4.3 for discrete feature assignments.

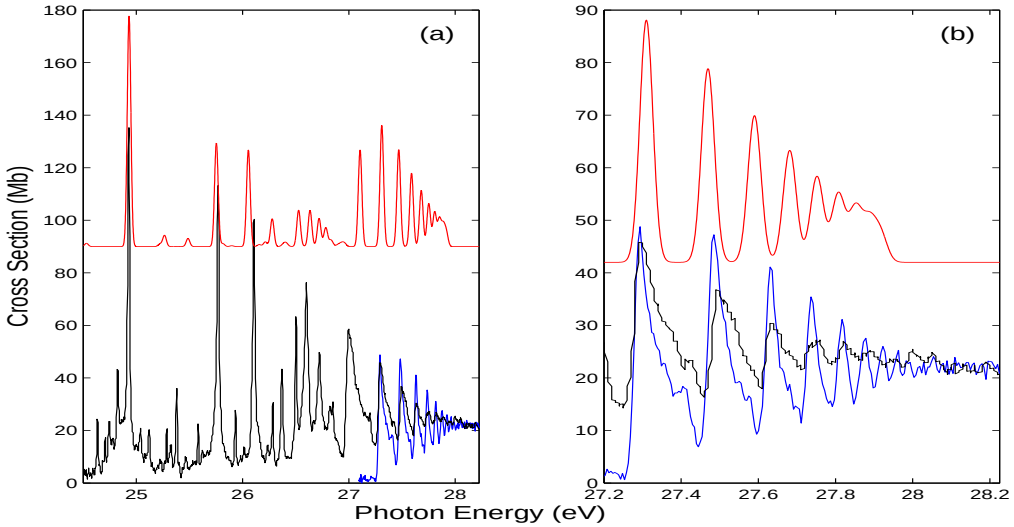

Figure 4.9: The experimental absolute photoionization cross section for Rb^{+} in the region of 4p $\rightarrow$ *n*s, *m*d excitations. (black) DLP, (blue) absolute single- photoionization spectrum and (red) synthetic spectrum shifted by -0.015 eV. The absolute spectrum was taken to start at $\sim$ 27.3 eV as it matched best with the DLP results in the 27.2 - 28.2 eV photon energy range. See Table 4.2 for discrete feature assignments.

spectrum was scaled down by a factor of 100 to bring it in line with the experimental spectra, (similar metastable problems were observed for the 4p-photoabsorption spectrum of Sr^+ in Chapter 5). Thus a small population in this state could be hugely problematic for the merged-beam method. However, as can be seen in Fig. 4.8, the cross section is close to zero just below the threshold for ionization, indicating negligible contribution from metastable levels and we concluded that the absolute data were reliable, within the uncertainty given.

Similarly for Rb^+, the HXR of the Cowan code [30] was used to assign discrete features in the 4p-photoionization spectra [16], see Table 4.3. Good agreement was observed between the DLP photoabsorption and merged beam experiments for the 4p to *n*d Rydberg series converging on the $^2P_{1/2}$ limit, see Fig. 4.9(b).

Table 4.2: Observed and calculated energies and gf-values for the $3d^{10}4s^24p^6 \rightarrow 3d^{10}4s^24p^5nd$, *m*s transition array of Rb^+. The final state jj coupling of the $3d^9$ core is denoted in brackets by J_{core},J_{nl}.

Upper state	E_{exp} (eV)	E_{emis} (eV)	E_{calc} (eV)	gf-value	δ
$6d(\frac{3}{2},\frac{5}{2})$	24.93	24.929 [a]	24.9313	0.53	
$8d(\frac{3}{2},\frac{5}{2})$	25.77	25.77 [a]	25.7530	0.24	
$8d(\frac{3}{2},\frac{5}{2})$	26.11	26.1090 [a]	26.0542	0.22	
$11d(\frac{3}{2},\frac{5}{2})$	26.37	26.5976 [a]	26.5270	0.08	3.31
$7d(\frac{3}{2},\frac{5}{2})$	26.50		26.6342	0.08	
$12d(\frac{3}{2},\frac{5}{2})$	26.60		26.7194	0.06	3.12
$13d(\frac{3}{2},\frac{5}{2})$	26.72		26.7845	0.04	3.20
$9d(\frac{1}{2},\frac{3}{2})$	27.00		27.1055	0.22	2.27
$10d(\frac{1}{2},\frac{3}{2})$	27.31		27.3099	0.28	2.22
$11d(\frac{1}{2},\frac{3}{2})$	27.50		27.4695	0.22	2.21
$12d(\frac{1}{2},\frac{3}{2})$	27.63		27.5900	0.17	2.23
$13d(\frac{1}{2},\frac{3}{2})$	27.74		27.6814	0.13	2.22
$14d(\frac{1}{2},\frac{3}{2})$	27.82		27.7519	0.10	2.04
$15d(\frac{1}{2},\frac{3}{2})$	27.89		27.8072	0.08	1.92
$16d(\frac{1}{2},\frac{3}{2})$	27.95		27.8515	0.06	1.34

Calculated energies are shifted by -0.015 eV. [a] Assignments in this work have been made using the jj coupling scheme and vary slightly from the original assignments made in the J_1l coupling scheme (for details of previous assignments see [148]).

Table 4.3: Observed and calculated energies and gf-values for the $3d^{10}4s^24p^6 \rightarrow 3d^{10}4s^24p^5nd$, ms transition array of Sr^{2+}. The final state jj coupling of the $3d^9$ core is denoted in brackets by J_{core},J_{nl}.

Upper state	E_{exp} (eV)	E_{emis} (eV)	E_{calc} (eV)	gf-value	δ
$5s(\frac{1}{2},\frac{1}{2})$	25.21	25.211 [a]	25.2724	0.36	2.45
$6s(\frac{1}{2},\frac{1}{2})$	34.55	34.555 [a]	34.5811	0.04	2.42
$7s(\frac{1}{2},\frac{1}{2})$	38.30		38.2829	0.02	2.40
$4d(\frac{3}{2},\frac{5}{2})$	28.35	28.356 [a]	28.6967	5.02	1.10
$5d(\frac{3}{2},\frac{5}{2})$	34.09	34.110 [a]	34.1169	0.41	1.27
$6d(\frac{3}{2},\frac{5}{2})$	37.50	37.496 [a]	37.5097	0.36	1.38
$7d(\frac{3}{2},\frac{5}{2})$	39.22	39.222 [a]	39.2244	0.28	1.21
$8d(\frac{3}{2},\frac{5}{2})$	40.18		40.1148	0.04	1.25
$9d(\frac{3}{2},\frac{5}{2})$	40.86		40.8007	0.11	1.19
$10d(\frac{3}{2},\frac{5}{2})$	41.29		41.1960	0.03	1.21
$11d(\frac{3}{2},\frac{5}{2})$	41.60		41.5336	0.08	1.17
$12d(\frac{3}{2},\frac{5}{2})$	41.81		41.7404	0.04	1.24
$14d(\frac{3}{2},\frac{5}{2})$	42.04		42.0606	0.06	1.27
$15d(\frac{3}{2},\frac{5}{2})$	42.13		42.1484	0.04	1.83
$16d(\frac{3}{2},\frac{5}{2})$	42.21		42.2275	0.03	2.10
$17d(\frac{3}{2},\frac{5}{2})$	42.28		42.2936	0.02	2.42
$18d(\frac{3}{2},\frac{5}{2})$	42.56		42.3486	0.02	2.62
$6s(\frac{3}{2},\frac{1}{2})$	33.37	33.400 [a]	33.3651	0.11	2.41
$7s(\frac{3}{2},\frac{1}{2})$	37.12		37.0377	0.03	2.39
$8s(\frac{3}{2},\frac{1}{2})$	38.99		38.9078	0.02	2.38
$9s(\frac{3}{2},\frac{1}{2})$	40.08		39.9886	0.01	2.38
$5d(\frac{1}{2},\frac{3}{2})$	35.26	35.261 [a]	35.3812	0.88	1.27
$6d(\frac{1}{2},\frac{3}{2})$	38.55	38.552 [a]	38.5636	0.14	1.29
$7d(\frac{1}{2},\frac{3}{2})$	40.37	40.362 [a]	40.3767	0.15	1.25
$8d(\frac{1}{2},\frac{3}{2})$	41.39		41.3645	0.06	1.25
$6d(\frac{3}{2},\frac{3}{2})$	37.15		37.0689	0.01	

[a] Assignments in this work have been made using the jj coupling scheme and vary slightly from the original assignments made in the J_1l coupling scheme (for details of previous assignments see [147]).

4.2.3 3d region

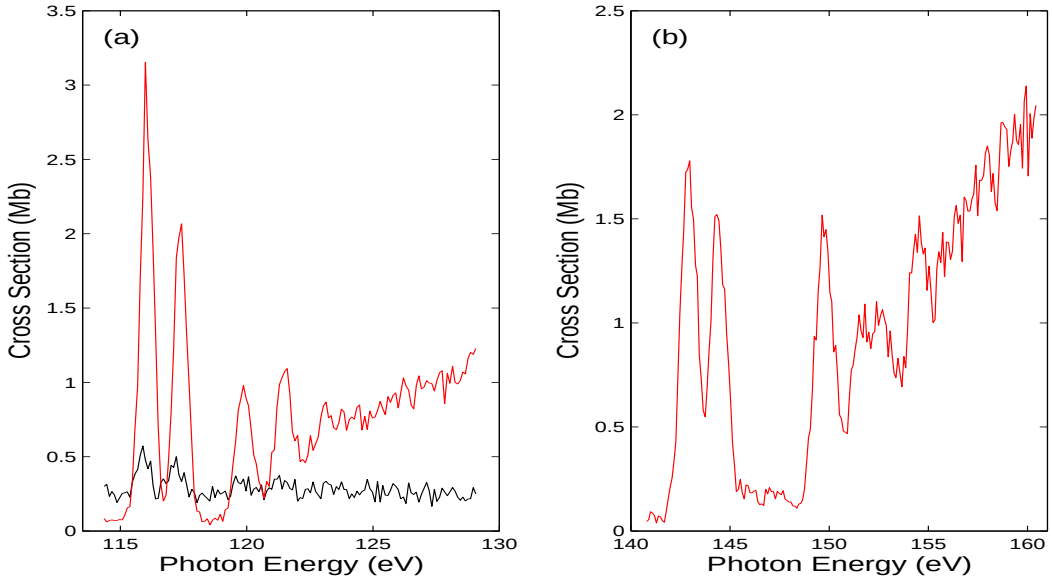

Figure 4.10: The experimental absolute photoionization cross section for (a) Rb^+ and (b) Sr^{2+} in the region of $3d$ excitations. Absolute single- photoionization (black) and absolute double- photoionization (red) yields are presented.

The experimental photoionization cross sections for Rb^+ and Sr^{2+} in the 3d region are shown in Fig. 4.10. The previous photoabsorption studies made in this region for Rb^+ and Sr^{2+} [113, 164] had better resolution ($\sim$200 meV) compared to the merged-beam experiment ($\sim$730 meV and $\sim$1100 meV, respectively) in this photon energy range. Similar to Xe, the dominant process in the 3d region is double photoionization, i.e., $Rb^+ \rightarrow Rb^{3+}$ and $Sr^{2+} \rightarrow Sr^{4+}$. Neogi *et al* [164] assigned the discrete features due to 3d excitation in Rb^+ (as observed in Fig. 4.10) to $3d^9 4s^2 4p^6 np$ (n = 5-7) transitions. The two large peaks in the Sr^{2+} spectrum at $\sim$ 143 eV and 144.5 eV were previously assigned to the $3d^9 4s^2 4p^6 5p[(\frac{3}{2},\frac{3}{2}),(\frac{3}{2},\frac{1}{2})]$ levels respectively in [113] while the same authors assigned the large resonance at $\sim$ 150 eV as the $3d^9 4s^2 4p^6 4f[(\frac{5}{2},\frac{7}{2})]$ transition. The other features observed in the spectrum are due to overlapping $3d \rightarrow mp$ and $3d \rightarrow nf$ transitions which combine such that only a few strong lines, corresponding to those observed, appear.

As double photoionization cannot be explained within the framework of a single-particle model like the Hartree-Fock used in this work, Grotrian diagrams were constructed[4] to act as a visual aid, see Fig. 4.11. Energy levels and ionization potentials were taken from the literature when available, otherwise they were calculated using the HXR mode of the Cowan code [30]. The single-photoionization cross sec-

[4]These diagrams were constructed by Deirdre Kilbane.

tion arises from either direct photoionization to the ground state $4s^2 4p^5$ of Rb^{2+} or by the following allowed Auger decay schemes [167]:

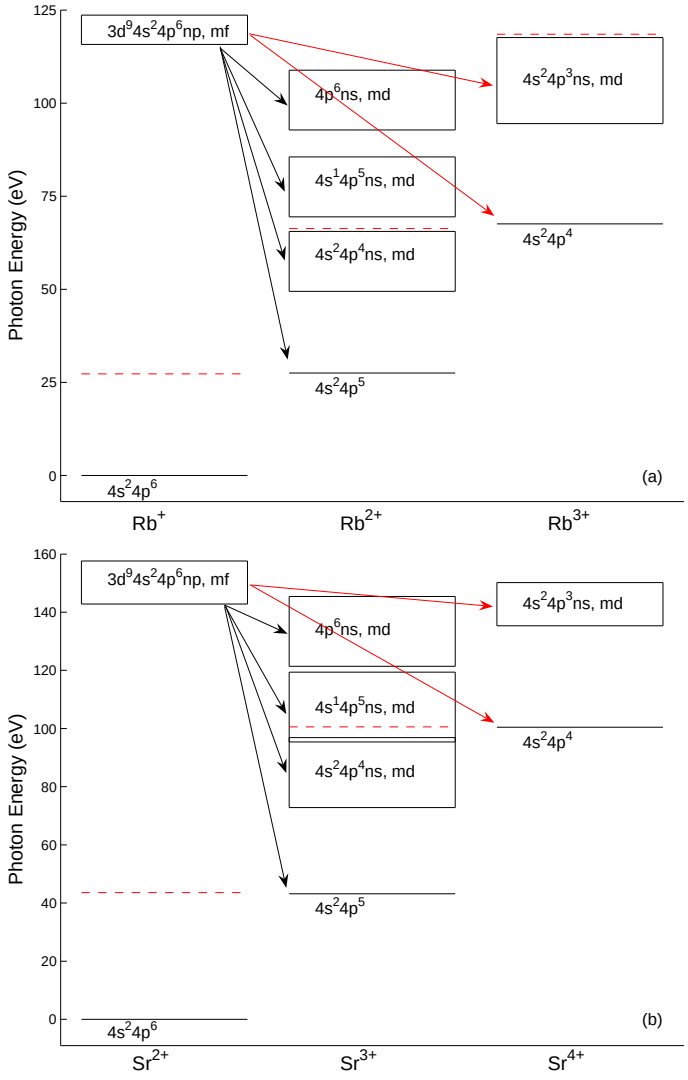

Figure 4.11: Grotrian diagrams for the decay of the $3d^{-1}$ excited state of (a) Rb^+ and (b) Sr^{2+}. Single- photoionization decay pathways are indicated by black arrows and double- photoionization decay pathways are indicated by red arrows. The ionization limits are indicated by the red dashed lines.

$$
\begin{aligned}
\mathrm{Rb}^+(3\mathrm{d}^9 4\mathrm{s}^2 4\mathrm{p}^6 n\mathrm{p},\, m\mathrm{f}) &\rightarrow \mathrm{Rb}^{2+*}(3\mathrm{d}^{10} 4\mathrm{s}^2 4\mathrm{p}^4 n\mathrm{s},\, m\mathrm{d}) + e_1 \\
&\rightarrow \mathrm{Rb}^{2+*}(3\mathrm{d}^{10} 4\mathrm{s}^1 4\mathrm{p}^5 n\mathrm{s},\, m\mathrm{d}) + e_2 \\
&\rightarrow \mathrm{Rb}^{2+*}(3\mathrm{d}^{10} 4\mathrm{s}^0 4\mathrm{p}^6 n\mathrm{s},\, m\mathrm{d}) + e_3
\end{aligned}
$$

Double photoionization can occur via direct photoionization to the ground state $4s^2 4p^4$ of Rb^{3+} or by Auger decay, $3d^9 4s^2 4p^6 np$, $mf \rightarrow Rb^{3+*}$ $3d^{10} 4s^2 4p^3 ns$, md + 2e' (Fig. 4.11); it has long been known that it is the latter which is responsible for the major part of the d-shell continuum cross section. A similar situation exists for Sr^{2+} as illustrated in Fig. 4.11. As seen for 4d excitation in Xe^+ and Xe^{2+}, 90% of the total cross section is accounted for by double photoionization in the 3d region for the early members of the Kr I isoelectronic sequence.

4.3 Conclusion

The 4s-, 4p- and 3d-photoionization spectra have been recorded for the Kr I isoelectronic sequence, Rb^+ and Sr^{2+}. Photoabsorption spectra were recorded using the dual laser plasma technique and absolute photoionization cross section measurements were made using the merged ion beam and synchrotron setup at ASTRID. In the 4s - np resonance region, good agreement was found between the absolute and photoabsorption data, with the fitted profile parameters matching experimental data quite well. Using HXR calculations, many $4p \rightarrow ns$, md transitions were identified from the experimental measurements. In agreement with previous observations [162], partial single and double absolute photoionization cross sections recorded in the 3d region for Rb^+ and Sr^{2+} show preferential decay via double photoionization.

Further isonuclear and isoelectronic studies in the 3d - excitation region are needed to determine if $3d \rightarrow nf$ excitations behave in the same fashion as in the case of $4d \rightarrow nf$ excitations in the lanthanides. The theoretical and experimental work stimulated by 4d excitations in the lanthanides led to a surmountable improvement in our knowledge of inner-shell dynamics and it is hoped this work on 3d excitations in the Kr-like ions will encourage further theoretical developments.

Chapter 5

The 4p photoabsorption spectrum of Sr II

5.1 Introduction

Inner-shell photoionization in atoms and ions has maintained interest throughout the years as it provides insight into the correlation effects that occur near-threshold; interchannel - coupling, relaxation, exchange, Auger decay etc. In this context, excitation and ionization of the highest filled p-subshell in alkaline earth metals are of particular interest, as previous studies show [36, 49, 168, 169, 170, 171, 172]. Due to electron-electron correlation between the inner and valence shells, one observes excitation of one or both valence electrons simultaneously. As a consequence, a wealth of structure is observed making identification of lines difficult and testing for theoretical codes.

Previous theoretical studies using multi configuration Hartree - Fock (MCHF) and Hartree-Fock with exchange (HFX) calculations in *LS* coupling have provided accurate results for p-subshell excitation in both Ca I [171] and Sr I [36]. The overall distribution of intensity was well explained by the consideration of $np^6(n{+}1)s^2 \rightarrow np^5(n{+}1)s^2md$, ms, (n=3 for Ca, 4 for Sr and $m \geq n$) transitions. To account for the large number of lines observed, multi-electron excitation needed to be considered. Double excitations of the type $np^5nd^2(n{+}1)s/d$ were found to be the most significant. Separate minimization calculations were necessary for the $np^5nd(n{+}1)s^2\ ^1P$ terms to account for the potential barrier that repels the d wavefunction out of the core, as discussed in Chapter 1.

The 5p-excited spectrum of Ba I caused controversy due to discrepancies between the observed spectrum and theoretical predictions. Anomalies concerning the double to single photoionization rates were reported [173, 174]; subsequent

proposed explanations differed [175, 176, 177]. A detailed study of the 5p photoabsorption structure by Connerade *et al* [178] and Rose *et al* [179] unraveled the mystery of the double-ionization process. The former group classified series converging to 12 limits of Ba II which agreed well with binding energy measurements for the 5p shell of Ba I obtained by Mehlhorn *et al* [180] by electron impact spectroscopy. Rose *et al* [179] successfully applied a fully relativistic ab-initio multi configuration Dirac-Fock (MCDF) procedure to assign six series limits observed in [178, 180]. They found that final ionic state configuration interaction (FISCI) calculations provided accurate energy values and intensities for the most prominent peaks in the electron-impact 5p-ionization spectrum. On the basis of their analysis, the energy viability of two-step autoionization was established, as had been predicted [176, 181].

However, in the case of the singly ionized counterparts, accurate theoretical results have proven more difficult to obtain. Hansen [176] showed that it was necessary to include exchange in his calculations to properly account for the observed electron-impact ionization functions of Mg II, Ca II, Sr II and Ba II. The measured electron-impact ionization functions for these ions displayed remarkable differences for the p^5ds excitations [182]. The ionization cross sections for Ca II, Sr II and Ba II exhibited abrupt thresholds, indicating strong contributions from autoionization, while there was no evidence for this in Mg II. Moores and Nussbaumer [183] proposed that this was due to the fact that the largest autoionization contribution arose from the $2p^63s \rightarrow 2p^53s3d$ transition, where $\Delta n = 1$. Since the two electrons have different principal quantum numbers, the overlap between their wavefunctions is much smaller than in the other alkaline earths where $\Delta n = 0$ for the p^5ds transitions (e.g. $3p \rightarrow 3d$ in Ca).

Theoretical analysis of the Ca II spectrum was first carried out by Miezcnik *et al* [184] using the R-matrix method. They managed to successfully reproduce the shape of the 3p-3d resonance but not the other structure present. Ivanov and West [185] used the spin-polarized version of the RPAE method to corroborate previous identifications of the main one-electron transitions [77, 184]. However, they were unable to account for two-electron excitations which appeared prominently in the spectrum. Hibbert and Hansen [186] carried out a large-scale *ab initio* CI calculation using the *R*-matrix method and succeeded in identifying most of the structure observed in Ca II ions.

Although the first 5p-photoabsorption spectrum of Ba II was recorded over 30 years ago by Roig *et al* [187] much of the structure remains unidentified. Absolute photoionization cross section measurements were made by Lyon *et al* [188] in 1987 and some identifications were possible by comparing the limits of series observed

in [178] for the neutral atom. A similar predicament is noted for singly ionized strontium.

As discussed above, several studies of Sr I have led to significantly improved agreement between theory and experiment [36, 189, 190], but only a small number of studies have been made on Sr II: electron impact ionization [182, 191, 192] studies, 3d - photoabsorption spectra of Sr I-IV by McGuinness *et al* [113] and photoion-yield spectra from the 3d-excited states of Sr II by Itoh *et al* [193]. Employing a multiconfiguration Dirac-Fock calculation, Itoh *et al* deduced that the numerous discrete lines observed in the spectra were due to strong 5s-4d mixing: After the 3d-hole creation, the 4d-wavefunction collapses and strong mixing occurs due to the now close proximity of the 4d and 5s orbitals. Mansfield and Newsom [36] photographed the Sr I spectrum and proposed eighteen series limits which were also observed by White *et al* [192] as ejected-electron lines, thus providing tentative assignments of 18 Sr II levels. Lyon *et al* [116] employed the merged beam technique to measure absolute photoionization cross sections of Sr II. Using the results of the previous studies just mentioned, they also compared their measurements with the results of Hansen [176] who employed Hartree-Fock (HF) and MCHF calculations. Hansen positioned the main resonance ($4p^5 4d\ ^1P)5s\ ^2P$ at 27.13 eV (HF), and 26.77 eV (MCHF) and Lyon measured a doublet positioned at 26.950 eV and 26.972 eV, in good agreement with Hansen's prediction. The cross section was dominated by a large number of autoionizing resonances which they did not assign to any specific configurations and associated terms.

In this study, the 4p-photoabsorption spectrum of Sr II has been measured in the photon energy range 26.0 - 37.4 eV. Over 60 new lines have been identified and ordered into Rydberg series converging onto seven limits with the aid of a MCHF calculation in the *jj* coupling scheme.

5.2 Experiment

The strontium spectra were recorded electronically using the dual laser plasma (DLP) technique as presented in Chapter 2. The strontium plasma was created by focusing a 410 mJ, 15 ns Nd:YAG laser pulse onto a strontium target to a line of length 4mm, while a second Nd:YAG laser pulse (~ 0.58 J in 15 ns) was tightly focussed ($\sim$60 μm spot diameter) onto a tungsten target to serve as the backlighting continuum emitting plasma. The spectra were calibrated against known emission lines of aluminium, manganese and oxygen. In this experiment the optimum parameters to isolate Sr II were Δt=500 ns and Δx=1 mm.

5.3 Discussion of results

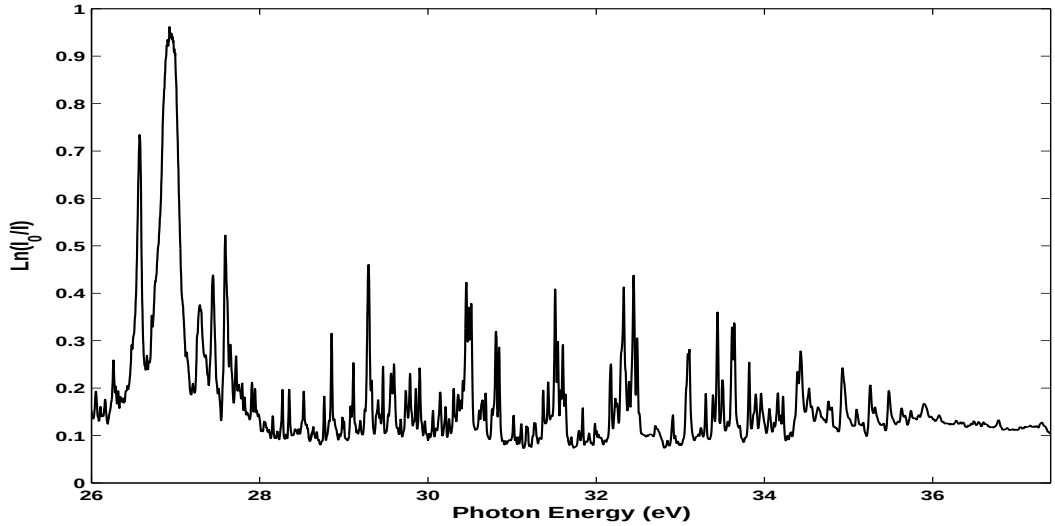

Figure 5.1: The 4p-innershell photoabsorption spectrum of Sr II recorded 1mm from the target surface and 500 ns after plasma generation.

The Sr II 4p-subshell spectrum is presented in Fig. 5.1. Using the Cowan suite of codes [29, 30], we performed multi-configuration interaction calculations for the following transitions:

$$
\begin{aligned}
4\mathrm{p}^6 5\mathrm{s} \quad &\rightarrow 4p^5 5\mathrm{s}n\mathrm{d} && (4 \le n \le 15)\\
&\rightarrow 4\mathrm{p}^5 5\mathrm{s}m\mathrm{s} && (5 \le m \le 13)\\
&\rightarrow 4\mathrm{p}^5 4\mathrm{d}n\mathrm{s} && (5 \le n \le 10)\\
&\rightarrow 4\mathrm{p}^5 4\mathrm{d}m\mathrm{d} && (4 \le m \le 10)\\
&\rightarrow 4\mathrm{p}^5 5\mathrm{p}^2 &&\\
4\mathrm{p}^6 4\mathrm{d} \quad &\rightarrow 4\mathrm{p}^5(5\mathrm{s}+4\mathrm{d})n\mathrm{s} && (5 \le n \le 10)\\
&\rightarrow 4\mathrm{p}^5(5\mathrm{s}+4\mathrm{d})m\mathrm{d} && (4 \le m \le 10)\\
&\rightarrow 4\mathrm{p}^5 5\mathrm{p}^2 &&
\end{aligned}
$$

The Slater-Condon parameters were reduced to optimize the theoretically calculated transitions with experiment as follows: *R*-integrals by 15%, *F*-integrals between equivalent electrons by 15% and by 10% for non-equivalent electrons. The *G*-integrals were reduced by 22% and the ζ-integrals were left unchanged. Reductions in the range 5-25% are required to allow for configuration-interaction effects not included explicitly in the calculation [30] (as discussed in Chapter 1). The above reductions in this case provided the best estimate of the energy separations observed in the spectrum. A separate minimization calculation for the ($4p^5 4d\ ^1P$)5s configuration was not needed for Sr II although it was necessary for Ca I,

II [171, 184] and Sr I [36]. We suggest that this is probably due to the greater extent of 4d-wavefunction collapse. As a result, strong configuration mixing between the $4p^5 5s nd$, *m*s and $4p^5 4d nd$, *m*s levels is expected. Fig. 5.2(a) displays the results of the 4p-excited calculations of the $4p^6 5s \rightarrow 4p^5 5s nl$ transitions only. A different intensity distribution is apparent and fewer transitions are noted, providing further validation for the inclusion of configuration interaction with the $4p^5 4d nd$, *m*s levels.

The *jj*-coupling scheme was favoured over the $[J_c]$K and LS coupling schemes as it gave the best overall fit to the experimental results. Although *LS*, *jj* and $[J_c]K$ percentage purities were comparable (36.0%, 46.0% and 30.3% respectively) neither scheme properly predicted ordered Rydberg series thus the labeling assigned in the tables is based on the quantum defect values and estimated Rydberg series limits.

Hansen [176] found that the $p^5 ds \leftrightarrow p^5 p'^2$ interaction plays an important role in $p^5 ds$ configurations in Sr II through configuration interaction. The $p^5 ds \leftrightarrow p^5 p'^2$ interaction is largest in the $(^1P)^2P$ state. Hansen explained that, due to the expansion of the d orbital in the $(^1P)^2P$ state, considerable overlap between the d, s and p' orbitals occurs; in effect the radial interaction integral is a factor of two larger for $(^1P)^2P$ than for $(^3P)^2P$. The $p^5 ds \leftrightarrow p^5 s^2$ interaction was also found to be important for the $(4p^5 4d\ ^3P)5s\ ^2P$ state due to the near coincidence between it and the $4p^5 5s^2\ ^2P$ level. Figure 5.2 displays the results of multi-configuration Hartree Fock calculations with and without the $5p^2$ and $4d^2$ configurations. One can see the effect of including the $4p^5 5p^2$ configuration, with a better energy observed for the large resonance ($(4p^5 4d\ ^1P)5s\ ^2P$ levels) positioned $\sim$ 27 eV. The inclusion of the $4p^5 4d^2$ configuration correctly predicts the strong lines observed on either side of the dominant resonance.

The first excited states of Sr II, $4p^6 4d\ ^2D_{3/2,5/2}$, lie a mere 1.805 eV and 1.840 eV respectively, above the ground state. Thus, metastable contributions to the overall photoabsorption spectrum are an unwanted but inevitable occurrence. From the collisional radiative (CR) model of Colombant and Tonon [104], one can deduce the electron temperature T_e in the plasma using the equation for irradiation at a laser wavelength λ (1.064 μm):

$$T_e = 5.2 \times 10^{-6} Z^{1/5} (\lambda^2 \phi)^{3/5} \tag{5.1}$$

where *Z* is the atomic number, ϕ is the mean laser power density. From this model, $T_e \sim$ 1.5 eV in our experiment. Assuming a simple Boltzmann distribution, this equates to $\sim$ 30% population distribution in the first two excited states given above. Separate calculations were performed to isolate the metastable regions in the spectrum from ground state absorption to assist in the identification of transitions.

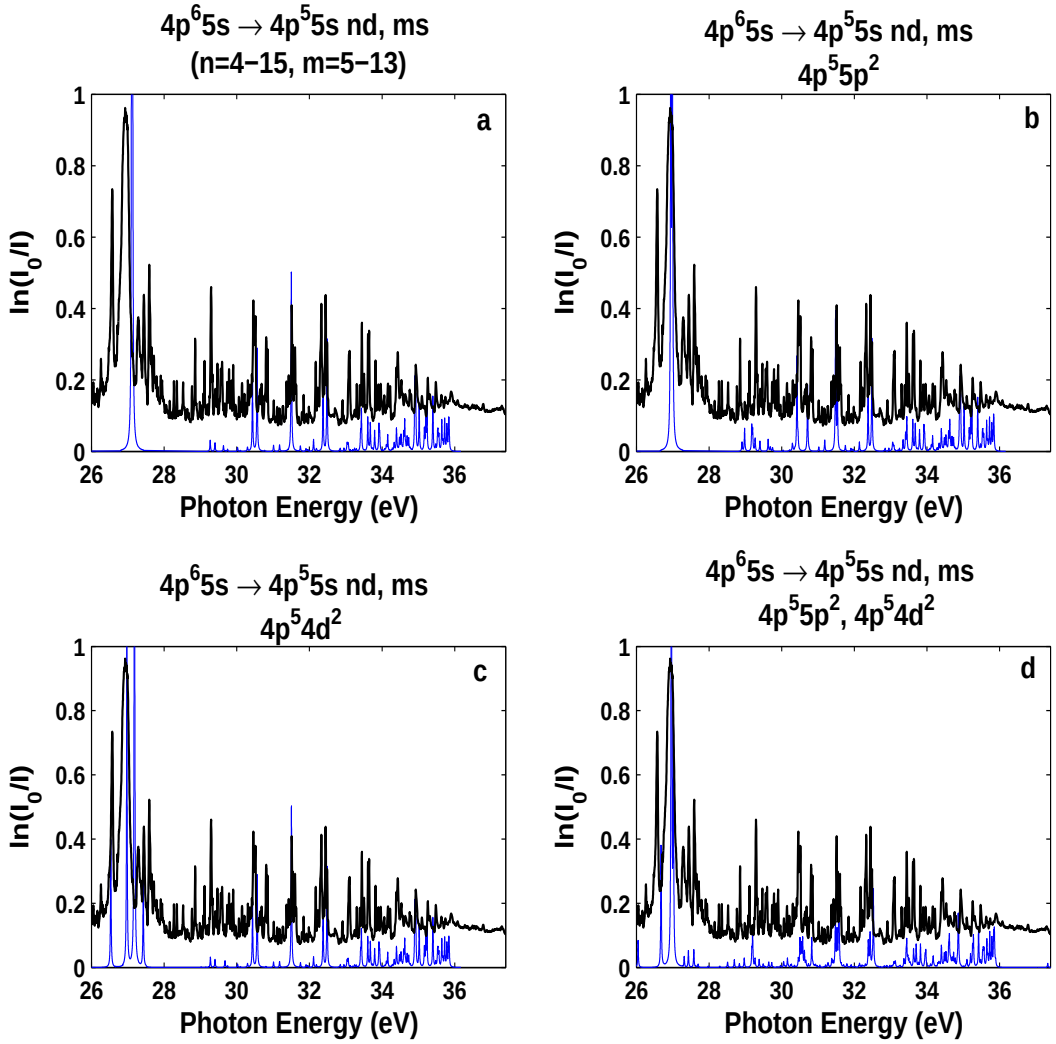

Figure 5.2: Photoabsorption spectrum of Sr II (black) with the separately calculated spectra to show the effect of the $5p^2$ and $4d^2$ configurations on the p^5ds levels. **(a)** Transitions to the $4p^55s$ *n*d, *m*s levels without configuration interaction. The predicted energy for the main resonance is slightly higher than observed. **(b)** The same as (a) including the $4p^55p^2$ configuration. The main resonance has shifted down to lower energy, matching the experimental value well. Notice a redistribution of oscillator strength also, a reduction can be seen around 30-32 eV and some new peaks are observed around 29 eV which can be attributed to the $5p^2$ configuration. **(c)** The same as (a) including the $4p^54d^2$ configuration, the appearance of peaks to the left and right of the main resonance confirm their identification as belonging to this configuration. **(d)** The full calculation performed which gives good overall agreement with the observed photoabsorption spectrum (metastable contribution is not included but can account for the other peaks). All lines in the theoretical plot have been fitted with a Lorentzian width of 0.02 eV to match the experimental instrument broadening.

Fig. 5.3 displays the results. Calculations were performed from the ground state ($4p^6 5s$) and metastable states ($4p^6 4d$) separately for transitions involving the upper state levels listed at the start of this section. This was for ease of comparision between the calculated and observed spectrum and a calculation performed to the listed upper states from both the ground and $4p^6 4d$ metastable state was found to have little effect on the energy positions. The series limits proposed were obtained by a least squares fit to the respective quantum defects.

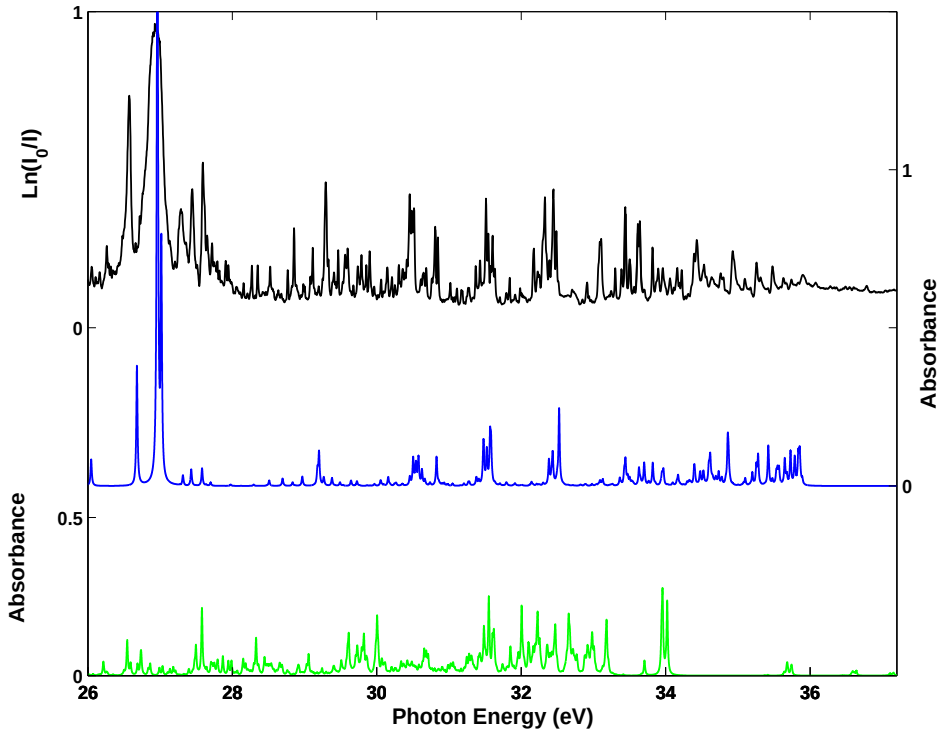

Figure 5.3: Photoabsorption spectrum of Sr II (top) with the separately calculated ground state absorption (middle) and metastable spectrum from the $4p^6 4d$ $^2D_{3/2,5/2}$ states (bottom). All lines in the theoretical plot have been fitted with a Lorentzian width of 0.02 eV to match the experimental spectrum.

When trying to match experimental peaks to the computed levels, *jj* coupling managed to predict the energy values for the higher members of certain Rydberg series well and gave purities greater than 65% for some of the levels. However for some of the early series members, *LS* coupling proved more reliable, see Table 5.1. In particular, the energy levels calculated for the $4p^5 4d5s$ configuration are shown with the *jj* and *LS* labels. Through comparisons with the experimentally observed energy levels by Lyon *et al* [116] and Mansfield and Newsom [36], the *LS* coupling labeling is most accurate for this configuration. It was therefore optimal to use the *LS* coupling nomenclature and energy predictions for the first member of the Ryd-

berg series and follow the *jj* coupling results for the higher members. It should be noted that in some cases *LS* coupling provided a better match with experiment and was used for all members of the series in those cases. Throughout the chapter we have chosen to use *LS* labeling for ease of comparison between this work and the previous work on Sr II described above. It proved useful to compare our photoabsorption spectrum with the absolute photoionization cross section measurements of Lyon *et al* [116] as their results are not contaminated with metastable structure. Care was taken to select only those peaks in our spectrum that corresponded to those observed in the cross section measurements.

Table 5.1: A comparison between computed energy level values and the corresponding labels for the terms of the $4p^5 4d\ 5s$ configuration in both *LS* and *jj* coupling

jj coupling *LS* Designation	Energy (eV)	*LS* coupling *LS* Designation	Energy (eV)	Lyon (eV)	Mansfield (eV)
$(^3P)^4P_{1/2}$	21.137	$(^3P)^4P_{1/2}$	21.137		21.224
$(^3P)^4P_{3/2}$	21.275	$(^3P)^4P_{3/2}$	21.275	21.37	21.363
$(^1P)^2P_{1/2}$	21.702	$(^3P)^2P_{1/2}$	21.702	21.81	21.804
$(^3D)^4D_{3/2}$	21.820	$(^3P)^2P_{3/2}$	21.820	21.915	21.914
$(^1D)^2D_{3/2}$	22.466	$(^3F)^4F_{3/2}$	22.466		
$(^3P)^2P_{1/2}$	23.690	$(^3D)^4D_{1/2}$	23.691		
$(^3P)^2P_{3/2}$	23.694	$(^3D)^4D_{3/2}$	23.694		
$(^3P)^2P_{1/2}$	23.836	$(^1D)^2D_{3/2}$	23.836		
$(^3D)^2D_{3/2}$	24.860	$(^3D)^2D_{3/2}$	24.860		
$(^1P)^2P_{3/2}$	26.962	$(^1P)^2P_{3/2}$	26.962	26.972	
$(^3D)^4D_{1/2}$	27.017	$(^1P)^2P_{1/2}$	27.017	26.95	

The first column displays the *jj* coupling transition assignments but in *LS* designation for ease of comparison with the *LS* coupling results. In *LS* coupling, one can see better designation agreement with previous results [116, 36].

Five series limits can be obtained from previous experimental work on Sr III [16, 194, 195, 196]. Persson and Valind [194] studied the emission spectrum of doubly ionized strontium from a sliding spark discharge and observed the $4p^5 5s\ ^1P_1$, $4p^5 5s\ ^3P_1$, $4p^5 4d\ ^3P_1$, $4p^5 4d\ ^3D_1$ and $4p^5 4d\ ^1P_1$ resonance lines. Reader *et al* [195] studied the resonance-line spectrum from the $4p^6\ ^1S_0$ ground state to the $4p^5 4d$ and $4p^5 5s$ configurations in Rb II through to Mo II using a sliding spark discharge also. The 4p photoabsorption spectrum of Sr III was recorded by Kilbane *et al* [16] which gives a value for the $4p^5 5s\ ^1P_1$ limit and the $4p^5 4d\ ^1P_1$ limit. Hansen [176] computed the $4p^5 4d\ ^1P_1$, $^3P_1$ limits and the $4p^5 5s$ average energy configuration using a least squares fit to the data obtained by Persson. The fitted parameter values were then compared to Hartree-Fock results which were found to be in good agreement. Table 5.2 displays the observed series limits in this work and compares them to previous results.

Table 5.2: Experimental and calculated series limits for the 4p-subshell of Sr II

Series Limit	No.	Banahan (eV)	Persson (eV)	Reader (eV)	Kilbane (eV)	Hansen[♮] (eV)
$4p^5 5s\ ^1P_1$	1	36.24	36.24	36.24	36.24	35.135
$4p^5 5s\ ^3P_1$	2	35.13	35.13	35.13		
$4p^5 5s\ ^3P_2$	3	35.03				
$4p^5 5s\ ^3P_0$	4	35.94				
$4p^5 4d\ ^3D_1$	5	35.48	35.48	35.48		
$4p^5 4d\ ^1P_1$	6	39.38	39.39	39.39	39.38	39.409
$4p^5 4d\ ^3P_1$	7	33.06	33.06	33.06		32.401

[♮] Calculated values, the remainder have been observed experimentally

5.3.1 The $4p^5 5s\ nd$, ms series

The 4p inner-shell excitation spectrum of Sr II involves four doubly-ionized states $4p^5 5s\ ^3P_{2,1,0},^1P_1$ which serve as series limits. In this study, we report on eight $4p^5 5snd$, ms series converging onto four series limits. Well developed Rydberg series are observed to the singlet based $4p^5 5s\ ^1P_1$ limit, whereas series converging to the $^3P_{2,1,0}$ limits are weak, except for the first few members. The $4p^5 5snd$ series members are stronger than the transitions to the $4p^5 5sms$ levels. A similar observation was made for the 4p-excitation of Rb I [197]. All the $4p^5 5snd$, ms levels have well defined and consistent quantum defect numbers. The quantum defects for the nd and ms series are 1.55 and 3.20 respectively, which compare well with those of Rb I, 1.70 and 3.30 [197].

One of the strongest series observed in the 4p photoabsorption spectrum was the $(4p^5 5s\ ^1P)nd\ ^2P$ series. The series was formed using levels calculated under the *LS* coupling scheme, the main reason being that it provided well-matched values to experimental peaks which in turn produced a regular quantum defect. The previously published limit for the $4p^5 5s\ ^1P$ level at 36.24 eV [16, 182] was used in this work as it provided the best fit with experiment as did the $4p^5 5s\ ^3P$ level at 35.13 eV observed by Persson and Valind [194] and Reader [195].

The $(4p^5 5s\ ^1P)ns\ ^2P_{1/2}$ Rydberg series are much weaker than their nd counterparts. The *jj* coupling scheme was favoured for these levels; the calculated $(4p^5 5s\ ^1P)ns\ ^2P_{1/2}$ levels have high purity for $n > 8$ in *jj* coupling and the energy level predictions matched better. The $4p^5 5s^2$ level had the same calculated energy and mixing in both *LS* and *jj* coupling. The $4p^5 5s^2$ level $^2P_{1/2}$ had 76% purity (configuration interaction from the $4d^2$ level being the most significant). Fig. 5.4 shows the $5snd$, ms Rydberg series converging on the $4p^5 5s\ ^1P_1$ and $^3P_1$ limits.

Fitting a limit to the $(4p^5 5s\ ^3P)nd\ ^4P_{1/2}$ and $^2D_{3/2}$ series gave a new value for

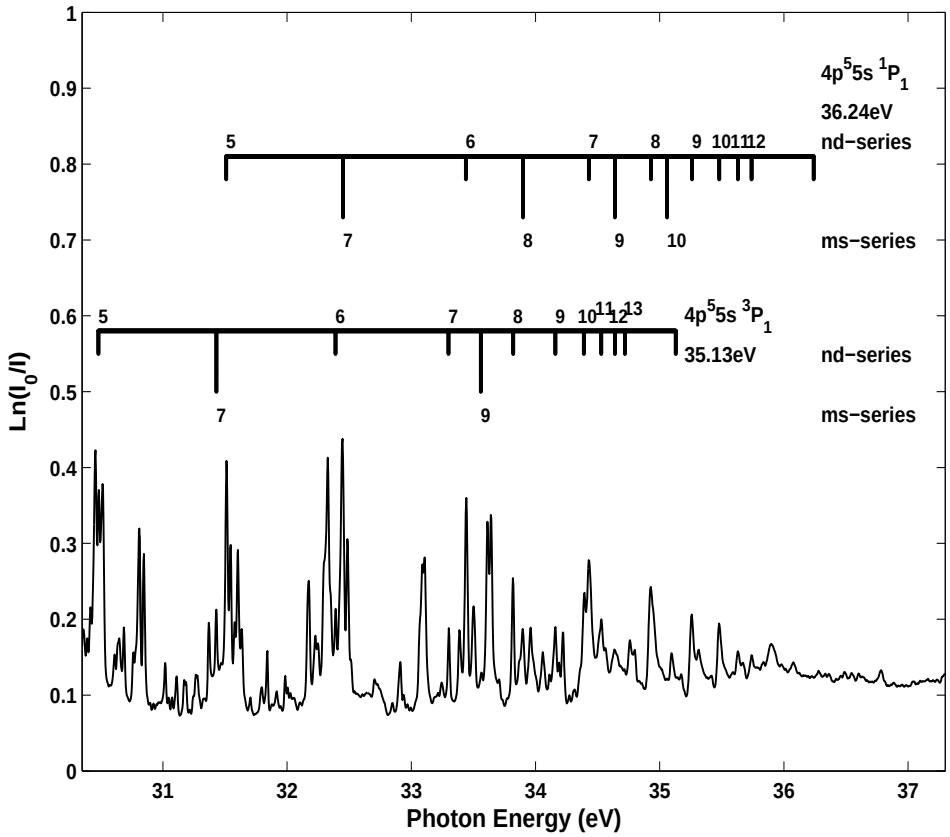

Figure 5.4: Photoabsorption spectrum of Sr II from 30.35 eV to 36.30 eV with the (4p^{5}5s ^1P)*n*d, *m*s ^{2}P series converging on the 4p^{5}5s $^1P_1$ and 4p^{5}5s $^3P_1$ core at 36.24 eV and 35.13 eV respectively.

the 4p^{5}5s $^3P_2$ level of Sr^{2+} of 35.03 eV. Our data for the (4p^{5}5s ^3P)*n*d $^4P_{3/2}$, $^4F_{3/2}$ series fitted well with the known 4p^{5}5s $^3P_1$ level at 35.13 eV [194, 195]. Peaks from these series were weak with some peaks obscured in the dense bunching of resonances. Although the energy of the (4p^{5}5s ^3P)4d ^4P level was predicted accurately in both *LS* and *jj* coupling (see table 5.1), the former gave over 90% purity. For the higher $^4P_{3/2}$ members ($n \geq 7$), *LS* coupling best labeled the levels given in Table 5.3 as $(^1P)^2D$. In *jj* coupling, the same calculated energies were labeled as $(^3P)^4P$ states with a higher degree of purity so this coupling scheme was favoured for the higher members.

5.3.2 Doubly-excited series - $4p^5 4d\,nd$, ms

Three series limits for the doubly-excited transitions can be obtained from previous work on Sr III, see Table 5.2. The first member of the $(4p^5 4d\ ^1P)ms\ ^2P_{3/2}$ Rydberg series is the large resonance positioned at ∼27 eV, see Fig. 5.1. Lyon *et al* [116] could resolve this resonance as the $(4p^5 4d\ ^1P)5s\ ^2P_{3/2,1/2}$ doublet located at 26.95 eV and 26.972 eV respectively. The higher members of the $(4p^5 4d\ ^1P)ms\ ^2P_{3/2}$ series are calculated to lie at a higher photon energy range ($>$ 35.5 eV) and so we could only observe up to the $4p^5 4d7s$ member. A large degree of mixing is predicted in *jj* coupling for this series particularly with the $(^3D)^4P$ Rydberg series as can be seen in Table 5.5. Two series were observed to converge on the $4p^5 4d\ ^3D_1$ limit at 35.48 eV [194, 198]. Both the $(4p^5 4d\ ^3D_1)\ nd$, ms series lie close together. Two peaks in the photoabsorption spectra (33.82 eV and 34.57 eV) have thus been assigned to members in both these series as we cannot select one series over another. The effective quantum defect numbers (n^*) for these doubly-excited series are not as consistent as was the case in the previous section and so the designated labeling is tentative.

The *ns* levels converging on the $4p^5 4d\ ^3P_1$ limit at 33.06 eV were determined by comparisons with the results of Lyon *et al* [116]. As certain peaks present in our photoabsorption spectra were still unassigned and they corresponded to peaks present in the absolute cross section spectrum, this *ns* Rydberg series was chosen in order to produce a quantum defect similar to the other *ns* series. Neither coupling scheme uniquely identified this series and so it is tentatively assigned using the previously observed limit [198, 182].

The large peak at 26.57 eV on the lower energy side of the $(4p^5 4d\ ^1P)5s\ ^2P$ doublet belongs to the $4p^5 4d^2$ configuration and the three strong peaks (27.29 eV, 27.44 eV and 27.59 eV respectively) to the higher energy side also belong to this configuration. Similar to the case for the $4p^5 4d5s$ configuration, there was little correlation between the labeling in *LS* and *jj* coupling with one or two exceptions. We therefore propose tentative labels (see Table 5.6) for these levels based on the following analysis. Three strong resonances are predicted at 27.31 eV, 27.43 eV and 27.58 eV and the $4p^5 4d^2\ (^3P)^2P_{1/2}$ level is predicted in both coupling procedures to lie at 27.31 eV. The next predicted peak at 27.43 eV is labelled as the $4p^5 4d^2\ (^3P)^2P_{3/2}$ in *LS* coupling and $4p^5 4d^2\ (^1S)^2P_{3/2}$ in *jj* coupling. As the calculated results for the $4p^5 4d5s$ configuration (see Table. 5.1) showed, *LS* coupling predicts the doublet components of this configuration accurately, whereas under the *jj* coupling scheme, several doublets are predicted with 2 or 3 eV between either component. We thus assume, analogous to that case, *LS* coupling is most appropriate for the $4p^5 4d^2\ (^3P)$ term here. The predicted peak at 27.58 eV is labelled as $(^3F)^2D_{3/2}$ in *LS*

coupling. In *jj* coupling this same peak is assigned to the $(^1D)^2P_{3/2}$ term, but this was deemed unlikely as it also gave a peak at 23.98 eV with this same label. This was further validated in *LS* coupling with the 23.98 eV peak also coming out as $(^1D)^2P_{3/2}$. The peak located at 29.29 eV is tentatively assigned to the $4p^5 5p^2$ configuration as both coupling schemes predict a strong transition from the ground state to this configuration at 29.20 eV. We do not assign a label to it as there is no clear argument to choose one coupling scheme over the other in this case.

5.4 Conclusion

In this work, we have recorded the 4p-photoabsorption spectrum of Sr II and have identified single and double excitations involving the 4d and 5s subshells. We have identified two new levels in Sr III and over 60 new transitions have been identified and ordered into 12 Rydberg series converging onto seven different series limits, eight due to 4p innershell excitation and four resulting from double excitations. Due to the significant overlap between the 4d and 5s orbital, strong configuration interaction is present with a high degree of mixing predicted between series making the assignment of levels difficult. With the aid of HF calculations in both *LS* and *jj* coupling we have made tentative assignments to the Rydberg series. This work has been accepted for publication in *Physical Review A*.

Table 5.3: Observed and calculated energies for the $4p^6 5s \rightarrow 4p^5 5s\ nd$, ms transitions of Sr II.

Level	E_{exp} (eV)	E_{calc} (eV)	gf	n*	$jj^{\dagger}$ / $LS^{\S}$ Coupling
			$4p^5 5s\ (^1P_1)\ nd\ ^2P_{1/2}$ series to limit (1) 36.24 eV		
5d	31.51	31.58	0.2330	3.39	§23.4% 5s5d (^1P) - 17.8% 4d9s (^3P)
6d	33.44	33.43	0.0669	4.41	§22.3% 5s6d (^1P) - 17.0% 5s8d (^3P)
7d	34.43	34.62	0.1385	5.48	§14.1% 5s7d (^1P) - 12.6% 4d10s (^3D)
8d	34.93	34.87	0.1481	6.45	§29.5% 5s8d (^1P) + 24.4% 4d6s (^1P)
9d	35.26	35.25	0.1192	7.45	§17.0% 5s9d (^1P) - 13.0% 4d6s (^1P)
10d	35.48	35.42	0.0940	8.46	§29.1% 5s10d (^1P) + 21.3% 5s10d (^3P)^4D
11d	35.63	35.55	0.0846	9.44	§32.1% 5s11d (^1P) + 22.8% 5s11d (^3P)^4D
12d	35.74	35.65	0.0669	10.43	§33.3% 5s12d (^1P) + 24.1% 5s12d (^3P)^4D
13d	35.83	35.73	0.0566	11.52	§24.7% 5s13d (^1P) - 10.9% 5s13d (^3P)^2D
14d	35.89	35.79	0.0530	12.47	§29.5% 5s14d (^1P) + 21.6% 5s14d (^3P)^4D
			$4p^5 5s\ (^1P_1)\ ns\ ^2P_{1/2}$ series to limit (1) 36.24 eV		
5s	23.46♮	23.42	0.1686	2.06	†76.6% (^1P) - 4.8% 4d^2 (^1S)
6s	29.33	30.27	0.0074	2.81	†33.3% 5s6s (^1P) - 11.4% 4d5d (^3D) ^4D
7s	32.45	32.88	0.0014	3.79	†44.8% 5s7s (^1P) + 14.9% 4d6d (^3P) ^2P
8s	33.90	33.97	0.0122	4.82	†78.6% 5s8s (^1P) + 3.0% 5s9d (^3P) ^4D
9s	34.64	34.57	0.0028	5.83	†81.9% 5s9s (^1P) + 4.3% 4d10d (^3D) ^2S
10s	35.06	34.94	0.0019	6.79	†94.1% 5s10s (^1P)
			$4p^5 5s\ (^3P_1)\ nd\ ^4F_{3/2}$ series to limit (2) 35.13 eV		
5d	30.48	30.58	0.1724	3.42	†19.1% 5s5d (^3P) + 7.2% 4d5d (^3F)^4P
6d	32.39	32.52	0.4802	4.45	†29.5% 5s6d (^3P) + 10.6% 5s6d (^3P)^4D
7d	33.30	33.24	0.0062	5.44	†32.3% 5s7d (^3P) - 17.9% 4d7d ($^3F\ ^4F$)
8d	33.82	33.82	0.1420	6.42	†54.3% 5s8d (^3P) - 11.6% 5s9d (^3P)^4D
9d	34.16	34.10	0.0043	7.45	†44.6% 5s9d (^3P) - 15.4% 5s7d (^1P)^2P
10d	34.39	34.30	0.0186	8.52	†41.7% 5s10d (^3P) - 26.6% 5s7d (^3P)^2P
11d	34.53	34.60	0.0935	9.45	†44.8% 5s11d (^3P) - 15.4% 5s13d (^1P)^2P
12d	34.64	34.65	0.0134	10.44	†37.2% 5s12d (^3P) + 28.5% 5s15d (^1P)^2P
13d	34.72	34.73	0.0806	11.39	†57.5% 5s13d (^3P) - 18.1% 5s14d (^3P)^2P
			$4p^5 5s\ (^3P_1)\ nd\ ^4P_{3/2}$ series to limit (2) 35.13 eV		
4d	21.37♮	21.27	0.0015	1.99	§92.9% 5s4d (^3P)
5d	30.42	30.18	0.0084	3.40	†25.3% 5s5d (^3P) - 11.4% 4d6s (^3D)^4D
6d	obscured	32.32	0.0006		†18.0% 5s6d (^3P) - 15.4% 5s6d (^1P)^2P
7d	33.25	33.26	0.0100	5.37	†25.0% 5s7d (^3P) - 21.2% 5s6d (^3P)^4D
8d	obscured	33.77	0.0001		†72.7% 5s8d (^3P) - 13.1% 5s8d (^1P)^2P
9d	obscured	34.09	0.0046		†49.0% 5s9d (^3P) + 20.5% 5s8s (^3D)^4D
			$4p^5 5s\ (^3P_2)\ nd\ ^2P_{1/2}$ series to limit (3) 35.03 eV		
4d	21.81♮	21.70	0.0077	2.03	§87.9% 5s4d (^3P) + 3.4% 5s^2 (^2P)^2P
5d	30.39	30.50	0.1691	3.42	§28.3% 5s5d (^3P)^4D + 15.7% 4d6d (^3P)^2P
6d	32.25			4.42	
7d	33.19	33.13	0.0347	5.44	§51.4% 5s7d (^3P) - 10.1% 5s6d (^3P)^4D
8d	33.72	33.70	0.1070	6.44	§33.2% 5s8d (^3P) - 9.5% 4d7d (^3D)^4D
9d	34.06	33.97	0.0625	7.48	§51.9% 5s9d (^3P) - 8.6% 5s9d (^3P)^4D
10d	34.27	34.15	0.0199	8.45	§59.5% 5s10d (^3P) - 11.4% 5s10d (^3P)^4D

♮ Values taken from Lyon *et al* [116].

Table 5.4: Observed and calculated energies for the $4p^6 5s \rightarrow 4p^5 5s\ nd$ transitions of Sr II cont.

Level	E_{exp} (eV)	E_{calc} (eV)	*gf*	n*	*jj*† / *LS*§ Coupling
			$4p^5 5s\ (^3P_2)\ nd\ ^2D_{3/2}$ series to limit (3) 35.03 eV		
5d	31.55	31.57	0.1820	3.44	†13.8% 5s5d $(^3P)^2P$ - 10.5% 4d7d $(^3P)^4D$
6d	33.39	33.36	0.0458	4.44	†62.1% 5s6d (^3P) + 3.2% 5s8d $(^3P)^2P$
7d	34.32	34.30	0.0060	5.44	†39.2% 5s7d (^3P) + 30.2% 5s7d $(^3P)^4P$
8d	34.86	34.83	0.0240	6.48	†81.4% 5s8d (^3P) - 5.1% 4d10d $(^3D)^2D$
9d	35.18	35.16	0.0040	7.47	†92.0% 5s9d (^3P)
10d	obscured	35.37	0.0045		†95.5% 5s10d (^3P)
			$4p^5 5s\ (^3P_2)\ nd\ ^4P_{1/2}$ series to limit (3) 35.03 eV		
4d	21.22[♭]	21.13	0.003	1.99	§96.4% 5s4d (^3P)
5d	30.42	29.87	0.0044	3.43	§27.6% 5s5d $(^3P)^2P$ + 22.7% 5s5d $(^3P)^4P$
6d	32.25	32.30	0.0156	4.42	†30.2% 5s6d (^3P) + 13.6% 4d9d $(^3P)^4D$
7d	33.22	33.23	0.0032	5.47	†69.4% 5s7d (^3P) + 8.3% 4d9d $(^3D)^4P$
8d	33.73	33.76	0.0073	6.45	†81.5% 5s8d (^3P) - 2.7% 4d7d $(^3P)^2P$
9d	34.06	34.09	0.0007	7.46	†49.6% 5s9d (^3P) - 21.2% 4d8d $(^3F)^2P$
10d	34.28	34.31	0.0001	8.47	†93.7% 5s10d (^3P)
			$4p^5 5s\ (^3P_0)\ nd\ ^4F_{3/2}$ series to limit (4) 35.94 eV		
5d	31.34	31.05	0.0138	3.44	§32.8% 5s5d (^3P) + 20.6% 5s5d $(^1P)^2D$
6d	33.19	33.17	0.0023	4.45	§34.4% 5s6d (^3P) - 15.8% 4d10s $(^3F)^4F$
7d	34.11	34.17	0.0622	5.45	§24.3% 5s7d (^3P) - 9.7% 5s10d $(^3P)^2D$
9d	obscured	34.69	0.0380		§19.5% 5s8d (^3P) - 7.1% 5s14d $(^1P)^2P$
10d	obscured	35.00	0.0048		§31.1% 5s9d (^3P) + 16.2% 4d6s $(^1P)^2P$
11d	35.18	35.28	0.1838	8.45	§34.6% 5s10d (^3P) + 8.9% 5s10d $(^1P)^2D$

[♭] Value taken from Mansfield and Newsom [36].

Table 5.5: Observed and calculated energies for the $4p^6 5s \rightarrow 4p^5 4d\ n$d, ms transitions of Sr II.

Level	E_{exp} (eV)	E_{calc} (eV)	*gf*	n*	*jj*† / *LS*§ Coupling
		$4p^5 4d\ (^3D_1)\ m$s $^2D_{3/2}$ series to limit (5) 35.48 eV			
6s	31.60	30.90	0.0111	3.74	†-43.5% 4d6s (^3D) - 6.1% 4d6d (^3P)^2D
7s	33.11	32.64	0.0021	4.79	†38.0% 4d7s (^3D) - 12.0% 4d7s (^3D)^4D
8s	33.82	33.70	0.0131	5.72	†-19.4% 4d8s (^3D) - 13.1% 5s9s (^3P)^4P
9s	34.30	34.23	0.0015	6.78	†52.6% 4d9s (^3D) - 20.4% 5s7d (^3P)^2D
10s	34.57	34.62	0.0368	7.72	†23.6% 4d10s (^3D) - 15.8% 4d10d (^3F)^2P
		$4p^5 4d\ (^3D_1)\ n$d $^2D_{3/2}$ series to limit (5) 35.48 eV			
5d	31.63	31.27	0.0194	3.76	†-9.4% 4d5d (^3D) + 7.8% 5p^2 (^2D)^2D
6d	33.09	33.03	0.0044	4.77	†15.1% 4d6d (^1D)^2P + 9.6% 4d6d (^3D)^2D
7d	33.82	33.83	0.0002	5.72	†22.0% 4d7d (^3D) + 19.3% 4d7d (^1P)^2P
8d	34.27	34.34	0.0015	6.70	†21.0% 4d8d (^1P)^2P + 10.7% 4d8d (^3D)^2D
9d	34.57	34.66	0.0092	7.72	†28.1% 4d9d (^3D) - 25.6% 4d9d (^3F)^2D
10d	34.76	34.88	0.0097	8.68	†28.7% 4d10d (^3D) - 27.8% 4d10d (^3F)^2D
		$4p^5 4d\ ^1P_1\ m$s $^2P_{3/2}$ series to limit (6) 39.38 eV			
5s	26.972♮	27.02	1.4561	2.09	§67.1% 5s4d (^1P) + 12.0% 5s5d (^3P)^2P
6s	35.59			3.79	
7s	36.99	37.32	0.0081	4.77	†52.0% 4d7s (^3D)^4D - 42.0% 4d7s (^1P)^2P
8s	out of range	38.38	0.0017		†52.0% 4d8s (^3D)^4D + 42.2% 4d8s (^1P)^2P
		$4p^5 4d\ ^3P_1\ m$s $^2P_{1/2}$ series to limit (7) 33.06 eV			
6s	29.19	27.70	0.0209	3.75	§77.8% 4d6s (^3P) + 11.5$ 4d6s (^3P)^4P
7s	30.68	29.96	0.0120	4.78	§44.8% 4d7s (^3P) + 23.8% 4d7s (^3P)^4P
8s	31.43	30.98	0.0092	5.77	§64.7% 4d8s (^3P) + 18.6% 4d8s (^3P)^4P
9s	31.88	31.52	0.1012	6.79	§27.9% 4d9s (^3P) + 12.6% 4d9s (^3P)^4P

♮ Values taken from Lyon *et al* [116] as doublet could not be resolved in our experiment.

Table 5.6: Observed and calculated energies for the $4p^5 4d^2$ configuration, we propose the *LS* labelling for these peaks, see Section 5.3.2.

Level	E_{exp} (eV)	E_{calc} (eV)	*gf*	*LS*	*jj*
4d^2	26.57	26.67	0.7577	(^1S)$^2P_{1/2}$	(^3P)$^2D_{3/2}$
4d^2	27.29	27.31	0.0654	(^3P)$^2P_{3/2}$	(^3P)$^2P_{3/2}$
4d^2	27.45	27.43	0.1041	(^3P)$^2P_{1/2}$	(^1S)$^2P_{3/2}$
4d^2	27.59	27.58	0.1109	(^3F)$^2D_{3/2}$	(^1D)$^2P_{3/2}$
♮5p^2	29.29	29.20	0.2059	(^1D)$^2D_{1/2}$	(^3P)$^4P_{1/2}$

♮ The strong transition observed at 29.29 eV is tentatively assigned to the 5p^2 configuration as a strong transition is predicted in both coupling schemes at 29.20 eV.

Chapter 6

The 5d photoabsorption spectrum of Pb III and Bi IV

6.1 Introduction

Investigations of multiply-charged ions with a partially filled 5d-subshell are of interest owing to the complexity of the 5d spectra caused by the large electrostatic and spin-orbit interaction between the configurations, which leads to strong intermediate coupling. Previous studies have shown this to be the case in lead and bismuth too, [199, 200, 201, 202, 203, 204, 205, 206]. In this study we show that there is a marked difference in the appearance of the spectra of the two isoelectronic partners. These differences along isoelectronic sequences can provide useful insights into the changing nature of the salient electron-electron and electron-nuclear physical interactions as the core charge changes. In addition to the fundamental interest in the atomic structure of the Hg I like ions of lead (Pb III) and bismuth (Bi IV), the photoionization data from these studies also provided useful information, for example, in investigations of the electronic and magnetic properties of thin films [207, 208].

The first EUV absorption spectra of lead and bismuth were obtained almost 40 years ago by Jaeglé *et al* [199] by irradiating thin films with synchrotron radiation. Using windowless furnaces [209] Connerade and co-workers achieved higher precision for the 4f subshell spectrum of Pb I [210]. In 1930 Smith [200] recorded the first spectra of doubly and triply ionized lead. Further studies on lead and bismuth followed with the recording of the spectra of bismuth Bi V [201] and Pb IV [202]. These spectra were generated by discharges in vapour and were recorded in the visible and near UV region. Autoionized lines in atomic lead and bismuth were recorded in a similar manner by Assous [203]. Loch *et al* [211] studied electron im-

pact ionization of Bi^{q+}, q=1-10 and compared configuration-average distorted wave calculations to experimental results finding good agreement between both for all ion stages. Müller *et al* [212] employed crossed electron and ion beams to study single and double ionization of Bi I where they observed a crossing of the cross-sections for singly and doubly-charged Bi ions at electron energies over 200 eV.

The 5d spectra of lowly ionized lead ions have been studied in the recent past through the use of two different methods. The energies and decay times for some $5d^{10}nl$, $5d^96s^2$ and $5d^96s6p$ levels have been measured by Pinnington *et al* using the beam foil spectroscopy technique [204, 213, 214, 215]. Raassen *et al* [205] reported the first observation of many features due to inner shell excitations in the spectrum of Pb III. Here a small number of features in the emission spectrum of lead were found to be due to transitions from the autoionizing states $5d^96s^2nf$ and $5d^96s^2np$ to the ground state $5d^{10}6s^2\ {}^1S_0$ of Pb III.

In this work the photoabsorption spectra of lead and bismuth ions has been recorded using the dual laser plasma (DLP) technique [55]. Photoexcitation from the 5d subshell is the dominant process in the 30 - 66 eV photon energy range. The experimentally recorded lines have been identified with the aid of Hartree-Fock calculations [29, 30] as $5p^65d^{10}6s^2 \rightarrow 5p^65d^96s^2np$, mf ($6 \leq n \leq 11$), ($5 \leq m \leq 15$). The results presented here have been published in J. Phys. B [37].

6.2 Experiment

The dual-laser plasma technique (Chapter 2) was used to record the photoabsorption spectra of Pb III and Bi IV. The output from a 650 mJ, 15 ns Nd:YAG laser was tightly focussed using a cylindrical (f=30 cm) lens to produce a 3 mm absorbing (Pb or Bi) line plasma. A second time-delayed 650 mJ, 15 ns Nd:YAG laser pulse tightly focussed onto a tungsten target generated the backlighting continuum plasma. Spectra were recorded at a time delay of $\Delta\tau = 110$ ns for Pb III and $\Delta\tau = 210$ ns for Bi IV at a position $\Delta x = 1$ mm from the target surface. The spectra were calibrated against known emission lines of aluminium and magnesium with residues of less than 0.06 eV.

6.3 Results and Discussion

6.3.1 The 5d photoabsorption spectrum of Pb III

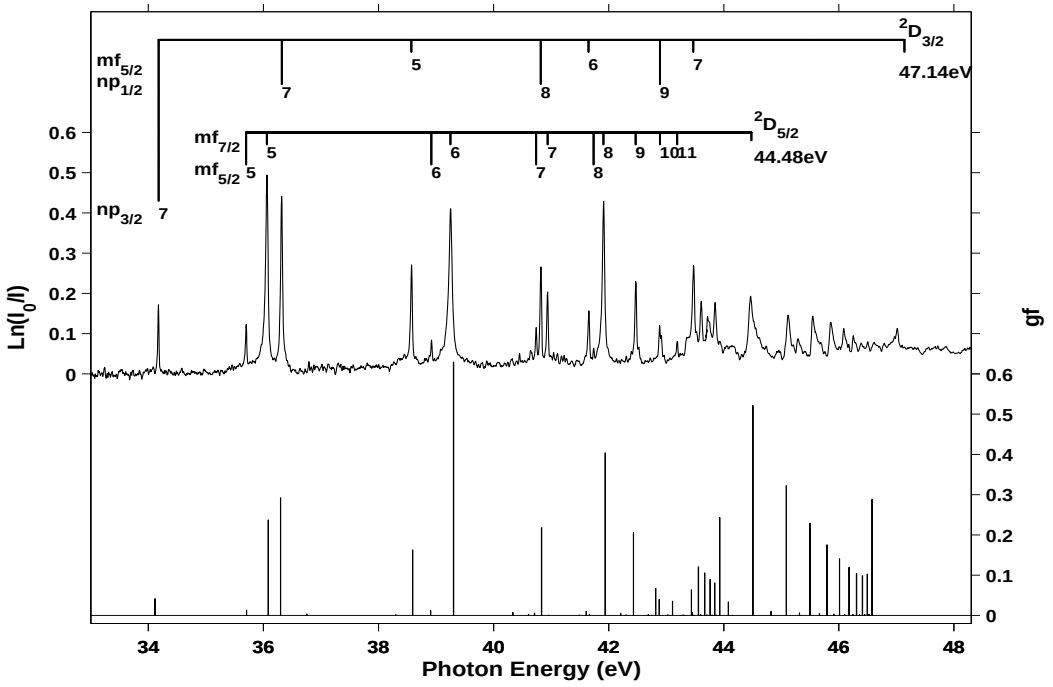

Figure 6.1: The observed (top) and calculated (bottom) 5d photoabsorption spectrum of Pb III. The calculated spectrum has been shifted by +0.3 eV to agree with the experimental data.

The lines recorded in the 5d absorption spectra of Pb III have been identified as due to the following transitions arrays:

$$\begin{aligned} 5d^{10}6s^2 &\rightarrow 5d^9 6s^2\, np \qquad (6 \leq n \leq 14) \\ 5d^{10}6s^2 &\rightarrow 5d^9 6s^2\, mf \qquad (5 \leq m \leq 15) \end{aligned} \tag{6.1}$$

In this experiment the 5d $\rightarrow$ 6p transition has not been observed as this occurs close to 21 eV and the instrument used has a lower photon energy limit of 23.5 eV. Configuration interaction calculations for these transitions were performed using the RCN / RCN2 and RCG Hartree-Fock suite of Cowan codes [29, 30] including the basis states $6 \leq n\text{p} \leq 19$ and $5 \leq m\text{f} \leq 17$ and the valence excitations $5d^{10}6snp$ *n* = 6-9. *Ab initio* values of the Slater parameters (F^k and G^k) and the configuration interaction parameter (R^k) were reduced by 15%; the spin-orbit parameter was left unchanged. The resulting intensities and energies are shown in Fig. 6.1. In this figure the calculated oscillator strength (*gf*-value) for the transitions is shown and

compared with the experimental spectrum.

It should be noted that the calculated oscillator strengths for the higher lying Rydberg members appear to be much greater than those with lower *n*. This artefact of the Cowan code has been commented on by Raassen *et al* [205]. The limitation of the number of $5d^9 6s nf$ configurations included in the calculation has the same consequences as the truncation of the $3s^2 3p^4 nd\ ^2S$ - $3s3p^6\ ^2S$ basis of Ar II [216] or the $3p^5 \epsilon d$ states in Ca III [217]. The largest calculated transition probability arises from the highest $5d^9 6s^2 nf$ configuration introduced in the basis set as it takes into account contributions from the neglected higher *n*'f members and even from the continuum. The inclusion of higher basis states results in a better agreement between experiment and theory, thus we included configurations up to 17f.

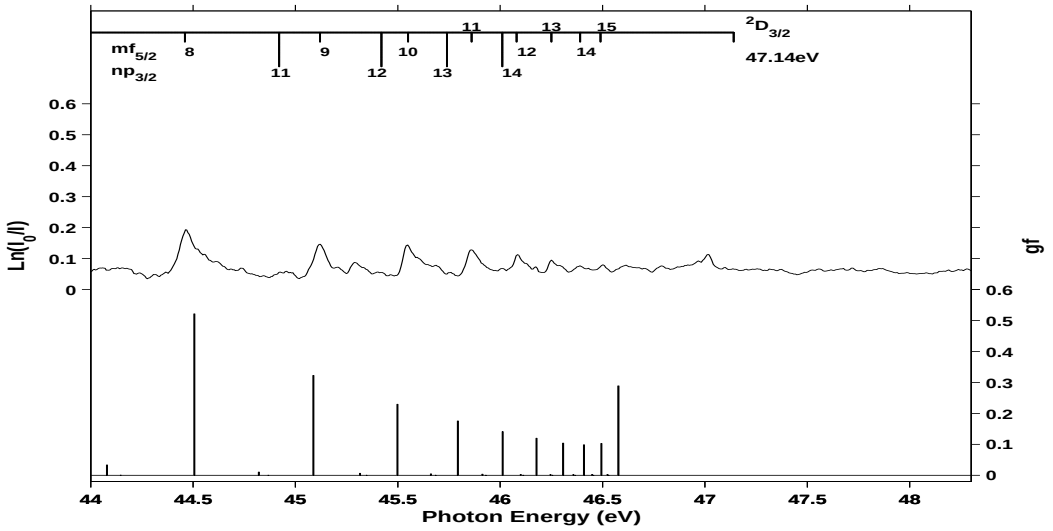

Figure 6.2: The observed (top) and calculated (bottom) 5d photoabsorption spectrum of Pb III for the higher *m*f, *n*p levels ending on the $^2D_{5/2}$ series limit. As before, the calculated spectrum has been shifted by +0.3 eV to agree with the experimental data.

The peaks in the experimental data are listed along with their identifications given in *jj* coupling in Table 6.3 and Table 6.4 at the end of this chapter. The *jj* coupling scheme was chosen over the *LS* and other coupling schemes as the percentage purity in each scheme was 89%, 73% and 65% for the *jj*, $[J_c]$ *K* and *LS* coupling schemes respectively. In contrast to the observed photoabsorption of Hg I [218], it can be seen that d $\rightarrow$ f transitions dominate over d $\rightarrow$ p transitions. This is explained by the increased core charge of the Pb III ion which results in a much greater radial overlap between the 5d and *n*f wavefunctions in this spectrum than is present in neutral mercury. The n_f^*[1] series compares well with those reported for the isoelectronic Hg I series [218, 219] while the n_p^* are slightly smaller.

[1]The effective quantum defect number for the d $\rightarrow$ f transitions.

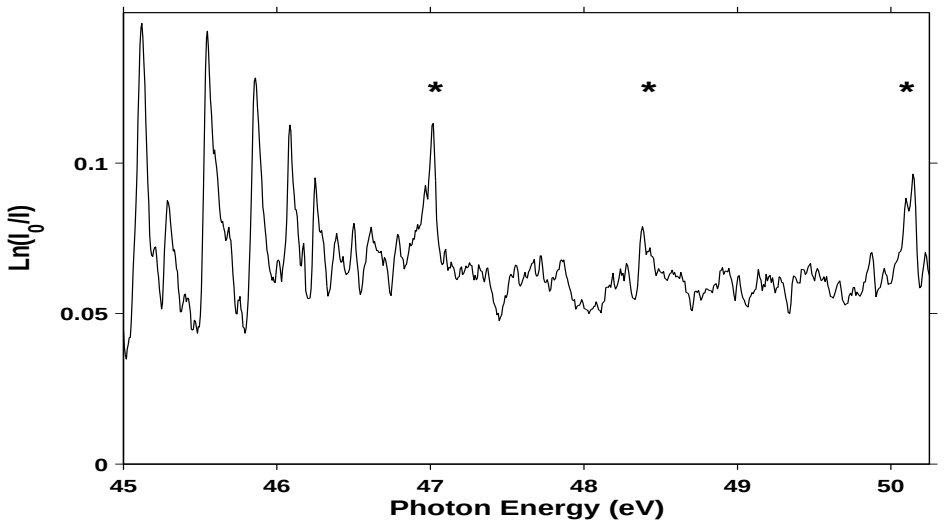

Figure 6.3: The three features observed at higher energy, 47.10 eV, 48.38 eV and 50.14 eV, which are not predicted by calculations. They are possibly due to double excitations.

A redistribution of oscillator strength due to configuration interaction is observed for the 7f[$\frac{5}{2}$, $\frac{5}{2}$] level. The 7f[$\frac{5}{2}$, $\frac{5}{2}$] 40.74 eV, 8p[$\frac{3}{2}$, $\frac{1}{2}$] 40.82 eV and the 7f[$\frac{5}{2}$, $\frac{7}{2}$] 40.94 eV levels show strong level mixing giving the otherwise weak 7f[$\frac{5}{2}$, $\frac{5}{2}$] comparable strength. The presence of configuration interaction is also noted with strong mixing among the 6f[$\frac{3}{2}$, $\frac{5}{2}$] level at 41.65 eV and 8f[$\frac{5}{2}$, $\frac{7}{2}$] level at 41.91 eV. The predicted 2:1 ratio of oscillator strengths between the 6f and 8f levels is reversed as a result.

Three features observed at 47.10 eV, 48.38 eV and 50.14 eV, as shown in Fig. 6.3, which are not predicted by the current calculations are suspected to be due to photoabsorption from an excited state. Calculations were performed for transitions from the excited ground state, $5d^{10}6s6p$, to $5d^{9}6s6pnf$, mp (n = 5-10, m = 6-10). In the energy range for these peaks, transitions from the excited state to the $5d^{9}6s6p5f$, 6f levels are dominant, however no attempt has been made to assign these features.

The observed Rydberg limits are $^2D_{5/2}$=44.48 eV and $^2D_{3/2}$=47.14 eV, which agree with those determined by Gutmann [220], 44.49 eV and 47.134 eV respectively. The asymmetry in profiles of the observed 5d spectrum of Pb III is present throughout, not just above the $^2D_{5/2}$ threshold, which is clearly seen in Fig. 6.1. Similar profiles observed in the Hg I spectrum have been commented on by Mansfield [219]. As in the spectrum of Hg I, the asymmetric lines would appear to have a Fano profile with a large negative value of the profile index q. To reproduce this result, a full calculation including mixing with the continuum would be required.

6.3.2 The 5d photoabsorption spectrum of Bi IV.

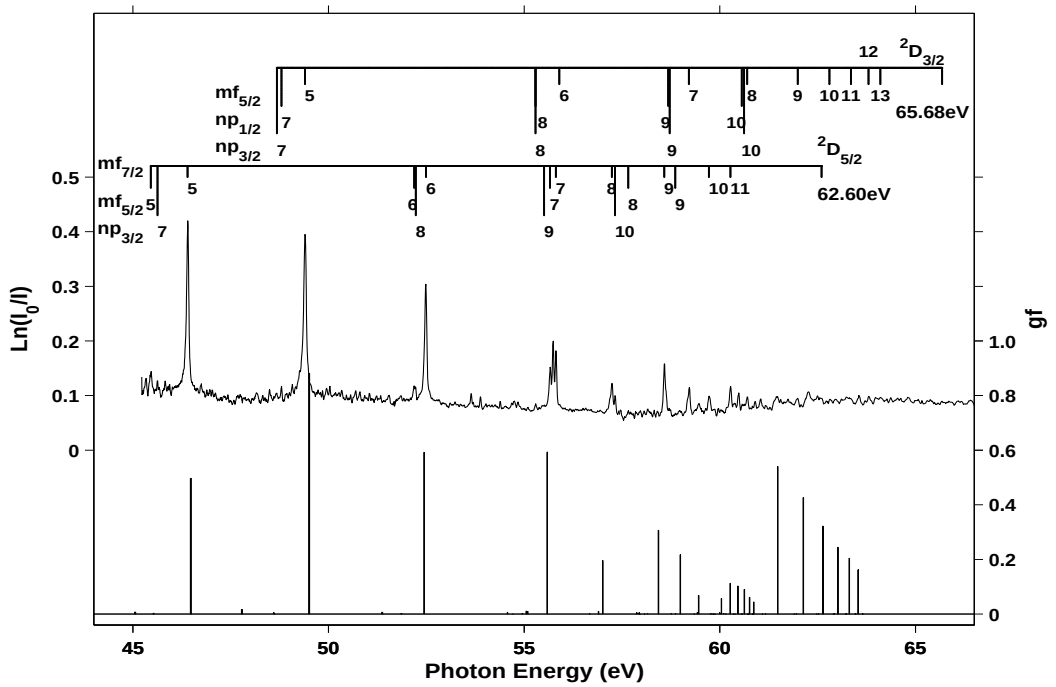

Figure 6.4: The observed (top) and calculated (bottom) 5d photoabsorption spectrum of Bi IV.

The 5d inner-shell electric dipole allowed transitions from the $5d^{10}6s^2\,{}^1S_0$ ground state in Bi IV are as follows:

$$\begin{aligned} 5d^{10}6s^2 &\rightarrow 5d^9 6s^2\, n\mathrm{p} \qquad (6 \le n \le 10) \\ 5d^{10}6s^2 &\rightarrow 5d^9 6s^2\, m\mathrm{f} \qquad (5 \le m \le 13) \end{aligned} \tag{6.2}$$

For Bi IV, it was possible to record the transition 5d $\rightarrow$ 6p, which occurs close to 29 eV (see Fig. 6.7). The observed 5d photoabsorption spectrum is shown along with the calculated *gf*-values in Fig. 6.4. Calculations for these transition energies and intensities were again made using the Cowan suite of codes [29, 30] and the range of basis states included in the calculation was $6 \le n\mathrm{p} \le 19$ and $5 \le m\mathrm{f} \le 17$. As in the case of Pb, the Slater parameters (F^k and G^k) and the configuration interaction parameter (R^k) were reduced by 15%; the spin-orbit parameter was left unchanged. Similar to the calculations for Pb III described earlier, the oscillator strengths of the higher lying *mf* levels are anomalously large and should not be taken as an accurate representation of the *gf* distribution.

It was found necessary to perform a term dependent minimization calculation

for the $5d^9(^2D_{3/2})\ 6s^2 6f_{5/2}$ level, (^1P in LS coupling), as the code over-estimated its position by almost +8 eV. The results of the minimization are compared with the configuration average results in Table 6.1. It should be noted that while the minimization calculation accurately predicts the position of the $6f_{5/2}$ level and the higher series members, the $5f_{5/2}$ and $5f_{7/2}$ levels are shifted towards higher energy. We have therefore chosen to enter the configuration average values in Table 6.5 for these two levels. Again *jj* coupling was favoured over *LS* and *JK* as it had the highest purity 84% compared to 60% and 58% respectively. The calculated spectrum is listed in Table 6.6, where it can be clearly seen that there exists a large degree of mixing within the Rydberg series, just as in the previous case for Pb III in Table 6.3 and Table 6.4.

Table 6.1: Hartree-Fock results for the minimization of the $5d^9 6s^2 6f[\frac{3}{2},\frac{5}{2}]$ configuration (^1P term in *LS* coupling).

	E_{av}	^1P (minimized)
Energy	64.37	55.56
F^2	1.042	0.501
F^4	0.562	0.204
G^1	0.952	0.254
G^3	0.579	0.154
G^5	0.408	0.108
ζ_{5d}	1.232	1.236
ζ_{6f}	0.0008	0.0010
$\int \Psi_{5d} r \Psi_{6f} dr$	0.86319	0.60538

All *n*p transitions are weak in Bi IV compared to Pb III with the *n*f$[\frac{5}{2},\frac{7}{2}]$, *n*f$[\frac{3}{2},\frac{5}{2}]$ series dominating the spectrum. This indicates an even stronger overlap between the d and f wavefunctions compared to Pb III and Hg I. It should be noted that due to the weakness of levels close to the series limit, level assignments are based mainly on the effective quantum numbers. The *n*p series in particular proved difficult to assign as all lines are weak and could have been assigned to many of the numerous largely indistinguishable features observed in this region of the spectrum. The assignments made are thus to be treated as tentative and chosen such that the effective quantum numbers are comparable for all three *n*p series.

The quantum defect for the *n*f$[\frac{5}{2},\frac{7}{2}]$ series shows some irregularity for the 8f and 9f levels but has a more consistent quantum defect of 1.33 for higher series members. A Lu-Fano plot (see Chapter 1) shows that this series is perturbed by the *n*f$_{5/2}$ series built on the $^2D_{3/2}$ limit. One can see both the 8f and 9f$[\frac{5}{2},\frac{7}{2}]$ levels at 57.24 eV and 58.58 eV are strongly perturbed by the *n*f$[\frac{3}{2},\frac{5}{2}]$ series in Fig. 6.5. The mixing coefficients determined from the Cowan code and presented in Table 6.6 for these two levels show the perturbation is due to electron correlation between the closely

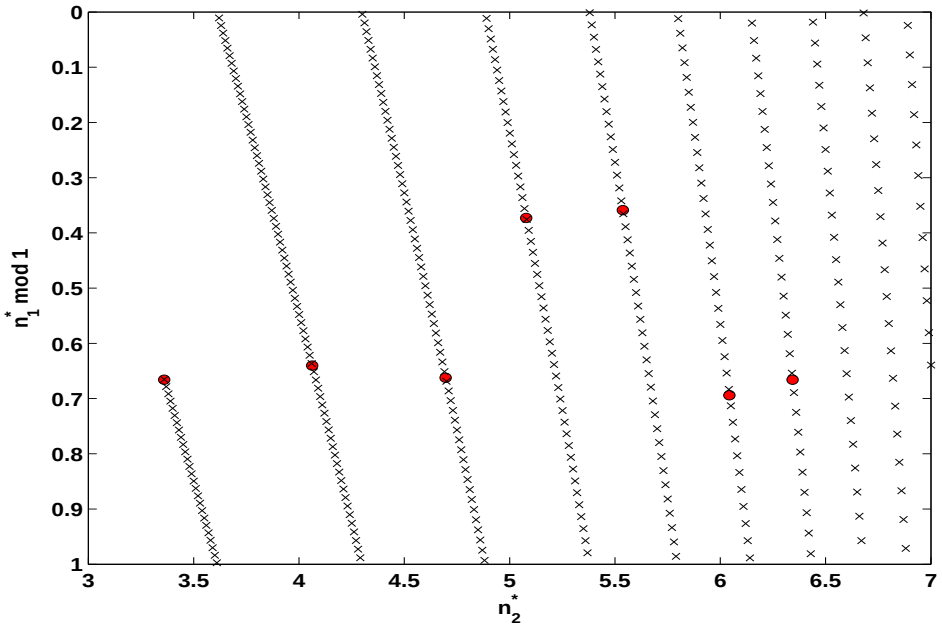

Figure 6.5: A two-dimensional Lu-Fano plot for the $nf[\frac{5}{2},\frac{7}{2}]$ and the $nf[\frac{3}{2},\frac{5}{2}]$ Rydberg series in Bi IV. The effective quantum numbers n_1^* and n_2^* are defined with respect to the first and second ionization potentials respectively. The broken curves are the functions $n_1^*(n_2^*)$. One can see both the 8f and 9f$[\frac{5}{2},\frac{7}{2}]$ levels are perturbed strongly from what would be an otherwise straight line in the graph.

spaced levels in both series. We did not find the MQDT parameters from fitting the determinantal equation (Eqn. 1.49) presented in Chapter 1 to the experimental data as it proved too difficult to fit all levels accurately. It is known that the quantum defects δ_1, δ_2 and the R parameter can have an energy dependence [53] and if this had been included we may have obtained more accurate results. As shown in Fig. 6.6, some series do not perturb each other, this is indicated by the straightness of the points in a Lu-Fano plot.

Similarly in the $nf[\frac{3}{2},\frac{5}{2}]$ series, the 7f member has an irregular quantum defect; a value of 1.23 concurs with the remaining series members. The strong contribution of the 7f$[\frac{3}{2},\frac{5}{2}]$ level to the 8-10f$[\frac{5}{2},\frac{7}{2}]$ series members results in a repulsion of these states towards higher energy, indicated by the 0.7-1.0 eV energy difference between calculated and experimental energy values. Strong configuration interaction among the 10p$[\frac{5}{2},\frac{3}{2}]$ and 7f$[\frac{3}{2},\frac{5}{2}]$ level at 57.24 eV results in the increased intensity for the 10p feature, appearing just above the 8f level at 59.32 eV. The close spacing of the 7f$[\frac{5}{2},\frac{5}{2}]$, 7f$[\frac{5}{2},\frac{7}{2}]$ and 6f$[\frac{3}{2},\frac{5}{2}]$ levels at 55.66 eV, 55.74 eV and 55.81 eV respectively, results in a redistribution of oscillator strength, as it did in the Pb III spectrum, giving the 7f$[\frac{5}{2},\frac{5}{2}]$ transition comparable strength, although it is predicted to be quite weak in the Cowan calculation.

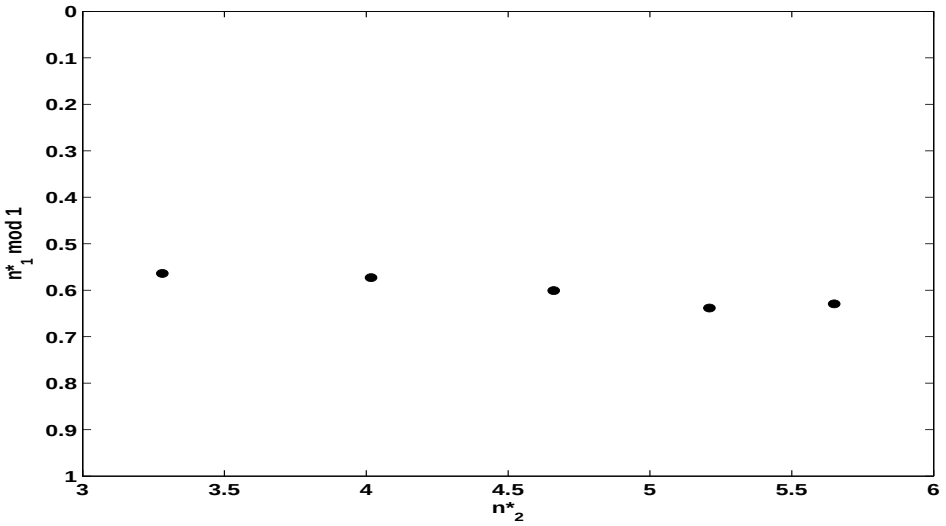

Figure 6.6: A two-dimensional Lu-Fano plot for the *n*f[$\frac{5}{2}$, $\frac{5}{2}$] and the *n*f[$\frac{5}{2}$, $\frac{3}{2}$] Rydberg series in Bi IV. As before, the effective quantum numbers n_1^* and n_2^* are defined with respect to the first and second ionization potentials respectively. In this case, no perturbation occurs between these two series as indicated by the straightness of the points. Similar 'straight' graphs were obtained for the *n*p Rydberg series too.

The low lying $5d^9 6s^2 6p[\frac{5}{2}, \frac{3}{2}]$ (28.29 eV) and $5d^9 6s^2 6p[\frac{3}{2}, \frac{1}{2}]$ (29.48 eV) levels agree with previous measurements made by Crawford [202] who obtained values of 28.284 eV and 29.47 eV respectively. The valence excited $5d^{10} 6s7p$ peak located at 28.76 eV compares well with the measurement of 28.75 eV, also reported by Crawford. Table 6.2 compares our experimental values of the $5d^9 6s^2 5f$ and 6f levels with Ryabtsev [221]. They analyzed autoionizing states of Bi III, Bi IV and Bi V ions with a 0.01 to 0.1 Å accuracy (as compared to 0.06 eV ($2{\cdot}10^5$ Å) in the present experiment). The only significant difference is for the $5d^9 6s^2 6f$ $[\frac{5}{2}, \frac{7}{2}]$ level, one of the three overlapping levels.

Level		$E_{Ryabtsev}$	$E_{Banahan}$
$5d^9 6s^2 5f$	$[\frac{5}{2}, \frac{5}{2}]$	45.00†	45.46
	$[\frac{5}{2}, \frac{7}{2}]$	46.41	46.40
	$[\frac{3}{2}, \frac{5}{2}]$	49.40	49.40
$5d^9 6s^2 6f$	$[\frac{5}{2}, \frac{7}{2}]$	52.51	52.49
	$[\frac{3}{2}, \frac{5}{2}]$	55.97	55.81

Table 6.2: Comparison of experimental values for the $5d^9 6s^2 5f$ and 6f levels from Ryabtsev [221] and this work. †Comparatively weak transition they assigned tentatively.

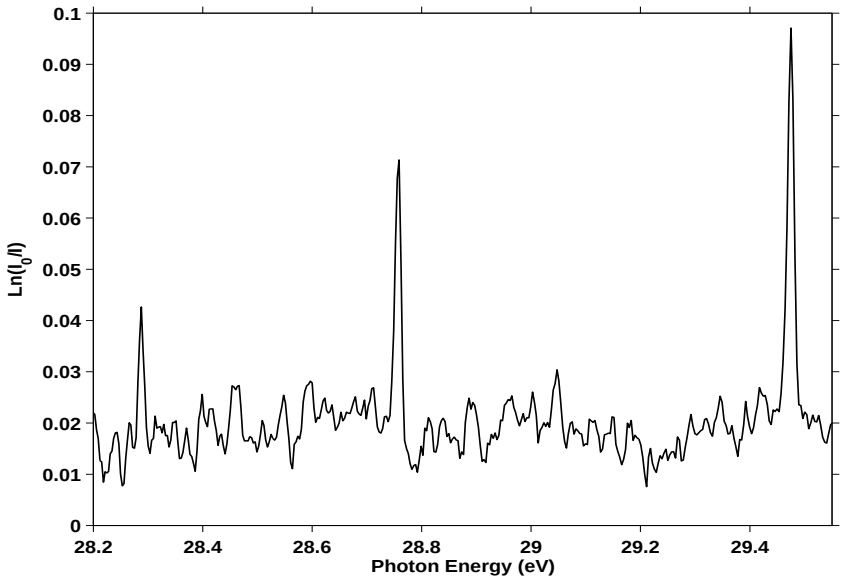

Figure 6.7: The observed $5d^9 6s^2 6p[\frac{5}{2}, \frac{3}{2}]$ level at 28.29 eV and $5d^9 6s^2 6p[\frac{3}{2}, \frac{1}{2}]$ level at 29.48 eV recorded for Bi IV. The peak at 28.76 eV is assigned as the $5d^{10} 6s7p[\frac{3}{2}, \frac{5}{2}]$ level [202].

The revised and extended analysis of Bi V reported by Raassen [222] determined the $5d^9 6s^2\ ^2D_{5/2}$ and $5d^9 6s^2\ ^2D_{3/2}$ series limits to be located at 17.24 eV and 20.32 eV above the $5d^{10} 6s$ ground state. The observed Rydberg limits for the 5d excitation series are $^2D_{5/2}$=62.60 eV and $^2D_{3/2}$=65.68 eV placing the ionization potential of Bi IV at the new value of 45.36 eV (45.32 eV [202]). Loch *et al* [211] calculated the configuration-average ionization potential of Bi IV to be 43.46 eV and the $5d^9 6s^2$ configuration-average placed at 62.95 eV which are in good agreement with our results.

6.4 Conclusion

The $5d$ photoabsorption spectra of Pb III and Bi IV have been recorded using the dual laser produced plasma technique in the photon energy range 30 - 66 eV. Theoretical calculations using the Cowan code allowed for the identification of numerous previously unknown or unidentified lines in this region. Strong configuration interaction is present in the Rydberg series of both ions. We have revised the ionization potential of Bi III to 45.36 eV.

Table 6.3: The 5d photoabsorption spectrum of Pb III.

Level	E_{exp} (eV)	E_{calc} (eV)	*gf* value	n^*	*jj* composition
			Series $5d_{3/2} \rightarrow np_{3/2}$		
$6p_{3/2}$		24.3346	0.1439		$94\%(\frac{3}{2},\frac{3}{2})$
$7p_{3/2}$		36.7549	0.0036		$96\%(\frac{3}{2},\frac{3}{2})$
$8p_{3/2}$		40.9571	0.0007		$96\%(\frac{3}{2},\frac{3}{2})$
$9p_{3/2}$		42.9896	0.0001		$91\%(\frac{3}{2},\frac{3}{2})$
$10p_{3/2}$		44.146	0.0002		$97\%(\frac{3}{2},\frac{3}{2})$
$11p_{3/2}$		44.8661	0.0001		$97\%(\frac{3}{2},\frac{3}{2})$
			Series $5d_{3/2} \rightarrow np_{1/2}$		
$6p_{1/2}$	22.846♭	22.5445	0.9947	2.25	$72\%(\frac{3}{2},\frac{3}{2}) - 26\%6p(\frac{5}{2},\frac{3}{2})$
$7p_{1/2}$	36.32♮	36.299	0.2924	3.36	$66\%(\frac{3}{2},\frac{1}{2}) - 25\%5f(\frac{5}{2},\frac{7}{2})$
$8p_{1/2}$	40.82	40.7109	0.0056	4.40	$80\%(\frac{3}{2},\frac{1}{2}) - 17\%7f(\frac{5}{2},\frac{7}{2})$
$9p_{1/2}$	42.89	42.8781	0.0399	5.37	$80\%(\frac{3}{2},\frac{1}{2}) + 8\%10f(\frac{5}{2},\frac{7}{2})$
$10p_{1/2}$		44.0788	0.0335		$92\%(\frac{3}{2},\frac{1}{2})$
$11p_{1/2}$	44.92	44.8203	0.0103	7.43	$96\%(\frac{3}{2},\frac{1}{2})$
$12p_{1/2}$	45.42	45.3141	0.0065	8.44	$96\%(\frac{3}{2},\frac{1}{2})$
$13p_{1/2}$	45.75	45.6606	0.0046	9.43	$96\%(\frac{3}{2},\frac{1}{2})$
$14p_{1/2}$	46.01	45.9199	0.0035	10.42	$96\%(\frac{3}{2},\frac{1}{2})$
			Series $5d_{5/2} \rightarrow np_{3/2}$		
$6p_{3/2}$	21.647♭	21.5754	0.0983	2.32	$69\%(\frac{5}{2},\frac{3}{2}) - 26\%6p(\frac{5}{2},\frac{7}{2})$
$7p_{3/2}$	34.18	34.1168	0.0417	3.45	$99\%(\frac{5}{2},\frac{3}{2})$
$8p_{3/2}$		38.3002	0.0017		$97\%(\frac{5}{2},\frac{3}{2})$
$9p_{3/2}$		40.3349	0.0073		$98\%(\frac{5}{2},\frac{3}{2})$
$10p_{3/2}$		41.4877	0.0009		$98\%(\frac{5}{2},\frac{3}{2})$
$11p_{3/2}$		42.209	0.0050		$97\%(\frac{5}{2},\frac{3}{2})$
			Series $5d_{3/2} \rightarrow nf_{5/2}$		
$5f_{5/2}$	38.57♮	38.5928	0.1625	3.78	$76\%(\frac{3}{2},\frac{5}{2}) - 26\%6f(\frac{5}{2},\frac{7}{2})$
$6f_{5/2}$	41.65	41.9391	0.4043	4.72	$39\%(\frac{3}{2},\frac{5}{2}) + 37\%8f(\frac{5}{2},\frac{7}{2}) - 11\%9f(\frac{5}{2},\frac{7}{2})$
$7f_{5/2}$	43.47	43.5583	0.1208	5.78	$35\%(\frac{3}{2},\frac{5}{2}) + 28\%13f(\frac{5}{2},\frac{7}{2}) + 14\%7f(\frac{5}{2},\frac{5}{2})$
$8f_{5/2}$	44.46	44.5051	0.5215	6.76	$78\%(\frac{3}{2},\frac{5}{2}) - 7\%9f(\frac{3}{2},\frac{5}{2})$
$9f_{5/2}$	45.12	45.0866	0.3224	7.79	$85\%(\frac{3}{2},\frac{5}{2}) - 6\%10f(\frac{3}{2},\frac{5}{2})$
$10f_{5/2}$	45.55	45.4969	0.2295	8.78	$85\%(\frac{3}{2},\frac{5}{2}) - 6\%11f(\frac{3}{2},\frac{5}{2})$
$11f_{5/2}$	45.86	45.7924	0.1756	9.79	$85\%(\frac{3}{2},\frac{5}{2}) - 6\%14f(\frac{3}{2},\frac{5}{2})$
$12f_{5/2}$	46.08	46.0111	0.1410	10.76	$84\%(\frac{3}{2},\frac{5}{2}) - 7\%13f(\frac{3}{2},\frac{5}{2})$
$13f_{5/2}$	46.25	46.1767	0.1198	11.74	$82\%(\frac{3}{2},\frac{5}{2}) - 8\%14f(\frac{3}{2},\frac{5}{2})$
$14f_{5/2}$	46.39	46.3063	0.1039	12.79	$80\%(\frac{3}{2},\frac{5}{2}) - 9\%15f(\frac{3}{2},\frac{5}{2})$
$15f_{5/2}$	46.49	46.4084	0.0985	13.75	$76\%(\frac{3}{2},\frac{5}{2}) - 12\%16f(\frac{3}{2},\frac{5}{2})$

Table 6.4: The 5d photoabsorption spectrum of Pb III cont.

Level	E_{exp} (eV)	E_{calc} (eV)	*gf* value	n^*	*jj* composition
			Series $5d_{5/2} \rightarrow n f_{7/2}$		
$5f_{7/2}$	36.06♮	36.0844	0.2373	3.81	$59\%(\frac{5}{2},\frac{7}{2}) - 30\%7p(\frac{3}{2},\frac{1}{2}) + 10\%5f(\frac{5}{2},\frac{5}{2})$
$6f_{7/2}$	39.25	39.304	0.6293	4.84	$73\%(\frac{5}{2},\frac{7}{2}) + 13\%5f(\frac{3}{2},\frac{5}{2})$
$7f_{7/2}$	40.94	40.833	0.2178	5.88	$64\%(\frac{5}{2},\frac{7}{2}) + 15\%8f(\frac{3}{2},\frac{1}{2})$
$8f_{7/2}$	41.91	42.4294	0.2057	6.90	$46\%(\frac{5}{2},\frac{7}{2}) - 26\%6f(\frac{3}{2},\frac{5}{2})$
$9f_{7/2}$	42.47	42.8170	0.0673	7.80	$74\%(\frac{5}{2},\frac{7}{2}) + 6\%9f(\frac{5}{2},\frac{5}{2})$
$10f_{7/2}$	42.89	43.1095	0.0354	8.76	$69\%(\frac{5}{2},\frac{7}{2}) - 15\%9p(\frac{3}{2},\frac{1}{2})$
$11f_{7/2}$	43.19	43.4369	0.0636	9.73	$71\%(\frac{5}{2},\frac{7}{2}) - 15\%11f(\frac{5}{2},\frac{5}{2})$
$12f_{7/2}$		43.6686	0.1056		$51\%(\frac{5}{2},\frac{7}{2}) - 40\%12f(\frac{5}{2},\frac{5}{2}) - 8\%7f(\frac{5}{2},\frac{3}{2})$
$13f_{7/2}$	43.61	43.7326	0.0897	11.86	$44\%(\frac{5}{2},\frac{7}{2}) - 23\%7f(\frac{3}{2},\frac{5}{2}) + 19\%15p(\frac{5}{2},\frac{3}{2})$
$14f_{7/2}$	43.72	43.8480	0.0807	12.69	$42\%(\frac{5}{2},\frac{7}{2}) - 28\%15f(\frac{3}{2},\frac{5}{2}) + 6\%7f(\frac{3}{2},\frac{5}{2})$
$15f_{7/2}$	43.85	43.9303	0.2432	13.94	$46\%(\frac{5}{2},\frac{7}{2}) - 27\%16f(\frac{3}{2},\frac{7}{2})$
			Series $5d_{5/2} \rightarrow n f_{5/2}$		
$5f_{5/2}$	35.70	35.7084	0.0133	3.73	$86\%(\frac{5}{2},\frac{5}{2}) - 14\%5f(\frac{5}{2},\frac{7}{2})$
$6f_{5/2}$	38.92	38.9057	0.0123	4.69	$92\%(\frac{5}{2},\frac{5}{2})$
$7f_{5/2}$	40.74	40.6071	0.0030	5.72	$88\%(\frac{5}{2},\frac{5}{2}) - 10\%7f(\frac{5}{2},\frac{7}{2})$
$8f_{5/2}$	41.74	41.6096	0.0102	6.69	$72\%(\frac{5}{2},\frac{5}{2}) - 19\%69f(\frac{3}{2},\frac{5}{2}) + 10\%8f(\frac{5}{2},\frac{7}{2})$
$9f_{5/2}$		42.3009	0.0014		$92\%(\frac{5}{2},\frac{5}{2})$
$10f_{5/2}$		42.7479	0.0007		$90\%(\frac{5}{2},\frac{5}{2}) - 9\%10f(\frac{5}{2},\frac{7}{2})$
$11f_{5/2}$		43.0657	0.0002		$84\%(\frac{5}{2},\frac{5}{2}) - 15\%11f(\frac{5}{2},\frac{7}{2})$
$12f_{5/2}$		43.2951	0.0013		$59\%(\frac{5}{2},\frac{5}{2}) + 25\%13f(\frac{5}{2},\frac{7}{2})$
$13f_{5/2}$		43.4768	0.0006		$97\%(\frac{5}{2},\frac{5}{2})$
$14f_{5/2}$		43.6129	0.0003		$95\%(\frac{5}{2},\frac{5}{2})$
$15f_{5/2}$		43.7191	0.0002		$94\%(\frac{5}{2},\frac{5}{2})$

E_{Calc}have been shifted by 0.3 eV to match the experimental values.

♭ Values taken from Moore's Tables.

♮ $5f_{7/2}$ at 30.063 eV, $7p_{7/2}$ at 36.32 eV and $5f_{5/2}$ at 38.576 were recorded by Raasen [222].

Table 6.5: The 5d photoabsorption spectrum of Bi IV.

Level	E_{exp} (eV)	E_{calc} (eV)	gf value	n^*	jj composition
			Series $5d_{3/2} \rightarrow n p_{3/2}$		
$6p_{3/2}$	31.44	31.3256	0.1984	2.52	$95\%(\frac{3}{2},\frac{3}{2})$
$7p_{3/2}$	48.68	48.6084	0.0041	3.58	$96\%(\frac{3}{2},\frac{3}{2})$
$8p_{3/2}$	55.29	54.9489	0.0024	4.59	$84\%(\frac{3}{2},\frac{3}{2}) + 10\%9p(\frac{5}{2},\frac{3}{2})$
$9p_{3/2}$	58.72	58.1561	0.0004	5.62	$93\%(\frac{3}{2},\frac{3}{2})$
$10p_{3/2}$	60.62	59.9990	0.0066	6.60	$90\%(\frac{3}{2},\frac{3}{2})$
$11p_{3/2}$		61.1682	0.0006		$97\%(\frac{3}{2},\frac{3}{2})$
			Series $5d_{3/2} \rightarrow n p_{1/2}$		
$6p_{1/2}$	29.48	29.0395	1.344	2.45	$46\%(\frac{3}{2},\frac{1}{2}) + 44\%6p(\frac{5}{2},\frac{3}{2})$
$7p_{1/2}$	48.80	47.7883	0.0264	3.59	$95\%(\frac{3}{2},\frac{1}{2})$
$8p_{1/2}$	55.29	54.5728	0.0098	4.58	$92\%(\frac{3}{2},\frac{1}{2})$
$9p_{1/2}$	58.68	57.9371	0.0060	5.58	$61\%(\frac{3}{2},\frac{1}{2}) - 16\%9f(\frac{5}{2},\frac{5}{2})$
$10p_{1/2}$	60.56	59.8712	0.0001	6.52	$94\%(\frac{3}{2},\frac{1}{2})$
$11p_{1/2}$		61.0824			$96\%(\frac{3}{2},\frac{1}{2})$
$12p_{1/2}$		61.8981			$95\%(\frac{3}{2},\frac{1}{2})$
$13p_{1/2}$		62.4738			$95\%(\frac{3}{2},\frac{1}{2})$
$14p_{1/2}$		62.8945			$95\%(\frac{3}{2},\frac{1}{2})$
			Series $5d_{5/2} \rightarrow n p_{3/2}$		
$6p_{3/2}$	28.29	28.0381	0.0001	2.52	$51\%(\frac{3}{2},\frac{1}{2}) - 35\%6p(\frac{5}{2},\frac{3}{2})$
$7p_{3/2}$	45.63	45.5301	0.0040	3.58	$92\%(\frac{5}{2},\frac{3}{2})$
$8p_{3/2}$	52.23	51.8784	0.0082	4.58	$93\%(\frac{5}{2},\frac{3}{2})$
$9p_{3/2}$	55.51	55.0901	0.0145	5.54	$53\%(\frac{5}{2},\frac{3}{2} - 30\%6f(\frac{3}{2},\frac{5}{2})$
$10p_{3/2}$	57.32	56.9011	0.0141	6.42	$82\%(\frac{5}{2},\frac{3}{2} - 13\%8f(\frac{5}{2},\frac{7}{2})$
$11p_{3/2}$		58.0758			$95\%(\frac{5}{2},\frac{3}{2})$
			Series $5d_{3/2} \rightarrow n f_{5/2}$		
$5f_{5/2}$	49.40	49.9119	0.7907	3.66	$66\%(\frac{5}{2},\frac{7}{2}) - 15\%5f(\frac{3}{2},\frac{5}{2})$
$6f_{5/2}$	55.74	55.5884	0.8897	4.68	$80\%(\frac{5}{2},\frac{7}{2}) + 7\%6f(\frac{5}{2},\frac{5}{2})$
$7f_{5/2}$	59.21	58.4295	0.4593	5.80	$31\%(\frac{3}{2},\frac{5}{2}) - 26\%10f(\frac{5}{2},\frac{5}{2}) + 24\%9f(\frac{5}{2},\frac{7}{2})$
$8f_{5/2}$	60.70	60.4608	0.1537	6.61	$36\%(\frac{3}{2},\frac{5}{2}) + 33\%14f(\frac{5}{2},\frac{7}{2})$
$9f_{5/2}$	61.99	61.4799	0.8104	7.68	$38\%(\frac{3}{2},\frac{5}{2}) - 31\%10f(\frac{3}{2},\frac{5}{2})$
$10f_{5/2}$	62.80	62.1332	0.6382	8.69	$52\%(\frac{3}{2},\frac{5}{2}) - 25\%11f(\frac{3}{2},\frac{5}{2})$
$11f_{5/2}$	63.35	62.6358	0.4829	9.67	$56\%(\frac{3}{2},\frac{5}{2}) - 24\%12f(\frac{3}{2},\frac{5}{2})$
$12f_{5/2}$	63.80	63.016	0.3665	10.76	$56\%(\frac{3}{2},\frac{5}{2}) - 25\%13f(\frac{3}{2},\frac{5}{2})$
$13f_{5/2}$	64.10	63.306	0.3060	11.73	$53\%(\frac{3}{2},\frac{5}{2}) - 27\%14f(\frac{3}{2},\frac{5}{2})$
$14f_{5/2}$		63.5347	0.2427		$50\%(\frac{3}{2},\frac{5}{2}) - 32\%15f(\frac{3}{2},\frac{5}{2})$
$15f_{5/2}$		63.7176	0.2199		$43\%(\frac{3}{2},\frac{5}{2}) - 39\%16f(\frac{3}{2},\frac{5}{2})$

Table 6.6: The 5d photoabsorption spectrum of Bi IV cont.

Level	E_{exp} (eV)	E_{calc} (eV)	*gf* value	n^*	*jj* composition
			Series $5d_{5/2} \rightarrow nf_{7/2}$		
$5f_{7/2}$	46.40	46.5638	0.7907	3.67	$66\%(\frac{5}{2},\frac{7}{2}) - 15\%5f(\frac{3}{2},\frac{5}{2})$
$6f_{7/2}$	52.49	52.4416	0.8881	4.64	$80\%(\frac{5}{2},\frac{7}{2}) + 7\%6f(\frac{5}{2},\frac{5}{2})$
$7f_{7/2}$	55.81	55.0522	0.0162	5.66	$30\%(\frac{5}{2},\frac{7}{2}) - 34\%9p(\frac{5}{2},\frac{7}{2}) - 15\%6f(\frac{3}{2},\frac{5}{2})$
$8f_{7/2}$	57.24	57.0099	0.2936	6.37	$60\%(\frac{5}{2},\frac{7}{2}) + 17\%10p(\frac{5}{2},\frac{3}{2}) - 8\%7f(\frac{3}{2},\frac{5}{2})$
$9f_{7/2}$	58.58	57.8808	0.0067	7.36	$44\%(\frac{5}{2},\frac{7}{2}) - 25\%9f(\frac{5}{2},\frac{5}{2}) - 23\%7f(\frac{3}{2},\frac{5}{2})$
$10f_{7/2}$	59.72	58.9908	0.3255	8.69	$55\%(\frac{5}{2},\frac{7}{2}) - 11\%11f(\frac{5}{2},\frac{7}{2}) + 6\%7f(\frac{3}{2},\frac{5}{2})$
$11f_{7/2}$	60.27	59.4586	0.1014	9.67	$53\%(\frac{5}{2},\frac{7}{2}) + 20\%13p(\frac{5}{2},\frac{3}{2}) - 12\%8f(\frac{3}{2},\frac{5}{2})$
$12f_{7/2}$		59.7689	0.0004		$52\%(\frac{5}{2},\frac{5}{2}) - 40\%12f(\frac{5}{2},\frac{7}{2})$
$13f_{7/2}$		60.0405	0.0851		$60\%(\frac{5}{2},\frac{7}{2}) - 18\%8f(\frac{3}{2},\frac{5}{2})$
$14f_{7/2}$		60.2646	0.1687		$47\%(\frac{5}{2},\frac{7}{2}) - 21\%13f(\frac{3}{2},\frac{7}{2}) - 11\%8f(\frac{3}{2},\frac{5}{2})$
$15f_{7/2}$		60.6246	0.1343		$40\%(\frac{5}{2},\frac{7}{2}) - 27\%16f(\frac{5}{2},\frac{7}{2})$
			Series $5d_{5/2} \rightarrow nf_{5/2}$		
$5f_{5/2}$	45.46	45.0755	0.0101	3.57	$79\%(\frac{5}{2},\frac{5}{2}) - 15\%5f(\frac{5}{2},\frac{7}{2})$
$6f_{5/2}$	52.19	52.0902	0.0097	4.57	$92\%(\frac{5}{2},\frac{5}{2})$
$7f_{5/2}$	55.66	54.7069	0.0002	5.60	$80\%(\frac{5}{2},\frac{5}{2}) - 13\%7f(\frac{5}{2},\frac{7}{2})$
$8f_{5/2}$	57.66	56.6736	0.0020	6.64	$89\%(\frac{5}{2},\frac{5}{2}) - 10\%8f(\frac{5}{2},\frac{7}{2})$
$9f_{5/2}$	58.86	57.9538	0.0001	7.63	$93\%(\frac{5}{2},\frac{5}{2})$
$10f_{5/2}$		58.7555	0.0010		$93\%(\frac{5}{2},\frac{5}{2})$
$11f_{5/2}$		59.3421	0.0004		$89\%(\frac{5}{2},\frac{5}{2}) - 10\%11f(\frac{5}{2},\frac{7}{2})$
$12f_{5/2}$		59.7934	0.0000		$46\%(\frac{5}{2},\frac{5}{2}) + 37\%12f(\frac{5}{2},\frac{7}{2})$
$13f_{5/2}$		60.0962	0.0005		$97\%(\frac{5}{2},\frac{5}{2})$
$14f_{5/2}$		60.3475	0.0003		$94\%(\frac{5}{2},\frac{5}{2})$
$15f_{5/2}$		60.5403	0.0002		$92\%(\frac{5}{2},\frac{5}{2})$

Chapter 7

Summary

7.1 Summary of work

The work presented in this thesis is concerned with fundamental inner shell processes that occur upon interaction of energetic photons with atoms and ions. The many-body nature inherent in inner-shell dynamics provides a stimulating and challenging study for both experimental and theoretical atomic physics. The dual laser plasma technique was successfully employed to measure the photoabsorption innershell spectra of the following ions: Rb^{+}, Sr^{+}, Sr^{2+}, Pb^{2+} and Bi^{3+}. The study of isoelectronic sequences provides useful information on the changing nature of the physical interactions that occur as the core charge, and correspondingly the degree of nuclear screening changes, for this reason members of both the Hg I and Kr I isoelectronic sequences were studied.

The experimental system was adapted to include a third laser to perform resonant excitation studies in a laser produced strontium plasma. Results obtained for one- and two-photon resonant absorption in Sr^{+} conform to the LIBORS model such that no ionization signal is observed if the ion is pumped with a non-resonant wavelength. In this case, superelastic heating via collision quenching of the overpopulated resonance level is the dominant mechanism for the ionization observed. The fact that non-resonant pumping in Sr still results in a strong ionization signal implies that there is more to it than just LIBORS. At present we can only suggest some likely candidates and molecular dissociation would provide a plausible explanation and it has already been suggested by Baig *et al* [112].

The photoabsorption measurements for Kr-like Rb^{+} and Sr^{2+} were combined with synchrotron results obtained at the ASTRID storage ring in Denmark where absolute photoionization cross sections were measured. The merged-beam technique employed at the storage ring enabled the detection of multiply charged ions and showed that 90% of the total cross section for 3d excitation in these ions could

be attributed to double photoionization. A similar trend was observed in the case of lanthanide 4d excitation previously. Strong interaction between the discrete s $\rightarrow$ p transitions and the p $\rightarrow \epsilon$d continuum manifested itself in the spectra as characteristic window resonances which were parametrised using Fano's theoretical resonance profile formula. Discrete features from 4p $\rightarrow$ *m*s, *n*d transitions were assigned using the Cowan code.

The 4p-subshell spectrum of Sr^{+} recorded was extremely complex due to strong overlap of the 4d and 5s wavefunctions. Doubly-excited transitions were also observed and it was found necessary to include the strongly correlated $4d^2$ and $5p^2$ configurations in our calculations to properly account for the spectrum observed. As neither pure *LS* nor *jj* coupling could reproduce the photoabsorption spectrum, we had to resort to an intermediate coupling scheme where transitions were assigned according to the highest purity given in one of the two coupling schemes above. It was found that, in general, *LS* coupling provided the highest purity for the first member of each series and *jj* coupling was better suited to describing the higher members of a Rydberg series.

From our observations, we inferred greater overlap between the d and f wavefunctions in Bi^{3+} than in the lower isoelectronic partner Pb^{2+}. This appeared in the spectra as a reduction in oscillator strength of the 5d $\rightarrow$ *n*p resonances while stronger d $\rightarrow$ f transitions were observed. Strong configuration interaction was present in both ions, particularly in Bi^{3+} where many levels deviated from the quantum defect value for their particular series. Lu-Fano plots were constructed to help visualise the perturbing or perturbed levels within a series and Hartree-Fock with configuration interaction calculations were performed to identify the discrete features observed in the spectra.

7.2 Conclusions and perspectives

There is no doubt that measurements and calculations on multiply charged ions still holds large interest in the atomic physics community. It would be useful to extend our study of the Kr I isoelectronic sequence to higher members, such as Y^{3+}, to see what trends persist or change. For example, we know that the 4s $\rightarrow$ *n*p series in Y^{3+} differs from Rb^{+} and Sr^{2+} such that the 4s-5p resonance drops below the 4p ionization limit so that the first autoionizing member of the 4s-*n*p resonance series becomes 4s-6p. Also unlike the window resonances observed for Rb^{+} and Sr^{2+}, this resonance switches to a normal, slightly asymmetric profile. It would be interesting to see if this is also the case for Zr^{4+}, the next highest member. Similarly, as previous investigations of 4d excitation in the lanthanides stimulated

important theoretical developments to account for the many-body nature of the excitation process, analogous studies along isonuclear and isoelectronic sequences for 3d excitation may provide a similar stimulus and uncover some new intriguing features.

Although the DLP technique has provided a wealth of information on inner-shell photoexcitation in atoms and ions, it is the absolute cross section measurements that provide the severest test for theoretical codes. Using both the DLP and merged-beam techniques is thus an obvious choice; results from both combine to give highly resolved absolute cross sections. Of course over the past decade, third generation synchrotron facilities e.g. the ALS, BESSY II, MAX II, SOLEIL etc. have come online and are capable of producing new data with much higher spectral resolution than previously obtained (10^{-2} eV for first generation to 10^{-4} eV for third generation). With the introduction of ECR sources on beam lines, absolute photoionization measurements are now possible on multiply charged ions (above the doubly charged state). The significant advantage still retained by the DLP technique however, is the relative ease in obtaining photoabsorption measurements of highly charged ions in almost any element.

Pump-probe experiments have opened up a more explorative research area as one can extend studies from the ground state to well prepared excited target states. Thus from these two-photon / colour experiments one can access excited states belonging to the same parity as the ground state exploring a manifold of highly excited states previously unseen. Studies of laser-excited and laser-polarized targets in pump-probe experiments using polarized radiation have proven itself as an ideal tool in gaining greater insight into the photoionization mechanism. Measurements of dichroism in electron spectra permit the determination of the relative amplitudes for the different dipole matrix elements and the relative phases of the outgoing electrons. These measurements are sensitive to the different electron interactions in the electron cloud thus making them ideal for comparisons with theory.

The development of free electron lasers (FEL), e.g. FLASH at Hamburg, which provide intense femtosecond pulses in the VUV and XUV regime, now make possible the study of dilute species (ions, mass selected clusters), multi-photon processes, direct two- or multi-electron ionization as well as time resolved phenomena on the femtosecond scale. Furthermore, future investigations will avail of the wavelength tunability of the FEL to study the coupling of two autoionizing states (AIS) via a pump-probe excitation scheme. The FEL will pump to one AIS while an optical laser will be used to couple to another AIS. Theoretical predications have yet to be experimentally verified and this new field of research will investigate electron correlations involved when coupling continua of opposite parity.

From our studies, a laser-produced plasma is not ideal for pump-probe experiments. The copious amount of seed electrons generated after laser irradiation, which in turn are superelastically heated and rapidly collisonally ionize the species of interest, masking any excited-state absorption that may occur. The 2.2 m grazing incidence spectrometer system will next be used to study both emission and absorption from laser-produced plasmas in search of an optimised 13.5 nm light source for applications in the semi-conductor industry. To perform complementary studies to the new phase of experiments (described above) that will take place at synchrotron and FEL facilities, a new ultrafast laser laboratory is being set up DCU. Pulses of 30 - 100 fs duration will be produced at wavelengths ranging from 266 - 2500 nm. Electron, ion and photo detection techniques will be employed to demonstrate, measure and ultimately use phase control in coherent EUV and optical laser ionization and fragmentation of atoms and molecules. Thus a new generation of experiments will be established at DCU that will hopefully provide first ever measurements and stimulate further investigations as its predecessor, the DLP technique, did decades ago.

Appendix A

Reference Material

A.1 List of Figures

Chapter 1

Chapter 2

Chapter 3

Chapter 5

Chapter 6

A.2 List of Tables

Chapter 2

Chapter 3

Chapter 4

Chapter 5

Chapter 6

Bibliography

[1] D. J. Kennedy and S. T. Manson. *Phys. Rev. A*, 5:227, 1972.

[2] H. P. Kelly. *Advances in Theoretical Physics*. New York: Academic, 1968.

[3] P. L. Altick and E. Glassgold. *Phys. Rev.*, 133:632, 1964.

[4] M. Ya. Amusia and N. A. Cherepkov. *Case Stud. At. Phys*, 5:47, 1975.

[5] K. A. Berrington, P. G. Burke, M. Le Dourneuf, W. D. Robb, K. T. Taylor, and L. Vo Ky. *Comp. Phys. Commun.*, 14:367, 1978.

[6] H. Beutler. *Z. Phys.*, 93:177, 1934.

[7] R. P. Madden and K Codling. *Phys. Rev. Lett.*, 10:516, 1963.

[8] G. Balloffet, J. Romand, and B. Vodar. *Comptes Rendus de l'Academie des Science*, 252(26):4139, 1961.

[9] G. Balloffet-Mehlmann and J. M. Esteva. *Astrophys. J.*, 157:945, 1969.

[10] A. Carillon, P. Jaegle, and P. Dhez. *Phys. Rev. Lett.*, 25:140, 1970.

[11] J. T. Costello, E. T. Kennedy, J.-P. Mosnier, P. K. Carroll, and G. O'Sullivan. *Phys. Scr.*, T 34:77, 1991.

[12] P. K. Carroll and G. O'Sullivan. *Phys. Rev. A*, 25:275, 1982.

[13] I. C. Lyon, B. Peart, K. Dolder, and J. B. West. *J. Phys. B*, **20**:1471, 1986.

[14] F. J. Rogers and C. A. Iglesias. *Science*, 263:50, 1994.

[15] The Opacity Project Team. *The Opacity Project*. Institute of Physics Publishing, Briston, UK, 1995.

[16] D. Kilbane, F. Folkmann, J.-M. Bizau, C. Banahan, S. Scully, H. Kjeldsen, P. van Kampen, M. W. D. Mansfield, J. T. Costello, and J. B. West. *Phys. Rev. A*, 75:032711, 2007.

[17] F. J. Wuilleumier and M. Meyer. *J. Phys. B: At. Mol. Opt. Phys.*, 39:R435, 2006.

[18] T. B. Lucatorto and T. J. McIlrath. *Phys. Rev. Lett*, 37:428, 1976.

[19] E. A. Hylleraas. *Z. Phys.*, 54:126, 1929.

[20] C. L. Pekeris. *Phys. Rev.*, 112:1649, 1958.

[21] Y. Accad, C. L. Pekeris, and B. Schiff. *Phys. Rev. A*, 4:516, 1971.

[22] D. R. Hartree. *Proceedings of the Cambridge Philosophical Society*, 24:426, 1928.

[23] V. Fock. *Z. Phys.*, 61:126, 1930.

[24] J. C. Slater. *Phys. Rev. A*, 34:1293, 1929.

[25] T. Koopmans. *Physica*, 1:104, 1934.

[26] E. U. Condon and H. Odabaşi. *Atomic Structure*. Cambridge University Press, 1978.

[27] C. Froese-Fischer. *The Hartree-Fock method for atoms: A numerical approach*. John Wiley & Sons, 1977.

[28] I. P. Grant, B. J. McKenzie, P. H. Norrington, D. F. Mayers, and N. C. Pyper. *Comp. Phys. Commun.*, 21:207, 1980.

[29] R. D. Cowan. *J. Opt. Soc. Am.*, 58:808, 1968.

[30] R. D. Cowan. *Theory of Atomic Structure and Spectra*. University of California Press, 1981.

[31] R. D. Cowan and D. C. Griffin. *J. Opt. Soc. Am.*, 66:1010, 1976.

[32] K. Rajnak and B. G. Wybourne. *Phys. Rev.*, 132:280, 1963.

[33] G. Racah and J. Stein. *Phys. Rev.*, 156:58, 1967.

[34] M. Goeppert Mayer. *Phys. Rev.*, 60:184, 1941.

[35] D. L. Ederer. *Phys. Rev. Lett.*, 13:1760, 1964.

[36] M. W. D. Mansfield and G. H. Newsom. *Proc. R. Soc. Lond. A*, 377:431, 1981.

[37] C. Banahan, C. McGuinness, J. T. Costello, D. Kilbane, J.-P. Mosnier, E. T. Kennedy, G. O'Sullivan, and P. van Kampen. *J. Phys. B: At. Mol. Opt. Phys.*, 41:205001, 2008.

[38] J. E. Hansen. *J. Phys. B: At. Mol. Opt. Phys.*, 5(6):1083, 1972.

[39] M. Ya. Amusia, L. V. Chernysheva, V. K. Ivanov, and V. A. Kupchenko. *Z. Phys. D*, 14:215, 1989.

[40] P. Auger. *J. de Physique et le Radium*, 6:205, 1925.

[41] U. Fano. *Phys. Rev.*, 124:1866, 1961.

[42] J. E. Hansen, J. Brilly, E. T. Kennedy, and G. O'Sullivan. *Phys. Rev. Lett.*, 63:1934, 1989.

[43] H. Kjeldsen. *J. Phys. B*, 39, 2006.

[44] M. Ya. Amusia, N. A. Cherepkov, L. V. Chernysheva, and S. T. Manson. *J. Phys. B: At. Mol. Opt. Phys.*, 33:L37, 2000.

[45] J. W. Cooper. *Phys. Rev.*, 128:681, 1962.

[46] P. van Kampen, G. O'Sullivan, V. K. Ivanov, A. N. Ipatov, J. T. Costello, and E. T. Kennedy. *Phys. Rev. Lett.*, 78:3082, 1997.

[47] N. F. Mott and H. S. W. Massey. *The Theory of Atomic Collisions*. Clarendon Press, Oxford, 1965.

[48] M. J. Seaton. *Proc. Phys. Soc*, 88:801, 1966.

[49] M. A. Baig, J. P. Connerade, C. Mayhew, and K. Sommer. *J. Phys. B: At. Mol. Opt. Phys.*, 17:371, 1984.

[50] K. T. Lu and U. Fano. *Phys. Rev. A*, 2:81, 1970.

[51] J. A. Armstrong, P. Esherick, and J. J. Wynne. *Phys. Rev. A*, 15:180, 1977.

[52] W. E. Cooke and C. L. Cromer. *Phys. Rev. A*, 32:2725, 1985.

[53] R. D. Knight. *Phys. Rev. A*, 34:3809, 1986.

[54] E. T. Kennedy and P. K. Carroll. *Contemp. Phys.*, 22:61, 1981.

[55] E. T. Kennedy. *Opt. Eng.*, 33:3984, 1994.

[56] A. W. Ehler and G. L. Weissler. *App. Phys. Lett.*, 89:8, 1966.

[57] P. K. Carroll and E. T. Kennedy. *Phys. Rev. Lett.*, 38:1068, 1977.

[58] P. K. Carroll, E. T. Kennedy, and G. O'Sullivan. *Appl. Opt.*, 19:1454, 1980.

[59] J. T. Costello. *XUV Emission and Absorption Spectroscopy of Laser-Produced Plasmas*. PhD thesis, University College Dublin, 1986.

[60] J. B. West. *J. Phys. B*, 34:R45, 2001.

[61] E. T. Kennedy, J. T. Costello, J.-P. Mosnier, and P. van Kampen. *Radiation Physics and Chemistry*, 70:291, 2004.

[62] L. M. Kiernan, E. T. Kennedy, J.-P. Mosnier, J. T. Costello, and B. F. Sonntag. *Phys. Rev. Lett.*, 72:2359, 1994.

[63] L. M. Kiernan, M.-K. Lee, B. F. Sonntag, P. Sladeczek, P. Zimmermann, E. T. Kennedy, J-P. Mosnier, and J. T. Costello. *J. Phys. B: At. Mol. Opt. Phys.*, 28:L161, 1995.

[64] Y. Azuma, S. Hasegawa, F. Koike, G. Kutluk, T. Nagata, E. Shigemasa, A. Yagishita, and A Sellin. *Phys. Rev. Lett.*, 74:3678, 1995.

[65] F. J. Wuilleumier, S. Diehl, D. Cubaynes, J.-M. Bizau, and E. T. Kennedy. *J. Electr. Spectr. Relat. Phen.*, 41:88, 1998.

[66] S. Diehl, D. Cubaynes, J.-M. Bizau, L. Journel, B. Rouvellou, S. Al Moussalami, F. J. Wuilleumier, E. T. Kennedy, N. Berrah, C. Blancard, T. J. Morgan, J. Bozek, A. S. Schlachter, L. VoKy, P. Faucher, and A. Hibbert. *Phys. Rev. Lett.*, 76:3915, 1996.

[67] K. T. Chung. *Phys. Rev. A*, 59:2065, 1999.

[68] G. Verbockhaven and J. E. Hansen. *Phys. Rev. Lett.*, 84:2810, 2000.

[69] B. M. Lagutin, Ph. V. Demekhin, I. D. Petrov, V. L. Sukhorukov, S. Lauer, H. Liebel, F. Vollweiler, H. Schmoranzer, O. Wilhelmi, G. Mentzel, and K.-H. Schartner. *J. Phys. B*, 32:1795, 1999.

[70] J.-P. Mosnier, J. T. Costello, E. T. Kennedy, L. Kiernan, and M. H. Sayyad. *Phys. Rev. A*, 49:755, 1994.

[71] J. T. Costello, D. Evans, R. B. Hopkins, E. T. Kennedy, L. Kiernan, M. W. D. Mansfield, J.-P. Mosnier, M. H. Sayyad, and B. F. Sonntag. *J. Phys. B: At. Mol. Opt. Phys.*, 25:5055, 1992.

[72] C. McGuinness, M. Martins, Ph. Wernet, B. F. Sonntag, P. van Kampen, J.-P. Mosnier, E. T. Kennedy, and J. T. Costello. *J. Phys. B: At. Mol. Opt. Phys.*, 32:L583L591, 1999.

[73] P. Nicolosi, E. Jannitti, and G. Tondello. *J. de Phys. IV Colloque C1*, page 89, 1991.

[74] E. Jannitti, P. Nicolosi, and G. Tondello. *Phys. Lett.*, 131:186, 1988.

[75] E. Jannitti, P. Nicolosi, and G. Tondello. *Phys. Scr.*, 41:458, 1990.

[76] R. F. Reilman and S. T. Manson. *Astrophys. J. Suppl.*, 40:815, 1979.

[77] I. C. Lyon, B. Peart, K. Dolder, and J. B. West. *J. Phys. B: At. Mol. Opt. Phys.*, 20:1471–1477, 1987.

[78] A. Gray. *XUV photoabsorption studies of calcium and the neon isoelectronic sequence*. PhD thesis, 1999.

[79] L. Kiernan. *Development of a multi-laser, multi-channel XUV spectrometer facility based on the dual laser plasma technique*. PhD thesis, 1994.

[80] M. Shaw. An extreme-uv optical multichannel analyser with resolution enhancement for laser plasma spectroscopy. Master's thesis, 1996.

[81] P. Yeates, E. T. Kennedy, J.-P. Mosnier, P. van Kampen, M. W. D. Mansfield, J. Pedregosa-Gutierrez, J. B. Greenwood, Ph. V. Demekhin, I. D. Petrov, B. M. Lagutin, V. L. Sukhorukov, L. A. Demekhina, and J. T. Costello. *J. Phys. B*, 37:4663, 2004.

[82] B. Doyle. A 1 m normal incidence multi-channel spectrometer for laser plasma spectroscopy. Master's thesis, 1995.

[83] W. Whitty. *A study of the expansion of a laser produced lithium plasma using spatially and temporally resolved imaging and spectroscopic techniques*. PhD thesis, Dublin City University, 1998.

[84] P. Yeates. *A Spectroscopic and Diagnostic Study of Laser Plasma Generation and Evolution under Multi-variable Target Conditioning*. PhD thesis, Dublin City University, 2000.

[85] Andor Technology. *Users Manual*. Andor Technology plc, 2007.

[86] www.photonicsolutions.co.uk.

[87] P. K. Carroll, E. T. Kennedy, and G. O'Sullivan. *J. Quant. Elect.*, 19:1807, 1983.

[88] T. J. McIlrath and T. B. Lucatorto. *Phys. Rev. Lett.*, 38:1390, 1977.

[89] C. H. Skinner. *J. Phys. B*, 13:55, 1980.

[90] H.-A. Bachor and M. Kock. *J. Phys. B: At. Mol. Opt. Phys.*, 14:2793, 1981.

[91] L. Jahreiss and M. C. E. Huber. *Phys. Rev. A*, 28:3382, 1983.

[92] M. C. E. Huber. *Modern Optical Methods in Gas Dynamic Research*. New York: Plenum, 1971.

[93] L. le Gouet, J. L. Picuqé, F. Wuilleumier, J.-M. Bizau, P. Dhez, P. Koch, and D. L. Ederer. *Phys. Rev. Lett*, 48:600, 1982.

[94] O. L. Landen, R. J. Winfield, D. D. Burgess, and J. D. Kilkenny. *Phys. Rev. A*, 32:2963, 1985.

[95] C. Bréchignac, Ph. Cahuzac, and A. Dèbarre. *Phys. Rev. A*, 31:2950, 1985.

[96] K. A. Menard and R. M. Measures. *Phys. Rev. A*, 35:2330, 1987.

[97] M. A. Khan, E. E. Khawaja, and M. F. Al-Kuhaili. *J. Phys. D: Appl. Phys*, 26:1614, 1993.

[98] R. M. Measures. *J. Appl. Phys.*, 48:2673, 1977.

[99] R. M. Measures, N. Drewell, and P. Cardinal. *Appl. Opt.*, 18:1824, 1979.

[100] R. M. Measures and P. G. Cardinal. *Phys. Rev. A*, 23:804, 1980.

[101] R. M. Measures, N. Drewell, and P. Cardinal. *J. Appl. Phys.*, 50:2662, 1978.

[102] Y. E. E. Gamal, M. A. Mahmoud, and H. A. Abd El-Rahman. *J. Quant. Spectrosc. Radiat.*, 90:29, 2005.

[103] W. R. Hunter. In *Spectroscopic Techniques*, volume IV, chapter 2. Academic Express, 1985.

[104] D. F. Colombant and G. F. Tonon. *J. Appl. Phys.*, 44:3524, 1973.

[105] J. M. Dawson. *Phys. Fluids*, 7:981, 1964.

[106] M. W. Sigrist. *Air Monitoring by Spectroscopic Techniques*. Wiley-IEEE, 1994.

[107] D. A. Miller, L. Yu, J. Cooper, and A. Gallagher. *Phys. Rev. A*, A46:1303, 1992.

[108] E. F. Worden, J. A. Paisner, and J. G. Conway. *Optics Letters*, 3:156, 1978.

[109] I. I. Shafranyosh and T. A. Snegurskaya. *Optics and Spectroscopy*, 101:76, 2005.

[110] V. Gedeon, V. Lengyel, O. Zatsarinny, and C. A. Kocher. *Phys. Rev. A*, 56:3753, 1997.

[111] A. Boutassetta, A. R. Allouche, and M. Aubert-Frecon. *Phys. Rev. A*, 53:3845, 1996.

[112] M. A. Baig, M. Yaseen, R. Ali, A. Nadeem, and S. A. Bhatti. *Eur. Phys. J. D*, 6:201, 1999.

[113] C. McGuinness, G. O'Sullivan, P. K. Carroll, D. Audley, and M. W. D. Mansfield. *Phys. Rev. A*, 51:2053, 1995.

[114] R. M. Measures, P. L. Wizinowich, and P. G. Cardinal. *J. Appl. Phys.*, 51:3622, 1980.

[115] H. R. Griem. *Phys. Rev.*, 165:258, 1968.

[116] I. C. Lyon, B. Peart, and K. Dolder. *J. Phys. B: Atom. Molec. Phys.*, 20:1925, 1987.

[117] D. G. Hummer, K. A. Berrington, W. Eissner, A. K. Pradhan, H.E. Saraph, and J. A. Tully. *Astron. Astrophys.*, 279:298, 1993.

[118] M. Oura, H. Yamaoka, K. Kawatsura, J. Kimata, T. Hayaishi, T. Takahashi, T. Koizumi, T. Sekioka, M. Terasawa, Y. Itoh, Y. Awaya, A. Yokoya, A. Agui, A. Yoshigoe, and Y. Saitoh. *Phys. Rev. A*, 63:014704, 2001.

[119] K. A. Berrington and C. Ballance. *J. Phys. B*, 34:2697, 2001.

[120] U. Fano and J. W. Cooper. *Phys. Rev.*, 137:A1364, 1965.

[121] U. Fano and J. W. Cooper. *Rev. Mod. Phys.*, 41:724, 1969.

[122] J. P. Connerade, J. M. Esteva, and R. C. Karnatak. Plenum, New York, 1987.

[123] I. C. Lyon, B. Peart, and K. Dolder J. B. West. *J. Phys. B*, 20:1471, 1987.

[124] I. C. Lyon, B. Peart, and K. Dolder. *J. Phys. B*, 20:1925, 1987.

[125] O. Almen and K. O. Nielsen. *Nucl. Instrum. Meth.*, 1:302, 1957.

[126] O. Heinz and R. T. Reaves. *Nucl. Instrum. Meth.*, 39:1229, 1968.

[127] J.-M. Bizau, E. Bouisset, C. Blancard, J. P. Champeaux, Compant la Fontaine A., C. Couillaud, D. Cubaynes, D. Hitz, C. Vinsot, and F. J. Wuilleumier. *Nucl. Instrum. Methods Phys. Res. B*, 205:290, 2003.

[128] P. van Kampen, Ch. Gerth, M. Martins, P. K. Carroll, J. Hirsch, E. T. Kennedy, O. Meighan, J.-P. Mosnier, P. Zimmermann, and J. T. Costello. *Phys. Rev. A*, 61:062706, 2000.

[129] H. Kjeldsen, F. Folkmann, B. Kristensen, J. B. West, and J. E. Hansen. *Nucl. Instrum. Methods Phys. Res. B*, 234:349, 2005.

[130] K. P. Miyake, R. Kato, and H. Yamashita. *Sci. Light*, 18:39, 1969.

[131] J. B. West, K. Codling, and G. V. Marr. *J. Phys. E: Sci. Instrum.*, 7:137, 1974.

[132] H. Kjeldsen. *Cross Sections for Phototionisation of Positive Atomic Ions: Absolute Measurements using Synchrotron Radiation*. PhD thesis, 1999.

[133] J. A. Samson. *Techniques of Vacuum Ultraviolet Spectroscopy*. John Wiley & Sons Inc., 1967.

[134] G. V. Marr and J. B. West. *At. Data Nucl. Data Tables*, 18:497, 1976.

[135] K. Rinn, A. Muller, H. Eichenauer, and E. Salzborn. *Rev. Sci. Instrum.*, 53:829, 1982.

[136] J.-M. Bizau, J.-P. Champeaux, D. Cubaynes, F. J. Wuilleumier, F. Folkmann, T. S. Jacobsen, F. Penent, C. Blancard, and H. Kjeldsen. *Astron. Astrophys.*, 439:387, 2005.

[137] H. Kjeldsen, F. Folkmann, T. S. Jacobsen, and J. B. West. *Phys. Rev. A*, 69:050501, 2004.

[138] J. M. Bizau, J.-M. Esteva, D. Cubaynes, F. J. Wuilleumier, C. Blancard, A. Compant La Fontaine, C. Couillaud, J. Lachkar, R. Marmoret, C. Remond, J. Bruneau, D. Hitz, P. Ludwig, and M. Delaunay. *Phys. Rev. Lett.*, 84:435, 2000.

[139] J.-M. Bizau, D. Cubaynes, J.-M. Esteva, F. J. Wuilleumier, C. Blancard, J. Bruneau, J. P. Champeaux, A. Compant La Fontaine, C. Couillaud, R. Marmoret, and C. Remond. *Phys. Rev. Lett.*, 87:273002, 2001.

[140] J.-P. Champeaux, J.-M. Bizau, D. Cubaynes, C. Blancard, S. N. Nahar, D. Hitz, J. Bruneau, and F. J. Wuilleumier. *Astrophys. J.*, 148:583, 2003.

[141] M. Domke, K. Schulz, G. Remmers, G. Kaindl, and D. Wintgen. *Phys. Rev. A*, 53:1424, 1996.

[142] K. Codling, R. P. Madden, and D. L. Ederer. *Phys. Rev.*, 155:26, 1967.

[143] G. C. King, M. Tronc, F. H. Read, and R. C. Bradfor. *J. Phys. B*, 10:2479, 1976.

[144] H. Kjeldsen, F. Folkmann, H. Knudsen, M. S. Rasmussen, J. B. West, and T. Andersen. *J. Phys. B*, 32:4457, 1999.

[145] A. Neogi, E. T. Kennedy, J.-P. Mosnier, P. van Kampen, J. T. Costello, G. O'Sullivan, M. W. D. Mansfield, Ph. V. Demekhin, B. M. Lagutin, and V. L. Sukhorukov. *Phys. Rev. A*, 67:042707, 2003.

[146] T. B. Lucatorto, T. J. McIlrath, J. Sugar, and S. M. Younger. *Phys. Rev. Lett.*, 47:1124, 1981.

[147] J. Reader, G. L. Epstein, and J. O. Ekberg. *J. Opt. Soc. Am.*, 62:273, 1972.

[148] J. Reader. *J. Opt. Soc. Am.*, 65:286, 1975.

[149] K. T. Cheng and W. R. Johnson. *Phys. Rev. A*, 28:2820, 1983.

[150] H. P. Kelly. *Phys. Scr.*, T17:109–119, 1987.

[151] U. Köble, J. T. Costello, J.-P. Mosnier, E. T. Kennedy, and M. Martins. *J. Phys. B: At. Mol. Phys.*, 28(2):181–190, 1995.

[152] H. Kjeldsen, P Andersen, F. Folkmann H. Knudsen, B. Kristensen, J. B. West, and T. Andersen. *Phys. Rev. A*, 62:020702(R), 2000.

[153] H. Kjeldsen, F. Folkmann, F. Innocenti, L. Zuin, and J. E. Hansen. *J. Phys. B*, 35:L375, 2002.

[154] H. Kjeldsen. *Dissertation - Absolute Photoionization Cross Sections: Measurements and Applications*. University of Århus, Denmark, 2006.

[155] K. Nuroh, M. J. Stott, and E. Zaremba. *Phys. Rev. Lett.*, 49:862, 1982.

[156] M. Sano, Y. Itoh, T. Koizumi, T. M. Kojima, S. D. Kravis, M. Oura, T. Sekioka, N. Watanabe, Y. Awaya, and F. Koike. *J. Phys. B*, 29:5305, 1996.

[157] N. Watanabe, Y. Awaya, A. Fijino, Y. Itoh, M. Kitajima, T. M. Kojima, M. Oura, R. Okuma, M. Sano, T. Sekioka, and T. Koizumi. *J. Phys. B*, 31:4137, 1998.

[158] T. Koizumi, Y. Awaya, A. Fujima, Y. Itoh, M. Katajima, M. Kojima, M. Oura, R. Okima, M. Sano, T. Sekioka, N. Watanabe, and F. Koike. *Phys. Scr.*, T 71:131, 1998.

[159] E. D. Emmons, A. Aguilar, M. F. Gharaibeh, S. W. J. Scully, R. A. Phaneuf, A. L. D. Kilcoyne, A. S. Schlachter, I. Álvarez, C. Cisneros, and G. Hinojosa. *Phys. Rev. A*, 71:042704, 2005.

[160] J.-M. Bizau, C. Blancard, D. Cubaynes, F. Folkmann, J.-P. Champeaux, J. L. Lemaire, and F. J. Wuilleumier. *Phys. Rev. A*, 73:022718, 2006.

[161] A. Aguilar, J. D. Gillaspy, G. F. Gribakin, R. A. Phaneuf, M. F. Gharaibeh, M. G. Kozlov, J. D. Bozek, and A. L. D. Kilcoyne. *Phys. Rev. A*, 73:032717, 2006.

[162] P. Andersen, T. Andersen, F. Folkmann, V. K. Ivanov, H. Kjeldsen, and J. B. West. *J. Phys. B*, 34:2009, 2001.

[163] H. Kjeldsen, P. Andersen, F. Folkmann, J. E. Hansen, M. Kitajima, and T. Andersen. *J. Phys. B*, 35:2845, 2002.

[164] A. Neogi, E. T. Kennedy, J.-P. Mosnier, P. van Kampen, J. T. Costello, C. McGuinness, and G. O'Sullivan. *J. Phys. B*, 34:L656, 2001.

[165] A. Neogi, M. Martins, C. McGuinness, G. O'Sullivan, E. T. Kennedy, J.-P. Mosnier, P. van Kampen, and J. T. Costello. *J. Phys. B*, 35:1329, 2002.

[166] W. Lochte-Holtgreven. *Plasma Diagnostics*. AIP Press, New York, 1995.

[167] H. Aksela, R. Lakanen, S. Aksela, S. Sairanen, O. P. Yagashita, M. Meyer, Th. Prescher, E. von Raven, M. Richter, and B. Sonntag. *Phys. Rev. A*, 38:3395, 1998.

[168] J.-M. Bizau, P. Gérard, and F. J. Wuilleumier. *Phys. Rev. A*, 36:1220, 1987.

[169] G. H. Newsom. *Astrophys. J*, 166:243, 1971.

[170] P. C. Deshmukh and S. T. Manson. *Phys. Rev. A*, 28:209, 1983.

[171] M. W. D. Mansfield and G. H. Newsom. *Communicated by W. R. S. Garton, F R S*. 1977.

[172] M. Aymar. *J. Phys. B: At. Mol. Opt. Phys.*, 20:6507, 1987.

[173] B. Brehm and A. Bucher. *Int. J. Mass Spectrom. Ion Phys.*, 15:463, 1974.

[174] H. Hotop and D. Mahr. *J. Phys. B: At. Mol. Opt. Phys.*, 8:L301, 1975.

[175] G. Wendin. *J. Phys. B: At. Mol. Opt. Phys.*, 6:42, 1973.

[176] J. E. Hansen. *J. Phys. B: Atom. Molec. Phys.*, 8:2759, 1975.

[177] J. P. Connerade and D. H. Tracy. *J. Phys. B: At. Mol. Opt. Phys.*, 10:L235, 1977.

[178] J. P. Connerade, M. W. D. Mansfield, G. H. Newsom, D. H. Tracy, M. A. Baig, and K. Thimm. *Proc. R. Soc. Lond. A*, 290:327, 1979.

[179] S. J. Rose, I. P. Grant, and J. P. Connerade. *Proc. R. Soc. Lond. A*, 296:527, 1980.

[180] W. Mehlhorn, B. Breuckmann, and D. Hausamann. *Phys. Scri.*, 16:177, 1977.

[181] J. P. Connerade and M. A. P. Martin. *J. Phys. B: At. Mol. Opt. Phys.*, 12:L53, 1979b.

[182] B. Peart and K. Dolder. *J. Phys. B: Atom. Molec. Phys.*, 8:56, 1975.

[183] D. L. Moores and H. Nussbaumer. *J. Phys. B: Atom. Molec. Phys.*, 3:161, 1970.

[184] G. Miecznik, K. A. Berrington, P. G. Burke, and A. Hibbert. *J. Phys. B: At. Mol. Opt. Phys.*, 23:3305, 1990.

[185] V. K. Ivanov and J. B. West. *J. Phys. B*, 26:2099, 1993.

[186] A. Hibbert and J. E. Hansen. *J. Phys. B: At. Mol. Opt. Phys.*, 32(17):4133, 1999.

[187] R. A. Roig. *J. Opt. Soc. Am.*, 66:1400, 1976.

[188] I. C. Lyon, B. Peart, J. B. West, and K. Dolder. *J. Phys. B: At. Mol. Opt. Phys.*, 19:4137, 1987.

[189] M. Kutzner, D. Winn, and S. Mattingly. *Phys. Rev. A*, 48:404, 1993.

[190] M. Kutzner, V. Maycock, J. Thorarinson, E. Pannwitz, and J. A. Robertson. *Phys. Rev. A*, 66:042715, 2002.

[191] W. Schmitz, B. Breuckmann, and W. Mehlhorn. *J. Phys. B: Atom. Molec. Phys.*, 9:L493, 1976.

[192] M. D. White, D. Rassi, and K. J. Ross. *J. Phys. B: Atom. Molec. Phys.*, 12:315, 1979.

[193] Y. Itoh, T Koizumi, Y. Awaya, S. D. Kravis, M. Oura, M. Sano, T. Sekioka, and F. Koike. *J. Phys. B: At. Mol. Opt. Phys.*, 28:4733, 1995.

[194] W. Persson and S. Valind. *Phys. Scrip.*, 5:187, 1972.

[195] J. Reader and G. L. Epstein. *J. Opt. Soc. Am.*, 62:273, 1972.

[196] C. E. Moore. *Ionization Potentials and Ionization Limits Derived from the Analyses of Optical Spectra*. National Bureau of Standards, Washington, DC, 1970.

[197] M. A. Baig, M. S. Mahmood, M. Akram, and J. Hormes. *J. Phys. B: At. Mol. Opt. Phys.*, 28:1777, 1995.

[198] J. Reader and J. O. Ekberg. *J. Opt. Soc. Am.*, 62(3):464, 1972.

[199] P. Jaegle, G. Missoni, and P. Dhez. *Phys. Rev. Lett.*, 18:887, 1967.

[200] S. Smith. *Phys. Rev.*, 36:1–4, 1930.

[201] G. K. Schoepfle. *Phys. Rev.*, 47:232, 1935.

[202] M. F. Crawford, A. B. McLay, and A. M. Crooker. *Proc. R. Soc. Lond. A.*, **158**:455, 1937.

[203] R. Assous. *J. Opt. Soc. Am.*, 62:544, 1972.

[204] E. H. Pinnington, W. Ansbacher, A. Tauheed, and J. A. Kernahan. *Can. J. Phys.*, 69:594, 1991.

[205] A. J. J. Raassen, Y. N. Joshi, and J.-F. Wyart. *Phys. Lett. A*, 154:453, 1991.

[206] M. Mazzoni, Y. N. Joshi, A. Nencioni, T. Grisendi, and W. H. Parkinson. *J. Phys. B: At. Mol. Opt. Phys.*, 20:2193, 1986.

[207] J. H. Hsu, H. X. Wang, and P. C. Kuo. *J. of Magn. and Magn. Mater.*, 294:99, 2005.

[208] D. T. Morelli, D. L. Partin, and J. Heremans. *Semicond. Sci. Technol.*, 5:257, 1990.

[209] D. T. Morelli, D. L. Partin, and J. Heremans. *App. Opt.*, 8:924, 1969.

[210] J. P. Connerade, B. Drerup, and M. W. D. Mansfield. *Proc. R. Soc. Lond. A.*, 348:235, 1976.

[211] S. D. Loch, M. S. Pindzola, and N. R. Badnell. *Phys. Rev. A*, 70:052714, 2004.

[212] A. Müller, K. Tinschert, C. Achenbach, E. Salzborn, R. Becker, and M. S. Pindzola. *Phys. Rev. Lett.*, 54:414, 1984.

[213] W. Ansbacher, E. H. Pinnington, and J. A. Kernahan. *Can. J. Phys.*, 66:402, 1988.

[214] E. H. Pinnington, W. Ansbacher, J. A. Kernahan, Z. Q. Ge, and A. S. Inamdar. *Nucl. Instrum. Methods Phys. Res., Sect. B*, 31:206, 1988.

[215] W. Ansbacher, E. H. Pinnington, A. Tauheed, and J. A. Kernahan. *Phys. Scr.*, 40:454, 1989.

[216] H. Smid and J. E. Hansen. *J. Phys. B: At. Mol. Opt. Phys.*, 14:L811, 1981.

[217] J. E. Hansen. *Phys. Scr.*, 21:510, 1980.

[218] W. R. S. Garton and J. P. Connerade. *Astrophys. J.*, 155:667, 1969.

[219] M. W. D. Mansfield. *Astrophys. J.*, 180:1011, 1973.

[220] F. Gutmann and A. M. Crooker. *Can. J. Phys.*, 51:1823, 1973.

[221] A. N. Ryabtsev, S. S. Churilov, and Y. N. Joshi. *Opt. Spec.*, 88:316, 2000.

[222] A. J. J. Raassen, A. A. van der Valk, and Y. N. Joshi. *J. Phys. B: At. Mol. Opt. Phys.*, 22:13, 1989.